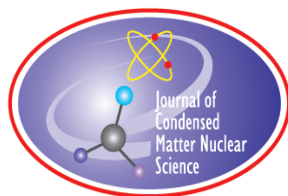


JOURNAL OF CONDENSED MATTER NUCLEAR SCIENCE

Experiments and Methods in Cold Fusion

VOLUME 31, February 2020



JOURNAL OF CONDENSED MATTER NUCLEAR SCIENCE

Experiments and Methods in Cold Fusion

Editor-in-Chief

Jean-Paul Biberian
Marseille, France

Editorial Board

Peter Hagelstein
MIT, USA

Xing Zhong Li
Tsinghua University, China

Edmund Storms
KivaLabs, LLC, USA

George Miley
*Fusion Studies Laboratory,
University of Illinois, USA*

Michael McKubre
SRI International, USA

JOURNAL OF CONDENSED MATTER NUCLEAR SCIENCE

Volume 31, February 2020

© 2020 ISCMNS. All rights reserved. ISSN 2227-3123

This journal and the individual contributions contained in it are protected under copyright by ISCMNS and the following terms and conditions apply.

Electronic usage or storage of data

JCMNS is an open-access scientific journal and no special permissions or fees are required to download for personal non-commercial use or for teaching purposes in an educational institution.

All other uses including printing, copying, distribution require the written consent of ISCMNS.

Permission of the ISCMNS and payment of a fee are required for photocopying, including multiple or systematic copying, copying for advertising or promotional purposes, resale, and all forms of document delivery.

Permissions may be sought directly from ISCMNS, E-mail: CMNSEditor@iscmns.org. For further details you may also visit our web site: <http://www.iscmns.org/CMNS/>

Members of ISCMNS may reproduce the table of contents or prepare lists of articles for internal circulation within their institutions.

Orders, claims, author inquiries and journal inquiries

Please contact the Editor in Chief, CMNSEditor@iscmns.org or webmaster@iscmns.org

Preface

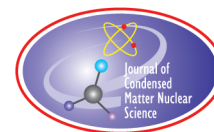
I am very pleased with the publication of this new volume of the Journal of Condensed Matter Nuclear Science. This volume includes both theoretical and experimental papers. The field is moving now at a steady pace. More data are adding credibility and understanding to the effect discovered more than 30 years ago by Professors Martin Fleishmann and Stanley Pons.

I would like to take this opportunity to thank the reviewers who are doing a very good job in improving the papers they review. This happens in many scientific journals, but here I can see that the level of help is really unprecedented.

The peer review system is not infallible, and critics and improvements are possible via comments and letters to the editor. All papers are open to discussion

Sincerely,

Dr. J.-P. Biberian
(Chief Editor)
February 2020



JOURNAL OF CONDENSED MATTER NUCLEAR SCIENCE

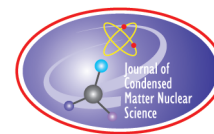
Volume 31

2020

CONTENTS

RESEARCH ARTICLES

- | | |
|---|-----|
| Plasmonic Field Enhancement at Oxide/Metal Interfaces for Condensed Matter Nuclear Fusion
<i>Katsuaki Tanabe</i> | 1 |
| Investigations of “Heat after Death” Analysis of the Factors which Determine the Tardive Thermal Power and HAD Enthalpy
<i>Mitchell R. Swartz</i> | 20 |
| A Tale of Two Journals
<i>Pamela A. Mosier-Boss and Lawrence P. Forsley</i> | 42 |
| The Eyring Rate Theory Applied to Cold Fusion
<i>Melvin H. Miles and Iraj Parchamazed</i> | 49 |
| Alternatives to Calorimetry
<i>Fabrice David and John Giles</i> | 53 |
| Heavy Electron Catalysis of Nuclear Reactions
<i>Anthony C. Zuppero and Thomas J Dolan</i> | 62 |
| Remark on Lehnert’s Revised Quantum Electrodynamics (RQED) as an Alternative to Francesco Celani’s et al. Maxwell–Clifford Equations: With an Outline of Chiral Cosmology Model and its Role to CMNS
<i>Victor Christianito, Florentin Smarandache and Yunita Umniyati</i> | 91 |
| On Enhancement of Transmission Probability through a High Potential Barrier Due to an Anti-Zeno Effect
<i>V.A. Namiot and L.Yu. Shchurova</i> | 103 |
| Atomic Nuclei Binding Energy: Case of ^{26}Fe Isotopes
<i>Philippe Hatt</i> | 113 |



Research Article

Plasmonic Field Enhancement at Oxide/Metal Interfaces for Condensed Matter Nuclear Fusion

Katsuaki Tanabe*

Department of Chemical Engineering, Kyoto University, Kyoto, Japan

Abstract

The enhancement of electromagnetic field energy density around planar metal/oxide interfaces and metal nanoparticles in oxide matrices has been quantitatively investigated, to analyze the experiments reported so far, as well as to provide a design guide for future experimental systems. We have found that a certain degree of enhancement is available for commonly used material combinations in the field of condensed-matter nuclear fusion, and use of Ag, Al, Au, and Cu would particularly provide significantly larger enhancement. This electromagnetic boosting effect may have unknowingly benefited the experiments reported so far, particularly for the electrolysis-type ones, and its active utilization by proper material and structure choices can improve condensed-matter fusion systems further.

© 2020 ISCMNS. All rights reserved. ISSN 2227-3123

Keywords: Electrolysis, Electromagnetic field, Interface, Laser, Metal, Nanoparticles, Nanophotonics, Plasmonics, Power/energy density

1. Introduction

The power density supplied to deuterium–metal systems may be one of the key factors to activate the condensed-matter nuclear fusion reaction. Free electrons in metals, particularly around metallic surfaces or interfaces with dielectric media, exhibit strong interaction with electromagnetic fields or light in a form of collective oscillation, named *surface plasmons* [1–6]. We previously proposed and analyzed the electromagnetic energy focusing effect around metal nanoparticles and nanoshells [7] and planar metal surfaces [8] to significantly increase the reaction probability. However, a number of experimental studies of condensed-matter fusion have also been conducted with oxide materials, not only with metals [9–18]. Such oxides have also been experimentally adopted mainly as mechanical supporting media for micro/nano metal particulate aggregates [14,18], as proton/deuteron-diffusion-barrier layers [15,17], or as proton/deuteron-conducting electrolytes [9–13,16]. The first and second categories consist of heterostructures of deuterium-absorbing metals, such as Pd, Ni, and Ti, and oxides, such as CaO [15,17] and ZrO₂ [14,18]. The third category comprises oxide electrolytes, such as β -alumina [9], BaCeO₃ [10,16], LaAlO₃ [13], and SrCeO₃ [10–12],

*E-mail: tanabe@cheme.kyoto-u.ac.jp.

and deuterium-absorbing metals or metal electrodes attached to the electrolytes. It is therefore important to analyze the field enhancement effects not only at metal/gas (D_2 , H_2 , or vacuum) and metal / liquid (D_2O or H_2O) interfaces as we previously investigated [7,8], but also at metal/oxide interfaces. In the present work, we calculated the plasmonic field enhancement at planar metal/oxide interfaces and around metal nanoparticles embedded in oxides.

2. Calculation Methods

We calculate the field enhancement factors, which are the intensity ratios of the fields around the object to those in the absence of the object (metals in this case), or the original incident fields, for planar metal/oxide interfaces and for spherical metal nanoparticles in oxide media. These calculations, which are based on the classical electromagnetic field theory, show quantitatively how much energy can be concentrated from the incident optical or electric power. The methods used to calculate the field enhancement factors are described in Refs. [7,8,19]. See these references for the assumptions used for the calculations and the validity range of the system for the calculation results.

For the planar-interface calculation, let ε_1 and ε_2 be the frequency-dependent complex permittivities or dielectric functions of the surrounding medium and the metal, respectively. θ is the incident angle. We assume an incidence of a p -polarized plane wave as the original electromagnetic field and its coupling into a surface-plasmon mode to determine the maximum field enhancement factors. Following the procedure described in [20], the energy flux towards the x direction per unit length in the y direction (i.e., the Poynting vector) can be formulated as

$$P_{SP} = \frac{c}{8\pi} \int_{-\infty}^{\infty} \text{Re} \left(\vec{E}_{SP} \times \vec{H}_{SP}^* \right) \cdot \hat{x} dz = \frac{\omega \varepsilon_1}{16\pi} \frac{|\vec{E}_{SP}(0^+)|^2}{|q_1|^2 + |k_{SP}|^2} \text{Re} \left\{ \frac{k_{SP} (\varepsilon_1 q_1' + \varepsilon_2 q_2')}{\varepsilon_2 q_1' q_2'} \right\}, \quad (1)$$

where c is the speed of light, \vec{E}_{SP} and \vec{H}_{SP} are the electric and magnetic fields of the surface-plasmon mode:

$$\begin{aligned} \vec{H}_{SP} &= H_y \hat{y} \exp \{ i (k_{SP} x - \omega t) - q_1 z \}, \quad z > 0 \\ &= H_y \hat{y} \exp \{ i (k_{SP} x - \omega t) + q_2 z \}, \quad z < 0, \end{aligned} \quad (2)$$

$$\begin{aligned} \vec{E}_{SP} &= \frac{c}{\varepsilon_1 \omega} H_y (i q_1 \hat{x} - k_{SP} \hat{z}) \exp \{ i (k_{SP} x - \omega t) - q_1 z \}, \quad z > 0 \\ &= \frac{c}{\varepsilon_2 \omega} H_y (-i q_2 \hat{x} - k_{SP} \hat{z}) \exp \{ i (k_{SP} x - \omega t) + q_2 z \}, \quad z < 0. \end{aligned} \quad (3)$$

H_y is the amplitude of the magnetic field of the mode. $\vec{E}_{SP}(0^+)$ is the electric field at the metal surface. ω is the frequency of the field. q_1 and q_2 are the complex wave vectors in the z -direction in the surrounding medium and the metal, respectively. k_{SP} is the complex wave vector of the surface-plasmon mode in the x -direction. The wave vectors are calculated by

$$q_j = \frac{\omega}{c} \left(\frac{-\varepsilon_j^2}{\varepsilon_1 + \varepsilon_2} \right)^{1/2} \quad (j = 1, 2), \quad (4)$$

$$k_{SP} = \frac{\omega}{c} \left(\frac{\varepsilon_1 \varepsilon_2}{\varepsilon_1 + \varepsilon_2} \right)^{1/2}. \quad (5)$$

The real and imaginary parts of complex quantities are indicated by primes and double primes, respectively. The energy dissipation flux of the surface plasmon mode is then

$$-\frac{dP_{\text{SP}}}{dx} = \alpha P_{\text{SP}} = 2k_{\text{SP}}'' P_{\text{SP}} = \frac{\omega \varepsilon_1}{8\pi} k_{\text{SP}}'' \frac{|\vec{E}_{\text{SP}}(0^+)|^2}{|q_1|^2 + |k_{\text{SP}}|^2} \text{Re} \left\{ \frac{k_{\text{SP}}(\varepsilon_1 q_1' + \varepsilon_2 q_2')}{\varepsilon_2 q_1' q_2'} \right\}, \quad (6)$$

where α is the absorption constant. On the other hand, the energy flux provided into the metal surface by the coupling of the external field into the surface-plasmon mode can be written as

$$\frac{c}{8\pi} \varepsilon_1^{1/2} \cos \theta |\vec{E}_0|^2 (1 - R), \quad (7)$$

where \vec{E}_0 is the electric field of the incident wave, or namely the external field. R is the reflectivity at the metal surface. In the steady state, those two energy fluxes are equal to each other based on the conservation of energy, and therefore

$$\frac{\omega \varepsilon_1}{8\pi} k_{\text{SP}}'' \frac{|\vec{E}_{\text{SP}}(0^+)|^2}{|q_1|^2 + |k_{\text{SP}}|^2} \text{Re} \left\{ \frac{k_{\text{SP}}(\varepsilon_1 q_1' + \varepsilon_2 q_2')}{\varepsilon_2 q_1' q_2'} \right\} = \frac{c}{8\pi} \varepsilon_1^{1/2} \cos \theta |\vec{E}_0|^2 (1 - R). \quad (8)$$

We come to derive the field enhancement factor this way:

$$\eta \equiv \frac{|\vec{E}_{\text{SP}}(0^+)|^2}{|\vec{E}_0|^2} = \frac{c(|q_1|^2 + |k_{\text{SP}}|^2) \cos \theta (1 - R)}{\omega \varepsilon_1^{1/2} k_{\text{SP}}'' \text{Re} \left\{ \frac{k_{\text{SP}}(\varepsilon_1 q_1' + \varepsilon_2 q_2')}{\varepsilon_2 q_1' q_2'} \right\}}. \quad (9)$$

Note that this field enhancement factor is defined as the ratio of field *intensities* and not field *magnitudes*. Weber and Ford used an approximation $\varepsilon_2'' \ll -\varepsilon_2'$. They rationalized this approximation by the non-lossy nature of the noble metals, which were the only materials they dealt with in [20], so they ended up with a much simpler formula. In contrast, we fully calculate the enhancement factors as Eq. (9) removing the approximation to properly deal with the relatively lossy metals in this study.

For the spherical-particle calculation, the method used in this study is described in [19]. In short, the field enhancement factor is calculated as

$$\eta \equiv \frac{|\vec{E}|^2}{|\vec{E}_0|^2} = \left| 1 + 2 \frac{\varepsilon_1 - \varepsilon_m}{\varepsilon_1 + 2\varepsilon_m} \right|^2, \quad (10)$$

where \vec{E} is the maximum static electric field around the metal nanoparticle, \vec{E}_0 is the original uniform electric field in the absence of the nanoparticle, and ε_1 and ε_m are the frequency-dependent complex permittivities or dielectric functions of the sphere and the surrounding medium, respectively.

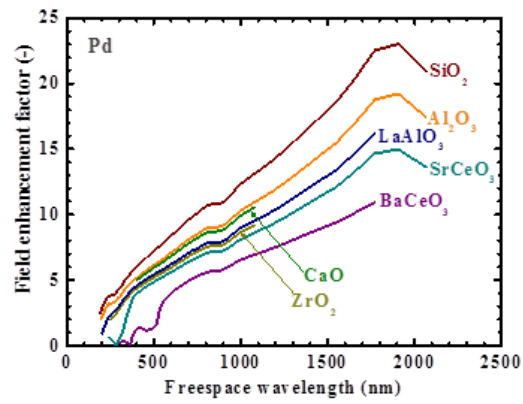
It should be noted that our calculations are only based on the Maxwell equations and involve nothing exotic or physically novel. The empirical complex dielectric functions of metals and of the most common, representative oxides SiO_2 and Al_2O_3 on frequencies listed in [19,21] are used for the computation in this paper. For dielectric functions of other oxides, we use polynomial fitting to the data in [22] for BaCeO_3 , [23,24] for CaO , [25] for LaAlO_3 , [26] for SrCeO_3 , and [24,27] for ZrO_2 in this work, as summarized in Appendix A. Incidentally, β -alumina was used in [9], but their material's details such as the composition including dopants are not available. Also, the dielectric function of β -alumina measured in [28] were close to the values of pure Al_2O_3 we previously formulated in [19]. For these reasons, we in this work adopted the dielectric function of pure Al_2O_3 (in [19]) as that of β -alumina.

3. Results and Discussion

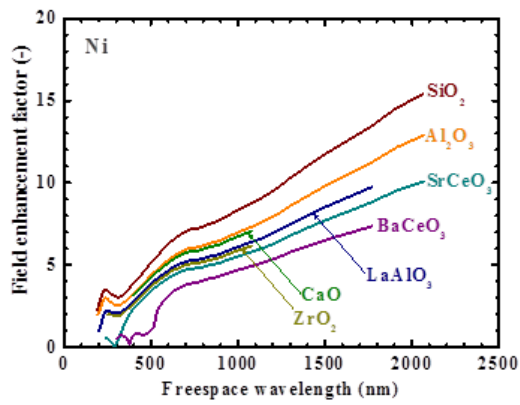
Figure 1 shows the calculated spectra of field enhancement factors at planar metal/oxide interfaces. For the reader's benefit in comparison, the same series of calculation results are organized by oxide in Appendix B. Local energy enhancement of a certain degree is seen in the spectra. The metal surfaces can this way concentrate optical or electromagnetic energy in their vicinity. Basically, oxides with smaller dielectric constants exhibit larger field enhancement, as understood with Eq. (9). Among all metal elements, Al and the noble metals Ag, Au, and Cu are known to exhibit distinctively higher field enhancement factors than other metals, due to their high conductivity [19,29]. A certain level of field enhancement, however, is still attainable even for the metals of Pd [9,10,13–15,17,30–32], Ni [18,33,34], and Ti [31,32,35], which have been conventionally used for deuterium-containing fuel materials in the field of condensed-matter nuclear fusion, as seen in Figs. 1 (a)–(c). Figure 1 (a) includes the material combinations corresponding to the experimental systems of [9,10,13]. Figure 1 (d) has the cases of [10–13,16]. Previous experimental studies with oxide electrolytes used sandwich-like double heterostructures of (Pd or Pt)/oxide/(Pd or Pt) [9–13,16]. Therefore, a certain number of the electrolysis-type condensed-matter nuclear fusion experiments reported so far may actually have unknowingly benefited from this plasmonic local energy enhancement effect. Such a plasmonic enhancement effect may be one of the multiple factors not yet understood for the energy supplied to overcome the gigantic Coulomb barrier to produce the fusion reaction observed with visible rates, as we discussed in [7,8].

Figure 2 shows the calculated spectra of field enhancement factors around metal nanoparticles in oxide matrices. For a comparison, the same series of calculation results are organized by oxide in Appendix C. The peaks seen in these spectra are associated with the resonance or surface mode, characterized by internal electric fields with no radial nodes [19]. Local energy enhancement over 10 times is seen for a wide range of optical frequencies, through visible to near infrared and beyond. These nanoparticles thus concentrate optical or electromagnetic energy in their vicinity like antennae. Similar to the case of planar metal/oxide interfaces above, Ag, Al, Au, and Cu exhibit distinctively higher field enhancement factors than other metals due to their high conductivities [19,29]. Particularly Ag has the highest electrical conductivity among the whole metal elements and therefore exhibits the highest field enhancement both for its planar interfaces and nanoparticles [19,29]. We can therefore take advantage of this high energy concentration, for instance by simply coating the conventional Pd-based fuel materials with noble metal nanoparticles. It is incidentally counterintuitive that for Ag, Au, and Cu nanoparticles the oxide electrolytes such as BaCeO₃, SrCeO₃, and ZrO₂ exhibit significantly higher peak enhancement factors rather than the representative low-index oxide SiO₂ and Al₂O₃. This is due to matching in dispersion, as seen in Figs. 2 (e), (g), and (h), and it is unlikely to be the case with the planar metal/oxide interfaces shown in Fig. 1. For Fig. 2 (f), Al is known to have plasmon resonance particularly in the shorter wavelength region [19], and therefore we unfortunately cannot produce the resonance for BaCeO₃ and CaO, whose dielectric-constant data in such a short-wavelength region was not acquired in this work, but their plots are buried in the long-wavelength region. However, it is thought that these oxides in fact also have sharp plasmon-resonance peaks in the short-wavelength region as other oxides do. A certain degree of field enhancement is still attainable even for the common metals used for condensed-matter fusion, as seen in Figs. 2 (a)–(c). Figure 2 (a) includes the material combination corresponding to the experimental system of metal nanoparticles embedded in oxide for [14]. Figure 2 (b) has the case of [18], for example. Again, a certain number of the condensed-matter fusion experiments reported so far may have unknowingly benefited from this plasmonic local energy enhancement effect. As mentioned in [7], the field-enhancement-factor spectra (peak positions, intensities) are independent of particle size under the quasistatic limit but are valid for particle diameters of 10–100 nm in this calculation [19]. Metal particles both smaller and larger than these limits exhibit broader plasmon resonances and smaller field enhancements due to surface scattering losses and radiative losses or electrodynamic damping, respectively [36,37].

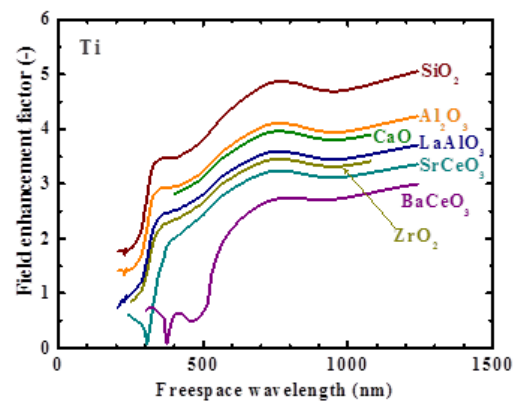
A potential picture of the condensed-matter fusion phenomena supported by the plasmonic field enhancement effect is as follows. Once an initial nuclear fusion reaction occurs in the energetic highly concentrated “hot spot”



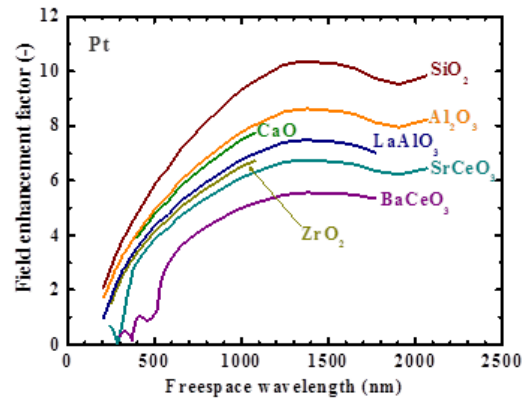
(a)



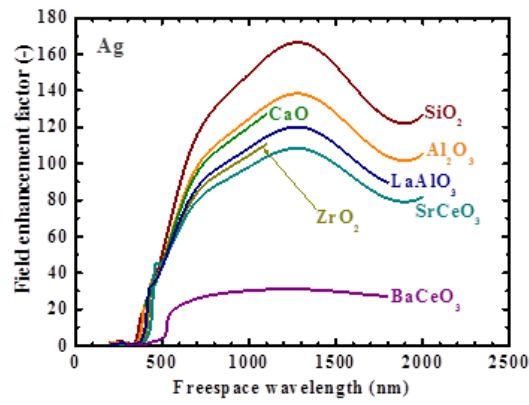
(b)



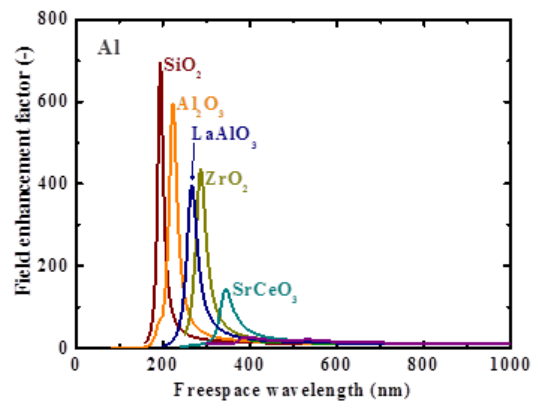
(c)



(d)



(e)



(f)

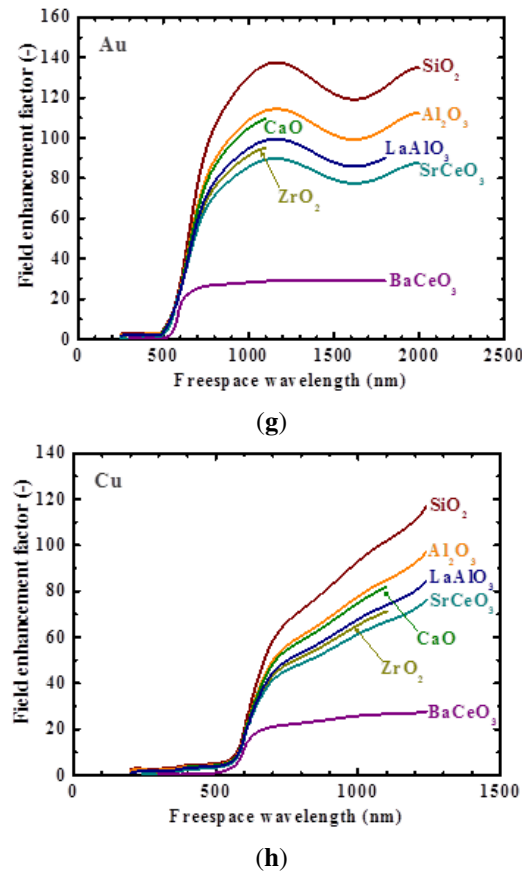
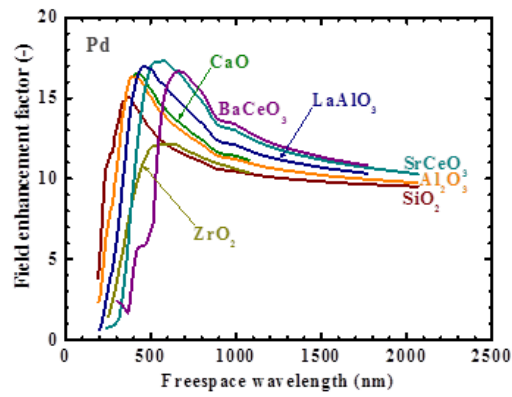
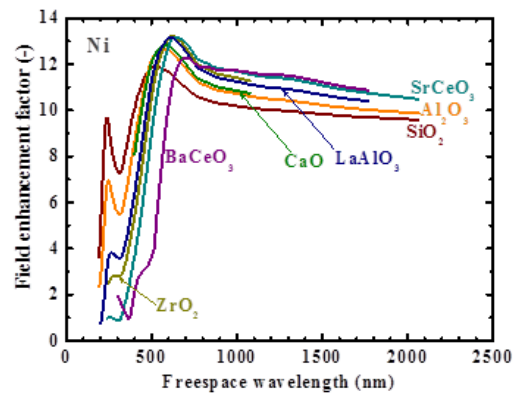


Figure 1. Electromagnetic field enhancement factors on planar metal/oxide interfaces, organized by metal: (a) Pd, (b) Ni, (c) Ti, (d) Pt, (e) Ag, (f) Al, (g) Au, and (h) Cu.

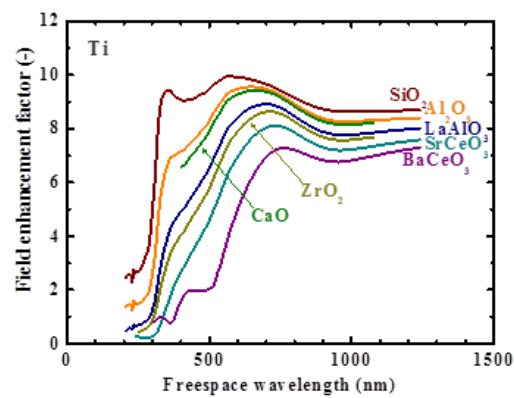
region around a metallic nanoparticulate, a gigantic amount of heat locally generated by the nuclear reaction induces subsequent reactions around the region by supplying the activation energy, and thus effectively initiates heat-mediated chain reactions to spread throughout the fuel material. The local energy focusing effect studied in this paper thus significantly increases the probability of the initial nuclear reaction even if the total power irradiated into the fuel material is the same, and therefore may effectively reduce the threshold input power. Note that the plasmonic energy focusing scheme we studied in this paper is applicable not only for the conventional electrolysis-type condensed-matter fusion but also with additional optical excitation sources such as lasers, since the electromagnetic field enhancement is equivalent for both systems. Although we dealt with stand-alone, spherical metal nanoparticles for simplicity in this paper, ellipsoidal ones would provide even higher field enhancement factors around their tips, because the sharper curvature of the metal/dielectric interfaces allows the electromagnetic field to concentrate further. This is known as the “lightning-rod effect” [38,39]. Also, surface plasmons located in between multiple metal nanostructures, or so-called “gap plasmons,” are known to have distinctive characteristics [40,41]. The size, shape, and structure aspects, as discussed in [7], should therefore be also accounted for the optimizing design of the deuterium-containing metal composite materials for condensed-matter fusion. In this work, we calculated the field enhancement factors for a



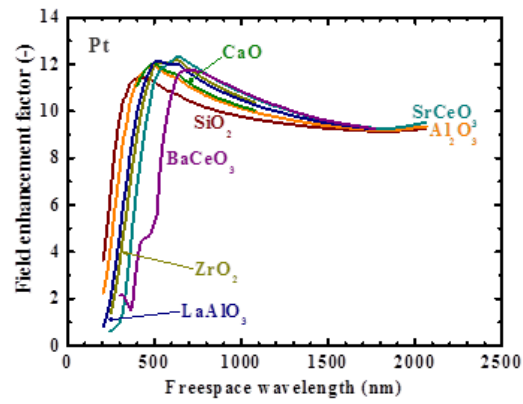
(a)



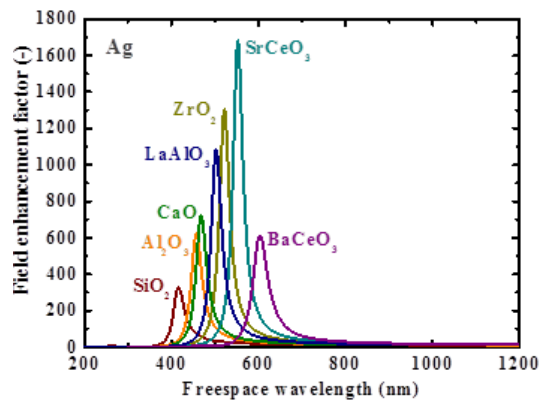
(b)



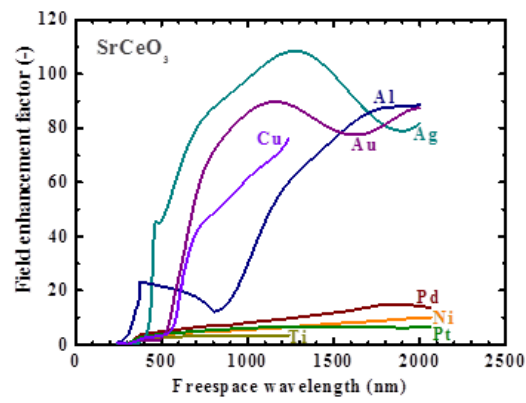
(c)



(d)



(e)



(f)

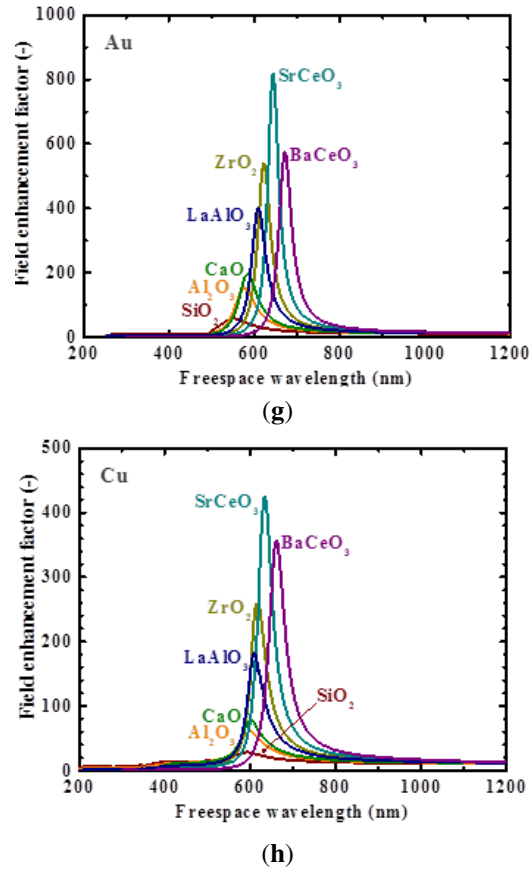


Figure 2. Electromagnetic field enhancement factors around metal nanoparticles in oxide matrices, organized by metal: (a) Pd, (b) Ni, (c) Ti, (d) Pt, (e) Ag, (f) Al, (g) Au, and (h) Cu.

certain range of frequencies, but extrapolations to longer wavelengths provide estimates for the cases of DC field or continuous-wave power application. While some of the calculation results presented in this paper correspond to the material combinations used in the experiments so far, many do not, and can be used as a guide to design future experimental systems. It should be noted that Biberian et al. reviewed a number of experimental reports using oxide materials, correlating the samples' structures with their output results, and his analysis suggests that it may be more preferable for the realization of nuclear reaction to have oxides around metal surfaces rather than inside bulk regions of metals [42]. Thus, metal/oxide interfaces can certainly play important roles in condensed-matter nuclear fusion reactions, and highly deserve further investigations.

4. Conclusion

In this work, we have quantitatively investigated the enhancement of electromagnetic field energy density around planar metal/oxide interfaces and metal nanoparticles in oxide matrices. We have shown that the metals of Pd, Ni, and Ti commonly used in the community of condensed-matter fusion intrinsically exhibit a certain degree of field enhance-

ment in the metal-oxide systems. We have also found that use of Ag, Al, Au, and Cu would particularly provide further enhancement. Our results indicate that this electromagnetic boosting effect may have been unknowingly produced in the experiments reported so far, particularly for the electrolysis-type ones, as one of the multiple factors not yet understood for the energy supplied to overcome the gigantic Coulomb barrier to produce the fusion reaction at macroscopic rates. Importantly, this plasmonic enhancement occurs in the case of an optical-power incidence as well as an electric-bias application. It is therefore desirable to design and optimize the experimental systems, including the choice of materials, structures, and operating conditions, while accounting for the plasmonic energy enhancement effect around the metal/oxide interfaces.

Acknowledgement

This work was financially supported, in part, by the Thermal and Electric Energy Technology Foundation.

References

- [1] R.H. Ritchie, *Phys. Rev.* **106** (1957) 874.
- [2] C.F. Bohren, *Am. J. Phys.* **51** (1983) 323.
- [3] J.B. Pendry, *Phys. Rev. Lett.* **85** (2000) 3966.
- [4] J.R. Lakowicz, *Anal. Biochem.* **337** (2005) 171.
- [5] M.A. Noginov, G. Zhu, A.M. Belgrave, R. Bakker, V.M. Shalae, E.E. Narimanov, S. Stout, E. Herz, T. Suteewong and U. Wiesner, *Nature* **460** (2009) 1110.
- [6] K. Tanabe, *Nanoscale Res. Lett.* **11** (2016) 236.
- [7] K. Tanabe, *J. Condensed Matter Nucl. Sci.* **24** (2017) 296.
- [8] K. Tanabe, *J. Condensed Matter Nucl. Sci.* **27** (2018) 152.
- [9] E. Granite and J. Jorne, *J. Electroanal. Chem.* **317** (1991) 285.
- [10] A.L. Samgin, A.N. Baraboshkin, I.V. Murigin, S.A. Tsvetkov, V.S. Andreev and S.V. Vakarin, *Proc. 4th Int. Conf. Condensed Matter Nucl. Sci.* **3** (1993) 65.
- [11] T. Mizuno, T. Akimoto, K. Azumi, M. Kitaichi, K. Kurokawa and M. Enyo, *Fusion Technol.* **29** (1996) 385.
- [12] R.A. Oriani, *Fusion Technol.* **30** (1996) 281.
- [13] J. Biberian, G. Lonchamp, L. Bonnetain and J. Delepine, *Proc. 7th Int. Conf. Cond. Matter Nucl. Sci.*, 1998, p. 27.
- [14] Y. Arata and Y. Zhang, *Proc. Jpn. Acad. B* **78** (2002) 57.
- [15] Y. Iwamura, M. Sakano and T. Itoh, *Jpn. J. Appl. Phys.* **41** (2002) 4642.
- [16] A. Santucci, V. Esposito, S. Licoccia and E. Traversa, *Abst. 15th Int. Conf. Cond. Matter Nucl. Sci.*, 2009, p. 57.
- [17] T. Hioki, N. Takahashi, S. Kosaka, T. Nishi, H. Azuma, S. Hibi, Y. Higuchi, A. Murase and T. Motohiro, *Jpn. J. Appl. Phys.* **52** (2013) 107301.
- [18] A. Kitamura, A. Takahashi, K. Takahashi, R. Seto, Y. Matsuda, Y. Iwamura, T. Itoh, J. Kasagi, M. Nakamura, M. Uchimura, H. Takahashi, T. Hioki, T. Motohiro, Y. Furuyama and M. Kishida, *J. Condensed Matter Nucl. Sci.* **24** (2017) 202.
- [19] K. Tanabe, *J. Phys. Chem. C* **112** (2008) 15721.
- [20] W.H. Weber and G.W. Ford, *Opt. Lett.* **6** (1981) 122.
- [21] E.D. Palik (Ed.), *Handbook of Optical Constants of Solids*, Academic Press, Orland, 1985.
- [22] M. Aycibin, B. Erding and H. Akkus, *J. Electron. Mater.* **43** (2014) 4301.
- [23] C.J. Liu and E.F. Sieckmann, *J. Appl. Phys.* **37** (1966) 2450.
- [24] R. Adair, L.L. Chase and S.A. Payne, *Phys. Rev. B* **39** (1989) 3337.
- [25] C.M. Nelson, M. Spies, L.S. Abdallah, S. Zollner, Y. Xu and H. Luo, *J. Vac. Sci. Technol. A* **30** (2012) 061404.
- [26] F. Goubin, X. Rocquefelte, M. Whangbo, Y. Montardi, R. Brec and S. Jobic, *Chem. Mater.* **16** (2004) 662.
- [27] J.C. Garcia, L.M.R. Scolfaro, A.T. Lino, V.N. Freire, G.A. Farias, C.C. Silva, H.W. Leite Alves, S.C.P. Rodrigues and E.F. da Silva, Jr., *J. Appl. Phys.* **100** (2006) 104103.
- [28] S.C. Adams, B. Dunn and O.M. Stafsudd, *Opt. Lett.* **13** (1988) 1072.

- [29] K. Tanabe, *Jpn. J. Appl. Phys.* **55** (2016) 08RG01.
- [30] M. Fleischmann, S. Pons and M. Hawkins, *J. Electroanal. Chem.* **261** (1989) 301.
- [31] S.E. Jones, E.P. Palmer, J.B. Czirr, D.L. Decker, G.L. Jensen, J.M. Thorne, S.F. Taylor and J. Rafelski, *Nature* **338** (1989) 737.
- [32] K.L. Wolf, N.J.C. Packham, D. Lawson, J. Shoemaker, F. Cheng and J.C. Wass, *J. Fusion Ener.* **9** (1990) 105.
- [33] R.L. Mills and S.P. Kneizys, *Fusion Technol.* **20** (1991) 65.
- [34] S. Focardi, R. Habel and F. Piantelli, *Nuovo Cimento* **107A** (1994) 163.
- [35] A. De Ninno, A. Frattolillo, G. Lollobattista, L. Martinis, M. Martone, L. Mori, S. Podda and F. Scaramuzzi, *Europhys. Lett.* **9** (1989) 221.
- [36] M. Moskovits, *Rev. Mod. Phys.* **57** (1985) 783.
- [37] E. Hao and G.C. Schatz, *J. Chem. Phys.* **120** (2004) 357.
- [38] P.F. Liao and A. Wokaun, *J. Chem. Phys.* **76** (1982) 751.
- [39] M.B. Mohamed, V. Volkov, S. Link and M.A. El-Sayed, *Chem. Phys. Lett.* **317** (2000):517.
- [40] K.H. Su, Q.H. Wei, X. Zhang, J.J. Mock, D.R. Smith and S. Schultz, *Nano Lett.* **3** (2003) 1087.
- [41] D.F.P. Pile, T. Ogawa, D.K. Gramotnev, Y. Matsuzaki, K.C. Vernon, K. Yamaguchi, T. Okamoto, M. Haraguchi and M. Fukui, *Appl. Phys. Lett.* **87** (2005) 261114.
- [42] J.-P. Biberian, I. Parchamazad and M. H. Miles, *J. Cond. Matter Nucl. Sci.* **13** (2014) 38.

Appendix A. Appendix A: Functional Fits to Dielectric Constant Data

ϵ' : real part of dielectric function, ϵ'' : imaginary part of dielectric function and λ : free space wavelength in nanometer.

BaCeO₃

$$\epsilon' = 1.288660 \times 10^{-3} \lambda^2 - 8.043836 \times 10^{-1} \lambda + 1.284666 \times 10^2$$

(300 nm < λ < 376 nm),

$$\epsilon' = -1.605052 \times 10^{-6} \lambda^3 + 2.480297 \times 10^{-3} \lambda^2 - 1.248131 \lambda + 2.119687 \times 10^2$$

(376 nm < λ < 532 nm),

$$\epsilon' = \frac{300}{\lambda - 435} + 5.28$$

(532 nm < λ < 1800 nm),

$$\epsilon'' = 2.340634 \times 10^{-4} \lambda^2 - 1.105413 \times 10^{-1} \lambda + 1.568768 \times 10$$

(300 nm < λ < 365 nm),

$$\epsilon'' = 5.498714 \times 10^{-8} \lambda^4 - 1.040972 \times 10^{-4} \lambda^3 + 7.353801 \times 10^{-2} \lambda^2 - 2.297329 \times 10 \lambda + 2.680562 \times 10^3$$

(365 nm < λ < 523 nm),

$$\varepsilon'' = \frac{40}{\lambda - 500} + 0.02$$

$$(523 \text{ nm} < \lambda < 1800 \text{ nm}).$$

CaO

$$\varepsilon' = n^2 - k^2,$$

$$\varepsilon'' = 2nk,$$

$$n = \frac{10}{\lambda - 240} + 1.814$$

$$(400 \text{ nm} < \lambda < 1100 \text{ nm}),$$

$$k = 0$$

$$(400 \text{ nm} < \lambda < 1100 \text{ nm}).$$

LaAlO₃

$$\varepsilon' = \frac{115}{\lambda - 150} + 4.03$$

$$(200 \text{ nm} < \lambda < 1800 \text{ nm}),$$

$$\varepsilon'' = \frac{9}{\lambda - 186} - 0.04$$

$$(200 \text{ nm} < \lambda < 410 \text{ nm}),$$

$$\varepsilon'' = 0$$

$$(410 \text{ nm} < \lambda < 1800 \text{ nm}).$$

SrCeO₃

$$n = 9.686165 \times 10^{-12} \lambda^6 - 1.504584 \times 10^{-8} \lambda^5 + 9.707331 \times 10^{-6} \lambda^4 - 3.331194 \times 10^{-3} \lambda^3 \\ + 6.415799 \times 10^{-1} \lambda^2 - 6.578062 \times 10 \lambda + 2.808060 \times 10^3 \\ (240 \text{ nm} < \lambda < 316 \text{ nm}),$$

$$n = \frac{50}{\lambda - 260} + 2.22 \\ (316 \text{ nm} < \lambda < 2000 \text{ nm}),$$

$$k = -4.987220 \times 10^{-12} \lambda^6 + 8.912293 \times 10^{-9} \lambda^5 - 6.597178 \times 10^{-6} \lambda^4 + 2.590263 \times 10^{-3} \lambda^3 - 5.692274 \times 10^{-1} \lambda^2 \\ + 6.641273 \times 10 \lambda - 3.213841 \times 10^3 \\ (240 \text{ nm} < \lambda < 372 \text{ nm}),$$

$$k = 0 \\ (372 \text{ nm} < \lambda < 2000 \text{ nm}).$$

ZrO₂

$$n = \frac{50}{\lambda - 150} + 2.07 \\ (250 \text{ nm} < \lambda < 1100 \text{ nm}),$$

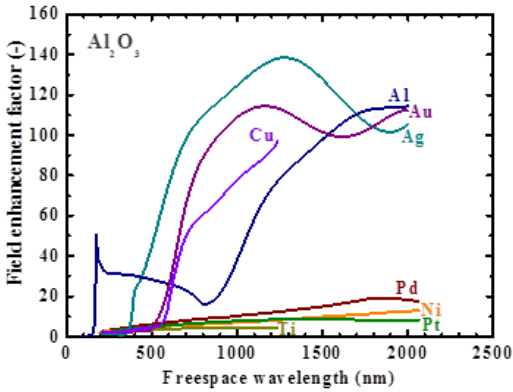
$$k = 0 \\ (250 \text{ nm} < \lambda < 1100 \text{ nm}).$$

Appendix B.

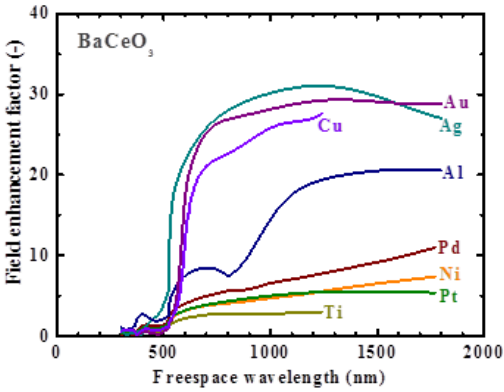
Electromagnetic field enhancement factors on planar metal/oxide interfaces, organized by oxide: Fig. 3: (a) Al₂O₃, (b) BaCeO₃, (c) CaO, (d) LaAlO₃, (e) SiO₂, (f) SrCeO₃, and (g) ZrO₂.

Appendix C.

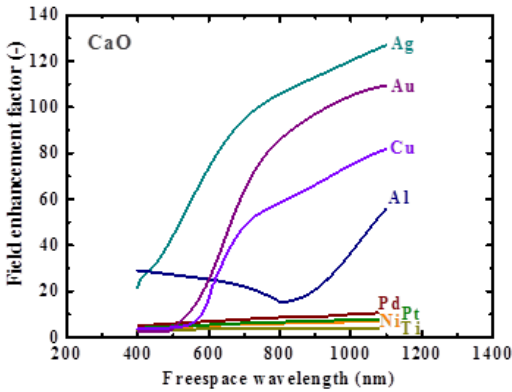
Electromagnetic field enhancement factors around metal nanoparticles in oxide matrices, organized by oxide, organized by oxide: Fig. 4: (a) Al₂O₃, (b) BaCeO₃, (c) CaO, (d) LaAlO₃, (e) SiO₂, (f) SrCeO₃, and (g) ZrO₂



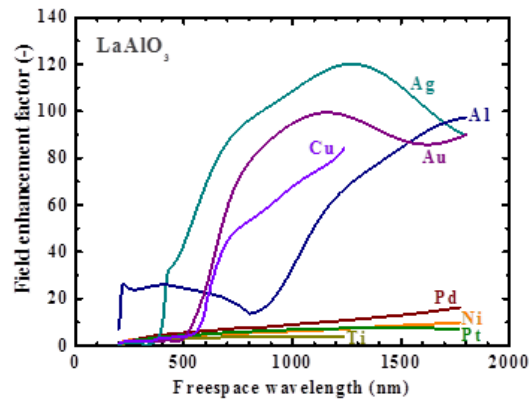
(a)



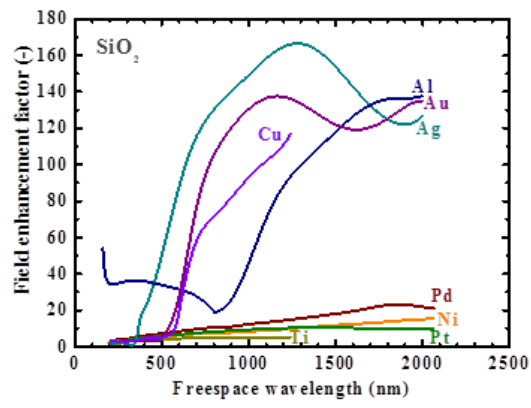
(b)



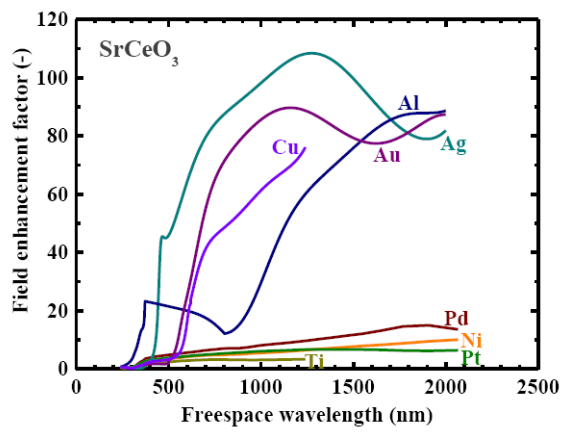
(c)



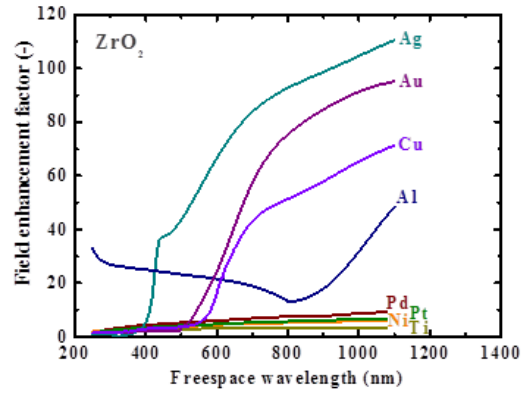
(d)



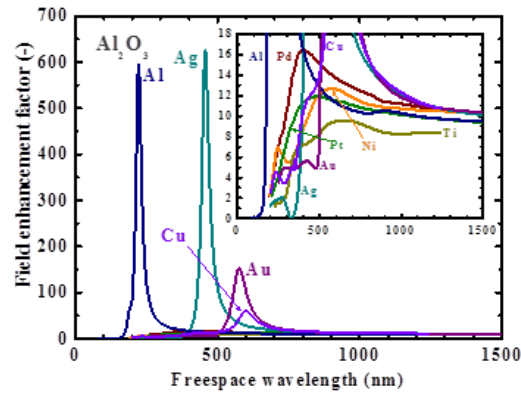
(e)



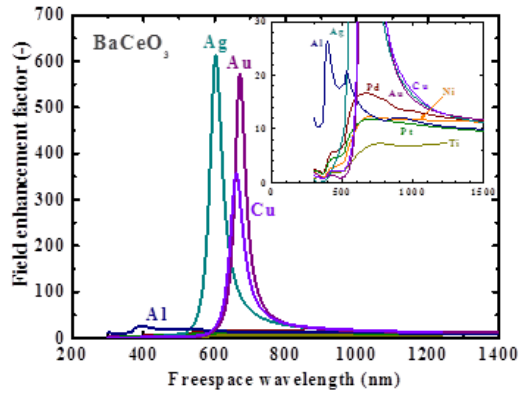
(f)



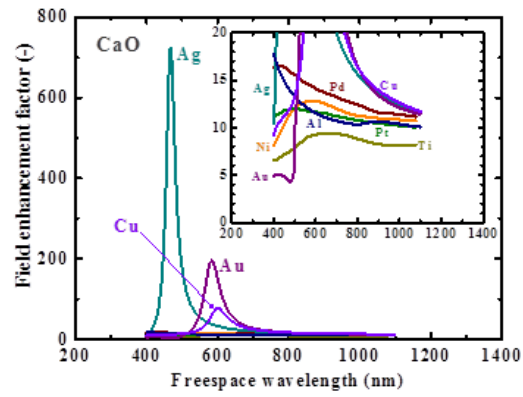
(g)

Figure 3. (a) Al₂O₃, (b) BaCeO₃, (c) CaO, (d) LaAlO₃, (e) SiO₂, (f) SrCeO₃, and (g) ZrO₂.

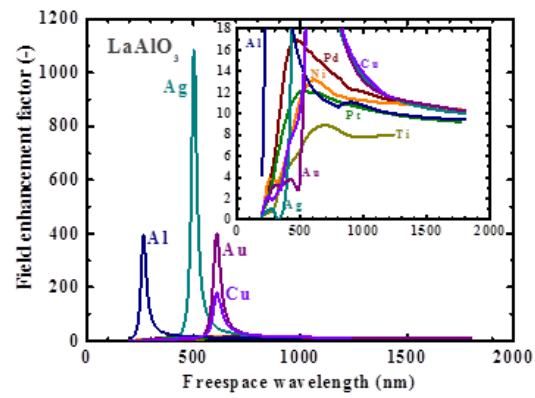
(a)



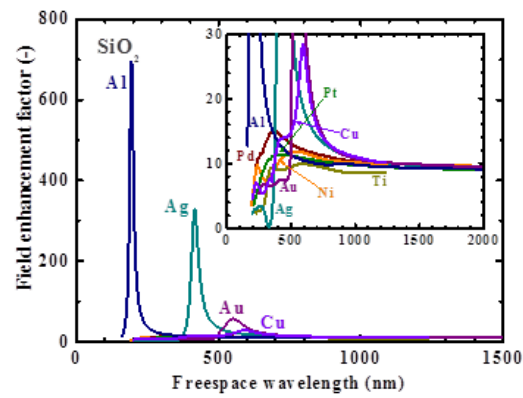
(b)



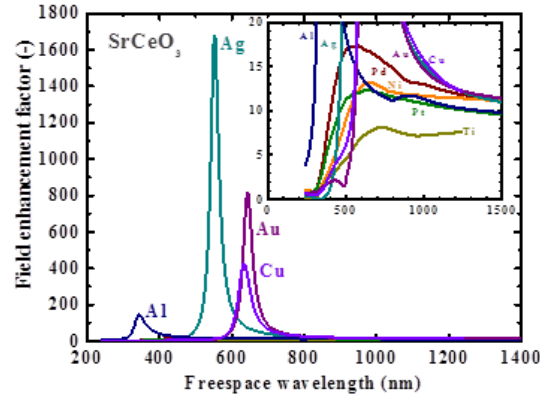
(a)



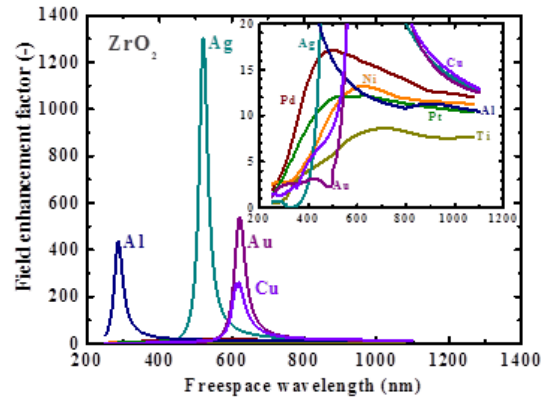
(b)



(c)

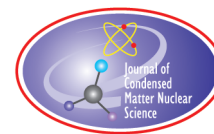


(f)



(g)

Figure 4. (a) Al_2O_3 , (b) BaCeO_3 , (c) CaO , (d) LaAlO_3 , (e) SiO_2 , (f) SrCeO_3 , and (g) ZrO_2 .



Research Article

Investigations of “Heat after Death”

Analysis of the Factors which Determine the Tardive Thermal Power and HAD Enthalpy

Mitchell R. Swartz*

JET Energy Inc., Wellesley Hills, MA 02481, USA

Abstract

This report closely examines the heat energy generated during the discharge period after cessation of all input electrical power to active CF/LANR components (“Heat after Death” or “HAD” energy). This is potentially a very important source of energy because the techniques shown here, can increase the excess energy gain of CF/LANR reactions by at least 410%. In addition, by monitoring both the calorimetry and the V_{oc} , detailed knowledge of the deuteron distribution and flows within the palladium are revealed. These experiments revealed that initially only one in 2300 deuterons takes part in the desired reactions of HAD excess enthalpy production, for a net utilization of 0.04% of the loaded deuterons at that time. This decreases over time. Integrated over the entire HAD regime, this deuteron participation levels falls, and eventually only 1 in 10^6 deuterons participates in the desired fusion reactions.

© 2020 ISCMNS. All rights reserved. ISSN 2227-3123

Keywords: Heat after death, Heterodyne excess power, Lumped parameter, Lumped component, Phusor[®], Phusor[®]-type component, Tardive thermal power

1. Introduction

1.1. Tardive thermal power and “Heat After Death”

After being successfully driven to excess heat conditions, some cold fusion systems [1–26] continue to produce significant delayed (“tardive”) thermal power (“TTP”), even after the input electric power is terminated (Fig. 1). It was first reported by Pons and Fleischmann [5] in a palladium cathode in heavy water after it was electrically driven to an active excess heat-producing state (“cold fusion”). They reported on this new phenomenon calling it “Heat After Death” (“HAD”).

*Dr. Mitchell R. Swartz ScD, MD, EE, E-mail: jet@nanortech.com.

The term “death” refers to cessation of the input electrical drive (electrical polarization) power. Aqueous cells containing D₂O were first electrically driven to boiling, and thereafter, when the electrolyte was fully electrolyzed and gone, did not cool down immediately as expected [5–9]. In one of the original HAD experiment reported by Pons and Fleischman, the electrolysis cell had finally run out of heavy water due to the electrolysis, thereby unintentionally and inadvertently creating the condition of no further input electrical power. This is due to the fact that the electrical circuit became “open circuited” and the heavy water system’s electrical circuit was cut-off.

The HAD has the units of energy. The rate of appearance (“time derivative”) of the heat after death [9–12] is the tardive thermal power. TTP is thus the heterodyne “excess” power which continues to be generated even AFTER after all of the input electrical power is terminated. The word “heterodyne” is used because of the actual denotation of the word (***). “Hetero” is an English word meaning “other”. “Dyne” is the root word of the words dynamite, dynamo and dynamic. “Dyne” comes from the Greek word dunamis (δυναμις) which means ‘power’ and was derived from the Greek translation of “koach” (קוּחַ), the Hebrew word used in the Bible to describe the miraculous deliverance of Israel at the Sea of Reeds (Exodus 15.6). Thus, with the correct denotation, tardive thermal power is the heterodyne response of an active Pd/D₂O cold fusion/LANR cell which is correctly electrically driven at its optimal operating point, with adequate phonons, and in the absence of quenching materials. (***) The popular use of heterodyne (“connotation”) is that it describes the phenomenon of a non-linear system changing of the frequency of two incoming radio signals or photons. The two are transformed to now four with the heterodyne action adding to the original two, the sum of, and difference between, the two signals (photons). In 1901, Canadian Reginald Fessenden coined the word “heterodyne”, when he invented and demonstrated his direct-conversion heterodyne receiver which made telegraphy signals audible. His unstable local oscillator (“LO”) was perfected in 1918, by American engineer Edwin Armstrong. Armstrong’s superheterodyne used a variable LO to move radio frequency signals, by dial, to the audio range making demodulation and broadcast radio possible. Nonetheless, this word “heterodyne” actually is quite precise and appropriate for HAD because it describes “power” in its denotation.

1.2. Studies of the “Heat After Death” phenomenon

Pons and Fleischmann’s (FP’s) heat after death enthalpies were reported in the range of 302–3240 J, with peak HAD excess power of 0.8 W (8 W/cm³). They described several possible HAD scenarios including those where the electrolyte solution remains or is lost, and whether boiling is achieved, along with other conditions.

Since then, HAD has been confirmed by Miles et al. [6,7], Mizuno [8] and Swartz and Verner [9–12]. Mizuno reported HAD which yielded 1.2×10^7 J over 10 days in 1991. Mengoli used an FP cell, and after five days of electrical drive, the cell is reported to have continued with HAD for 27.3 h, initially at 0.82 W.

Swartz and Verner [9–12] reported at ICCF10, and thereafter, that TTP information was resolvable using high impedance Phusor[®]-type LANR devices with “Dual ohmic control calorimeters” after they were loaded, activated, and driven at their OOP [9], and analyzed for their kinetics [10–12].

1.3. Tardive thermal power

The advantages of studying TTP are many. First, the most important advantage is that this may be one of the most electrically noise-free operational modes in which to examine the materials. During this mode of operation there is no synchronous interfering input electrical power and resultant noise. Therefore, one is able to more closely examine the time course of the rate of heat energy (HAD) generated during this discharge period, long after cessation of all input electrical power. HAD excess heat production was measured from active devices after they were initially loaded and driven for several hours.

The second advantage is that understanding this region of operation has led to maximizing the output of these systems by at least 410% (*vide infra*).

A third advantage is that “lumped component” (also called “lumped parameter”) models can be used to analyze the kinetics. The kinetics reveals HAD has more than one evanescent heat generating site [10–12] and instead multiple sites contribute to the observed TTP. HAD fall off is characterized by one site (or group of sites) with a time constant of several minutes, and a second site having a longer time constant of ~ 20 minutes to hours. This is consistent with their being vicinal surfaces and deeper sites in the volume, with the longer time constant secondary to the deeper location within the lattice. It could also be due to shallow and deeper traps. As a result, in 2005, we suggested a two-site TTP reaction system in the palladium heavy water Phusor[®]-type system. This was felt to be consistent with both the deep, and the more superficial sites, perhaps up at least to ~ 40 – $100\ \mu\text{m}$ from the surface. This plurality of sites was previously suggested by both our data, and independent, codeposition results [10–12]. Later, we added a third region to the model at ICCF-14 to account for all the involved loaded layers, from the most superficial from codeposition to the range of deeper sites [12]. This paper begins with a review of those findings, and continues with other significant discoveries from those investigations.

2. Experimental

2.1. Overview

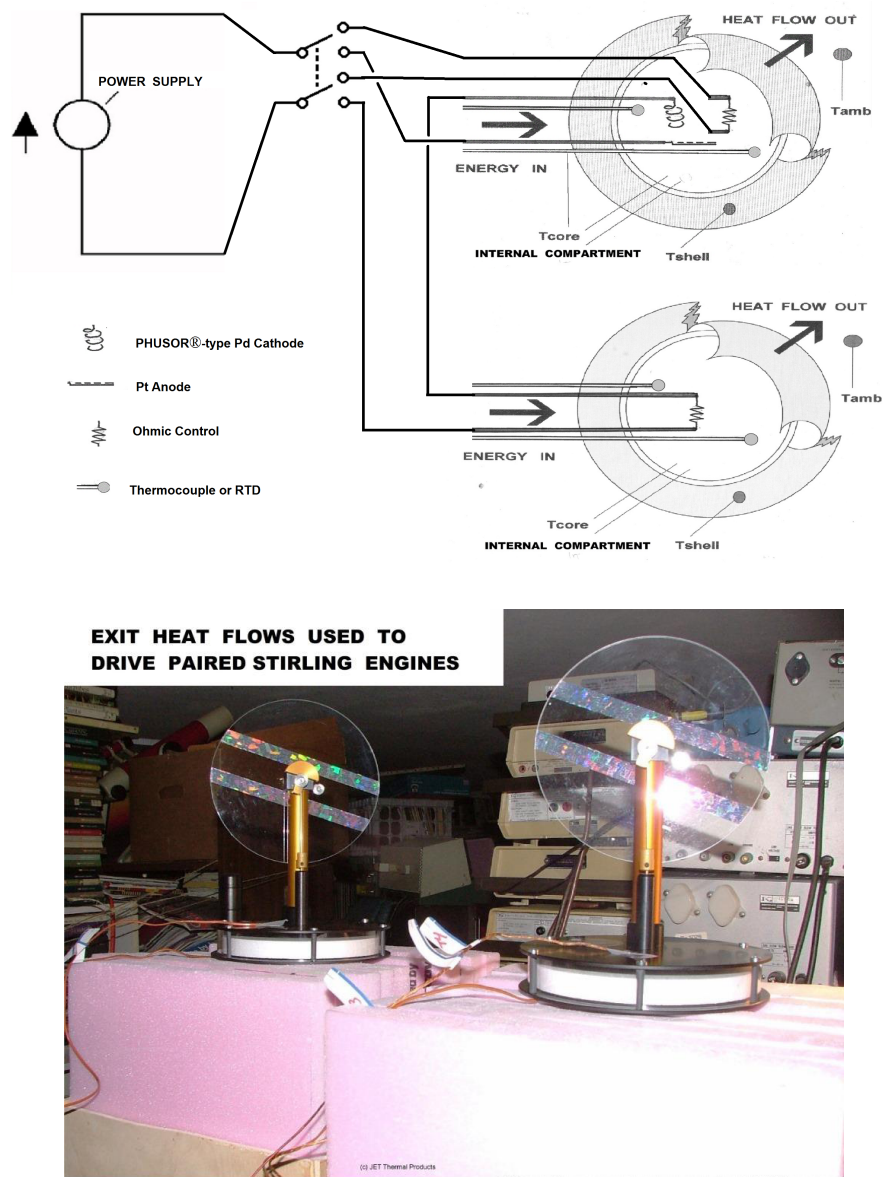
For these HAD investigations, paired joule (thermal) controls and power integration enabled TTP/HAD calorimetry with semiquantitative corrections for both cooling and deuteron-deloding. We then investigated the magnitude of heat production, including with electric discharge spectroscopy. A “lumped component” (also call a “lumped parameter”) model was used to analyze HAD not as energy only, but by using the tardive thermal power as a function of time.

2.2. Materials

These experiments used materials and procedures discussed in detail elsewhere [13–20]. The solutions were comprised of a very low electrical conductivity heavy water (deuterium oxide, low paramagnetic, 99.99%, Cambridge Isotope Laboratories, Andover, MA) to minimize the unwanted reactions of electrolysis. The volume of the heavy water solution ranged from 30 to 40 cm³. The cells are not open to the atmosphere, and efforts are made to keep ordinary water out of them, and to minimize any possible contamination, as we previously reported [13–19]. The anodes were platinum (99.998% metals basis, Alfa Aesar). The cathodes were palladium (99.98+% metals basis, Alfa Aesar).

2.3. PHUSOR[®]-type system

Figure 1 is a schematic which shows all three bottles, the electrodes, the ohmic controls, and just a small portion of the diagnostics and temperature probes. The anodes had an active metallic area of 3 cm², and a volume of 0.077 cm³. The cathodes were PHUSOR[®]-type. Previously, we reported [14,19] on excess heat obtained from PHUSOR[®]-type spiral-wound palladium cathodes (cathode volume $\sim 0.5\ \text{cm}^3$) immersed in very low electrical conductivity D₂O with no additional electrolyte, electrically polarized against a platinum anode. These devices can yield significant excess heat (peak excess power production circa 1.5 W, peak electrical power gain of ~ 2.7). Here, these types of systems are examined even more closely after termination of the applied electrical power. The PHUSOR[®]-type cathode consists of a spiral wound wire electrode with an area of 6.7 cm². The 12 turns of palladium wire created an active volume of palladium of 0.17 cm³. The enclosed volume subtended ranged from 1.6 to 58 cm³.



2.4. Calorimetric setup

The calorimetric setup used identical paired polypropylene reactor containers, and a third with no electrical connections as a local thermal control. Each identical container held 30–40 ml of heavy water, and were contained within a second, partially adiabatic, chamber [13–19]. The first container holds the CF/LANR system with the two electrodes, a palladium cathode and a platinum anode, and an internal ohmic control. The second container holds only an ohmic control. The second container was either driven alternatively with the first container holding the CF/LANR cell, or was driven in electrical series with the first cell. Normal cool-off effects of both the PHUSOR[®]-containing calorimeter and its control are eliminated by subtracting the cool-off of the paired control.

The third container, the internal background control, is not electrically connected to anything. It is a thermal ballast (an additional control of the local average background temperature) and has no internal components, except for its external temperature sensors.

Several types of calibration were used. First, we use thermal (joule) electrical ohmic controls to calibrate the system for semiquantitative accurate calorimetry. The ohmic controls are absolutely needed because calculations by brute force are likely to be quite inaccurate, as has been shown in several flow calorimetry experiments, repeatedly.

In addition, to correct for normal prosaic cool-off, in this system there were TWO ohmic controls, one in each of the paired containers constituting the calorimeter. One ohmic control is used in the main reaction vessel, containing the heavy water and the palladium cathode, to calibrate that cell. A separate ohmic control was also used in the second cell. That ohmic resistor (typically 98.6 k Ω but matched as well as possible to the working impedance of the active cell) is immersed in the identical second container.

2.5. Electrical drive

The electrodes, and control in electrical series, were electrically polarized. This causes a variety of conduction and polarization reactions including loading of the cathode with deuterons. The electrical series arrangement of the paired matched containers in this calorimeter were used as the thermal cool-off (and heat-up) control to correct for possible time-variant changes in thermal heat leakage to the environment, if any, which might occur during the experiment (as has been brought up by Dr. Shanahan, and has been corrected here for years [13–16,18,19]. In that configuration, when the CF/LANR cell is driven to examine its active mode, the electrodes are in electrical series with the joule (ohmic) control immersed in the second container, which is also used during the HAD-measurement run (Fig. 1). This arrangement can semiquantitatively correct for those possible time-variant differences in heat flow loss. Driving was usually at voltages below 150 V, by an electrical current source (Norton equivalent). Either when full loading is achieved, or when an electric potential of ~ 125 – 1500 + V is needed, we used an electrical voltage source (Thevenin equivalent). All electrical input power was terminated when the HAD regime was monitored by V_{oc} and calorimetry.

Electrical currents were derived from electrical current sources (Keithley 225), and were also measured to confirm the outputs ($\pm 1\%$ accuracy). Electrical voltage sources included the LAMBDA 340A, HP/Harrison 6525A, and the JET Energy 10K control unit. Electrical potentials were measured with high performance units ($\pm 0.5\%$ accuracy, Keithley 610C Electrometer, Keithley 160B, Dana Electronics 5900, Fluke 8350A, and HP 3455A, 5334A and 3490A voltmeters).

The actual applied electric field DOES partially penetrate the cathode as we can measure the voltage across the cathode, and it has a very small resistance which is not zero [26]. As reported, in very high impedance systems, using 4-terminal measurements experiments with anodic platinum plates (0.001–20 mA; 99.7 V, with solution impedances of circa 254 k Ω ; excess power of $\sim 175\%$) determined the cathode palladium coil (1 mm diameter) to have an impedance of circa 50 m Ω . This intracathodic E-field [26] has led to the discovery that there may even be quasiparticles and quasi-collective particles existing within the cathode, and whose behavior changes just prior to the appearance of excess heat.

2.6. Temperature measurement

Data acquisition is achieved by an Omega OMB-DaqTemp (Omega Technologies; 16 bit resolution, 200 kHz maximum sampling rate, voltage accuracy and precision of 0.015 ± 0.005 V, temperature accuracy $\sim 0.6^\circ\text{C}$ (the lower number is the accuracy, the superscript number is the precision). We use multiple temperature probes and heat flow measurements. Temperature measurements are made by several groups of thermocouples (accuracy of ± 0.8 K).

Generally there are at least two probes at the core. However, for a high temperature measurements ($>125^\circ\text{C}$) or when we fear possible quenching contamination the probes are taken to the outside of most inner vessel, and the notions are given that this may be a lower limit to the temperature of the inner container (and derived putative excess heat).

To avoid sampling errors, samples are taken at rates of at least 10 Hz. The noise of the system is mainly quantization and thermal noise and ranges from $1\ \mu\text{W}$ to $\sim 10\ \text{mW}$ [14,19]. The power gain and excess energy are determined from the differences in temperature between the heavy water cell and background.

2.7. Recombination issues are moot

Recombination issues are moot both experimentally and analytically, and it can not be the origin of these observations for several reasons. First, recombination is not relevant in these experiments because these high impedance aqueous cells were electrically driven at levels below the voltage where any significant amount of heavy hydrogen gas (D_2) was generated. This was done to minimize gas evolution – and therefore possible recombination – the CF/LANR cells, as has been taught in the author's papers since 1990s.

Second, recombination is not a factor because the electrical input is defined as $V \times I$, and the thermoneutral potential is not subtracted in any derivation. The reason that the thermoneutral potential is not subtracted in determining the power gain is because that it is in the denominator of the incremental power gain factor, and any subtraction can, and does, lead to a false positive or false magnification of the actual excess incremental power gain, if any.

Third, as reported below, we have discovered that the XSH HAD result is shown to be dependent on the magnitude of the previously applied driving voltage. This would not be present and occur this way, if this was just recombination.

2.8. Methods

2.8.1. Calorimetry data analysis

The calorimetry curves shown are derived using carefully calibrated techniques. The reader is referred back to the key papers where the two pole calorimetry, augmented by heat flow measurements, is discussed, and for space they have not been reconsidered here. This system was used at ICCF10 in the open demonstration and at many thereafter, as reported [1,9,13–15], where the methods of calorimetry were discussed.

The exact setup used to derive the excess heat results before the “HAD” region, the exact calculations of input and output power, and how the incremental power gain and excess energy are determined have been discussed in the previous papers [9,13–16, 18,19].

In these measurements, time integration of the electrical input power and output thermal power are each used to generate total energies, both input and output. Therefore, the binding energies associated with deuteron loading into the palladium, and that associated with phase changes if any, are also measured and can be resolved and considered, too.

2.8.2. Lumped component analysis

In actuality, the physics of cold fusion involves material and energy flow in a very inhomogeneous stereoconstellation of parts (“system” which becomes even more inhomogeneous on the application of the applied electric field intensity. A “lumped component” (also call a “lumped parameter”) model was used to analyze HAD, examining the tardive thermal power and V_{oc} as a function of time (Sections 5.1–5.6). This lumped parameter model simplifies this analysis by considering how the system appears when visualized as a two-wire ‘lumped component’ model. Thus, it involves the notion of two resistive, and a capacitive (storage), components.

These are first order simplifications that enable further analysis. In fact, by examining the temporal changes, lumped component electrical analysis clarifies the excess heat production which continues for several hours after cessation of input electrical power to an active loaded spiral-wound palladium cathode/ D_2O /platinum anode system.

3. Results

3.1. Post-electrical TTP measurements

The PHUSOR[®]-type CF/LANR components were initially loaded and driven for several hours and more, during the active phase. After the devices were driven, determination of the possible heat after death was made by semiquantitative analysis with semiquantitative correction for (a) the joule (thermal) ohmic controls, (b) the deloading (followed through V_{oc}), and (c) the normal cooling by the paired system.

After accounting for other sources of energy, including Poynting vector, prosaic energy storage and release, and D loading and deloading energies, D_2 and O_2 recombination, and possible phase changes, it is clear that HAD does exist for Pd, at least under these conditions (Figs. 2A,B and 3A,B). These figures show the results of four experiments producing HAD. They show TTP and its integrated E_{HAD} . Shown in Figs. 2A,B and 3B are the excess enthalpies observed during electrical activation, and after disconnection of the electrical drive (the “HAD regime”). There is significant continued emission of excess heat, long after the termination of all electric input power. Figure 3B shows the heating of a second volume of water using the HAD from the previously active cell in its heterodyne TTP-producing mode.

Figure 2A shows the calorimetry of a PHUSOR[®]-type Pd/ D_2O /Pt cell and its joule control during both the active state and during the HAD region. It shows the input electrical powers and observed output thermal powers (and energies).

There are eight curves. Four involve power and four others involve energy. They present the input electrical powers and observed output thermal powers (and energies) for a Pd/ D_2O /Pt cell and the joule control as a function of time. Eight curves are shown; four involve power; four involve energy. In Fig. 2A, the input and output powers are linear. The HAD instantaneous power (tardive thermal power) is marked.

It can be seen that the observed output thermal power is much greater compared to the electrical input power for the deuteron-loaded system, as compared to the joule control. With an initial drive potential of ~300 V to 330 V) for several hours, the Pd phusor system produced an initial peak tardive thermal power of 1.3 W (~7.7 W/cm³ [9]). The integrated HAD excess enthalpy was 5200 J, and the time constant of the falloff was ~70 min. The time was determined by curve fitting on the computer and by using exponential approximations which make the slope linear on a log time axis. Examples are shown in Figs. 4A,B and 5.

It can also be seen that for the ohmic joule (thermal) control that the integrated energies of the input and output rise with parallel slopes. By contrast, in the deuterium-loaded heavy water systems, there is a gap increasing over time, corroborating that there has been active heat generated.

The curves in Fig. 2A confirm, both by the difference between the control and observed excess power and the differential in excess energy by slope, there is excess heat output; and by the calorimeter-matched calorimetry, there is

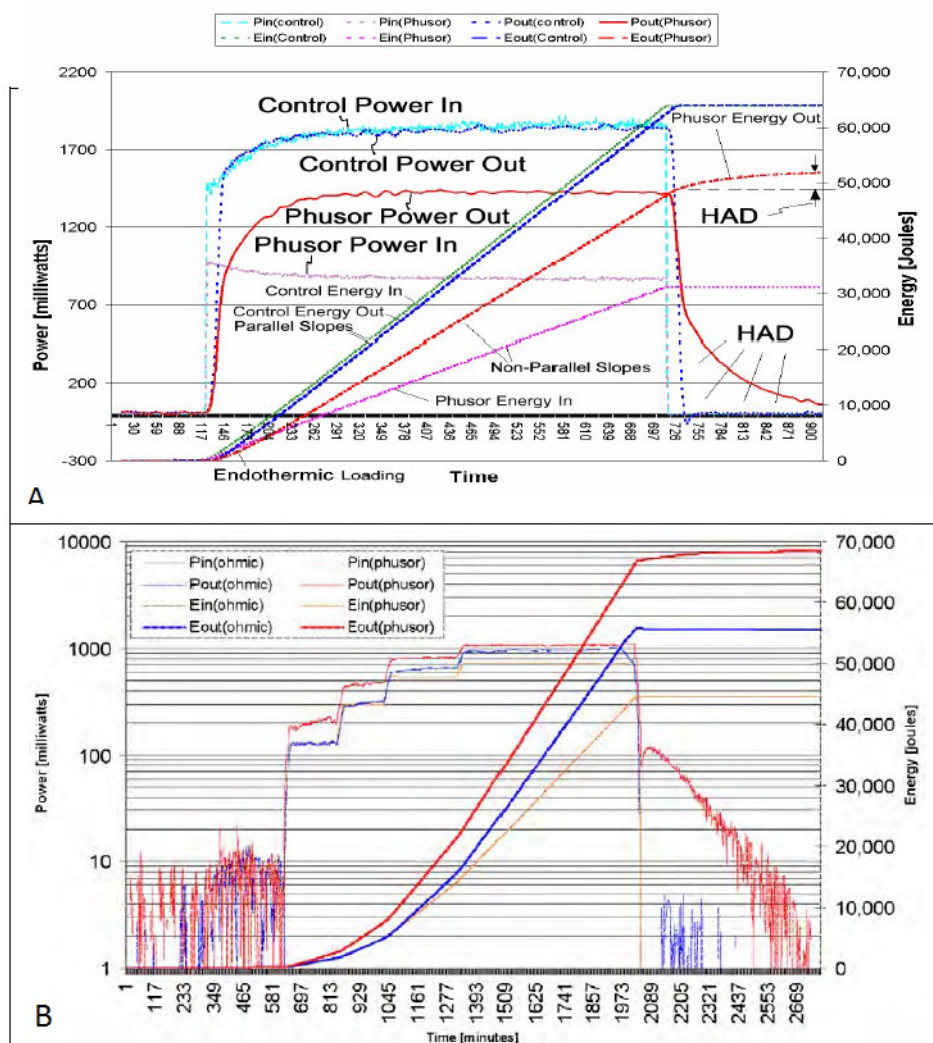


Figure 2. Calorimetry of PHUSOR®-type Pd/D₂O/Pt cells and their joule controls, showing the input electrical powers and observed output thermal powers (and energies). (A) (top) – Input electrical powers and observed output thermal powers (and energies) for a PHUSOR®-type Pd/D₂O/Pt cell and the joule control as a function of time. (B) (bottom) – Input electrical powers and observed output thermal powers (and energies) for both the heavy water PHUSOR®-type Pd/D₂O/Pt cell and the joule control as a function of time.

HAD output of this deuterium-loaded system.

Figure 2B shows the calorimetry of a PHUSOR®-type Pd/D₂O/Pt cell and its joule control during both the active state and during the HAD region. This figure, of a different run, has the input and output powers plotted on logarithmic axes so that the background noise of the system before, during the electrical drive, and after the electrical drive is finished, are clearly shown. It shows the input electrical powers and observed output thermal powers (and energies) in eight curves.

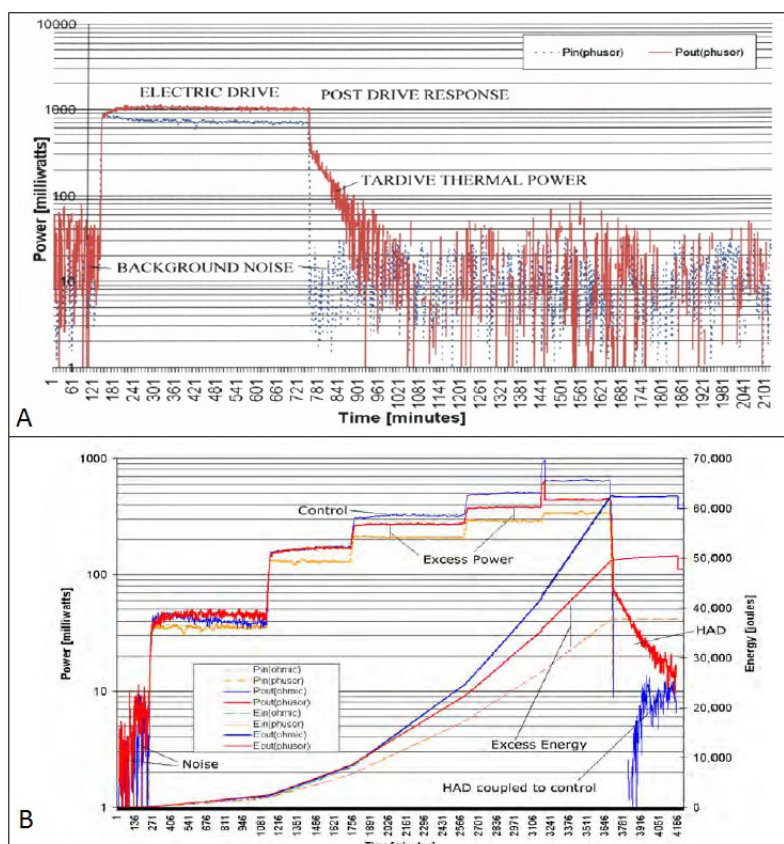


Figure 3. Calorimetry of PHUSOR®-type Pd/D₂O/Pt cells and control. (A) (*top*): Input electrical powers and observed output thermal powers as a function of time for a heavy water PHUSOR®-type Pd/D₂O/Pt cell and the joule control as a function of time. The background noise levels can be seen. (B) (*bottom*): Input electrical powers and observed output thermal powers as a function of time for a heavy water PHUSOR®-type Pd/D₂O/Pt cell and the joule control as a function of time. The background noise levels can be seen, and here they show transfer of the HAD energy to the control container which is heated (labeled HAD coupled to control)], further proving the existence of HAD.

Figure 2B shows the results of a run with a incremental excess power gain of 1.98, and peak output power of 1.1 W. The incremental excess power was 366 mW. There was an integrated excess heat of 153% beyond the input energy, which was 23,613 J. The energy obtained during HAD was 3610 J.

The active cell was driven at four levels with V_{applied} ranging from 100 to 230 V. The loading energy was 22 J. At the end of the active drive state, V_{oc} was 2.0 V, suggestively heralding the excess heat indirectly, as we reported at ICCF-10 [14–16].

It can be seen that for the ohmic joule (thermal) control that the integrated energies of the input and output rise with parallel slopes, and they overlap. By contrast, in the deuterium-loaded heavy water systems, there is a gap which increases over time, corroborating that there has been generated excess heat.

The curves in Fig. 2B confirm, both by the difference between the control and observed excess power and the differential in excess energy by slope, there is excess heat output; and by the calorimeter-matched calorimetry, there is HAD output of this deuterium-loaded system.

Figure 3A shows the calorimetry of a PHUSOR[®]-type Pd/D₂O/Pt cell and its joule control during both the active state and during the HAD region. In this case, they had a slightly different adiabatic shell and is designed as a 6000Neo1-modified PHUSOR[®]-type system. The “Neo” refers to the neoprene isolation chamber used in the system.

This figure, of an additional different run, has the input and output powers plotted on logarithmic axes so that the background noise of the system before, during the electrical drive, and after the electrical drive is finished, are clearly shown.

Figure 3A shows the results of a run with a incremental excess power gain of 2.23 (223% beyond the input electrical power), and peak output power of 1.26 W. The incremental excess power was 293 mW. The integrated excess energy was 144% beyond the input which was 11,839 J. The energy obtained during HAD was 1558 J. V_{applied} was 600 V. The curves in Fig. 3A confirm by the difference between the control and observed excess power, there is excess heat output; and by the calorimeter-matched calorimetry, there is HAD output of this deuterium-loaded system.

Figure 3B is very important. It presents the very first time tardive thermal power (the time derivative of HAD energy) was used to heat another volume of water. This transfer of energy from HAD to a second volume is shown clearly, further proving the existence of HAD. This region is labeled (“HAD coupled to control”). Figure 3B shows the calorimetry of a PHUSOR[®]-type Pd/D₂O/Pt cell and its joule control during both the active state and during the HAD region. Presented are the input electrical powers and observed output thermal powers as a function of time for a PHUSOR[®]-type Pd/D₂O system over a four day run. Shown in Fig. 3B are four power curves, and four energy curves, but because two overlap so well, only three are easily observed. This figure, of a very different run, has the input and output powers plotted on logarithmic axes so that, again, the background noise of the system before, during the electrical drive, and after the electrical drive is finished, are clearly shown.

Figure 3B shows the results of a run with a incremental excess power gain of 1.70, and peak output power of 460 mW. The incremental excess power was 140 mW. There was an integrated excess heat of 134% beyond the input energy, which was 12,681 J. The energy obtained during HAD was 1011 J. The loading energy was 8 J. The system shown in Fig. 3B was driven at five levels with V_{applied} ranging from 50, 100, 130, 155, to 170 V. V_{oc} ranged from 1.7 to 2.1 V, consistent with excess heat.

It can be seen that for the ohmic joule (thermal) control that the integrated energies of the input and output rise with parallel slopes, and they overlap. By contrast, in the deuterium-loaded heavy water systems, there is a gap which increases over time, corroborating that there has been generated excess heat.

There is significant transfer of energy to the ohmic control volume as demonstrated convincingly by the rising in its thermal background (labeled where the background rises from circa 2 mW to circa 10 mW equivalent background power).

Therefore, the curves in Fig. 3B confirm, both by the difference between the control and observed excess power and the differential in excess energy by slope, there is excess heat output; and by the calorimeter-matched calorimetry and by the transfer of heat to the control compartment, there is HAD output of this deuterium-loaded system.

Furthermore, the existence of energy (heat) transfer to the second container proves conclusively that this is no ordinary cool-off, but that excess energy continues to be made by the CF/LANR system – even after cutoff of the applied electric field intensity.

3.2. Determination of time constants from decay rates

Time constants are observed in both the measured “excess” enthalpy after disconnection of the electrical driving source, and also in the V_{oc} (observed by “electric discharge spectroscopy”) also during that period. The decline in excess heat and the V_{oc} are presumably be related to loss of deuterons from the previously fully loaded cathode (“deloading”). In that light, the decline occurs because the lowest energy of the PdD₂ alloy system appears to be at a loading between approximately 0.25 and 0.45.

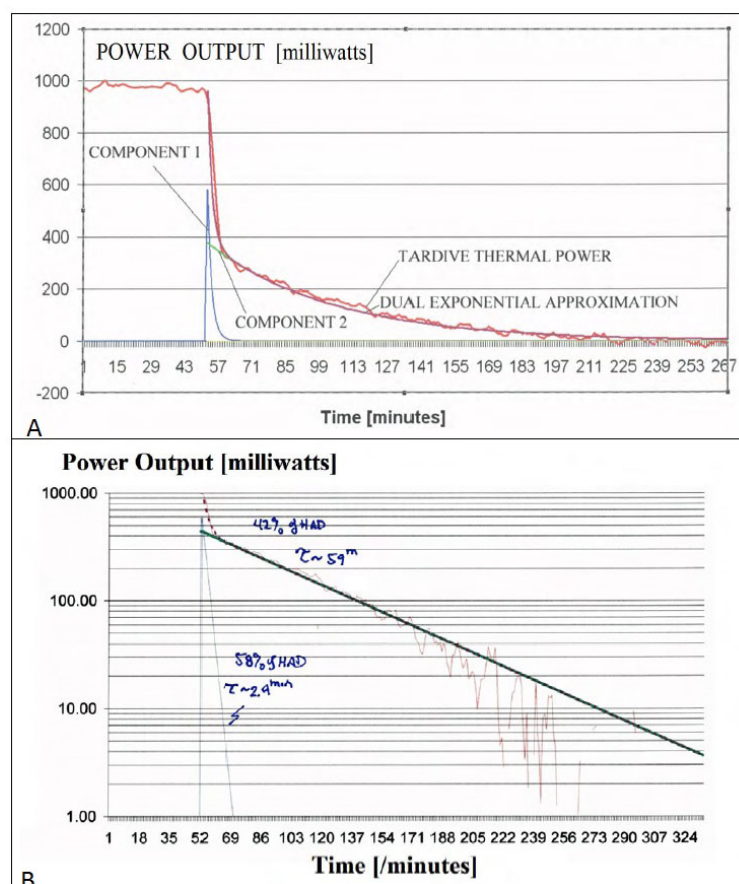


Figure 4. Demonstration of Multiple Time Constants in TTP and V_{OC} . (A) (top): TTP discharge spectrum of a Pd/D₂O system (6000Neo1-type PHUSOR®) with a power gain of 2.23, and an incremental integrated excess heat of 1.44%. (B) (bottom): TP discharge spectrum of a Pd/D₂O system 6000Neo1-type PHUSOR® with a power gain of 3.66, and an integrated excess heat of 173%.

The time constants were determined by computer fit using standard packages, and is also clearly seen in Figs. 4B and 5 where the horizontal times are arranged to make the exponential fall-off appear as a straight line.

Close examination of the TTP as a function of time shows that there are two, or sometimes, three, time constants involved. The presence of two- and then three-compartment models being required to fit the falloff V_{oc} data of the tardive thermal power was discussed at ICCF14 [21,24]. Whether these are determined by deuterons being in shallow or deep energy traps, or by the deuterons (also) being at disparate locations within the palladium (which they are clearly because there is the codepositional surface and the sites deeper within the loaded Pd) is not clear at the moment. Three examples follow; two demonstrating a 2-compartment model.

Figure 4A shows the TTP discharge spectrum of a Pd/D₂O system (6000Neo1-type PHUSOR®) with a power gain of 2.23, and an incremental excess power was 293 mW. The integrated excess heat was 1.44% beyond the input which was 11,839 J. The HAD energy was 1,558 J. The time constants are ~2 and 53 min, using the 2-compartment model. These comprise 60% and 40% of the loaded sites within the palladium respectively.

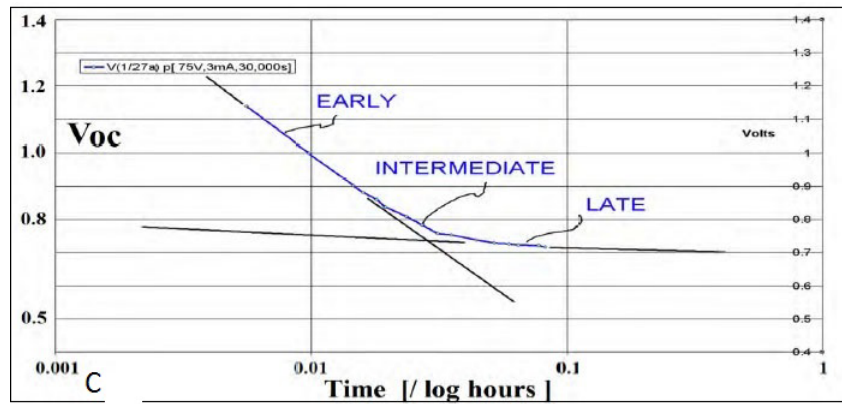


Figure 5. Demonstration of multiple time constants in TTP and V_{oc} . V_{oc} (open circuit) Discharge spectrum of palladium electrode 3-compartment TTP discharge spectrum of a Pd/D₂O system PHUSOR®) with a power gain of, and an integrated excess heat of beyond the input. Three time constants are seen suggesting a possible need for a three-site model. $V_{applied}$ was 75 V, delivering circa 3 mA current for circa 30,000 s.

Figure 4B shows the TTP discharge spectrum of a Pd/D₂O system (6000Neo1-type PHUSOR® with a power gain of 3.66 (366%), and an integrated excess heat of 173% beyond the input which was 10,104 J. The HAD energy was 206 J. The peak output power was 1.26 W. $V_{applied}$ was 600 V. The time constants are ~2.9 and 59 min. The first occupation site (shallow site) constituted about 58% of the palladium.

3.3. Electric discharge spectroscopy

We have reported that electric discharge spectroscopy is extremely useful, and that it offers insight into excess heat and as to whether adequate loading has been achieved for a palladium sample [10–12]. The open circuit voltage (V_{oc} ; remnant voltage after cessation of the electrical input) is the measured electric potential between the deuterium-loaded palladium cathode and the anode of platinum, beginning immediately after the active phase. After charging, if the voltage source (or electric current source) is disconnected, the open circuit voltage (V_{oc}) between the palladium and the anode can be followed as a function of time [10–12]. The post-electrical excess enthalpy can be followed *in situ* by the open-circuit voltage (V_{oc}).

Figures 4A,B and 5 show the examples of electric discharge spectroscopy during the heat after death phenomenon. Shown is the electrical discharge spectrum of a palladium electrode after full loading achieved by driving the system with 75 V, 3 mA, for 30,000 s. The vertical axis is the open circuit voltage, V_{oc} . This electric discharge spectrogram is made by following the V_{oc} while also measuring the excess enthalpy after disconnection of the electrical driving source. There is enough resolution that it is apparent that there are probable three regions of electrical discharge behavior [19,21,24].

The decay rate of all active Pd/D₂O samples studied has been similar, both in time, and in the fact that they appear to consist of at least two, possibly three contributing independent decay rates.

It is not clear why there is linear falloff of the TTP. It may be due to the deloading which is limited by the surface. It may be due to the fact that the heterodyne tardive thermal power strictly follows the V_{oc} which has linear fall off in the early exponential region.

3.4. V_{oc} Can Herald excess heat and HAD

Previously, we reported [10–12] that the post-drive open circuit voltage (V_{oc}) is a useful predictor of excess heat generation, and that there is a threshold potential V_{oc} required for the excess heat generation. A V_{oc} greater than 0.7 V (threshold) is consistent with generated excess heat [14], as follows: Prior to full loading and activation of excess heat, the V_{oc} remains on the order of, or less than, ~ 0.7 V, and the palladium–platinum system does not demonstrate excess heat. However, if the open circuit voltage (V_{oc}) is ~ 1.8 to 2.7 V, then excess power is observed. A V_{oc} of 1.9 V corresponds to a system with a reasonable power gain of about 170%. A V_{oc} of 2.4–2.7 V corresponds to a better system with a power gain of about 230% or more.

Given that is a dynamically evanescent exponential falloff, it is necessary to state when it is taken after cut-off of the active state. Here, it is characterized by the 1 min, and it is a useful metric of estimating how the cell/system/electrode has performed with respect to producing excess heat. It is not specific, however, and the excess heat also must be measured by calorimetry and heat flux measurements.

We now report that the post-electrical input “excess” enthalpy can be followed *in situ* by the open-circuit voltage (V_{oc}), as well. Over time, as the TTP decreases, there is a decreasing V_{oc} . The threshold potential V_{oc} required for the excess heat generation during active drive in these devices is the same threshold potential V_{oc} at which the heat after death terminates. V_{oc} at equilibrium ($V_{oc, equilibrium}$) is 0.7 V. When the HAD ceases, the V_{oc} is ~ 0.7 V.

3.5. Applied previous driving voltage is also predictive

We now report that V_{oc} alone is NOT predictive of the actual magnitude of the HAD excess enthalpy. V_{oc} and the charging voltage, $V_{applied}$ both play a role in determining the presence and magnitude of HAD excess enthalpy. TTP is controlled by the prior history of the system, including input electrical power, and if it was driven at its optimal operating point. Figure 5 shows the heterodyne TTP of a PHUSOR[®]-type Pd/D₂O/Pt cell as a function of V_{oc} and the previous $V_{applied}$ during the active drive mode, for three different experiments. The three runs were driven by three different initial filling (“drive”) applied voltages of 115, 200 and 300 V. Attention is directed to the fact that there are three characteristic curves (dependent upon $V_{applied}$) which each describe the HAD enthalpy as a function of V_{oc} (Fig. 6). The implication is that HAD enthalpy cannot be directly related to only V_{oc} because different characteristic curves are observed when HAD excess enthalpy is plotted as function of V_{oc} .

It can also be seen that the tardive thermal power decreases as V_{oc} falls, and there exists a clear threshold potential of 0.7 V. Previously, we reported that V_{oc} at equilibrium ($V_{oc, equilibrium}$) prior to a cathode showing excess heat is 0.7 V. Now when the rate of change of HAD (TTP) ceases, the V_{oc} is also ~ 0.7 V. Although these curves look as if the falloff might be in the range and 0.72–0.75 V, it is noted that there is both dispersion on the graph in the x -direction,

Table 1. Observed and Expected HAD excess enthalpies.

$V_{applied}$ (nominal) (V)	$V_{applied}$ (range) (V)	$C_{Pd,D}$ micromoles/volt †	V_{oc} 1 min ave.	V_{oc}^* (V) ‡	E expected ($C_{Pd,D} \times V_{applied} \times V_{oc}$) (J)	E observed (J)	$\frac{(O-E)}{O}$ (%)
115	107–120	64	1.5	0.8	567	700	19%
200	188–201	64	1.5	0.8	987	2,800	65%
300	270–330	64	1.6	0.9	1,665	5,200	68%

†The star (*) is added to remind the reader that the units are voltage, but the value is semiquantitatively corrected with respect to the equilibrium threshold potential ($V_{oc, equil}$).

‡This is a lower limit because of the averaging process.

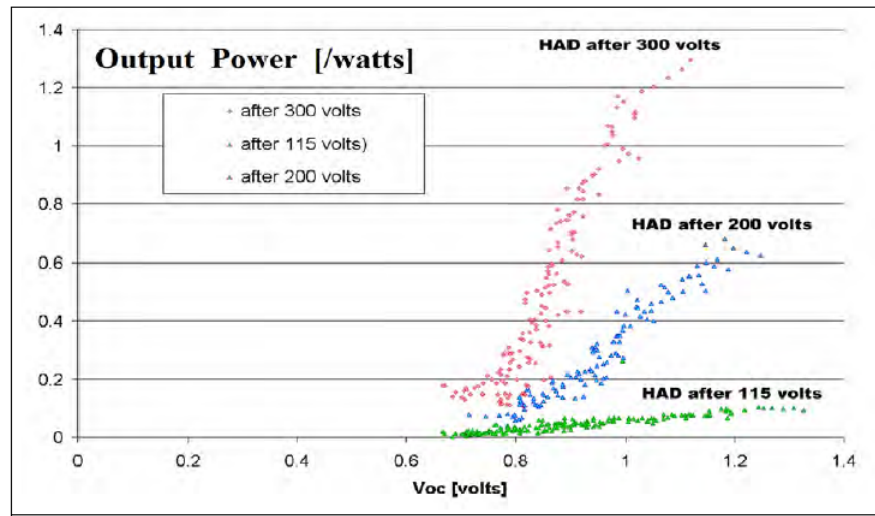


Figure 6. Tardive thermal power as a function of V_{oc} and $V_{applied}$, after disconnection of all input electrical power, for three different experiments (input drive potentials from 115 to 300 V) as a function of V_{oc} .

and there appears to be a horizontal component close to the x -axis for some of the curves.

There are three important conclusions. First, V_{oc} alone is NOT predictive of the actual magnitude of the HAD excess enthalpy, as stated above, since there are several HAD- V_{oc} curves. In fact, the observed and expected HAD excess enthalpies based on the linear model is shown in Table 1, and is fairly good above 160 V applied during the active phase.

Second, most importantly, the charging voltage used to drive the system before the HAD plays a major role in the HAD excess enthalpy. In the HAD regime, the HAD enthalpy is controlled by V_{oc} and $V_{applied}$. In each case, the excess enthalpy (HAD) increases with V_{oc} .

Third, there is a threshold V_{oc} potential for successful HAD which is ~ 0.7 V.

4. Interpretation

4.1. The engineering results

4.1.1. The control of HAD and TTP

Figure 7 shows the terrific new method used to improve the efficiency by using a duty cycle of <1.0 . Figure 7 has eight curves, and four involve power; four involve energy. Shown are the input electrical powers to the Pd/D₂O/Pt system and the control and observed output thermal powers. Also shown are the input and output energies. The input electrical powers and observed output thermal powers are in milliwatts and the energies are in joules, with the values plotted as function of minutes.

To generate Fig. 7, a series of six electrical pulses and rest periods were given, alternately to the ohmic control and the Phusor[®]-type component. During each pulse $V_{applied}$ was 200 V and the ratio of the active to the rest regime was 1:1, with each pulse width being 1 h. The times of the active drive and the rest periods define the duty cycle. Two representative pulses are labeled. After each active pulse, there is a rest period. when the electrical power source is completely disconnected. Two representative rest times are labeled (“HAD Regime”).

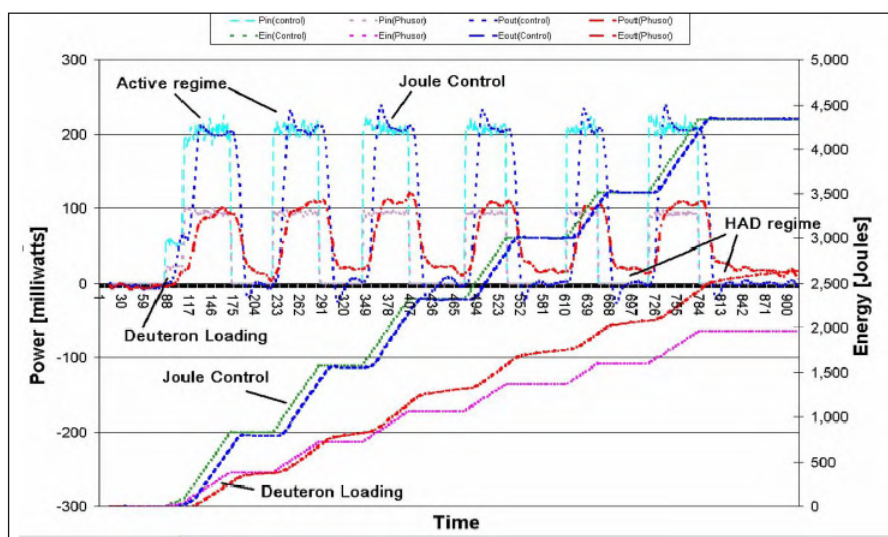


Figure 7. Calorimetry of PHUSOR®-type Pd/D₂O/Pt cell and its joule control* as a function of time, with six pulses and a 1:1 duty cycle.

The energy required for loading is small and endothermic, and is accounted for when given off. It is also small compared to the observed excess heat (and the HAD). It can be seen that the observed output power is much greater compared to the electrical input power for the deuteron-loaded Pd/D₂O/Pt device, as compared to the joule control. There is incremental excess power, and tardive thermal power, and net XSH and HAD.

Four additional curves in Fig. 7. also confirm the difference between the control and observed excess heat output of the deuterium-loaded system. They are the integrated energy curves. It can be seen that for the ohmic joule (thermal) control that the integrated energies of the input and output rise with parallel slopes. In contrast, in the deuterium-loaded heavy water systems, there is again the appearance of a gap which increases over time, corroborating that there has been excess heat generated.

Thus, these curves also demonstrate tardive thermal power and HAD. After the devices were driven for several hours, examination of the possible heat after death was made by semiquantitative analysis with correction for a joule (thermal) control, with correction for deloading, with correction for the normal cooling. After accounting for other sources of energy storage and release such as thermal cool-off and deuteron-deloading, it can be seen that HAD does exist and is clearly demonstrated by this apparatus and method.

4.1.2. Importance of HAD and TTP control

How important is this new technique? Figure 8 is a bar graph which shows the excess heat gain for a heavy water palladium Phusor®-type Pd/D₂O/Pt system, both during the active phase only, and also the summation of the active phase heat gain with the HAD gain. This set of metrics is shown for three runs, each using one of three different driving voltages. These were applied for two types of duty cycles; the first two runs were 1:1, and the last (300 V applied) was 1:5. In the figure, both the active regime energy gain (front row) and the combined gain using the HAD (back row) are plotted as for the three applied voltages.

Note that there is a significant increase in efficiency when the energy gain including the HAD region is also considered. There is an increase of excess energy 410% beyond that of the active phase alone. Notice also the major

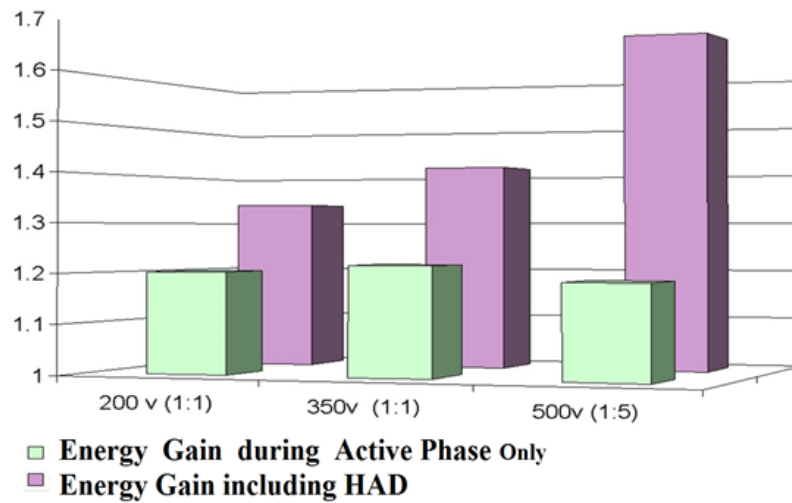


Figure 8. Energy gain in a palladium Phusor[®]-type Pd/D₂O/Pt system. The front row presents the results during the active phase, alone. The second row presents the results of both the excess energy gain and the semiquantitative HAD enthalpy in the same time period. The duty cycles are discussed in the text.

impact of applied voltage *before* the HAD regime. Thus, Fig. 8 shows the importance of this method for driving CF/LANR cells. This is not trivial in any way.

In fact, a important corollary is that some may have missed observing HAD for a new reason. The failure may have been their failure to look for HAD, or it might mean the absence of all conditions needed for making the active state, or it might indicate that the cells were driven at too low a driving voltage, or they may have had an incorrect indication of CF/LANR (false positive).

4.1.3. Lumped component engineering analysis

To understand these findings about HAD behavior, a lumped component electrical model was used to analyze the HAD excess heat production which continues for several hours after cessation of input electrical power to an active loaded spiral-wound palladium cathode/D₂O/platinum anode system. This resistor – capacitor model allows a rough analysis by separating the flow of deuterons from the charged palladium lattice after cessation of electrical input power into two loss pathways. In the model, these pathways are represented as loss resistors from the loaded (charged palladium lattice) capacitor (Fig. 9). Both V_{applied} and V_{oc} are corrected by the equilibrium threshold potential ($V_{\text{oc, equil}}$), which is 0.7 V.

As shown above, analysis of the several curves which describe the HAD excess enthalpy as a function of V_{oc} (Fig. 6) indicates that the HAD excess enthalpy cannot be directly related to solely V_{oc} . The previously applied voltage has a major role. It appears that the processes might be modeled as follows. In an electrical process, the cold fusion cell can be treated from the anode and cathode ports as a two terminal device [11]. We now analyze the cathode loading itself as a lumped component linear model using a capacitor to represent the deuteron-loaded palladium cathode. This is used for an approximation for several reasons. First, the palladium cathode is actually loaded by the applied electric field. Second, the losses by fusion and deloading offer a rough analysis by separating the two into loss resistors of a loaded (charged) capacitor (Fig. 9).

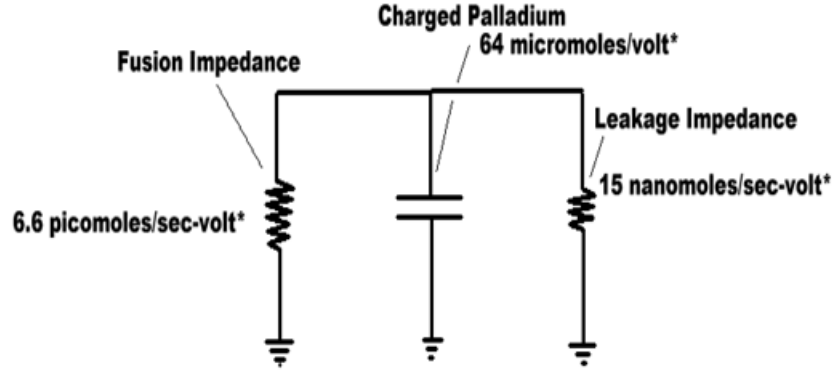


Figure 9. Lumped component linear model of a D-loaded Pd cathode. Shown is the circuit diagram of the simplified lumped component linear model using a capacitor to represent the deuterium-loaded cathode, and the two loss pathways of deuterons from the loaded cathode which are leakage and fusion. The values shown are derived in the text.

Given a cathodic electrode palladium mass, M_{Pd} , palladium's atomic weight of 106.4, the density of the pure palladium metal of 11.97 g/cm^3 , and the value of the Avogadro number, then for this electrode with an active volume of $\sim 0.17 \text{ cm}^3$, there are (at most, and probably less when the active number are considered) Q_{Pd} moles of Pd atoms.

$$Q_{\text{Pd}} \sim \text{Vol} \times \rho_{\text{Pd}} \times A_v / M_w = 0.019 \text{ (mol)}, \quad (1)$$

$$Q_{\text{Pd}} = 1.15 \times 10^{22} \text{ Pd atoms}. \quad (2)$$

For reasons discussed elsewhere [10–12], and for reasons involving the two weeks required for preparation of active cathodes, we can assume there is nearly full loading. Hence, the molar quantity of deuterons is on the order of the number of palladium atoms.

$$Q_{\text{D,Pd}} \sim 0.019 \text{ (mol)}. \quad (3)$$

We now consider the univalent deuterons which are generally believed to lose their electron when they enter the palladium metal from the surface as an equivalent charge, and use the Faraday constant, F , with the applied voltage analyzed by a linear model. Assume that V_{applied} (300 V to the PHUSOR[®]-type cell over several weeks of loading) is sufficient to yield a loading of about 1. Then, the proposed linear model based upon the results of this paper (Figs. 6 and 7) suggests that the loading, and HAD, can be handled using a lumped component model using the palladium lattice's deuterium-loading capacitance, and the loss of deuterons to either leakage (most likely) or the desired fusion reactions.

4.1.4. Pd/D capacitance ($C_{D/Pd}$)

Using an analogy to capacitors, but corrected from equivalents to moles, we can write the requirement for full loading of the palladium with deuterons (at equilibrium, but which may not occur if the solution electrical conductivity is too high, or if the palladium is cracked, or for any of many other reasons).

The capacitance is determined by the total quantity of deuterons present in the palladium electrode (“concentration”). This is an approximation because complications are that the true proportions which contribute (“activity”) may not equal the concentration, and that this is a nonlinear and non-equilibrium system when it is generating excess heat.

$$Q_{D,Pd} = C_{D,Pd} * (V_{\text{applied}} - V_{\text{oc,equl}}) = C_{D,Pd} * (V_{\text{applied}} - 0.7). \quad (4)$$

Here, as elsewhere, V_{applied} is corrected by the observed equilibrium threshold potential ($V_{\text{oc,equl}}$) of 0.7 V*. The superscript star (*) is added to remind the reader that 0.7 V is subtracted.

Since V_{applied} is about 300 V, and $Q_{D,Pd}$ is about 0.019 mol, then the active palladium lattice can be characterized by a deuteron loading capacitance, $C_{D,Pd}$, on the order of 64 $\mu\text{mol/V}$ *. Again, the star [*] is added to remind the reader that the units used are in volt, but the actual value is semiquantitatively corrected with respect to the equilibrium threshold potential ($V_{\text{oc,equl}}$). This is negligible for the 300 V initially applied, but is especially relevant during the HAD.

$$C_{D,Pd} = 6.39 \times 10^{-5} (\text{mol/V}^*). \quad (5)$$

4.1.5. Deuteron HAD fusion current ($I_{\text{HADfusion}}$)

The initial HAD excess enthalpy is about 1 W. Analysis, and independent measurements, have indicated that helium-4 production is the probable ash of these deuteron-loaded palladium reactions during the active phase [1,2,4].

The same products are probably also produced during the HAD regime, as well. Therefore, for 1 W HAD excess power, there are about 1.2×10^{12} helium nuclei generated per second. Since it takes two deuterons for each reaction, there is a putative fusion current (i.e. deuteron loss) of 2.4×10^{12} deuterons/s, or about 4 pmol/s.

$$I_{\text{HADfusion}} = 3.98 \times 10^{-12} (\text{mol/s}). \quad (6)$$

4.1.6. Admittance for fusion reactions, $Y_{\text{fusion,Pd,D}}$

In the lumped component model, during the HAD regime, the HAD fusion current, $I_{\text{HADfusion}}$, is the product of an admittance and the electric potential available (equal to the open circuit voltage minus the equilibrium threshold potential ($V_{\text{oc,equl}}$)).

$$I_{\text{HADfusion}} = Y_{\text{fusion,Pd,D}} * (V_{\text{oc}} - 0.7) (\text{mol/s}), \quad (7)$$

$$Y_{\text{fusion,Pd,D}} = 6.64 \times 10^{-12} (\text{mol/s-V}^*). \quad (8)$$

$Y_{\text{fusion,Pd,D}}$ is linear approximation of the loss of deuterons to the desired fusion reactions. $Y_{\text{fusion,Pd,D}}$ is thus the functional admittance for the HAD fusion reactions, and is about 6.6 pmol/s-V*. The star [*] is again added to remind the reader that the units used are in volt, but the value is semiquantitatively corrected with respect to the equilibrium threshold potential ($V_{\text{oc,equl}}$). This is especially important relevant during the time of the HAD.

4.1.7. Analysis of admittance for leakage ($Y_{leakage}$)

It is the inevitable loss of deuterons by leakage from the loaded palladium lattice that ultimately terminates the desired HAD reactions. The lumped component values representing deuteron-leakage can be determined from the washout of the HAD excess power. Consideration of the RC time constant of 70 min (4200 s) can be used to determine the loss resistance representing deuteron leakage.

It is reasonable to assume that deuteron loss by leakage is much greater than deuteron loss by the desired reactions, and this will be checked to confirm that the deuteron leakage resistance is much smaller than the deuteron fusion resistance, after deriving the leakage resistance. The fusion resistance is determined from the fusion admittance by an inverse function. By circuit analogy, the $Y_{fusion,Pd,D}$ has an equivalent HAD fusion resistance of 1.5×10^{11} (s-V*/mol).

$$Y_{fusion,Pd,D} = 1/R_{fusionPd,D}(\text{mol}/(\text{s-V}^*)), \quad (9)$$

$$R_{fusionPd,D} = 1.5 \times 10^{11}(\text{s-V}^*/\text{mol}). \quad (10)$$

The leakage resistance is derived using the lumped component model (see Fig. 9), where the model correctly includes the losses of deuterons to both leakage and fusion. Here, for an approximation the fusion resistance is assumed to be infinite for this calculation.

Therefore, because $C_{D,Pd} = 6.39 \times 10^{-5}$ mol/V*, then the solution can be found because the time constant, τ , is RC.

$$\tau = 4200\text{s} \cong R_{Leakage} * C_{D,Pd} = R_{Leakage}(\text{s-V}^*/\text{mol}) 6.39 \times 10^{-5}(\text{mol/V}^*). \quad (11)$$

Thus, $R_{Leakage}$ is derived to be about 6.57×10^7 s-V*/mol. Inverting this deuteron leakage resistance from actual deloading results in the deuteron loss admittance.

$$R_{Leakage} = 6.57 \times 10^7(\text{s-V}^*/\text{mol}), \quad (12)$$

$$Y_{Leakage} = 1.52 \times 10^{-8}(\text{mol}/(\text{s-V}^*)). \quad (13)$$

This value of deuteron leakage admittance must be compared to the HAD fusion admittance. Using this lumped component model, the ratio of the two admittances determines the efficiency of the desired HAD excess enthalpy reactions.

The experiments here suggest that initially only one in 2300 deuterons takes part in the desired reactions of HAD excess enthalpy production, for a net utilization of 0.04% of the loaded deuterons at that time. This decreases over time. Integrated over the entire HAD regime, this deuteron participation levels falls, and eventually only 1 in 10^6 deuterons participates in the desired fusion reactions.

The small number of the ratio is consistent with the fact that the desired reactions are infrequent to very rare. The small number is also consistent with the approximation used to derive these values.

5. Conclusions

5.1. Comparison of model with observation

In the HAD regime, the excess enthalpy appears to be controlled by V_{oc} , $V_{applied}$, and the capacitance of the cathode ($\sim 64\mu\text{mol/V}^*$). The form factor might be similar to that for other electrical engineering systems such that $E_{HADfusion}$

is related to Q_{Pd} , V_{applied} , and V_{oc} . $E_{\text{HADfusion}}$ is the energy in the filled lattice availed for, and delivered to, fusion in the HAD regime. Given the capacitance of the palladium lattice ($C_{\text{Pd,D}}$), then the total quantity of deuterons available for fusion within the loaded palladium (Q_{Pd}) is determined from V_{applied} , and $E_{\text{HADfusion}}$ is determined by both V_{applied} and V_{oc} .

$$Q_{\text{Pd}} = (C_{\text{Pd,D}} V_{\text{applied}}), \quad (14)$$

$$E_{\text{HADfusion}} = Q_{\text{Pd}} V_{\text{oc}} = (C_{\text{Pd,D}} V_{\text{applied}}) V_{\text{oc}}. \quad (15)$$

Plugging in measured and derived values for the three cases, and correcting by the Faraday, F , to correct for the use of Farads and volts, yields the results of Table 1. In the table, it can be seen that the values expected, generated by the model (E), are in the general range expected compared with the observed values of HAD excess enthalpy (O).

This fairly good correlation is encouraging. In fact, if the actual V_{oc} had been used instead of the 1 min average, then the correlations might have been more accurate, because the expected values would have increased, consistent with the higher electrical drive levels.

5.2. Final implications and summary

There remain some very important results and implications of these TTP measurements. First, TTP is apparent in palladium in heavy water driven in active excess heat-producing cold fusion systems. This is very important because the energy gain can be increased by at least 410%.

Second, the advantages of studying TTP are many. Most importantly, there is no interfering input electrical power and resultant, and inexorably associated, noise. Examination of TTP provides improved understanding of cold fusion reaction kinetics, as well as where the desired reactions occur and what are their magnitudes. However, good engineering requires that TTP voltages be redefined with respect to removing 0.7 V to make them more useful as an engineering quantity. The experiments here measured the active palladium lattice's HAD deuteron-loading capacitance which is $64 \mu \text{ mol/V}^*$. The admittance for the desired excess enthalpy HAD reactions ($Y_{\text{fusion,Pd,D}}$) is $6.6 \text{ pmol/(s-V}^*)$. That admittance is dwarfed by the system's deloading loss admittance (Y_{Leakage}) which is $15 \text{ nmol/(s-V}^*)$. This is what causes the deloading and penultimate loss of the HAD excess enthalpy.

Third, the experiments here revealed that initially only one in 2300 deuterons takes part in the desired reactions of HAD excess enthalpy production, for a net utilization of 0.04% of the loaded deuterons at that time. This decreases over time. Importantly, integrated over the entire HAD regime, this deuteron participation levels falls, and eventually only 1 in 10^6 deuterons participates in the desired fusion reactions.

There are several important implications for scientific experiments and commerce. One implication of the presence of heat after death is that complete sample characterization requires more than simply the knowledge of the power gain and the optimal operating point ("peak production") curves. Full and proper sample characterization requires measuring not only the driving manifold (which elicits knowledge of the optimal operating point) but also the changes of the sample which actually is producing TTP.

Second, another implication of this study of heat after death is that the use of a simple power gain factor to characterize a device is incomplete. It might be several times greater.

Third, these discoveries are an important group of findings because the error in measuring heat after death might be quite high, as well. This is especially true if one does not take into account the impact of duty cycle, and the previously applied electrical potential during the active state, and other issues such as HAD-region enhancing and quenching materials.

Fourth, as a corollary, others may be reporting lower limit of what is actually achieved in terms of their samples' performances. Simply put, the excess heat ("XSH") generated by an active conventional aqueous cold fusion system may be at their lower limits. The corrected sample activity is actually obtained only when using a calibrated active device which has been properly loaded, and run with the full consideration of the HAD excess enthalpy.

Fifth, there are implications involving the HAD and outgassing from proton- and deuteron-loaded metal, and the roles of gold (Swartz) and boron (Miles) and mercury (McKubre, Tanzella) must be reconsidered. Materials which control deloading are critical.

In summary, these measurements of HAD excess enthalpy, the roles of V_{oc} and $V_{applied}$ in that excess heat, and the existence of the equilibrium threshold potential ($V_{oc, equil}$), herald improved ways of both characterizing and operating deuteron-loaded palladium cathodes. Therefore, the optimization of cold fusion devices has a new dimension. Due to magnitude of the parameters involved during the HAD regime, it must be considered and factored in for optimization of any sample's true over-unity performance. Engineered-TTP [27] clearly can make some cold fusion devices and systems more efficient.

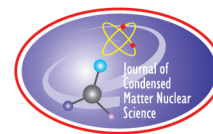
Acknowledgments

The author acknowledges and thanks Gayle Verner for her experimental and editorial assistance, and Prof. David Nagel for his significant suggestions and comments. This effort was supported by JET Energy Inc. and the New Energy Foundation. PHUSOR[®] is a registered trademark. PHUSOR[®]-technology and some of the other technologies described here are protected by patents pending.

References

- [1] M. Swartz, Survey of the observed excess energy and emissions in lattice assisted nuclear reactions, *J. Scientific Exploration* **23**(4) (2009). 419–436.
- [2] C. Beaudette, *Excess Heat & Why Cold Fusion Research Prevailed*, Second Edition, ISBN 9-9678548-2-2 (2002).
- [3] M. Swartz, Codeposition of palladium and deuterium, *Fusion Technol.* **32** (1997) 126–130.
- [4] M.H. Miles, *Thermal and Nuclear Aspects of the Pd/D₂O Systems*, Volume 1: A Decade of Research at Navy Laboratories, S. Szpak and P.A. Mosier-Boss (Eds.), Technical Report 1862, SSC San Diego (February 2002).
- [5] S. Pons and M. Fleischmann, *Heat After Death*, *Proc. ICCF4*, Lahaina, Maui, Dec. 6–9, 1993. EPRI TR104188-V2, Vol. 2 : p. 8-1 (1994); and *Trans. Fusion Technol.* **26** (4T), Part 2, (December 1994) 87.
- [6] M.H. Miles, S. Szpak, P.A. Mosier-Boss and M. Fleischmann, Thermal behavior of polarized Pd/D electrodes prepared by codeposition, *The Ninth Int. Conf. on Cold Fusion* (2002).
- [7] M.H. Miles, M. Fleischmann and M.A. Imam, Calorimetric analysis of a heavy water electrolysis experiment using a Pd-B alloy cathode, Naval Research Laboratory Report NRL/MR/6320-01-8526, 155 pp. (March 16, 2001).
- [8] Mizuno, Tadahiko "Nuclear Transmutation: The Reality of Cold Fusion", Infinite Energy Press Concord, New Hampshire, (1998)
- [9] M. Swartz and G. Verner, Dual Ohmic Controls Improve Understanding of "Heat after Death", *Trans American Nuclear Soc.*, vol. 93, ISSN:0003-018X, 891-892 (2005).
- [10] M. Swartz and G. Verner, Two site of cold fusion reactions viewed by their evanescent tardive thermal power, Abstract ICCF-11 (2004).
- [11] M. Swartz, Kinetics and lumped parameter model of excess tardive thermal power, Mitchell Swartz, APS (2005).
- [12] M. Swartz, Spatial and temporal resolution of three sites characterizing lattice-assisted nuclear reactions, APS 2008; M. Swartz, Colloquium on LANR in Deuterated Metals Colloquium on LANR at MIT, August 2007.
- [13] M. Swartz, Consistency of the biphasic nature of excess enthalpy in solid state anomalous phenomena with the quasi-1-dimensional model of isotope loading into a material, *Fusion Technol.* **31** (1997) 63–74.

- [14] M. Swartz and G. Verner, Excess heat from low electrical conductivity heavy water spiral-wound Pd/D₂O/Pt and Pd/D₂O–PdCl₂/Pt devices, Condensed Matter Nuclear Science, *Proc. ICCF-10*, Peter L. Hagelstein and Scott, R. Chubb (Eds.), World Scientific, NJ, ISBN 981-256-564-6, 29-44 (2006).
- [15] M. Swartz, Can a Pd/D₂O/Pt device be made portable to demonstrate the optimal operating point? *ICCF-10* (Cambridge, MA), 2003.
- [16] M. Swartz and G. Verner, Photoinduced excess heat from laser-irradiated electrically-polarized palladium cathodes in D₂O, Condensed Matter Nuclear Science, *Proc. ICCF-10*, ISBN 981-256-564-6, 213-226 (2006).
- [17] M. Swartz, Improved electrolytic reactor performance using OOP system operation and gold anode, *Trans. Amer. Nucl. Assoc.*, Nashville **78** (1998) 84–85. Meeting, (ISSN:0003-018X publisher LaGrange, Ill).
- [18] M. Swartz and G. Verner, The Phusor[®]-type LANR cathode is a metamaterial creating deuteron flux for excess power gain, *Proc. ICCF14 2*, (2008), p 458; ISBN: 978-0-578-06694-3, 458, (2010); www.iscmns.org/iccf14/ProcICCF14b.pdf.
- [19] M. Swartz, Excess power gain using high impedance and codepositional LANR devices monitored by calorimetry, heat flow, and paired stirling engines, *Proc. ICCF14 1*, (2008), p 123; ISBN: 978-0-578-06694-3, 123, (2010); www.iscmns.org/iccf14/ProcICCF14a.pdf.
- [20] M. Swartz, Metamaterial shaped LANR-cathodes produce deuteron flux, *Infinite Energy* **90** (2010).
- [21] M. Swartz, Optimal operating point manifolds in active, loaded palladium linked to three distinct physical regions, *Proc. ICCF14 2*, (2008), p 639; ISBN: 978-0-578-06694-3, 639, (2010); www.iscmns.org/iccf14/ProcICCF14b.pdf
- [22] M. Swartz, Optimal operating point characteristics of nickel light water experiments, *Proc. ICCF-7*, 1998.
- [23] M. Swartz, Control of low energy nuclear systems through loading and optimal operating points, ANS/2000 Int. Winter Meeting, Nov. 12–17, 2000, Washington, D.C. (2000).
- [24] M. Swartz, Three Physical regions of anomalous activity in deuterided palladium, *Infinite Energy* **14**(61) (2008) 19–31.
- [25] D. Nagel, ICCF13, Sochi, Russia, Powers, Materials and radiations from low energy nuclear reactions on surfaces (2007).
- [26] M.R. Swartz, Excess heat and electrical characteristics of type “B” anode-plate high impedance Phusor-type LANR devices, American Chemical Society, Salt Lake City, UT, *J. Sci. Exploration* **23** (4) (2009)491–495.



Research Article

A Tale of Two Journals

Pamela A. Mosier-Boss*

GEC, 5101B Backlick Rd., Annandale, Virginia 22003, USA

Lawrence P. Forsley

University of Texas Austin, Nuclear Engineering Teaching Lab, Pickle Research Campus, R-9000, Austin, TX, USA

Abstract

Earlier we discussed the flawed journal review process and how it stifles innovation and the diffusion of knowledge. Recently we tried to publish a paper describing our LENR experiences working with undergraduate chemical engineering students in an education journal. One journal had a word limit for articles as well as a fairly rigid format which prevented us from telling the story the way we wanted to. Although we addressed all the issues of the reviewers, the paper was rejected, after ten months and multiple revisions, on the grounds *that independent research projects were outside the scope of the journal*. We eventually published the paper in another education journal. In this journal, we were able to tell the narrative the way we originally wanted to, all the while emphasizing the advantages of involving students in verifying new scientific phenomena. This paper describes the events that transpired.

© 2020 ISCMNS. All rights reserved. ISSN 2227-3123

Keywords: Mentoring, Review process, Undergraduate projects

1. Introduction

As members of the Low Energy Nuclear Reactions/Condensed Matter Nuclear Science (LENR/CMNS) community continue to age and retire, the question has been posed how to reverse this process. Clearly the answer is to engage younger people and some members of the community have had some success. Before his passing in 2016, John Dash of Portland State University had mentored a number of high school/undergraduate/graduate students. These students had done calorimetry of the Pd/D and Ti/D system and had analyzed their cathodes using SEM-EDX. From their measurements they not only saw excess heat but evidence of the transmutation of Pd to Ag [1,2]. Both George Miley, University of Illinois, and Peter Hagelstein, MIT, have been the advisors of graduate students who have conducted research on LENR-related projects. Miley et al. [3] developed thin film electrodes that gave both excess heat and emitted charged particles as well as low-intensity X-rays. Hagelstein [4] has primarily been involved in developing

*Corresponding author. E-mail: pboss@san.rr.com.

theories/models to explain LENR. More recently his group has been investigating the non-exponential decay of X-ray and γ lines from Co-57 on steel plates [5]. Fran Tanzella and Mike McKubre of SRI International have had undergraduate interns conduct LENR experiments. Most notably one of their Stanford University interns, Ben Earle, had conducted Pd/D co-deposition experiments with CR-39 detectors. However, in his early experiments using Fukuvi CR-39, Earle had deviated from the original protocol [6] and had left the 60 μm thick polyethylene covers on the surface of the detectors. Rather than terminate the experiments, it was decided to allow them to run to completion. The detectors were etched and *still showed tracks*. The polyethylene covers had protected the CR-39 from both chemical and mechanical damage providing further evidence that the pits observed on the detectors were nuclear in nature. These detectors were subjected to extensive analysis by groups from SPAWAR, NASA, and the Russian Academy of Sciences. From these analyses it was determined that the tracks observed in the CR-39 detectors were due to ≥ 3 MeV protons, ≥ 1.8 MeV alphas, and secondary particles due to recoils from either energetic protons and/or neutrons [7,8].

Our own group has also had some success in mentoring students. We had approached chemistry professors at the University of California, San Diego (UCSD) asking them if they would be willing to replicate our results of track formation in solid state nuclear track detectors used in Pd/D co-deposition. It happened that the Chemical Engineering Process Laboratory I and II classes at the UCSD were required for senior undergraduate students. In these classes, the students work in groups of four. In Laboratory I, projects in the areas of applied chemical research and unit operations are conducted. As indicated in the curriculum:

The emphasis of this class is the application of engineering concepts and fundamentals to solve practical and research problems. In Laboratory II, the students plan research projects in the areas of applied chemical technology and engineering operations. Each group executes the experimental work and articulates (both orally and in written form) the research plan and results. Students are given the opportunity to propose, design, and test new ideas and experimental procedures and to work with researchers from other facilities.

Consequently, given the scope of these classes, our Pd/D co-deposition experiment was considered to be a good candidate for a group of students to execute. Between 2007 and 2010, three different groups of senior undergraduate students in the chemical engineering department of UCSD conducted Pd/D co-deposition experiments as part of their independent research projects. Specifically, they replicated the experiments using CR-39 detectors to detect the emission of energetic particles. Controls and simulations were done by the students to rule out a chemical explanation for the tracks. In these efforts, we provided the students with chemicals, a protocol, and copies of pertinent publications. In turn, the students conducted the experiments independently of us and achieved positive results.

While these efforts to engage with younger future scientists are commendable, we need to reach out to an even greater number of students, scientists, and professors. To this end, we decided to publish our experiences with the chemical engineering undergraduate students in an educational journal with the hope that this would provide a broader audience for the field. In this communication we discuss what transpired. What we experienced was reminiscent of what we discussed in our earlier paper describing the flawed journal review process [9]. This is despite the protocol being granted a US Patent, 8,419,919, “System and Method for Generating Particles”, in 2013. The protocol has been replicated in laboratories and facilities in five countries over 200 times resulting in 59 peer reviewed papers by 2017.

2. Journal of Chemical Education

The first journal we approached was the ACS Journal of Chemical Education. According to the journal’s web site [10], the journal publishes papers on laboratory experiments “that have been successfully used with students to investigate chemical phenomena as well as to develop skills with laboratory techniques, equipment, or instrumentation.” Much earlier Stan Szpak, the inventor of the co-deposition process, had indicated that a colleague of his had previously used this journal to gain acceptance of some unconventional ideas. Szpak did try to publish a paper on Pd/D co-deposition

in this journal only to be told that the journal did not publish science research papers unless they had a direct link to the teaching and learning of chemistry. Since we had directly worked with undergraduate students, we thought this journal would be a good vehicle for our purpose which was to gain wider acceptance of LENR or, at the very least, to stimulate interest.

We submitted our first version of the paper, 'Use of Pd/D co-deposition to Generate Energetic Particles,' on January 30, 2016. In this first version of the paper, we simply presented what was required of the students in their research project. We then described the experiments that were done by the students and the results they obtained. Specifically, the students learned how to do electroplating. They did an electroplating experiment using PdCl_2 and LiCl in D_2O . Cyclic voltammetry [11,12] and galvanostatic pulsing experiments [13] had shown that, as the Pd plated out, an ever-expanding electrode surface was created that assured non-steady state conditions and local high D loading in the lattice ($\text{D/Pd ratio} \geq 1$). A suitable control would be to electroplate a metal that did not absorb deuterium into its lattice. As their control, the students used a solution of CuCl_2 and LiCl in D_2O for another electroplating experiment. When they used the PdCl_2 – LiCl – D_2O plating solution, the students saw tracks in the CR-39 detector. However, when they used the CuCl_2 – LiCl – D_2O plating solution, no tracks were observed in the CR-39 detector.

On February 2, 2016, the journal withdrew the submission. We were told that before the manuscript could be sent for review, we had a few issues that needed to be resolved and we were advised to review their guidelines and to use their template. From both the guidelines and the template, it became clear we had to be more specific as to what the students would learn after conducting their experiments. The keywords had to include the categories of audience (educational level of a student), domain (general area of study or interest within chemistry), pedagogy (describes an aid to learning or an instructional approach), and topic (indicates with greater specificity than Domain an area within chemistry). Within these categories were drop down lists to choose from. Upon reflection, we decided the main learning objective for the students was the importance of controls as part of the scientific method. The paper was rewritten emphasizing this. On February 16, 2016 we resubmitted the paper, now titled 'Energetic Particle Emission in Pd/D co-deposition: The Importance of Controls,' to the journal. On March 9, 2016, the paper passed internal review and was assigned to an editor who sent it out for assessment by three reviewers.

On May 1, 2016, we received the reviewer reports. The recommendations ranged from 'minor revision' to 'do not publish.' One reviewer thought that the project was well designed and met highest standards for scientific and scholarly rigor. Another reviewer, when asked 'If articles were published in order of value to readers, when should this one appear?,' said 'Never.' The editor's decision was:

On the basis of the reviewers appraisals and my own careful study of your manuscript, I have decided that your manuscript is not suitable for publication in the Journal of Chemical Education in its present form. However, your research has some positive components. I would consider a thoroughly rewritten manuscript, with substantial modification, incorporating the reviewers points and including any additional data they recommended.

As this was an encouraging response from the editor, we revised the manuscript taking into account the reviewer comments. The reviewer comments and our responses are shown *vide infra*.

One reviewer asked 'How many readers would actually consider doing this experiment or even just distribute the article to teach about controls?' In our response, we indicated that this was an independent research project. In science, unexpected results occur and it is only through control experiments that they are verified as being correct and that this was as good an experiment as any to demonstrate this. We further said that science is supposed to be thought provoking and to encourage independent thinking as only then can advances be made. Clearly this experiment falls in that category. This same reviewer questioned the validity of using CuCl_2 electroplating as a control. In the paper we stated that a suitable control experiment would be to plate out a metal that does not absorb deuterium. No tracks were observed in the Cu/D co-deposition experiment which led to the conclusion, by the students, that the tracks were not due to chemical/mechanical damage. The reviewer said that does not prove it at all, it just proves copper acts

differently than palladium. We disagreed with the reviewer on this statement. All the electrochemical reaction products are the same (dendritic metal plates out; D_2 , O_2 , and Cl_2 gases form; OD^- forms at the cathode). This was stated in the original text. These are the only chemical species that are available to attack the detector. The only difference is that Pd absorbs D and Cu does not. Pd/D gives tracks, Cu/D does not. Consequently, the tracks formed in the detector used in the Pd/D co-deposition experiment could not be due to chemical damage nor could they be due to mechanical damage caused by the metal dendrites. The reviewer also said the students could/should do more control experiments to raise the level of confidence that the tracks are not the result of chemical/mechanical damage or to radioactive contamination and that this would be a great class project. In our response, we agreed with the reviewer that the students could do more control experiments. To address this, we added a table to the revised paper which summarized additional control experiments that had been done and what the results were [6]. We further suggested, in the revised manuscript, that these control experiments could be a class project that could result in thought-provoking discussions as to the origins of the tracks observed in the Pd/D experiments. To further increase the confidence that the tracks were nuclear in origin, we included track modeling using TRACK-TEST, a free downloadable program developed by Nikezic and Yu [14,15]. TRACK-TEST allows one to estimate the energy of the particle that entered the detector as well as the angle of incidence. The calculated results obtained using TRACK-TEST match with the measured features of the imaged track (shape as well as minor and major axes).

The reviewers complained about the length of the experiment. We pointed out that, for an independent research project, it is acceptable for experiments to last more than a week. There were questions about reproducibility. In our response to the reviewer we indicated that we would never have given an experiment for students to do if it was not reproducible. We then modified the paper to say:

Formation of tracks in CR-39 detectors used in Pd/D co-deposition experiments has been extremely reproducible. However, control experiments need to be done to show that the tracks are not due to either radioactive contamination or mechanical/chemical damage.

There were other questions on hazards and safety. We were instructed to provide stronger language regarding the use of fume hoods. We complied by saying that the cell should be placed in a well ventilated area, *i.e.* a fume hood, as D_2 , O_2 and Cl_2 gases are generated. Also the potentiostat/constant current power source should be grounded. They also wanted to know if there were any concerns about the emission of high energy particles. We indicated that linear energy transfer (LET) analysis indicated that the solution and cell components will moderate the charged particles and that they will not escape the cell. The rate of particle production was on the order of 1 particle/s. Also the NRC limits on public exposure to radiation is 2 mrem/h and we were orders of magnitude below that.

The revised manuscript was submitted on September 14, 2016. On November 30, 2016, the editor rejected the manuscript saying:

The reviewers have expressed serious reservations about this work that I do not believe could be addressed through a standard major revision. In light of the comments received, I am unable to accept the manuscript for publication. A key concern is whether this has actually been run as part of an undergraduate laboratory with typical student results (as is required by the journal for publication). Independent research projects are outside the scope of this journal.

Throughout the process we had indicated that we were describing an independent research project conducted at a university by senior undergraduate students. Only now did the editor and reviewers indicate, after ten months of review and multiple revisions of the manuscript, that independent research projects were outside the scope of the journal. This was disingenuous. The reviewers acknowledged that we had addressed their earlier concerns in the revised manuscript yet they still had reservations and did not, or refused to, accept our explanations. One reviewer went so far as to say that we had to ‘make the case that the underlying science is not crackpot.’ Another reviewer complained that there was

the assumption that readers would be familiar with Pd/D co-deposition. This was an unfair comment as we did define co-deposition and provided references. We could not go in-depth into co-deposition as the journal had a 6000 word limit for articles.

Our experience with the Journal of Chemical Education was disappointing. For the most part, the editor had treated us fairly. We were, however, constrained by the journal's word limit and how they wanted the article to be organized, which was not the way we wanted to tell our story. We wanted to explain how it was we were able to connect with the students. But given the rigid format of the journal, we were unable to do so. Also, of the four reviewers, two clearly were never going to allow the manuscript to be published in the journal. There was nothing we could have done to have persuaded them otherwise. Undeterred, we began to search for another journal to publish our narrative.

3. Journal of Laboratory Chemical Education

In June 2017 we saw that the Journal of Laboratory Chemical Education had a call for papers for a special issue on Chemistry Laboratory in Graduation Projects. The scope of the special issue was:

All undergraduate students have the requirement of completing a graduation project as part of their graduation. The purpose of the graduation projects is to provide students with an opportunity to progress in the strengthening of knowledge and skills acquired throughout their years in the educational system. These graduation projects can be considered as pilot projects on topics related to real problems. The aim of this Special Issue is to offer laboratory experiences that can be used as basis of graduation projects.

We contacted the editor of the special issue to see if the journal would consider a submission from us. We told the editor how it came about that the undergraduate students did a replication of our Pd/D co-deposition experiment using CR-39 detectors. We acknowledged that the area of research was controversial. However, we had published our results in peer-reviewed journals. We indicated that two necessary requirements to achieve acceptance in the scientific community of a new phenomenon are replications and reproducibility, which was one of the lessons learned by the students. Furthermore, having students involved in replications could result in a new paradigm for scientists to obtain verification of their work. We also sent the editor the abstract for a paper that was now entitled 'Energetic Particle Emission in Pd/D co-deposition: Using Undergraduate Research Projects to Verify New Scientific Phenomena.' On June 15, 2017 the editor responded with:

The data and the experience that you have collected during some years, with undergraduate students in a scientific area with some controversy, can provide challenging insight into the understanding of the scientific method. Therefore, according to the guidelines of the Special Edition, I invite you to send me the manuscript.

As there was no word limit, we rewrote the Journal of Chemical Education paper taking into account the comments of the reviewers of the original manuscript. The journal also allowed us to include, as supplementary material, a write-up of the protocol used by the students. On July 6, 2017, we submitted our manuscript for the special issue. A few weeks later, we got a positive reviewer's report and the paper was accepted. The special issue on Chemistry Laboratory in Graduation Projects was published in June 2018 [16]. In the introduction for the special issue the editor wrote:

A number of research groups have contributed to this Special Issue of the Journal of Laboratory Chemical Education, 2018. In total, nine papers have been compiled covering various aspects of the Chemistry laboratory experience which can be used as a basis for designing undergraduate projects. These papers exhibit all aspects of proper scientific methodology: revision of available literature on the specific topic, replication of published data, hypothesis testing, verification of experimental procedures with literature, acquisition of experimental data, and even development of some basic instrumentation tailored to meet the specific demands of the project.

The paper by Mosier-Boss highlights the importance of replication in science by analyzing the track formation in solid state nuclear detectors. The project described here extended over several years and was carried out by different groups at different levels. The subject area is not entirely free from controversy, but rather than this being a reason to shun the topic, it can be seized upon to offer an opportunity to gain insight into the scientific method by seeing it in action. The experiments illustrate the importance of replication of results reported in the literature as a means of quality control within the framework of scientific methodology, especially in the case of unexpected or anomalous results.

One year after the paper appeared in the Open Access Journal and had been posted to academia.edu and researchgate.net sites, it had been viewed or downloaded over 2000 times. This indicates to us that, despite the comments/concerns of the reviewers for the original paper submitted to the Journal of Chemical Education, there is interest in the field.

4. Conclusions

All we wanted to do was to tell our experience having undergraduate chemical engineering students do our LENR-related experiment. It was very rewarding working with young people who had no recollection of the events that had transpired in 1989. We, as well as the students, benefitted from the experience. For us, it counted as a replication and introduced younger, future professionals to the field. For the students, they got an opportunity to see how the scientific process worked and the importance of controls/simulations in verifying new phenomena. They also learned about metal electroplating, Faradaic efficiency, solid state nuclear track detectors, and modeling. Our attempt to publish our story in one journal was met with disdain by two out of four reviewers and showed that, even after almost 30 years, the phenomenon was still widely not accepted. Despite what others in the LENR/CMNS field believe, we still have to convince the scientific community that nuclear reactions can occur in metal lattices once the appropriate conditions are achieved. Furthermore, the burden of proof is upon us. We did eventually find a journal that allowed us to tell our story the way we wanted to.

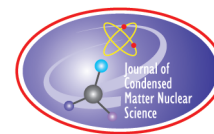
We would like to point out that there are many advantages to using undergraduate students to verify new scientific phenomena. For the most part they do not have pre-conceived ideas and are open to new concepts. Nor do they have reputations or funding to protect. Last year we were contacted by an adjunct professor at Point Loma Nazarene University (PLNU). One of her students was interested in plasmas and fusion experiments. After a literature search he had found our papers and wanted to do some experiments for his honor's project. The professor then asked for our help. We gave her the protocol that had been published in 2018. We also provided them with CR-39 detectors and met periodically to see how they were progressing. They have also successfully replicated the Pd/D and Cu/D co-deposition experiments. Currently they are conducting additional control experiments that were suggested in the published protocol [16].

5. Epilogue

One of the UCSD undergraduate teams had a poster session at an international Conference in Italy [17] and two years later they gave an invited talk to the American Chemical Society national Meeting in Salt Lake City, Utah that was published separately [18]. The PLNU undergraduate had a poster session at the American Physics Society national meeting in Boston in 2019 [19]. Recently, he has submitted a paper to an undergraduate physics journal, where he is experiencing some of the same bias we had.

References

- [1] J. Dash, R. Kopecek and S. Miguet, Excess heat and unexpected elements from aqueous electrolysis with titanium and palladium cathodes, *Proceedings of the 32nd Intersociety Energy Conversion Engineering Conference* **2** (1997) 1350–1355.
- [2] J. Dash and A. Ambadkar, Co-deposition of palladium with hydrogen isotopes, *Proc. ICCF11*, 2004.
- [3] G.H. Miley, H. Hora, A. Lipson, S.-O. Kim, N. Luo, C.H. Castano Giraldo and T. Woo, Progress in thin-film LENR research at the University of Illinois, *Proc. ICCF9*, 2002.
- [4] P.L. Hagelstein and I.U. Chaudhary, Models relevant to excess heat production in Fleischmann–Pons experiments, in *Low-Energy Nuclear Reactions Sourcebook* **998** (2008) 249–267.
- [5] F. Metzler, P. Hagelstein and S. Lu, Observation of non-exponential decay of X-ray and γ lines from Co-57 on steel plates, *Proc. ICCF21*, 2019.
- [6] P.A. Mosier-Boss, S. Szpak, F.E. Gordon and F.P.G. Forsley, Use of CR-39 in Pd/D co-deposition experiments, *Eur. Phys. J. Appl. Phys.* **40** (2007) 293–303.
- [7] P.A. Mosier-Boss, F.E. Gordon, L.P. Forsley and D. Zhou, Detection of high energy particles using CR-39 detectors part 1: Results of microscopic examination, scanning, and LET analysis, *Int. J. Hydrogen Energy* **142** (2017) 416–428.
- [8] A.S. Roussetski, A.G. Lipson, E.I. Saunin, F. Tanzella and M. McKubre, Detection of high energy particles using CR-39 detectors part 2: Results of in-depth destructive etching analysis, *Int. J. Hydrogen Energy* **142** (2017) 429–436.
- [9] P.A. Mosier-Boss, L.P. Forsley and F.E. Gordon, How the flawed journal review process impeded paradigm shifting discoveries?, *J. Condensed Matter Nucl. Sci.* **12** (2013) 1–12.
- [10] <https://pubs.acs.org/page/jceda8/submission/authors.html>
- [11] S. Szpak, P.A. Mosier-Boss, S.R. Scharber and J.J. Smith, Charging of the Pd/¹¹H system: role of the interphase, *J. Electroanal. Chem.* **337** (1992) 147–163.
- [12] S. Szpak, P.A. Mosier-Boss, S.R. Scharber and J.J. Smith, Cyclic voltammetry of Pd+D codeposition, *J. Electroanal. Chem.* **380** (1995) 1–6.
- [13] S. Szpak, P.A. Mosier-Boss and J.J. Smith, Deuterium uptake during Pd–D codeposition, *J. Electroanal. Chem.* **379** (1994) 121–127.
- [14] D. Nikezic and K.N. Yu, Formation and growth of tracks in nuclear track materials, *Mat. Sci. Eng. R.* **46** (2004) 51–123.
- [15] <http://www.cityu.edu.hk/ap/nru/test.htm>
- [16] P.A. Mosier-Boss and L.P. Forsley, Energetic particle emission in Pd/D co-deposition: An undergraduate research project to replicate a new scientific phenomenon, *J. Labor. Chem. Educ.* Special Issue **6** (2018) 69–76.
- [17] R. Robertson, H. Saito, J. Yurkovic and S. Zakskorn, Field assisted electroplating, *8th Int. Workshop on Anomalies in Hydrogen and Deuterium-Loaded Metals* (Sicily, Italy, 2007) Poster Session.
- [18] R. Robertson, H. Saito, J. Yurkovic and S. Zakskorn, Field assisted electroplating, *J. Sci. Explor.* **23** (2009) 452–455.
- [19] M. Karahadian and H. M. Doss, Evidence of particles during electrochemical Pd–D co-deposition, *American Physical Society*, March Meeting (Boston, MA, 2019). Poster Session <http://meetings.aps.org/Meeting/MAR19/Session/G70.24>.



Research Article

The Eyring Rate Theory Applied to Cold Fusion

Melvin H. Miles* and Iraj Parchamazed

Department of Chemistry, University of LaVerne, LaVerne, CA 91750, USA

Abstract

The Eyring Absolute Rate Theory is generally applied to chemical reactions where bonds between atoms are broken and new bonds formed to give a transition state or activated complex. This theory has also been applied to physical rate processes such as diffusion and the viscosity of liquids. The activation parameters obtained from the Eyring theory when applied to cold fusion are all suggestive of a deuterium fusion rate controlled by the diffusion of deuterons within the palladium lattice. The D+D fusion process in the Pd/D system is apparently a zero-ordered reaction where only a small fraction of the reactants are in a location in which they are able to react.

© 2020 ISCMNS. All rights reserved. ISSN 2227-3123

Keywords: Activation energy, Activation entropy, Deuterium, Diffusion, Palladium, Reaction zones

1. Introduction

The Eyring Rate Theory can yield theoretical rate constants for chemical reactions by calculations involving the energy contours of the transition state and then using the lowest energy pathway in going from reactants to products [1,2]. It is claimed that this Eyring theory is not simply for chemical reactions, but it can be applied to any rate process [1]. This Eyring theory also treats the possibility of quantum mechanical tunneling [1]. The application of the Eyring theory to the D+D fusion reaction shows that the reaction rate would be extremely slow outside the palladium lattice due to the coulombic barrier. The catalysis of a chemical reaction, which greatly increases the reaction rate by providing a more favorable reaction pathway, is well known in chemistry. Apparently, a much more favorable pathway for D+D fusion is provided by the palladium lattice.

2. Thermodynamic Definitions

The Eyring theory involves thermodynamic activation parameters, therefore, a few definitions are required. The internal energy (U) can be expressed by

$$U = q + w, \quad (1)$$

*Corresponding author. E-mail: mhmiles1937@gmail.com.

where q is energy in the form of heat and w is energy in the form of work. Equation (1) is a statement of the First Law of Thermodynamics. The enthalpy (H) is defined by

$$H = U + PV, \quad (2)$$

where P and V are the pressure and volume, respectively, for a system. The Gibbs energy (G) is defined by

$$G = U + PV - TS = H - TS, \quad (3)$$

where T is the thermodynamic temperature in Kelvin (K) and S is the entropy introduced by the Second Law of Thermodynamics. At constant temperature, any changes in G is given by

$$\Delta G = \Delta H - T\Delta S. \quad (4)$$

At constant pressure with only $P - V$ work, the change in H is given by

$$\Delta H = \Delta U + P\Delta V = (q - P\Delta V) + P\Delta V = q. \quad (5)$$

Therefore, at constant pressure with only $P - V$ work, the change in the enthalpy is simply the heat involved in such changes. For typical laboratory conditions of constant temperature and pressure, it can be shown that spontaneous reactions require the change in the Gibbs energy to be less than zero (negative) as expressed by Eq. (6).

$$(\Delta G)_{T,P} < 0. \quad (6)$$

3. Thermodynamics For The D+D → He-4 Fusion Reaction

At $T = 298.15$ K and $P = 10^5$ Pa (approximately room conditions) it was shown previously [3] for D+D fusion to form helium-4 that

$$\Delta H = q = -23.846478 \times 10^6 \text{ eV} = -2.30084 \times 10^{12} \text{ J mol}^{-1}, \quad (7)$$

$$\Delta S = S^\circ(\text{He-4}) - 2S^\circ(\text{D}) = -120.548 \text{ J mol}^{-1} \text{ K}^{-1}, \quad (8)$$

$$\Delta G = \Delta H - T\Delta S \approx \Delta H = -2.30084 \times 10^{12} \text{ J mol}^{-1}. \quad (9)$$

Therefore, D+D fusion to form He-4 is certainly thermodynamically possible at room temperature [3]. However, thermodynamics provides no information on reaction rates or the coulombic barrier. Nevertheless, the favorable thermodynamics at room temperatures allows the possibility of catalysis or new reaction pathways that can increase the rate of this reaction.

4. Eyring Rate Equations

From the Eyring Absolute Rate Theory [1], the rate constant (k) for a reaction is given by

$$k = (k_B T / h) \exp(-\Delta G^\ddagger / RT), \quad (10)$$

where k_B is the Boltzman constant ($1.3806488 \times 10^{-23} \text{ JK}^{-1}$), h the Planck constant ($6.62606957 \times 10^{-34} \text{ Js}$), ΔG^\ddagger the activation Gibbs energy, R the molar gas constant ($8.3144621 \text{ J mol}^{-1} \text{ K}^{-1}$), and T is the thermodynamic temperature in Kelvin. This Eyring rate constant can also be written as

$$k = (k_B T / h) \exp(\Delta S^\ddagger / R) \exp(-\Delta H^\ddagger / RT) \quad (11)$$

by using the thermodynamic relationship, $\Delta G^\ddagger = \Delta H^\ddagger - T\Delta S^\ddagger$ for the activation Gibbs energy, ΔG^\ddagger . The Arrhenius rate equation is given by

$$k = A \exp(-E_A/RT), \quad (12)$$

where E_A is the activation energy. Comparing the Eyring and Arrhenius equations, it can be shown [1] that

$$A = (ek_B T/h) \exp(\Delta S^\ddagger/R) \quad (13)$$

and

$$E_A = \Delta H^\ddagger + RT = \Delta G^\ddagger + T\Delta S^\ddagger + RT. \quad (14)$$

5. Application of the Eyring Rate Theory to Cold Fusion

For a typical cold fusion experiment using a palladium cathode volume of 0.1 cm^3 , the expected excess power near room temperature would be about 0.100 W. The D+D fusion reaction yields 2.6174×10^{11} He-4 atoms per second per watt of excess power. Therefore, for 0.100 W of excess power, the rate of helium-4 production would be $k = 2.6174 \times 10^{10}$ He-4/s.

Rearranging Eq. (10) gives

$$\Delta G^\ddagger = -RT \ln(kh/k_B T). \quad (15)$$

Therefore, at $T = 300 \text{ K}$, $\Delta G^\ddagger = 13,700 \text{ J mol}^{-1}$.

From Eq. (14), the ΔG^\ddagger value is found to be in good agreement with the reported activation energy of $E_A = 0.206 \text{ eV}$ or $19,900 \text{ J mol}^{-1}$ for the diffusion of deuterons in palladium [4]. In fact, from Eq. (14) and using $E_A = 19,900 \text{ J mol}^{-1}$, a reasonable value of $\Delta S^\ddagger = 12.3 \text{ J mol}^{-1} \text{ K}^{-1}$ is obtained for the activation entropy. The Eyring theory applied to the diffusion of hydrogen in metals gives similar values for activation energies and entropies.

The assumption of different values of excess power for palladium cathodes in D_2O electrolysis experiments would give different values for ΔG^\ddagger and ΔS^\ddagger as shown in Table 1. However, the assumption of 0.100 W of excess power at 300 K for a palladium volume of 0.100 cm^3 seems to be the best assumption.

6. Eyring Theory For Diffusion

The Eyring Rate Theory for diffusion [1] is expressed by the equation

$$D = \lambda^2 (k_B T/h) \exp(\Delta S^\ddagger/R) \exp(-\Delta H^\ddagger/RT), \quad (16)$$

where D is the diffusion constant ($\text{cm}^2 \text{s}^{-1}$) and λ is the distance (cm) between successive diffusion positions. Using $\Delta H^\ddagger = E_A - RT$, this equation becomes

$$D = e\lambda^2 (k_B T/h) \exp(\Delta S^\ddagger/R) \exp(-E_A/RT). \quad (17)$$

Table 1. Different assumptions for excess power at 300 K.

$P_X (\text{W})$	$k (\text{s}^{-1})$	$\Delta G^\ddagger (\text{J mol}^{-1})^a$	$\Delta H^\ddagger (\text{J mol}^{-1})^b$	$\Delta S^\ddagger (\text{J mol}^{-1} \text{K}^{-1})^c$
0.050	1.3050×10^{10}	15,400	17,400	6.7
0.100	2.6174×10^{10}	13,700	17,400	12.3
0.200	5.2348×10^{10}	11,900	17,400	18.3

^a $\Delta G^\ddagger = -RT \ln(kh/k_B T)$.

^b $\Delta H^\ddagger = E_A - RT$, where $E_A = 0.206 \text{ eV}$ ($19,900 \text{ J mol}^{-1}$).

^c $\Delta S^\ddagger = (\Delta H^\ddagger - \Delta G^\ddagger)/T$.

The Arrhenius equation for the diffusion of deuterium in palladium [4] is given by

$$D = A \exp(-E_A/RT), \quad (18)$$

where experimentally $A = 1.7 \times 10^{-3} \text{cm}^2 \text{s}^{-1}$ [4]. Therefore,

$$\lambda^2 \exp(\Delta S^\ddagger/R) = Ah/ek_B T = 1.00 \times 10^{-16} \text{cm}^2 \quad (19)$$

at $T = 300 \text{ K}$. For $\Delta S^\ddagger = 12.3 \text{ J mol}^{-1} \text{K}^{-1}$, $\lambda = 0.48 \times 10^{-8} \text{ cm}$, or 0.48 \AA . For this cold fusion application, the diffusion distance of 0.48 \AA is for a reacting deuteron just prior to undergoing the fusion reaction to form helium-4. This rather small distance may be related to the very small size of D^+ involving only the atomic nucleus. This small value also suggests a large concentration of D^+ ions for the location where the fusion reaction takes place.

7. Results and Discussion

The application of the Eyring Rate Theory to the $\text{D} + \text{D}$ fusion reaction suggest that this reaction is controlled by the diffusion of deuterons within the palladium into some fusion reaction zones. Such reaction zones may also be called a nuclear active environment or NAE at the palladium surface as suggested by Storms [5]. However, other reaction zones within the palladium, especially near the electrochemical double layer, cannot be ruled out [3]. Vacancies in the palladium lattice are also possible fusion reaction zones as suggested by Hagelstein and others [6]. These reaction zones likely contain an unusually high concentration of deuterons and electrons. Proposed reaction zones were presented in a previous publication [3].

The small positive value for the entropy of activation obtained from the Eyring theory ($\Delta S^\ddagger = 12.3 \text{ J mol}^{-1} \text{K}^{-1}$, see Table 1) is quite different from the large and negative entropy change for the $\text{D} + \text{D}$ fusion reaction to form helium-4 ($\Delta S = -120.548 \text{ J mol}^{-1} \text{K}^{-1}$, see Eq. 8). However, such small positive values for ΔS^\ddagger have been reported for the diffusion of hydrogen in metals and were explained by a transition state that is less ordered than the initial state. This is another indication that the rate of the $\text{D} + \text{D}$ fusion reaction in palladium is controlled by the diffusion rate of deuterons within the palladium and not by the coulombic barrier.

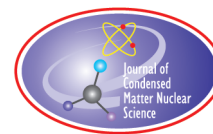
Features of the $\text{D} + \text{D}$ fusion reaction in palladium suggests that a zero-order reaction is involved. For a zero-order reaction, only a small fraction of the reacting species are in a location or state in which they are able to react. This small fraction is continually replenished from the larger pool. Furthermore, zero-order reactions are typically found when a material that is required for the reaction to proceed, such as a surface or a catalyst, is saturated by the reactants. The $\text{D} + \text{D}$ fusion reaction is possibly a pseudo-zero order reaction due to the fact that the concentration of deuterons remains relatively constant.

Acknowledgement

This work was supported from an anonymous fund at the Denver Foundation via Dixie State University and administered by “the Dixie Foundation”.

References

- [1] S. Glasstone, K.J. Laidler and H. Eyring, *The Theory of Rate Processes*, McGraw-Hill, NY, 1941.
- [2] K.S. Laidler and M.C. King, The development of transition-state theory, *J. Phys. Chem.* **87**, (1983) 2657–2664.
- [3] M.H. Miles, Thermodynamic and kinetic observations concerning the $\text{D} + \text{D}$ fusion reaction for the Pd/D system, *J. Condensed Matter Nucl. Sci.* **16** (2015) 17–22.
- [4] Y. Fukai, *The Metal–Hydrogen System: Basic Bulk Properties*, Springer, Berlin, 1992, pp. 229–231.
- [5] E. Storms, *The Explanation of Low Energy Nuclear Reaction*, Infinite Energy Press, Concord, NH, USA, 2014, pp. 2–8.
- [6] D. Letts and P.L. Hagelstein, Modified Szpak protocol for excess heat, *J. Condensed Matter Nucl. Sci.* **6** (2012) 44–54.



Research Article

Alternatives to Calorimetry

Fabrice David*

Laboratoire de Recherches Associatives, BP 4, 95131 Franconville Cedex, France

John Giles

Deuo Dynamics, United Kingdom

Abstract

Since the first publication of Martin Fleischman and Stanley Pons in 1989, the majority of articles in the LENR field have focused on calorimetry. Many calorimetry experiments are masterpieces of science. Nevertheless, despite the experimental evidence, the results indicating excessive heat have not convinced the scientific community. For this purpose, we propose three relatively simple techniques: The “Fusion Diode” effect, the Reifenschweiler effect and a new postulated effect, not yet observed: the magnetic alignment of the tritium pairs.

© 2020 ISCMNS. All rights reserved. ISSN 2227-3123

Keywords: Bose–Einstein condensate, Deuterium, Direct conversion, Fusion diode, Tritium

1. Introduction

Since the first publication of Martin Fleischman and Stanley Pons in 1989, the majority of articles in the LENR field have focused on calorimetry [1]. This is true for both electrolysis experiments and gaseous loading experiments [2].

Many calorimetry experiments are masterpieces of science [3]. Nevertheless, despite the experimental evidence, the results indicating excessive heat have not convinced the scientific community. Well-designed calorimetry experiments take a very long time to be developed. It’s an issue, because it would be good to test many alloys systematically. It is likely that there are still unknown alloys whose ability to generate what Dr. Ed Storms calls a “Nuclear Active Environment” [4] is greater than that of palladium. It is certain that low concentrations of elements such as lithium, boron, beryllium in these alloys will have undoubtedly positive effects. We need fast and reproducible tests to sort all these alloys and select the most promising samples. Several authors have suggested that the quantum condensation of deuterium nuclei is at the root of the appearance of “NAE” [6–9]. It would be very useful to provide irrefutable proof of the existence of these quantum phases. But on top of that, these quantum phases could provide a relatively easy way to sort out the most useful alloys for LENRs.

*Corresponding author. E-mail: fabrice.david95@yahoo.com.

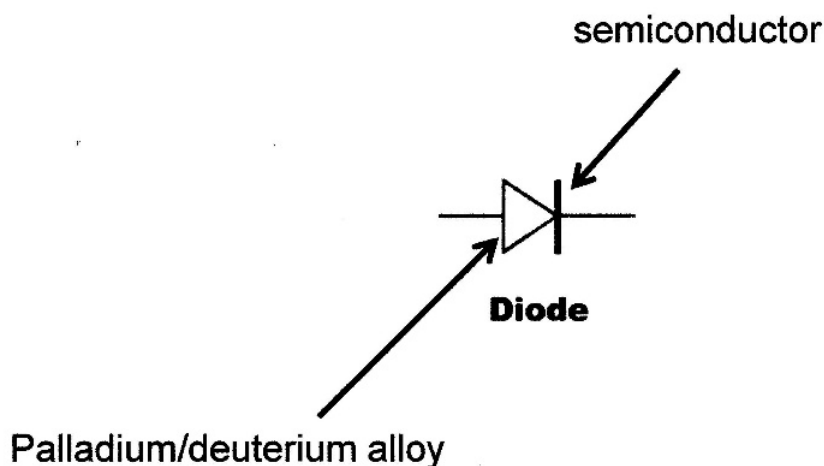


Figure 1. Fusion diode.

For this purpose, we propose three relatively simple techniques:

- (1) The “Fusion Diode” effect: deuterated alloys in contact with a semiconductor cause the appearance of an easy-to-measure electrical voltage. If this voltage is actually due to the direct conversion of LENR, we have a simple method to select the most promising alloys (Fig. 1).
- (2) The Reifenschweiler effect: the variation of tritium beta-rays bremsstrahlung conversion efficiency as a function of temperature is also a simple method for sorting the most efficient alloys [10].
- (3) The magnetic alignment of the tritium pairs: this effect, which we have postulated, but not yet observed, would make it possible to very quickly test many new alloys [11].

In this article, we want to discuss how it is possible to find alternatives to calorimetric experiments.

2. The Fusion Diode Effect

It is very difficult to make good calorimetric recordings. It is easier to count X-rays. But the easiest way to get a scientific evidence about any kind of phenomena is to do electrical recording. We have suggested the idea of “Fusion Diodes”. Fusion diodes are made of a palladium (or other alloys) in close contact with a semiconductor. This is a semiconducting diode.

When fusion reactions take place near the metal/semiconductor contact, at the beginning we had high energy quanta (in the MeV range), and then thermalization occurs, leading to Anomalous Heat Effect (down-conversion of Hagedorn). But before thermalization, the decaying energy match the level of excitation of the electrons of the metal: some energy is transmitted to the electrons before thermalization (like in a photovoltaic cell, but in our diodes, the energy source is expected to be the fusion of deuterium, protium, or perhaps lithium, boron, or beryllium).

At the contact between metal hydride and metal, pairs of electrons and holes are created, and depending to the height of the potential barrier between the two material, a voltage is created (and also an electrical current, of course).

We can record the voltage and the intensity of the resulting current at the positive and negative side of the diode. This simple device allows a simple recording of the total output power, because there is no electrical input. We plan

to record this electrical energy during months or even years, to exclude the possibility of a chemical origin. It is important to note that these devices have no electrical input. There is also no thermal input. The energy is released as electrical current, and this is very easy to record with high accuracy. We are using diodes made of palladium as the metal, and silicon as the semiconductor. We have also tried other semiconductors like aluminum nitride and organic semiconducting ink. But we only published our experiments with silicon. The palladium is loaded with deuterium simply by the gas-loading method. We do not know the effective loading value, but it is probably rather high, because of the micrometer size of the palladium powder. A diode is basically a surface of contact with a metal (electronic conductor) and a semiconductor (hole conductor).

We think that the deuterium nuclei which are in the palladium will be driven in the direction of the electric field. Once these deuterium nuclei will arrive at the interface between palladium and the semiconductor, they will accumulate there. The probability of fusion probably will increase [4].

Better: if reactions of cold nuclear transmutation take place into the junction, an excitation of the electrons will occur at this place (as in the junction zone of a photovoltaic cell). A solar cell is a nothing than a flat diode with a large surface. When photons fall on the junction zone, some atoms are excited, and electrons pass from a low energy level to a higher energy level. A spontaneous electric voltage thus will appear. It is what we observed. In our diodes, the nuclear energy is transmitted to the electrons before thermalization.

In order to get a surface of junction as large as possible, our fusion diodes are made as powder diodes, with a large surface junction made up of a semiconductor powder in contact with palladium powder charged with deuterium [5]. The weight of palladium powder is comprised between 1 and 2 g by diode. This energy very quickly appears as a spontaneous potential difference which can reach over 0.5 V/junction (open circuit) (Fig. 2).

- 1 -Electrical connection.
- 2 -End cap, with threading.
- 3 -Mix of silicon and palladium powder.
 - At the bottom : pure palladium, and then an increasing concentration of silicon.
 - At the middle of the diode : 50% silicon; 50% palladium
 - At the top : pure silicon
 - The result is a very large surface rectifier diode.
- 4 -Inner plastic tube for insulation
- 5 -Aluminium container
- 7 -End cap
- 8 - Valve

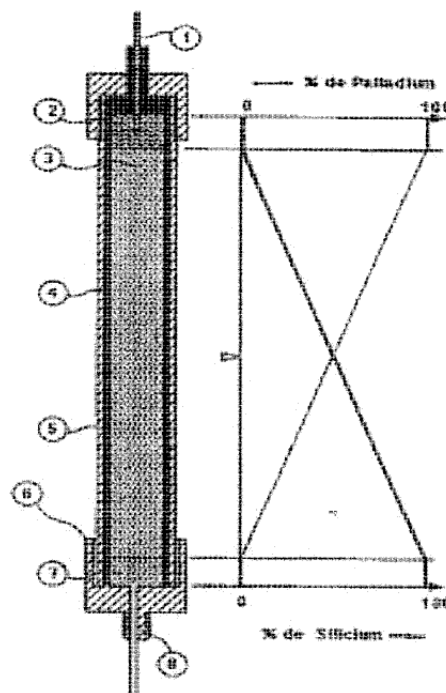


Figure 2. Powder fusion diode (length: 14 cm, diameter: 1.6 cm).

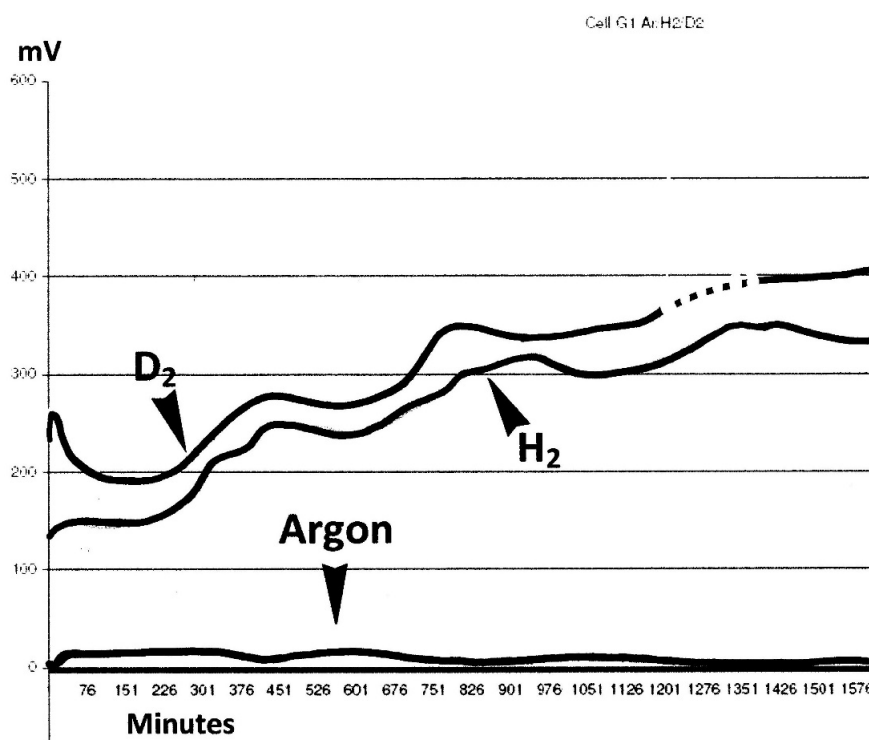


Figure 3. Voltage recording at the ends of a fusion diode.

Diodes comprising of a stack of junctions were made, making it possible to obtain over 1 V at the poles of a very compact device of a few centimeters' length. The released power remains very low for the moment, (in the nanowatt range) but it should be noted that it is presented in the form of directly usable electrical energy, and not of thermal energy (Fig. 3).

Of course, we have made blank and control experiments. We have built three diodes each time, one filed with pure deuterium (1.5 bar) another filed with hydrogen at the same pressure, and another filled with pure argon. We observed no voltage with argon filling, a little voltage with hydrogen, twice the voltage with deuterium. We think that the observed voltage with hydrogen is generated by the little amount of deuterium in the hydrogen (0.015% of deuterium in natural hydrogen). But it is difficult to avoid the deuterium leak, and the ensuing voltage drop. We plan to seal a diode in a glass tube, and measure the energy produced for several months.

Thus, it will be possible to determine whether the energy observed is actually of nuclear origin, or if it is an artefact of electrochemical origin. After several months, it will be sufficient to weigh the copper deposited on a cathode (a tiny wire of copper) whose weight is known at the beginning of the experiment to prove that the energy produced is of nuclear origin (or not...).

Of course, it is rather tedious to work with powders. But the "Fusion Diode" effect is highly reproducible, even with thin films of organic semiconductors. The authors used many different embodiments of the "Fusion Diode". Another team working on "fusion diodes" has made diodes by vacuum metallizing silicon wafers. On one side is deposited a palladium film, and on the other a gold film (forthcoming publication).

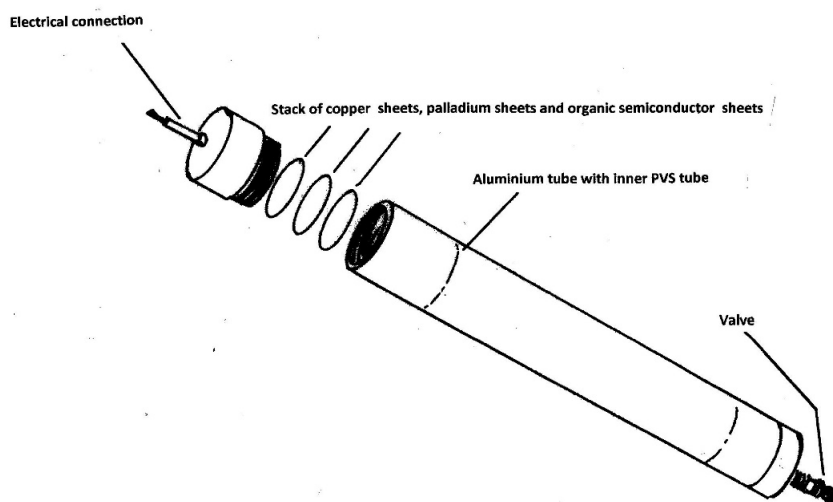


Figure 4. Stack of fusion diodes (please read “PVC” instead of the wrong acronym “PVS”).

We used sheets of aluminum foil covered on one side by a thin sheet of palladium, and on the other by a layer of semiconducting paint (Plexcore[®] Organic Conductive Ink, Sigma). Little disks are then cut with a punch and these disks are stacked on top of one another and compressed with a hydraulic press. A valve makes it possible to pressurize the container with deuterium (Fig. 4).

A better method would be to use a plastic semiconductor film covered with a palladium sheet on one side, and a gold leaf on the other side. Whether in the form of metal powders or thin metal foils, it is possible to quickly test a large number of alloys containing deuterium or hydrogen. The higher the voltage, the better the LENR properties of the tested alloy. A large number of new alloys have been developed over the last 20 years by the metal-hydride battery industry, and also for the storage of hydrogen. Many of these alloys are available in the supplier’s catalogs (Sigma–Aldrich). These alloys are much cheaper than palladium, and their price will drop considerably as soon as they are produced in industrial quantities. Nickel alloys look promising [2].

By way of example, the properties of the ZrV2 H5.5 alloy are better than those of pure palladium (3% weight of hydrogen versus 0.5% for PdH0.6 and equivalent pressure at 300 K of 10^{-8} bar versus 0.02 bar for palladium) (Ref: D. Chandra et al., Material Matters, Vol 6, no. 2, Sigma–Aldrich eds., 2010).

3. The Use of the Reifenschweiler Effect

The Dr. Otto Reifenschweiler was heading the neutrons generators department of PHILIPS during the 1960s. In 1964, Reifenschweiler noticed that the *apparent* beta-decay of the tritium absorbed into titanium changes with the temperature of the titanium. Reifenschweiler has waited his retirement to publish his observations [10]. Here is the curve obtained by Reifenschweiler: the apparent radioactivity of tritium decreases by 40% (Fig. 5).

In our opinion, the number of disintegrations per second does not change, it is just the yield of counting X-rays produced by bremsstrahlung that varies. We believe that at low temperatures, the tritium nuclei contained in the metal combine two by two to form composite bosons (two tritium nuclei of opposite spin form a composite boson, such as helium-3 nuclei in superfluid helium-3). The tritium nuclei have a spin of $1/2$. They are therefore fermions. In superconductors, the electrons combine two by two to form composite bosons of spin 0 (the two electrons of each pair

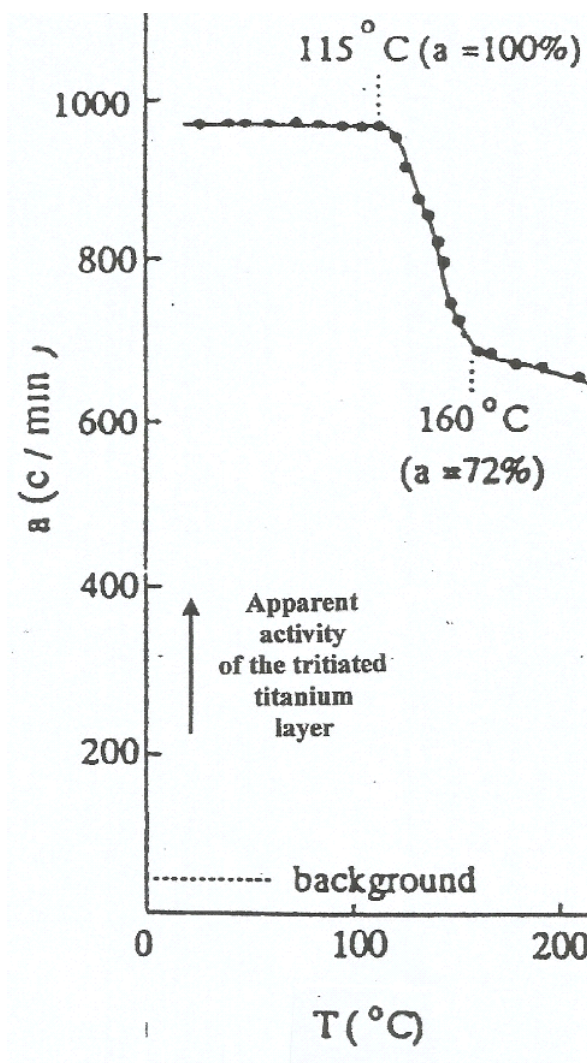


Figure 5. Decrease of the (apparent) radioactivity of tritium as a function of temperature.

are of opposite spin $1/2$). These composite bosons can form a superconducting quantum phase. We hypothesize that tritium nuclei can also associate two by two to form composite spin-zero bosons.

These composite bosons can therefore form a Bose–Einstein Condensate (we will not discuss here the physical phenomena that make possible the existence of a BEC at room temperature) [11,12]. In this case, during the beta decay of a triton in this BEC, there is no more recoil of the nucleus: the energy of beta rays and neutrinos increases. The whole spectrum of beta electrons is shifted slightly towards high energies, and the counting efficiency increases. As the temperature increases, the pairs of tritium nuclei break and the Bose–Einstein Condensate disappears, and thus the counting efficiency of the radioactivity decreases.

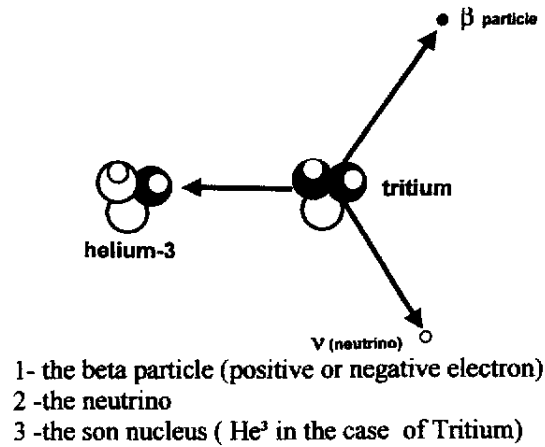


Figure 6. Balance of beta-decay energy.

The decay energy of tritium is divided into three parts: the electron energy, the neutrino energy, and the recoil energy of the helium-3 nucleus (Fig. 6). We hypothesize that when the tritium nuclei are engaged in a BEC, it is the whole BEC that absorbs the recoil energy. As a result, there is very little energy transmitted to the BEC, and therefore,

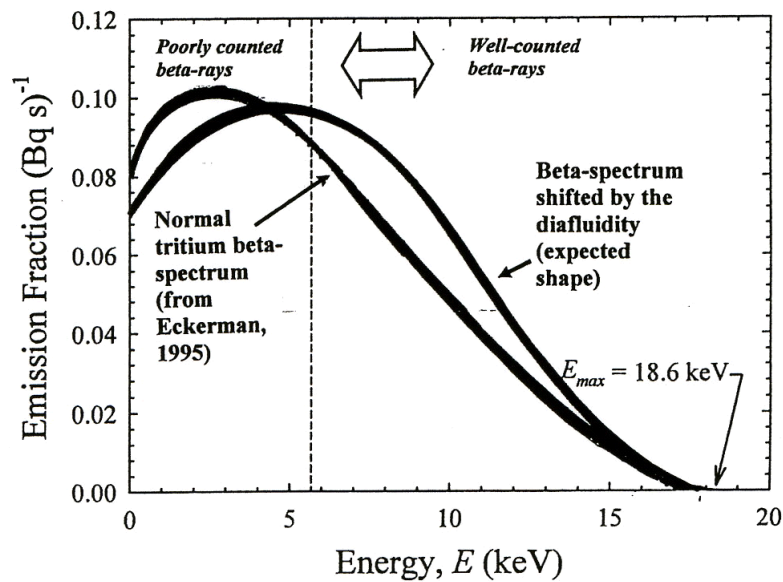


Figure 7. Spectrum of normal tritium decay and expected BEC tritium decay spectrum.

correlatively, there is more energy carried by the neutrino and the beta electron. The spectrum of the beta rays is thus shifted to the “high” energies (Fig. 7). If the BEC is suppressed by the rise of the temperature, in the opposite way, the spectrum is moved towards the low energies. This effect is extremely weak. But by chance, we have a natural amplifier that helps us to highlight it. Indeed, in the Reifenschweiler experiments, the conversion of beta rays into X-rays by bremsstrahlung is used. This effect is mainly caused by the upper part of the energy spectrum of tritium (low energy X-rays do not come out of the experimental setup, nor do they enter the Geiger counter, so they are not counted). A small shift to high energy will therefore have a relatively large effect.

This phenomenon is very important for our field of research because many authors have asserted that the “Nuclear Active Environment” that allows the LENRs is due to the formation of Bose–Einstein Condensates [4–7].

It is therefore possible to use the Reifenschweiler effect to sort the new alloys containing hydrogen according to their capacity to house BECs. (Of course, we will use a simpler experimental device than that of Reifenschweiler: small sealed ampoules glass containing the alloy powder and tritium, and a small programmable oven.) It is probably possible to design experimental devices even simpler, and bringing even more convincing results.

4. The Magnetic Alignment of the Tritium Pairs

This effect, which we have postulated, but not yet observed, would make it possible to very quickly test many new hybrid-forming alloys. We propose to make sealed glass sources containing alloy powder and tritium. These sources will be placed in the gap of a powerful electromagnet. When the electromagnet will be turned on, the spins of the tritium nuclei will align with the magnetic field and the composite bosons will be destroyed. The condensate of Bose–Einstein will disappear. The beta spectrum will be shifted slightly towards the low energies and the counting efficiency of the radioactivity will decrease.

If it exists, this new effect will be easy to prove and it can be very useful to sort the best NAE alloys, regardless of the theoretical importance of this effect.

5. Conclusion

Despite the quality of the experimental results proving the reality of the Fleischman–Pons effect (excess heat in palladium and deuterium alloys), the majority of scientists are still not convinced of the existence of LENRs. We believe that the three phenomena of the “Fusion Diode” effect, the Reifenschweiler effect, and the magnetic suppression of the triton’s pairs, if confirmed, could be the basis for new techniques to confirm the calorimetry experiments. It would also be possible to use these effects to quickly select new alloys that can be used to produce LENRs.

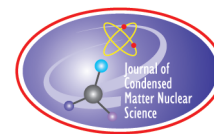
Acknowledgement

Fabrice David thanks the BIOCLINIC Group (Paris) for the help given to the realization of this work.

References

- [1] M. Fleischman and S. Pons, *J. Electroanal. Chem.* **261** (1989) 301.
- [2] A. Parkhomov and E. Belousova, Research into heat generators similar to high-temperature Rossi reactor, *J. Condensed Matter Nucl. Sci.* **19** (2016) 244.
- [3] Michael C.H. McKubre, Romeu C. Rocha-Filho, Stuart Smedley, Francis Tanzella, Jason Chao, Bindi Chexal, Tom Passell and Joseph Santucci, Calorimetry and electrochemistry in the D/Pd system, In *the First Annual Conf. on Cold Fusion*, 1990, University of Utah Research Park, Salt Lake City, Utah, National Cold Fusion Institute.
- [4] E. Storms, What conditions are required to initiate the LENR effect? in *Tenth Int. Conf. on Cold Fusion*, 2003, Cambridge, MA.

- [5] Fabrice David and John Giles, Self-polarisation of fusion diodes: from excess energy to energy, *Proc. of the ICCF14*.
- [6] Fabrice David, Hypothesis of the diafluidity, *FUSION* no. 49, Jan.-Rev. 1994, (French edition of *XXIth Century Science et Technology*).
- [7] F. Premuda, D. Boni and De Pasca, La superconduttività nel palladio carico di deuterio, *XXI Secolo Scienza e Tecnologia*, Vol. 1, 1997, pp. 24–31.
- [8] Paolo Tripodi, Daniele Di Gioacchino and Jenny Darja Vinko, Superconductivity in PdH: Phenomenological explanation, *Physica C (Superconductivity)* **408**(1) (2004) 350–352.
- [9] Y.E. Kim, and T.O. Passell, Alternative interpretation of low-energy nuclear reaction processes with deuterated metals based on the Bose–Einstein condensation mechanism, in *Eleventh Int. Conf. on Condensed Matter Nucl. Sci.*, 2004, Marseille, France.
- [10] O. Reifenschweiler, *Phys. Lett. A*. **184** (1994) 149.
- [11] F. David and J. Giles, Beta-decay of tritium as a probe for Bose–Einstein condensates in metallic lattices, *Proc. of the 17th RCCNT-BL*, Sochi, September 26–Oct. 3, 2010.
- [12] Fabrice David, About discrete breathers and LENR, *14th Int. Workshop on Anomalies in Hydrogen Loaded Metals*, Asti, Italy, 5–9 June 2017.



Research Article

Heavy Electron Catalysis of Nuclear Reactions

Anthony C. Zuppero*

Tionesta Applied Research Corporation, Sequim, WA, USA

Thomas J. Dolan†

University of Illinois at Urbana-Champaign, Urbana, IL, USA

Abstract

Our proposed three-body model attempts to understand the transmutations that have been observed in many experiments. The model combines several phenomena to derive the conditions where a binding potential energy and an electron's Coulomb bond can combine to attract the ions together to form a new nucleus. We hypothesize that heavy electron quasiparticles are created by placing electrons near inflection points of a lattice band diagram and last about one collision time (~ 10 fs). They are placed near the inflection point by injection of phonons carrying crystal momentum, which last picoseconds, long enough to create many generations of transient heavy electron quasiparticles. We consider the interaction of two ions, such as a nickel nucleus and a proton, separated by a distance x with an electron of mass m trapped between them. The increase in energy needed to confine the electron (Kinetic Energy of Confinement, KEC) $\propto 1/(mx^2)$ from the Heisenberg Uncertainty Principle acts like a repulsive potential. The KEC keeps the ions separated by many picometers, but with a heavy electron that distance can be reduced to tens of femtometers, from where the heavy electron tunnels through the region between reactant ions. The transient shielding by the evanescent electron wavefunction at the nucleus permits the f and R nuclear bond to form, and scatters the electron. The electron may be ejected with much or all of the nuclear binding energy, or the excited compound nucleus may break into stable fragments. The Hamiltonian is

$$H = T_e + T_i + V_e + V_b,$$

where T_e is the kinetic energy of the electrons, T_i the kinetic energy of the nuclei, V_e the net Coulomb potential, and V_b is the independent binding energy (other than V_e). For example, V_b may be a nuclear binding potential V_{nuc} , which is zero except at very small $x \sim$ several fm. We approximate these potentials using a one-dimensional analysis, calculate the approach distances, calculate the threshold electron mass for tunneling to occur, and estimate the tunneling probability for many possible reactions. (continued in the next page)

© 2020 ISCMNS. All rights reserved. ISSN 2227-3123

Keywords: Band structure, Catalysis, Heavy electron, Muon, Transmutation, Tunneling

*Corresponding author. Address for correspondence: 211 North Citrus STN 27, Escondido, CA 92037, USA, Tel.: +1-858-753-8964, E-mail: zuppero@thetionestagroup.com.

†Address for correspondence: 1061 210th Street, Ionia, Iowa, 50646, USA, Tel.: +1-217-369-0489, E-mail: dolantj@illinois.edu.

(continued from the title page)

We compare the 1D model predictions with data from experiments, such as transmutation of Ni into Fe, Cu, and Zn. If we can create many heavy electron quasiparticles, then our model predictions are consistent with transmutation data from many experiments, showing which isotopes are probable and which are improbable.

1. Introduction

This proposed model considers several elements:

- Molecular chemistry.
- Coulomb potential and tri-body attraction reaction.
- Kinetic Energy of Confinement (KEC), due to the Heisenberg Uncertainty Principle.
- Nuclear binding and muon catalyzed reactions.
- Production of heavy electron quasiparticles in a lattice.
- Quantum mechanical tunneling of an electron through a potential barrier.

We will discuss each phenomenon, and then combine them to model nuclear transmutations that have been reported experimentally.

Consider a three-body reaction where two reactants R and f can bond together by the Coulomb attraction of an electron bond between them, and also by an independent binding mechanism (chemical or nuclear), as in Fig. 1. There are two separate potentials: a three-body Coulomb potential of $R + e + f$; and an independent, two-body potential binding only the reactant R and fuel f .

Chemists have discovered that when the R and f merge into a new entity, Rf , the bonding electron between ions R and f can be ejected with most of the binding energy, and the new molecule Rf is left in a lower energy vibration state. The other electrons are responsible for the independent chemical binding mechanism. That a single electron captures the binding energy instead of a thermal bath was an unexpected discovery.

2. Chemical Physics

The binding reaction of R and f with an ejection of a single electron was discovered in chemical physics during the 2000s. The principle of operation for the chemical physics case had a potential energy diagram the same as a hydrogen

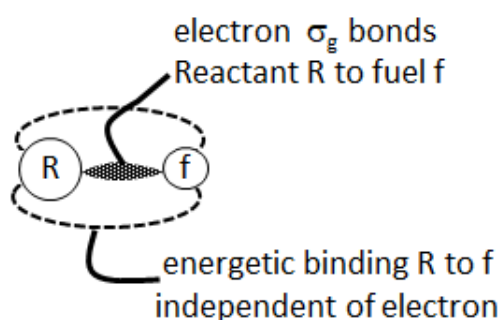


Figure 1. The reaction includes a three-body electron σ_g (“sigma gerade”) bond plus an independent binding potential between a reactant R and a fuel f that does not require the σ_g electron.

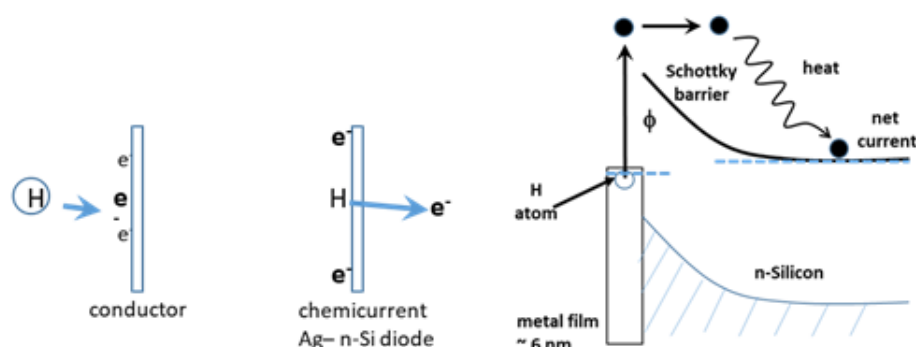


Figure 2. H gives up electron at Ag surface. Principle of *chemicurrent* detection. H atoms react and bond with the metal surface creating e–h pairs. The hot electrons travel ballistically through the film into the semiconductor where they are detected. Right-hand side: Schematic cut view through the H sensing Schottky diode. The ultrathin metal film is connected to the Ag pad during evaporation [1].

and nickel nuclear reaction. Understanding the chemical physics case would mean that we could understand the H–Ni reaction.

Before 2000, a common assumption for chemists and physicists was that a vibrating molecule would lose 1, or at most 2, vibrational quanta during a chemical reaction. The energy released would either be radiated or given to a sea of thermal electrons at the Fermi level of a conducting wall where the vibrating molecule collided or was attached.

The “molecule” in the first observation comprised a free radical bonded to a conductor surface. Nienhaus et al. at UC Santa Barbara provided the first observations in April 1999, Fig. 2.

During 1999, Nienhaus provided free radicals such as H, OH, CH₂, and O to a 6 nm thin silver conducting nanolayer sheet [2]. The nanolayer on top of n-silicon made a Schottky diode that put a voltage barrier preventing any electron with energy less than the barrier from going over the barrier. Nienhaus was one of the few who knew a higher energy electron would be emitted. He measured electron current which had to have higher energy than the barrier. The barrier was about 700 mV, and the electrons with only thermal energy, according to dogma, only had about 20 mV. Immediately upon his April 1999 publication colleagues in the field proclaimed the discovery of a rule-breaking observation. The electron had more energy than expected. Figure 2 shows the schematic and the diode configuration.

In October 2000 Huang et al. published the observation that a highly stretched gaseous NO molecule would collide with a conductor surface and suddenly have many vibration levels less energy (Fig. 3 [3]). A laser excited the NO molecule to a high vibration state, between 12 and 15. The NO attracted an electron from the metal chamber wall. The vibration spectrum after the wall collision showed final vibration levels as low as the ground state, and peaked at levels between 5 and 8. An electron emission experiment showed a corresponding emitted electron energy with as much as all the binding energy, e.g. a ground state final product.

In 2005 Xiao, Ji and Somorjai (University of California – Berkeley) deposited thin films (<10 nm) of Pt or Pd on TiO₂ or GaN to form Schottky diodes. They monitored the continuous electron flow across the metal–oxide interfaces during the catalytic oxidation of carbon monoxide, due to conversion of energy released by the oxidation of carbon monoxide into the kinetic energy of free electrons in platinum and palladium (Fig. 4).

Zuppero and Dolan considered electrical power generation by the ejected electron [5].

That a single electron would get all the energy was still controversial. But in 2011 LaRue, of the same UC Santa Barbara Chemistry department as Huang, published the observation of the partition of energy between a single electron and the vibrational energy remaining in the NO molecule [6]. However, Ji, Zuppero et al. suspecting that the Nienhaus and Huang observations were correct, reacted carbon monoxide with oxygen on a 3 nm conducting catalyst. One

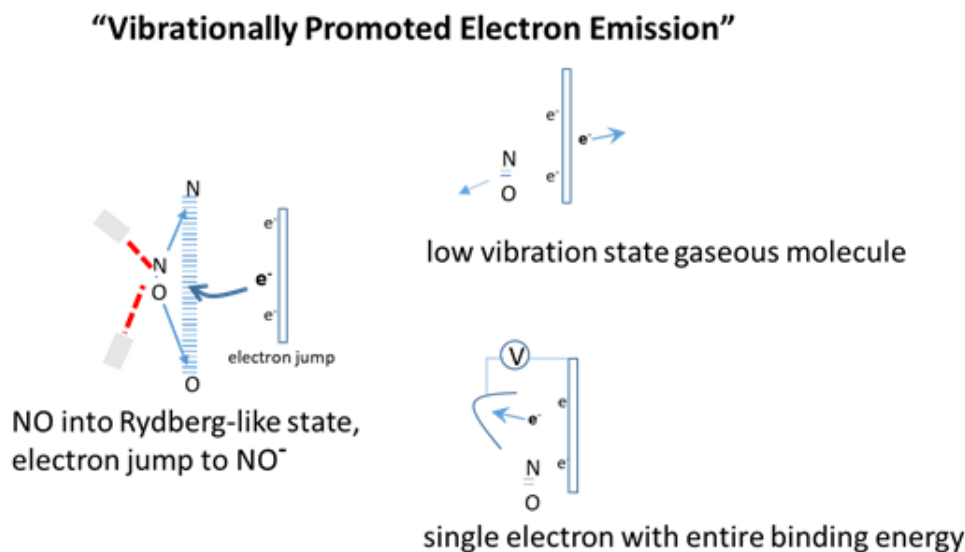


Figure 3. Left-hand side, NO molecule energized to a highly vibrationally excited state by lasers come close to a metal substrate, attracting an electron to form NO^- . Right-hand side upper, the NO^- immediately ejected the electron, leaving the NO molecule in a much lower vibration state than it originally started with. Right side lower, the same excited state NO^- ejected the electron into a multichannel plate detector (MCP) in a vacuum, overcoming the work function of the contacted surface, proving that a single electron can carry off the entire binding energy in a single reaction.

experiment developed a forward voltage of about 0.68 V, far above thermal [7]. This meant the CO_2 gas leaving the surface would have almost no internal vibration energy, because adsorbing on the catalyst took most of it. The process was apparently like that reported by Huang and LaRue, called “Vibrationally Promoted Electron Emission.”

During 2015 Zuppero realized that the first muon catalyzed fusion experiment by Alvarez at UC Berkeley in 1957 had the same potential energy diagram and had the same result: the entire binding energy went into the heavy electron (a muon) and the resulting fusion nucleus, helium-3, was in the ground state [8,9]. The reactants attracted each other with 5.3 MeV of binding energy. The model provided by muon catalyzed fusion had two reactants, R and f , attracted together by a nuclear binding potential totally independent of the electron. The muon provided an electron with enough effective mass to create a new, electron bond at the nucleus and with a bonding, sigma grade σ_g wave function. This model had the same properties as the chemical physics discovery.

We refer to this as a “tri-body attraction reaction.”

3. Tri-body Attraction Reaction

First we need to estimate the energy in the electron bond. Consider a one-dimensional approximation of an electron confined in an electrostatic potential well, between two positive particles that are separated a distance x , as in Fig. 5. If the electron has an energy above the energy of the equilibrium point, it will oscillate between the positives.

We will calculate the Coulomb attractive energy at the equilibrium of the “ $R - e - f$ ” entity. (See Section 4.)

A novel property discovered during research on muon catalyzed fusion is the mandate to “ignore core electrons” which is a key point discovered by the first observers of muon catalyzed reactions in liquid hydrogen. (Here “core electrons” means normal mass atomic electrons.) Subsequent muon experiments strongly supported this mandate. Including liquid neon with its 10 protons of Coulomb charge in the liquid hydrogen totally quenched the fusion re-

nanodiode electron emission

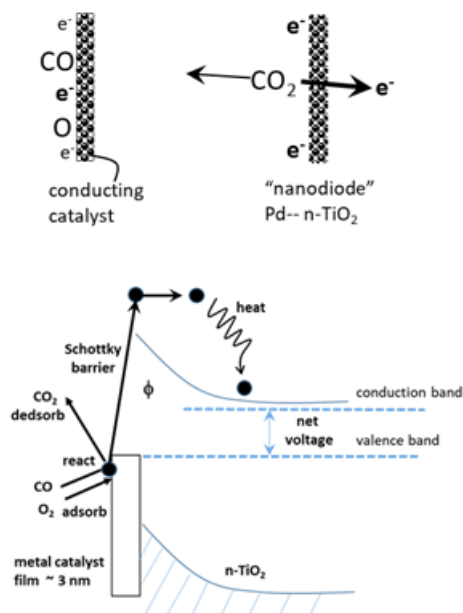


Figure 4. The oxidation of carbon monoxide [4] by Xiao, Ji and Somorjai produced a net voltage in excess of 0.68 eV across a Schottky diode when an electron was promptly emitted upon reaction at room temperature.

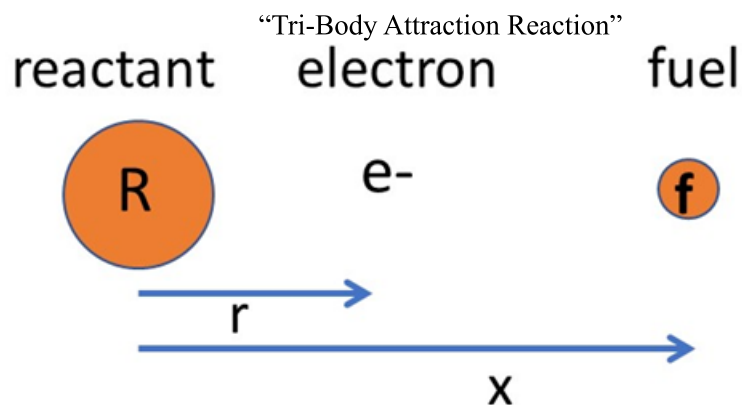


Figure 5. Reactant ion R and fuel ion f form an electrostatic potential well that concentrates the electron wave function between them.

actions. This led to the conclusion that the heavy electron is not much moved or affected by the core electrons. The heavy electron repels the low mass, core electrons out of the way as if they were zero mass. The muons were strongly attracted to the charge of the 10 protons and “ignored” the liquid hydrogen’s and the liquid deuterium’s single positive charge. The ground state (or lower states) of the muon are quite close to the nucleus compared to the other electrons. The discovery was that charge shielding by low mass core electrons can be mostly ignored when high mass electrons are present.

Chemists never ignore the core electrons which shield the nuclear positive charge. Jackson (1957) the first to analyze the p–d fusion to ^3He using a muon, instructed “... any electrons that may be present may be ignored. The bound system will be the mu-mesonic analog of the $(\text{H}^1\text{H}^2)^+$ electronic molecular ion [10].”

Bleser reported that when a mere 1% neon was present in the liquid hydrogen/liquid deuterium mix used as a target for muons, the muons immediately migrated to the neon, and thereby quenched the reaction [11]. The key mandate, contradicting conventional chemistry, is that a system with a mix of heavy and normal electrons, to ignore the normal electrons. The muons and heavy electrons migrate to the largest charged nucleus, as if there were no core electrons.

More recently, Inagaki repeated this observation:

... Therefore, the charge of the muonic hydrogen nucleus is strongly shielded by the compact muon orbital and muonic hydrogen atom can behave like a neutron. As a result, muonic hydrogen atom can diffuse freely, it can even pass through the electron clouds of other atoms. When the muonic hydrogen atom approaches the nucleus of another $Z \geq 2$ atom, the muon moves from the muonic hydrogen atom to a deeper atomic muon level of the $Z > 2$ atom and forms a new $Z > 2$ muonic atom. This process in compounds and mixtures is called muon transfer [12].

To compute the 1D electrostatic potential between bare nuclei and an electron between them, let x is the distance between R and f , and r is the distance from R to the electron centroid. The charges of R and f are assumed to be Qe and qe . Usually f is hydrogen or deuterium with $q = 1$.

The average position of the electron is at the equilibrium point. Especially when the electron has an energy above the energy of the equilibrium point, it will oscillate back and forth so rapidly (compared to the motion of the ions) that we may use its expected or average value (the Born Oppenheimer approximation).

The one-dimensional Hamiltonian may be written

$$H = V_e + V_{\text{nuc}} + T_i + T_e, \quad (1)$$

where V_e is the three-body Coulomb potential, V_{nuc} is an independent nuclear binding energy, T_i is the kinetic energy of the nuclei, and T_e is the kinetic energy of the electron including its confinement energy KEC. V_e is relatively weak ($\sim \text{eV}$) with a chemical range of order 100 pm. The nuclear binding potential, V_{nuc} , is relatively strong (MeV), with a very short range (several fm). We will discuss V_e and then T_e .

4. Coulomb Potential

The electrostatic potential energy of a three-body molecule (Fig. 5) is

$$V_e = (e^2/4\pi\epsilon_0)[Qq/x - Q/r - q/(x - r)], \quad (2)$$

where ϵ_0 is the permittivity of free space. We need to know what value of “ Q ” to use. “Ignore all normal electrons” is the lesson from muon particle physics. For example, we use $Q = 28$ electrons as the charge for nickel, and no “core” electrons need be considered, so long as the main electron is heavy.

We need to know the effective value of r in order to calculate V_e . The equilibrium value of r is derived as follows:

$$dV_e/dr = (e^2/4\pi\epsilon_0)[0 + Q/r^2 - q/(x - r)^2] = 0, \quad (3)$$

$$r/(x-r) = (Q/q)^{1/2}, \quad (4)$$

$$r = x(Q/q)^{1/2} / ((Q/q)^{1/2} + 1). \quad (5)$$

Using this value of r we find

$$V_e = (e^2/4\pi\epsilon_0 x)F(Q), \quad (6)$$

where

$$F(Q) = [Qq - Q - q - 2(Qq)^{1/2}]. \quad (7)$$

Usually $q = 1$, giving

$$F(Q) = -(1 + 2Q^{1/2}), \quad (8)$$

V_e is negative (attractive potential). If $Q = 1$, then $F(Q) = -3$, and $V_e = -6.92 \times 10^{-28}/x$ (J). Large Q or q makes the Coulomb bonding potential V_e stronger. R and f comprise a diatomic molecule that vibrates. As R and f converge what keeps the molecule from collapse?

5. Kinetic Energy of Confinement

If there were no repulsive forces the molecule would quickly collapse to nuclear dimensions. However, it takes energy to confine the electron to a region the size of the “*Ref*” molecule. Squeezing the electron confinement x increases its momentum p , according to the Robertson–Schrödinger relation (modern version of the Heisenberg uncertainty principle). We calculate the momentum using a one-dimensional model, which is a vibration along the x -direction. The binding potential between R and f acts along the x -direction between them. Momentum components in the y - and z -directions are not directly affected by compression along x .

The Robertson–Schrödinger relation valid for all solutions of the Schrödinger equation, is

$$\sigma_p^2 \sigma_x^2 = (\hbar/2)^2 K(n), \quad (9)$$

where the variances are

$$\sigma_x^2 = \langle x^2 \rangle - \langle x \rangle^2, \quad (10)$$

$$\sigma_p^2 = \langle p^2 \rangle - \langle p \rangle^2, \quad (11)$$

and \hbar is the reduced Planck constant. To reduce the three-body problem to a two-body problem, we use the Born–Oppenheimer approximation: the electron accommodates and equilibrates far faster than the ions. This allows us to use the electron’s quantum expected values. With these assumptions, for oscillatory motion $\langle p \rangle = 0$, and $\sigma_p^2 = \langle p^2 \rangle$. The constant multiplier, $K(n)$ for a given vibrational energy level, n , is conveniently close to unity for ground states:

For ground states

$$K(\text{ground state}) \sim 1. \quad (12)$$

For quantum harmonic oscillator stationary states

$$K(n) = (2n+1)^2, \quad n = 0, 1, \dots \quad (13)$$

For a gaussian initial condition or for a coherent state

$$K = 1. \quad (14)$$

For a particle in a box

$$K(n) = (n^2\pi^2/3 - 2)n = 1, 2, \dots \quad (15)$$

Decreasing the electron confinement into smaller space x results in its x -momentum p rising proportionally.

$$\langle p^2 \rangle = \hbar^2 K(n)/4\sigma_x^2. \quad (16)$$

The expected value of the electron KEC is therefore

$$\langle T_e \rangle = \langle p^2/2m \rangle = \hbar^2 K(n)/8m\sigma_x^2. \quad (17)$$

In this article the symbol m always refers to the *effective electron mass*, which is usually different from its rest mass m_0 . From the above relation we see that it takes energy $\langle T_e \rangle$ to confine an electron into a space whose size is characterized by σ_x .

The *confinement parameter* σ_x is a measure of the size of the compressed electron wave-function. These results are sensitive to the assumption about how σ_x relates to the ion separation distance x . Resolution of the relationship requires analysis beyond the scope of this work. We considered three cases:

$$\sigma_x^2 \approx 2x^2, \quad \text{optimistic values of required } m, \quad (18)$$

$$\sigma_x^2 \approx x^2, \quad \text{nominal values,} \quad (19)$$

$$\sigma_x^2 \approx x^2/2, \quad \text{conservative values.} \quad (20)$$

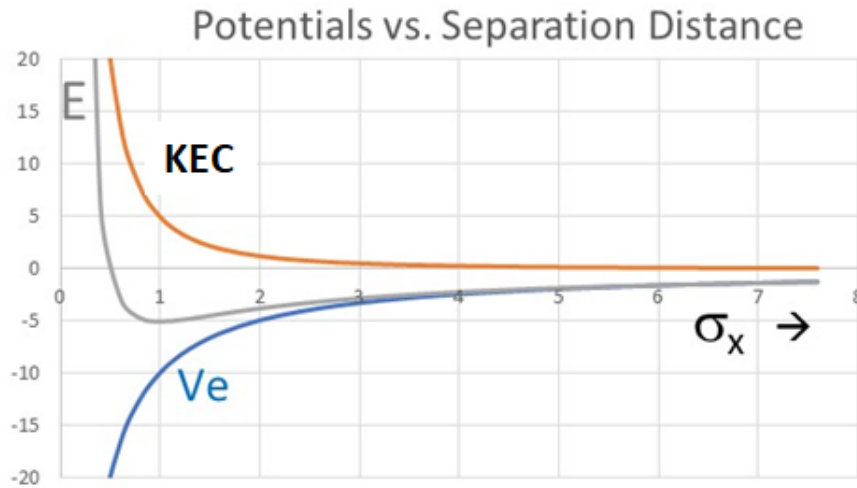


Figure 6. Approximate variations of the electron bonding potential V_e and KEC with separation distance σ_x , arbitrary units $E \approx V_e + T_e$, since T_i is small and $V_{\text{nuc}} = 0$ (except at tiny separations). The valley at $\sigma_x \sim 1$ is a potential energy valley.

The nominal values are consistent with the spread of the ground state wavefunction of the H_2^+ ion [13]. A simple evaluation of a variance for sinusoidal oscillations in a harmonic potential well, valid near the ground state of the nuclear case, gives the optimistic $\sigma_x^2 \approx 2x^2$. Our calculations here use the nominal assumption (19).

The bonding potential $V_e \propto 1/x$ is attractive to ions (negative), while the KEC $\propto 1/m\sigma_x^2$ acts like a repulsive (positive) potential, as in Fig. 6, where the ions and electrons must reside to be in a stable state.

How many valleys are there below zero energy? “Below zero” implies a stable state. For a chemical bond with only an electron, there is only one. The valley is the well in which chemical vibration states are formed. When we add an independent nuclear binding of the reactants, another valley appears (Fig. 7). The valley must be below zero energy to be stable.

Even when we add a strong V_{nuc} to the total energy E the repulsive KEC $\gg V_{\text{nuc}}$ at $\sigma_x = a$ ($\sim 3 - 10$ fm). However, if we could increase m , then the KEC term would decrease, as shown in Fig. 7. When m is heavy enough, the attractive potentials $V_e + V_{\text{nuc}}$ are strong enough to overcome the repulsive KEC at $\sigma_x = a$, and a stable, new potential energy valley with energy less than zero appears, Fig. 7.

The condition $E < 0$ at $\sigma_x = a$ quantifies the minimum m required to form a bonding wave function between two positive entities. The electron starting in a stable valley at chemical dimensions may tunnel through the repulsive momentum barrier (KEC) and reach nuclear dimensions.

6. Threshold Effective Mass

We use the effective mass approximation as a fictitious mass to represent how the lattice provides a momentum to the reactant and electron quasiparticles. This is similar to the Mössbauer effect, where the lattice takes up the momentum as if the nucleus that emits or absorbs a high energy gamma ray had a very large mass, minimizing the recoil Doppler shift. In the VPPE effect at nuclear dimensions, the lattice takes up the momentum as if the electron had a large mass.

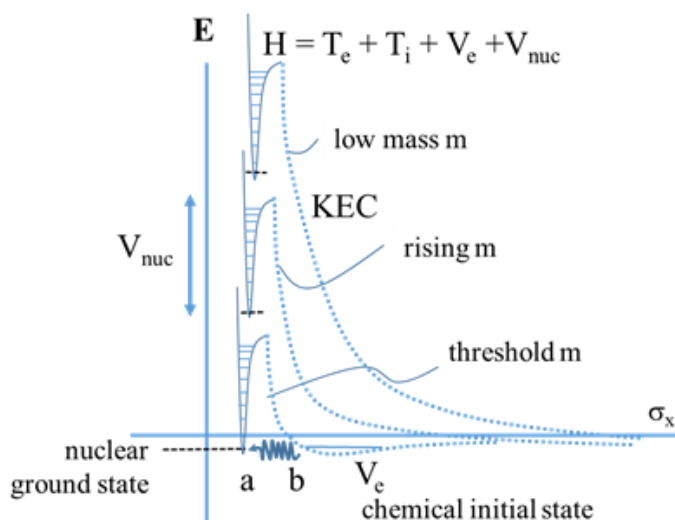


Figure 7. Reduction of KEC barrier by increasing electron mass. When the electron effective mass surpasses a threshold, the nuclear ground state at $\sigma_x = a$ can match the energy level of the chemical state at $\sigma_x \approx b$ and prompt tunneling can occur (Eqs. (32) and (33)), forming a compound nucleus Rf . (Upper curves are offset slightly for clarity.)

This fictitious “heavy electron” provides a simple model.

For tunneling to be possible the electron effective mass must be heavy enough to make the magnitudes of the attractive potentials $U = V_e + V_{\text{nuc}}$ equal to the repulsive KEC.

$$\hbar^2 K(n)/m\sigma_x^2 = U = V_e + V_{\text{nuc}}, \quad (21)$$

where we use Eqs.(6) and (7) to find

$$U = (e^2/4\pi\epsilon_0 x)|F(Q)| + V_{\text{nuc}}, \quad (22)$$

$$F(Q) = [Qq - Q - q - 2(Qq)^{1/2}]. \quad (23)$$

V_{nuc} is many MeV at $x \leq a$, and $V_{\text{nuc}} = 0$ at $x > a$. Solving Eq. (21) for the *threshold effective mass* m gives

$$m_{\text{th}} = \hbar^2 K(n)/U\sigma_x^2. \quad (24)$$

At the *inner chemical turning point* b_i and assuming the molecule was vibrating at its highest vibrational state (at the top of the potential energy surface well), $V_i = V_{\text{nuc}} = 0$, and

$$T_e + V_e = 0. \quad (25)$$

Using Eqs. (6), (7), (17) and (25) with $K(n) = 1$, we find

$$\hbar^2/8mb^2 = (e^2/4\pi\epsilon_0 b)F(Q). \quad (26)$$

Solving for b_i the result is

$$b_i = 4\pi\epsilon_0 \hbar^2/8me^2 F(Q). \quad (27)$$

For example, if $Q = 1$ and $m = m_0$, then $b_i = 2.2$ pm. This is also the value of deuteron separation distance (2.3 ± 0.1 pm) in Rydberg matter [14].

7. Catalysis of Nuclear Reactions

For nuclear reactions the binding energy is

$$\begin{aligned} V_{\text{nuc}} &= \text{many MeV}, & x \leq a, \\ V_{\text{nuc}} &= 0, & x > a, \end{aligned} \quad (28)$$

where a is the sum of the nuclear force radii

$$a = R_Q + R_q. \quad (29)$$

Each radius is either taken from tables of nuclear ground state charge radii [15] or from the approximation:

$$R = R_0 A^{1/3}, \quad (30)$$

A is the atomic mass number, and $R_0 = 1.4 \pm 0.1$ fm [16].

For the calculations below, the simple algebraic relation is used. The charge radii tables may be used when evaluating reactions for more precise analyses.

A heavy electron, such as a muon ($m_\mu = 206.77m_0$, where m_0 is the free electron rest mass), may become bonded between two positive ions, pulling them close enough for the strong nuclear force to act, fusing them together and ejecting the muon, as was observed between protons and deuterons [17,18]. However, accelerators are expensive and cannot produce many muons.

Other heavy electrons may have similar catalytic action if they can bring the reactants within electron tunneling range of the nuclear force distance.

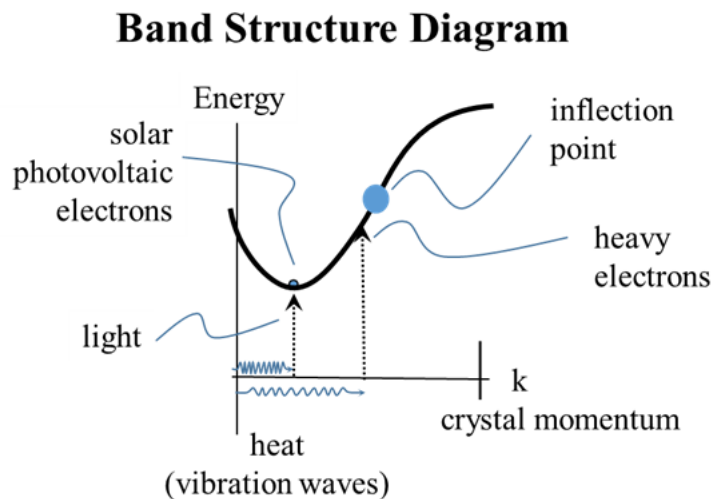


Figure 8. Example band structure diagram, defining the allowed values of E and k . Photovoltaic energy conversion in silicon uses thermal vibration waves for crystal momentum addition, and photons for energy addition.

8. Heavy Electrons

Electrons in a real crystal respond to Coulomb forces according to the Schrödinger equation for a periodic crystal potential. If the electron is not undergoing a collision, then it moves according to a solution of the Schrödinger equation for the crystal, which is represented in a band structure diagram. The effect of the entire crystal on a conduction band electron is that the charge and spin are that of an electron, but the motion in response to electric forces is as if the electron had an effective mass. The relation between energy E and crystal momentum k is given by a band structure diagram. Heavy electron quasiparticles are transiently created when the electron is energized to be in the region of an inflection point on the band structure, where curvature vanishes and effective mass diverges, as in Fig. 8.

The effective mass of an electron quasiparticle is

$$m = \hbar^2 / (\partial^2 E / \partial k^2) = \hbar^2 / \text{curvature}, \quad (31)$$

where \hbar is the reduced Planck constant [19]. Electrons can be placed in the region of an inflection point by simultaneous injection of appropriate values of crystal momentum (phonons) and electron energy into a crystallite region. Then the electrons behave as if they were “heavy”.

If heavy electrons reduce nuclei separation distances to near the modified Bohr radius (which would be (m_0/m) times the conventional Bohr radius), then the resulting particle density could be much higher than normal density.

The validity of our model depends on the attainment of heavy electrons produced by Eq. (31) exceeding the threshold mass of Eq. (24). We will discuss how this might be accomplished, and then compare model predictions with experimental transmutation data.

Short wavelength distortions and localized energy injection can provide a spread of crystal momentum and energy into the first Brillouin zone, and some electrons will be placed near an inflection point, where their effective masses increase (Fig. 9).

Such localized spreads of energy and crystal momentum in the first Brillouin zone of the crystal can be induced by fast distortions having a wavelength about the size of an atom.

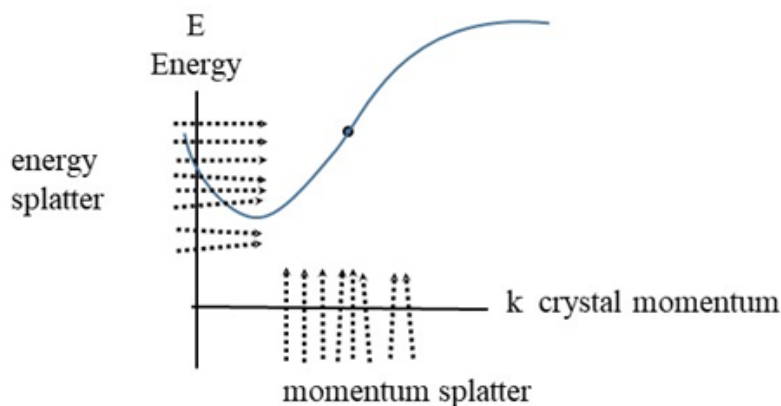


Figure 9. Illustration of simplified band diagram with spreads of injected energy and momentum.

Experimental evidence suggests that heavy electrons may be responsible for sometimes dramatic chemical reaction rate acceleration. We suspect the involvement of crystal momentum and electron effective mass in the unexplained acceleration of surface oxidation. An unexplained, and in some cases dramatic chemical acceleration of hydrocarbon oxidation reaction rates on thin, TiO_2 , NiO , WO_3 , Pd or Pt catalyst surface was reported by several different research groups [20–23]. Their common process included a piezoelectric Surface Acoustic Wave generator (SAW) under a thin catalyst for hydrocarbon oxidation reactions. When the SAW power was increased above a threshold it incidentally injected crystal momentum into the catalyst on top of it. The catalyst lattice was also the reaction surface region. An increase in effective mass would change the reactant separation proportionally. Changes less than a factor of 1.5 would result in a contraction by less than 1.5 and account for the reaction rate changes observed.

In experiments of ethanol or CO oxidation on a catalyst surface formed on a Surface Acoustic Wave generator energized to a relatively intense power level, the reaction rate increased dramatically from one to three orders of magnitude. Saito et al. (200) in Japan observed typical activation energy reductions from ~ 90 kJ/mol to ~ 40 kJ/mol for CO oxidation [24]. Reaction rates increased from 4 to 7 times upon energizing SAW. Mitrelias et al. [25] in Britain

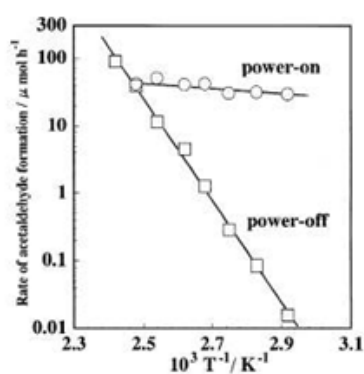


Figure 10. Ethanol oxidation rate on a cooler Pd catalyst approaches that of a hot substrate when the SAW catalyst substrate is turned on.

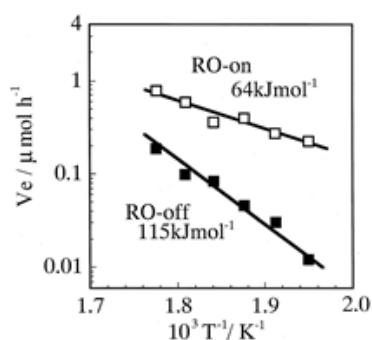


Figure 11. The slope of the ethylene production rate is the activation energy, which decreases by about a factor of 2 when the resonance oscillation (RO) of the catalyst substrate is turned on.

observed similar accelerations. Saito [26] observed activation energy for ethanol oxidation of about 156 kJ/mol. Upon energizing SAW, activation dropped to 12 kJ/mol ([26], Fig. 10). A similar change in activation energy was observed on a WO_3 catalyst ([27], Fig. 11).

Crystal momentum can be injected within a few atom layers of a stimulation site by many means, including:

- gas adsorption,
- desorption,
- electrolysis,
- X-ray and gamma ray impact
- particle impact (injection of protons, deuterons, alpha, beta, ...),
- glow discharge bombardment,
- sub-mm waves,
- laser beams.

Adding facets and dislocations to a crystal adds pairs of inflection points. A disintegrating crystallite will experience multiple facets. Crystals may be deliberately made to have multiple dislocations. When the band structure has many inflection points then a given degree of splatter will bring commensurately more electrons into a high effective mass zone. Targeting specific phonon frequencies, such 8–22 THz, may facilitate more efficient generation of heavy electrons [28]. Real materials have complex band diagrams, as shown in Fig. 12 for Pd and PdH.

There are many inflection points, some of which are near the Fermi level. Then electrons at energies near the Fermi level only need crystal momentum addition to reach an inflection point. Lasers and other methods can be used to access inflection points not near the Fermi level.

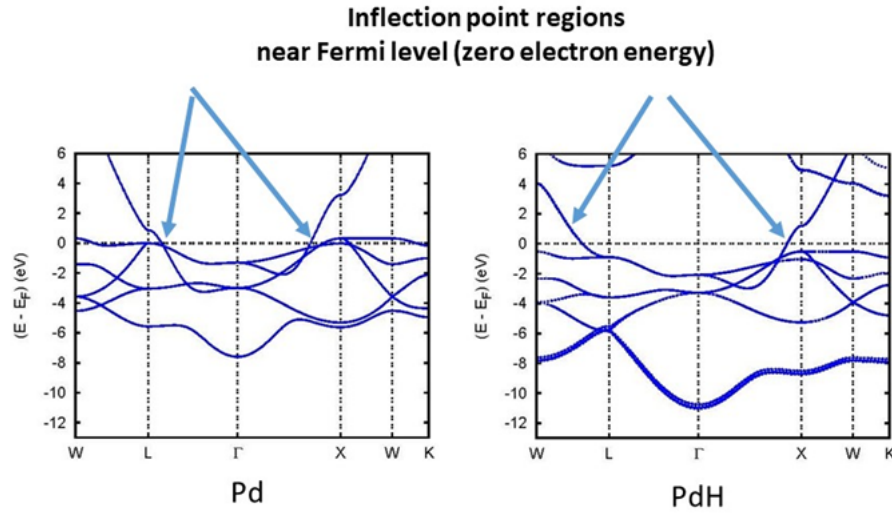
Band structures for NiH show apparent inflection points near the Fermi level between L and W , between W and X , and between K and Γ . Band structures for NiH_2 show apparent inflection points near the Fermi level between L and W and between W and K [30]. Tungsten (W) shows apparent inflection points within 2 eV of the Fermi level between N and Γ and between Γ and P [31].

The existence of inflection points near zero electron energy in palladium, nickel, and titanium is fortunate. Some estimates of effective electron masses attainable in various metals are listed in Table 1. High values appear for Ni, Pd, and Pt.

Widom and Larsen proposed using heavy electrons to change protons into ultracold neutrons, but they relied on oscillations accelerating the electrons up to high energies [33].

Table 1. Estimates of apparent effective electron masses in various metals [32]. (Other elements were not listed.)

Metal	m/m_0
Cu	1.5
Al	1.6
La	4.3
a-Fe	12
Co	14
Ni	28
Pd	27
Pt	13

**Figure 12.** The band structures of Pd and PdH, showing the energy values associated with certain inflection points are close to the thermal, Fermi level, implying that only crystal momentum need be added [29].

9. Nuclear Reactions

Normal mass electrons (m_0) impart enough KEC to limit the convergence of R and f to the large separation values ($x \sim \text{pm}$) of chemical binding, Eq. (27) and Fig. 7 (top curve). The strong nuclear force is not accessible, and nuclear bonding cannot occur. To approach nuclear dimensions (fm) and facilitate nuclear binding the repulsive KEC must be reduced.

The potential curve of Fig. 7 is similar to the HD^+ ion of the muon catalyzed fusion experiment at UC Berkeley [34]. For muons ($m_\mu = 206.77m_0$) the KEC is greatly reduced, and the reactants can come close enough for nuclear tunneling to be feasible. When H and D tunnel together, due to a muon next to one of them, H and D could merge to become ground state helium-3, and a gamma ray should be emitted with 5.3 MeV. However, H–D nuclear tunneling is apparently not what actually happened first.

We now suspect the muon first formed a sigma gerade bond between the H and D, forming a familiar HD^+ ion,

and then promptly tunneled to a nuclear size, permitting H and D to undergo *Coulomb collapse*, and ejected the *muon* with 5.3 MeV, again leaving HD as helium-3 in the ground state, 66% of the time. The other 34% were H tunneling into D producing a gamma ray of the same energy [35].

This was the first nuclear example of the tri-body catalysis reaction described here. A sufficiently heavy electron wavefunction could exist between the reactants in either the chemical bonding state at $\sigma_x \approx b$ or the nuclear binding state at $\sigma_x = a$ (Fig. 7).

10. Tunneling Probability

In Fig. 7 the sharp dip of E at $\sigma_x = a$ is due to the attractive nuclear binding energy $V_{\text{nuc}} \sim 5 - 15$ MeV. The KEC of a normal mass electron m_0 can be ~ 100 MeV at $\sigma_x = a$, so V_{nuc} is insufficient to reduce E to below zero. Because of the kinetic energy of confinement, the nuclei will not be completely shielded from each other and nuclear–nuclear repulsions will still have a contribution. Another way to view it is that the repulsion comes from the fact that the electron cannot be confined due to the Heisenberg uncertainty principle

At electron masses above threshold (Eq. (24)) electron tunneling can join R to f promptly, causing a transition to a new compound nucleus “ Rf ” and an energetic electron (Fig. 13).

At the inner chemical turning point b_i , $T_i = 0$ and the KEC is balanced by V_e , Eq. (26). At the nuclear force distance $\sigma_x = a$, the potential energies $V_e + V_{\text{nuc}}$ counteract the KEC potential barrier. After tunneling, the compound nucleus Rf has new energy T_i , and the electron has a new T_e . Conveniently, the nuclear ground state is first to appear as a stable state when the effective mass surpasses the threshold. Figure 14 recognizes that tunneling may occur from any point σ_x in the $R - f$ molecular oscillation range.

The electron is never confined at nuclear dimensions, but part of its evanescent wave function tunneling to nuclear dimensions can overcome the repulsion due to KEC that holds R and f apart, facilitating a reaction.

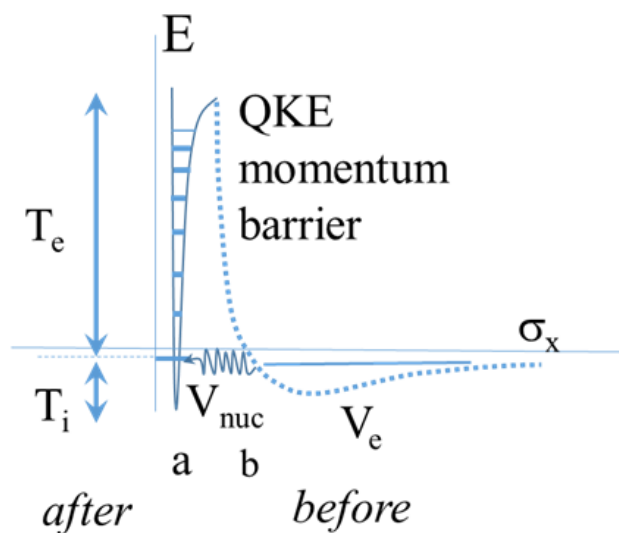


Figure 13. V_{nuc} counteracts KEC to facilitate heavy electron tunneling (wiggly line) from the chemical dimension $\sigma_x = b$ to a nuclear state at $\sigma_x = a$. *Before* tunneling V_e and KEC are dominant, and *after* tunneling the energy is shared by compound nucleus T_i and the freed electron T_e .

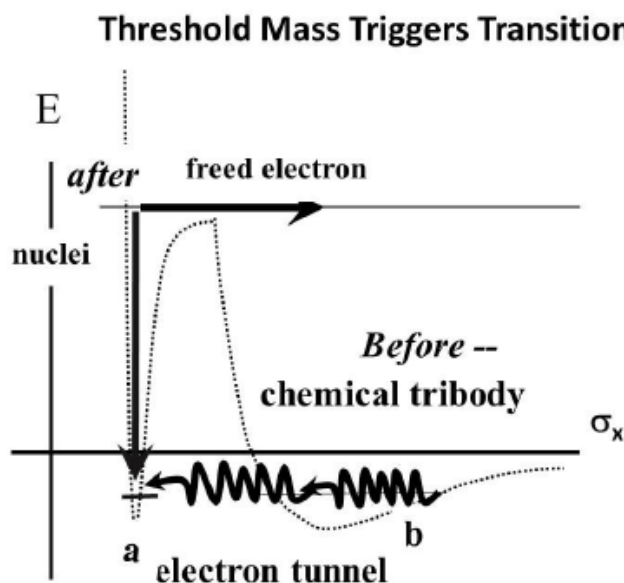


Figure 14. Detail showing tunneling integral extended to the outer turning point b and freed electron escaping over the barrier after the reaction.

This tri-body catalysis reaction differs from conventional two-particle nuclear fusion, which has strong Coulomb repulsion and *ion tunneling* [36].

The “fuel” f may be singly or multiply charged, and in many cases it appears that there may be multiple f particles. Multiple reactants (Fig. 2 with several particles f) in almost dissociated Rydberg states may undergo a transition to a converged or condensed state.

When several particles f surround a reactant R , the reaction happens as if the size of chemistry were reduced by a factor equal to the effective mass. The “change the size of chemistry” was Alvarez’s intuition that resulted in muon catalyzed fusion.

An electron quasiparticle at chemical dimensions has an evanescent wavefunction density at the nucleus that can be estimated using the Gamow integral formalism. Gamow described how to estimate the tunneling of a wavefunction between two potential wells separated by a barrier such as alpha particle emission. In our application the electron tunnels from a chemical dimension to a nuclear dimension through the KEC potential barrier, facilitating a nuclear reaction if the KEC barrier is not too high (if the effective mass exceeds threshold, Fig. 7).

By virtue of the heavy effective mass of Eqs. (24) and (31) a small fraction of the evanescent wave function may penetrate from chemical dimensions to nuclear dimension a . A reaction rate is usually estimated from the oscillation frequency times the tunneling probability. The limits of integration are usually between the nuclear force dimension a and the molecular chemical turning point b_1 . Here we assume the outer turning point $b \approx 10b_1$ (Eq. (27)), which gives a conservative low estimation of tunneling probability. (See Fig 14.)

Crossing the effective mass threshold appears to trigger the transition. The Gamow tunneling probability of the heavy electron quasiparticle is [37,38].

$$P = \exp(-2G), \quad (32)$$

where the Gamow integral is given by

$$G = (2m)^{1/2} \int_a^b [E(x) - E_0]^{1/2} dx / \hbar, \quad (33)$$

where a is the nuclear force distance and $b \approx 10b_i$. The energy $E = V_e + T_e + V_i$. The initial kinetic energy $E_0 = V_i \ll E$ so we assume it to be negligible, slightly over-estimating G . Using the assumption of Eq. (19). $\sigma_x^2 \approx x^2$ and

$$G \approx (2m)^{1/2} \int_a^b dx \{ \hbar^2 K(n) / 8mx^2 + V_e \}^{1/2} / \hbar. \quad (34)$$

In most of the interval $(a, b)T_e \gg V_e$, so the V_e term may also be neglected, yielding a conservatively higher estimate of G , and lower estimate of P . Now the integration is simple, yielding

$$G \approx (K(n)^{1/2} / 2) \ln(b/a). \quad (35)$$

States above ground state have large $K(n)$, making G larger and inhibiting tunneling, so excited states of the compound nucleus are far less likely. From Eqs. (12)–(15) we will assume $K(n) = 1$

$$P = \exp(-2G) \approx \exp[-\ln(b/a)], \quad (36)$$

$$P \approx a/b. \quad (37)$$

Heavier masses decrease $b \propto 1/m$.

Example case

Deuteron and proton. The threshold mass from Eq. (24) is $m \approx 138 m_0$, $a = 3.16$ fm, $b \approx 16$ fm, and $P \approx 0.02$. (This threshold mass would be easily exceeded by a muon with $m_\mu \approx 207 m_0$.) Such estimates depend strongly on assumptions about σ_x and b , but serve to illustrate the possible feasibility of the model.

To show the importance of phonon lifetime we also estimate the “total reaction probability $\Pr\{rxn\}$ ”, given that an enabling phonon has energized electrons to have at least the threshold effective mass. We combine the tunneling probability P during the lifetime τ_e (~ 10 fs) of the ballistic electron [39,40] with the number of times tunneling can happen during the lifetime τ_{ph} of the phonons. When an electron collides at the end of its lifetime, a new electron appears in the distribution. When the energy is provided by thermal processes, the crystal momentum of the enabling phonon may then regenerate new heavy electrons of the same effective mass. This allows us to re-use the phonon’s momentum and provide another heavy electron to tunnel.

Phonon lifetimes are typically 0.3–30 ps [41–43]. For rough estimates we will assume $\tau_{ph} \approx 3$ ps. The number of opportunities for a reaction are therefore

$$N = \tau_{ph}/\tau_e \sim 3 \text{ ps}/10 \text{ fs} \sim 300 \text{ chances.}$$

The probability that a reaction does *not* happen during one attempt is $1-P$.

The probability that no tunneling happens for N attempts is $(1-P)^N$, so the probability that a reaction *does* occur is

$$\Pr(rxn) = 1 - (1 - P)^N.$$

For example, if $P = 0.006$ and $N = 300$, then $\Pr(rxn) = 0.83$ during the phonon lifetime. This crude estimate just shows the importance of lattices with long phonon lifetimes, but does not yield a reaction rate.

11. Comparison of Expected and Observed Reactions

The book by Storms provides a good introduction to the field [43]. Apparent transmutations of nuclei, such as Ni into other elements, have been observed experimentally, with energetic reaction products. Many transmutations have been reported [44–49].

Some will be analyzed below.

12. Deuterium + ^{105}Pd Reaction

In deuterium–palladium experiments prompt bursts of electrons and charged particles were observed and helium-3 and helium-4 emission have been observed by McCubre, Biberian, and others [50,51]. The selective production of ^{107}Ag over ^{109}Ag is reported [52]. In Table 2 reactions of the ^{105}Pd isotope with one or two deuterons are shown, and they exhibit these effects. The ^{105}Pd isotope comprises more than 22% of natural palladium.

Reaction of deuterium with ^{105}Pd has several reaction branches exhibiting prompt electron emission production of ^3He and ^4He , and preferential production of ^{107}Ag over ^{109}Ag , enabled by a phonon. The effective mass threshold is about $10 m_0$, yielding a Gamow tunneling probability P of about 0.6% and a “net reaction probability” $\Pr(rxn)$ of about 0.26 per enabling phonon. Fracture energies of 13.1 and 26.4 MeV are both above the 6–10 MeV threshold for fracturing the product into stable nuclei such as helium [53].

The single deuteron fuel f and a heavy quasiparticle reacted with palladium reactant using electrolysis stimulation to form ^{107}Ag releasing a prompt, 13.1 MeV electron quasiparticle. No reports of 13.1 MeV electrons are reported. We

Table 2. Some expected and observed Pd D reactions and isotopes. (e_h means heavy electron.)

$\text{Pr}\{rxn\}$	P	m^*	Biberian's ^{107}Ag anomaly	Fracture (MeV)
0.27	6×10^{-3}	10	$^{105}\text{Pd} \text{ D } e_h^- \rightarrow ^{107}\text{Ag} \text{ 13.1 MeV}$ $^{105}\text{Pd} \text{ 2D } e_h^- \rightarrow ^{109}\text{Cd} \text{ 462 days EC, 26.4 MeV}$ $\rightarrow ^{101}\text{Ru} + 2^4\text{He} \text{ (single charged) 21.0 MeV}$ $\rightarrow ^{107}\text{Ag} + \text{D (neutral) 13.1 MeV}$ $\rightarrow ^{105}\text{Pd} + ^4\text{He (neutral) 23.6 MeV}$ $\rightarrow ^{106}\text{Pd} + ^3\text{He (neutral) 12.8 MeV}$	13.1
0.26	6×10^{-3}	10	$\rightarrow ^{109}\text{Ag}$ after 462 days by electron capture	26.40

estimate that the quasiparticle thermalized rapidly. The quasiparticle emerging from the ^{107}Ag product may encounter a heavy quasiparticle density surrounding the nucleus.

The existence of ^3He and ^4He suggests that the alternative reaction of two deuteron fuels with palladium may also happen with the same effective mass threshold. When we observe the isotopes of many different reactions in this field, the data seem to indicate that a major branch is with pairs of fuel reactants f . The pair of deuterons would deposit a fracture energy of about 26.4 MeV inside the nucleus and would fracture it.

One fracture branch would produce a ^{107}Ag , and a deuteron with energy about 13.1 MeV. We expect some ejected deuterons to be neutral because they may encounter a greatly increased heavy electron quasiparticle density surrounding the nucleus [54]. The energetic deuteron atom would be difficult to observe because the reactant gas is deuterium, and the neutral deuterium with 13.1 MeV acts like a neutron, having smaller reaction cross section than a proton.

Another branch uses two deuterons and a ^{105}Pd to produce ^{109}Cd with a fracture energy of 26.4 MeV. This branch has the same effective mass threshold ($\sim 10 m_0$) as the one-deuteron branch. The branch probably exists, because we see ^4He . *Autocatalysis* seems to be a common reaction. A compound nucleus is created with heavy electron quasiparticles. This nucleus fractures into the original nucleus and a stable nucleus made of the reactants that caused the reaction. This seems to be possible for isotopes that can undergo a reaction with one or more pairs of deuterons [55].

The two deuterons create ^{109}Cd and 26.4 MeV energy in the form of heavy quasiparticles inside the boundaries of the ^{109}Cd nucleus. This allows fracturing to break the nucleus into stable sub-nuclei, such as helium. This is deceptive because it looks like d–d fusion, where in fact it is a cadmium nucleus with too much internal energy undergoing alpha particle emission, as observed in muon–nucleus physics.

In one branch the 26.4 MeV fracture energy dislodges one helium from the ^{109}Cd and ejects it. Presumably the ejection divides 23.6 MeV between the helium and the recoil of ^{109}Pd . The helium might become neutralized upon ejection into the surrounding region, if a cloud of elevated effective mass electron quasiparticles is available to neutralize it. When autocatalysis occurs the original ^{105}Pd is left unreacted and ready to catalyze another 2D reaction.

In another branch, the ^{109}Cd with two heavy electron quasiparticles inside the nucleus with 26.4 MeV fracture into ^{101}Ru and two alpha particles, which would share 21.0 MeV. If the reaction is symmetric, no recoil would occur and there would be no recoil signature. If the helium were neutralized by the surrounding heavy electron cloud, many neutrals might escape the chamber without depositing heat. The remaining signature would be a ^{101}Ru atom, not reported. The activation energy for this branch is not known.

In yet another reaction branch, the ^{109}Cd and its two heavy electron quasiparticles with 23.6 MeV can fracture into ^{106}Pd and ^3He , in an almost-catalytic reaction. The ^3He is observed. It might also become neutral.

In all these cases the $P \sim 0.0061$ Gamow tunneling can enable $\text{Pr}\{rxn\} \sim 26\%$ net reaction rate per enabling phonon. This set of reactions is typical of what is observed in other reactions.

13. H+D+Pd Reactions Yielding ^3He and ^4He

Alexandrov reports observing both ^3He and ^4He in a plasma-stimulated reaction in palladium. Because H and D are present at the same time we examine HH, HD and DD reactions with palladium.

Table 3 shows that the H+H+Pd reactions should be possible with the 101, 106, 108 and 110 amu isotopes of Pd. The effective mass threshold is about 22–29 m_0 . The result is cadmium isotopes with between 12.3 and 16.8 MeV internal energy. In each case helium can be fractured from the cadmium, using the two protons and two neutrons from cadmium, leaving the palladium with two fewer neutrons. Whenever a reactant can form an isotope that exists and has two fewer neutrons, helium emission and transmutation to a different isotope of the same element is a candidate.

When H+D+Pd are reacted, autocatalytic ^3He can be created with almost each Pd isotope. The effective mass threshold is about 12–14 m_0 which is about half the threshold for the proton reactions. We expect the H+D+Pd autocatalytic reactions will happen before the H+H+Pd reactions. The fracture energy is between 18 and 21 MeV. Other branches can also be expected.

When two deuterons are reacted, an autocatalytic ^4He is generated by nearly every palladium isotope. The effective mass threshold is about 10 m_0 for all deuteron pair reactions with Pd and 12–14 for proton–deuteron reactions with Pd. The lower effective mass, 10 m_0 vs. 12–14 m_0 for the H+D+Pd branch, suggests that the D+D+Pd reaction will tend to dominate.

Alexandrov's observations of excess heat, ^3He and ^4He are shown to have several paths, most with effective masses between 10 and 14 m_0 . Recoil of ^3He and ^4He also cause heat.

Table 3 shows that H+H+Pd reactions are less expected than those involving deuterons because the required effective mass of 22–29 m_0 is twice that of the D+D+Pd reactions.

Table 3. Reactions from a plasma-stimulated reaction of a mixture of hydrogen and deuterium reported by Alexandrov revealed both helium-3 and helium-4, and excess heat. The H+H+Pd reactions require about 22–29 m_0 effective mass, would have about 1% tunneling and about 40+% reaction probability per enabling phonon [56].

Deuterium hydrogen palladium, forming ^3He and ^4He			
Pr{rxn}	P	m	Fracture MeV
HH catalyze helium (Alexandrov 2018)			
0.51	0.01	29	$^{104}\text{Pd HH } 2\text{eh}^- \rightarrow ^{106}\text{Cd } 12.3 \text{ MeV} \rightarrow ^{102}\text{Pd} + \text{He } 10.7 \text{ Me}$
0.47	0.01	26	$^{106}\text{Pd HH } 2\text{eh}^- \rightarrow ^{108}\text{Cd } 13.9 \text{ MeV} \rightarrow ^{104}\text{Pd} + \text{He } 11.6 \text{ Me}$
0.45	0.01	24	$^{108}\text{Pd HH } 2\text{eh}^- \rightarrow ^{110}\text{Cd } 15.4 \text{ MeV} \rightarrow ^{106}\text{Pd} + \text{He } 12.5 \text{ Me}$
0.42	0.01	22	$^{110}\text{Pd HH } 2\text{eh}^- \rightarrow ^{112}\text{Cd } 16.8 \text{ MeV} \rightarrow ^{108}\text{Pd} + \text{He } 13.3 \text{ Me}$
HD catalyze helium-3			
0.35	0.009	14	$^{104}\text{Pd HD } 2\text{eh}^- \rightarrow ^{107}\text{Cd EC } 6.5 \text{ h } 18 \text{ MeV} \rightarrow ^{104}\text{Pd} + ^3\text{He } 5.3 \text{ MeV}$
0.31	0.007	12	$^{105}\text{Pd HD } 2\text{eh}^- \rightarrow ^{108}\text{Cd } 21.3 \text{ MeV} \rightarrow ^{105}\text{Pd} + ^3\text{He } 5.3 \text{ MeV}$
0.34	0.008	14	$^{106}\text{Pd HD } 2\text{eh}^- \rightarrow ^{109}\text{Cd EC } 462 \text{ d } 19.1 \text{ MeV} \rightarrow ^{106}\text{Pd} + ^3\text{He } 5.3 \text{ MeV}$
0.32	0.008	13	$^{108}\text{Pd HD } 2\text{eh}^- \rightarrow ^{111}\text{Cd } 20.2 \text{ MeV} \rightarrow ^{108}\text{Pd} + ^3\text{He } 5.3 \text{ Me}$
0.31	0.00	12	$^{101}\text{Pd HD } 2\text{eh}^- \rightarrow ^{113}\text{Cd } 21.1 \text{ MeV} \rightarrow ^{110}\text{Pd} + ^3\text{He } 5.3 \text{ Me}$
DD catalyze helium			
0.27	0.00	10	$^{104}\text{Pd DD } 2\text{eh}^- \rightarrow ^{108}\text{Cd } 26.1 \text{ MeV} \rightarrow ^{104}\text{Pd} + ^4\text{He } 23.6 \text{ MeV} \rightarrow ^{105}\text{Pd} + ^3\text{He} + 10.1 \text{ MeV}$
0.26	0.00	10	$^{105}\text{Pd DD } 2\text{eh}^- \rightarrow ^{109}\text{Cd EC } 462 \text{ days } 26.4 \text{ MeV}$ (electron capture cadmium isotope intermediate) $\rightarrow ^{105}\text{Pd} + ^4\text{He } 23.6 \text{ MeV} \rightarrow ^{106}\text{Pd} + ^3\text{He} + 12.8 \text{ Me}$
0.26	0.00	10	$^{106}\text{Pd DD } 2\text{eh}^- \rightarrow ^{110}\text{Cd } 26.7 \text{ MeV} \rightarrow ^{106}\text{Pd} + ^4\text{He } 23.6 \text{ MeV}$
0.25	0.00	10	$^{108}\text{Pd DD } 2\text{eh}^- \rightarrow ^{112}\text{Cd } 28.3 \text{ MeV} \rightarrow ^{108}\text{Pd} + ^4\text{He } 23.6 \text{ MeV}$
0.25	0.00	10	$^{110}\text{Pd DD } 2\text{eh}^- \rightarrow ^{114}\text{Cd } 28.0 \text{ MeV} \rightarrow ^{110}\text{Pd} + ^4\text{He } 23.6 \text{ MeV}$

Table 4. Effective mass thresholds for direct HD and DD reactions, for carbon-12 production, and for ${}^7\text{Li}+\text{H}$ reactions. Reactions with high threshold m are less probable, and reactions with low atomic number are strongly suppressed by any heavy atomic mass nuclei in the same region.

$\text{Pr}\{rxn\}$	Tunnel P	m^*	Attraction reactions	Fracture (MeV)
0.29	0.007	121	H muon $\text{D} \rightarrow {}^3\text{He}$ 5.4 MeV Alvarez (1957)	5.40
0.29	0.007	121	H $\text{eh}^- \text{D} \rightarrow {}^3\text{He}$ 5.4 MeV	5.40
0.06	0.001	15	D(lattice) $\text{D} + \text{eh}^- \rightarrow \text{helium}$ 23.6 MeV $m^* 15$	23.6
0.09	0.002	22	D(lattice) $5\text{D} 5\text{eh}^- \rightarrow {}^{12}\text{C}$ 78 MeV	78.0
0.14	0.003	33	${}^7\text{Li}(\text{lattice}) \text{H} \text{eh}^- \rightarrow {}^8\text{Be}$ 17.1 MeV $\rightarrow 2 \alpha$ 0.1 MeV	17.1

Table 4 shows no direct H–D reactions are expected because the effective mass threshold is 121. No direct H–D, D–D or ${}^7\text{Li}$ –H are also expected because the quasiparticles are strongly attracted to heavy nuclei, leaving direct H and D reactions with no reacting quasiparticles, exactly as was observed by Blesser [57].

Table 4 also shows no direct D+D reactions are expected, even though the D+D reaction would have an effective mass threshold of only 15. Blesser discovered that the heavy electrons or quasiparticles are strongly attracted to the most positive nucleus, as if the core electrons were not there. When 1% neon was introduced into a liquid H+D mixture, the H+D muon catalyzed fusion was quenched. This means that the heavy quasiparticles migrate to the palladium with 46 protons, totally ignoring the 1 proton of D, so no direct D+D or H+D reactions are expected.

14. H+Ni Reactions

Bazhutov reported isotopes observed when hydrogen was apparently reacted with nickel. No details for the isotopic composition were available. The yield amounts quoted were “11% iron, 10% copper, some zinc, and cobalt.” Presuming only the ${}^{62}\text{Ni}$ and ${}^{64}\text{Ni}$ isotopes react, because they are the only ones with an exothermic non-radioactive product, we expect to see these isotopes, as shown in Table 5. We include the chrome and titanium reactions because both carbon and oxygen have been reported as transmutation products for this reaction, which is similar to other known reactions [58].

The required effective masses are $30 m_0$ and $35 m_0$ for ${}^{64}\text{Zn}$ and ${}^{66}\text{Zn}$. If ${}^{64}\text{Zn}$ or cobalt is observed then this implies the nickel host can provide an effective mass of about $35 m_0$. (To transmute ${}^{137}\text{Cs}$ $m \sim 19 - 23 m_0$ would be

Table 5. H+Ni reaction. This shows the expected isotopes from a reaction of two hydrogens with the only ${}^{62}\text{Ni}$ and ${}^{64}\text{Ni}$ expected to react, The tunneling probabilities of about 1% result in about 40% reaction probability per enabling phonon [59].

$\text{Pr}\{rxn\}$	Tunnel P	m^*	Nickel–hydrogen	Fracture (MeV)
0.45	0.012	35	${}^{62}\text{Ni} + 2\text{H} + 2\text{eh}^- \rightarrow {}^{64}\text{Zn}$ 13.8 MeV $\rightarrow {}^{60}\text{Ni} + {}^4\text{He}$ (neutral) 9.9 MeV $\rightarrow {}^{56}\text{Fe} + 2 {}^4\text{He}^+$ 3.6 MeV $\rightarrow {}^{63}\text{Cu} + \text{H}$ (neutral) 6.1 MeV $\rightarrow {}^{59}\text{Co} + \text{H} + {}^4\text{He}^+$ 0.3 MeV $\rightarrow {}^{52}\text{Cr} + {}^{12}\text{C}$ 3.2 MeV $\rightarrow {}^{48}\text{Ti} + {}^{16}\text{O}$ 1.1 MeV	13.80
0.40	0.010	30	${}^{64}\text{Ni} + 2\text{H} + 2\text{eh}^- \rightarrow {}^{66}\text{Zn} + 2\text{eh}^-$ 16.4 MeV $\rightarrow {}^{62}\text{Ni} + \text{He}$ (neutral) 11.8 MeV $\rightarrow {}^{58}\text{Fe} + 2 \text{He}^+$ 4.8 MeV $\rightarrow {}^{65}\text{Cu} + \text{H}$ (neutral) 7.5 MeV $\rightarrow {}^{54}\text{Cr} + {}^{12}\text{C}$ 4.4 MeV $\rightarrow {}^{50}\text{Ti} + {}^{16}\text{O}$ 3.6 MeV	16.40

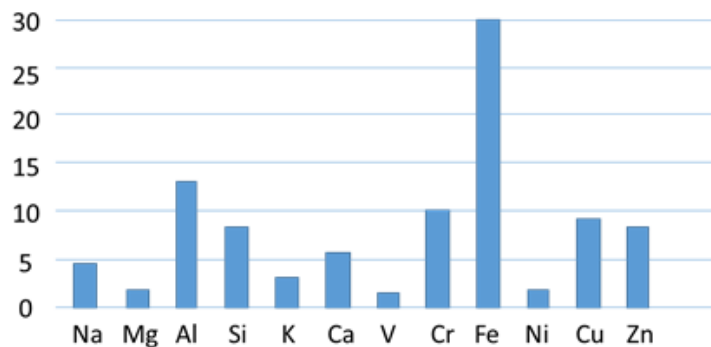


Figure 15. Chemical compositions of Urutskoev experiment products [60].

required. The Cs would attract heavy electron quasiparticles from the nickel because cesium has 55 proton attractors of heavy electrons, and nickel has only 28, so nickel lattice atoms would tend to escape transmutation until there is too little cesium.)

In all cases, if one sees **iron**, two alpha particles or helium atoms should also be emitted, or the neutron budget would not balance. If one sees zinc in smaller quantities than any of its fracture products, one must infer that the intermediate, zinc, represents an early termination of the reaction. In other isotope transmutations of this type, Iwamura observed Pr (praseodymium). This observation of helium and helium-3 in the palladium reactions suggests Pr would be a termination reaction, and that helium would be the dominant transmutation product. The nickel reaction is therefore useful to predict what should be seen in other isotope systems.

15. Hydrogen from Titanium and Heavy Water

Urutskoev reported observation of hydrogen when titanium foils were vaporized by pulsed electric discharge in either heavy or light water. Multiple repeated observations confirmed that there was more hydrogen than could be released by electrolysis, and there was negligible hydrogen in the heavy water. The analysis in Table 6 shows not only the hydrogen production but confirms the curious observation of a zinc–nickel isotope sequence, shown in Table 6 and in Fig. 15. A few other reactions are shown which could produce some of the other isotopes that Urutskoev observed.

Our reaction model predicts the hydrogen emission and all the heavier principle isotopes observed. The reaction demands the highest m noted so far, $64 m_0$, compared to nickel's 30–35, but it has about 2% tunneling and about 70%

Table 6. The reaction of titanium with oxygen (indicating that we should ignore the core electrons, as in muon–nucleus physics experiments).

Pr{ <i>rxn</i> }	Tunnel <i>P</i>	<i>m</i> *	Urutskoev's hydrogen	Fracture (MeV)
0.19	0.004	11	$^{48}\text{Ti} + 2^*\text{D} + 2 \text{e}^-$ $\rightarrow ^{52}\text{Cr } m^* 11$ Dash, Kopecek $\rightarrow ^{48}\text{Ti} + ^4\text{He (neutral)} 23.6 \text{ Me}$ $\rightarrow ^{50}\text{Ti} + 2 \text{H (neutral)} 14.6 \text{ Me}$	33.2
0.39	0.01	35	$^{48}\text{Ti} + 2\text{H} + 2 \text{e}^-$ $\rightarrow ^{50}\text{Cr } 16.3 \text{ MeV } m^* 3$ $\rightarrow ^{46}\text{Ti} + \text{He (neutral)} + 7.8 \text{ Me}$ $\rightarrow ^{49}\text{V}^- + \text{H (neutral)} + 6.8 \text{ MeV}$	16.3

total reaction probability per enabling phonon [60].

Note that the only reactants in the mix are titanium, oxygen and either hydrogen or deuterium. This led us to ask how could oxygen be a reactant when it has eight protons? It would require eight heavy electron quasiparticles between it and a titanium. There are no known examples in muon–nucleus physics because the muon generator produces so few muons there are almost never two muons in the same nucleus. Titanium may also interact with multiple deuterons, Table 7.

Using eight heavy quasiparticles would only be justified if it reproduced the otherwise puzzling and apparently impossible zinc–nickel–iron–copper sequence of isotopes, as shown in Table 7, where hydrogen is also emitted. In Table 7, the cobalt reaction appears to be just slightly endothermic, not exothermic. This could account for the missing cobalt.

The compound three-body attraction reaction shown in Table 7 accounts for the hydrogen from only heavy water and titanium and requires one of the lowest effective mass thresholds, about $12 m_0$.

The violent destruction and vaporization of the titanium foil could account for achieving $64 m_0$ in the light water reaction. And the energies can dislodge an oxygen from the heavy or light water, causing it to act like a delocalized atom, at the surface of Ti, causing crystal momentum injection upon adsorption/desorption.

Our model apparently also does NOT predict some of the other, trace isotopes principally because the energies are endothermic and the neutron budgets do not seem to balance. This branch category (endothermic and neutron budget failure) appears in nearly every isotope analysis. Therefore, this Ti+H₂O or D₂O reaction may reveal another type of reaction. Our associate W.D. Jansen suggested the proton is a quasiparticle that could also have elevated, decreased or negative mass. This might be part of the endothermic branch where lattice energy cause a “negative proton” to enter the nucleus, cause Weak Interactions with a heavy electron quasiparticle and create the neutron deficit.

Afanasyev has suggested that delocalized proton quasiparticles may form a Bose–Einstein Condensate, facilitating nuclear reactions [63].

Kovacs and Wang suggest that nuclear capture of energetic electrons can mediate nuclear chain reactions and generate more energetic electrons [64].

16. Electron Beam Impact on Cu

Adamenko et al. bombarded 0.5 mm diameter Cu targets with high energy electron beams in vacuum, compressing and destroying the targets, similar to the compression and explosion of Ti in water by Urutskoev. Adamenko’s Proton-21 Laboratory group measured a great variety of reaction product elements, and proposed that natural mechanisms

Table 7. Ti + D₂O reaction [62]. The reaction with N deuterium pairs, liberated for transmutation reaction by pulsed, high current explosion of the Ti foil in heavy water, where ⁴⁸Ti is the 78% majority isotope, should produce an isotope sequence like that seen with nickel, with a relatively low threshold effective mass of about 11–13 m_e .

Pr{rxn}	Tunnel P	m^*	Titanium deuterium forming nickel-like isotope sequence	Fracture (MeV)
0.22	0.005	13	⁴⁸ Ti D eh [−] → ⁵⁰ V Dash, Kopece	13.9
0.19	0.004	11	⁴⁸ Ti 2D 2 eh [−] → ⁵² Cr Dash, Kopece → ⁴⁸ Ti + ⁴ He 23.6 MeV	33.2
All N D ₂ pairs may catalytically produce ⁴ He neutral				
0.19	0.004	12	⁴⁸ Ti 4D 4eh [−] → ⁵⁶ Fe Dash	64.7
0.20	0.004	12	⁴⁸ Ti 6D 6eh [−] → ⁶⁰ Ni Dash	94.8
0.20	0.004	12	⁴⁸ Ti 8D 8eh [−] → ⁶⁴ Zn Das	122.40

Table 8. Reactions involving Ni, Al, Li, and H. This tables shows every nickel isotope reacting with LiAlH₄ elements, and that radioactive isotopes can be intermediate products of a catalytic process. The tell-tale aluminum reaction with hydrogen results in silicon, and with ⁷Li+H, resulting in chlorine, where both were uniquely present in the data only after reaction. Oxygen and carbon were observed in significant quantities, also shown in the table [67].

Pr{rxn}	Tunnel <i>P</i>	<i>m</i> *	Hot nickel + LiAlH ₄	Fracture (MeV)
0.28	0.007	33	Aluminum + hydrogen + eh [−] → ²⁸ Si 11.6 MeV	11.6
0.28	0.006	23	Aluminum+hydrogen+ ⁷ Li + 4 eh [−] → ³⁵ Cl 34 MeV	34.0
			→ aluminum + 2 * ⁴ He neutral 17.3 MeV	
0.42	0.01	24	⁵⁸ Ni ⁷ Li H 4eh [−] → ⁶⁶ Ge (EC 9 h) 23.6 MeV	23.6
			→ ⁵⁴ Fe + ¹² C 18.2 MeV	
			→ ⁵² Cr + ¹⁶ O 17.0 MeV	
			→ ⁵⁸ Ni + 2 * ⁴ He neutral 17.3 MeV	
0.41	0.01	23	⁶⁰ Ni ⁷ Li H 4eh [−] → ⁶⁸ Ge 24.7 MeV	24.7
			→ ⁵⁶ Fe + ¹² C 18.2 MeV	
			→ ⁵² Cr + ¹⁶ O 17.9 MeV	
			→ ⁶⁰ Ni + 2 * ⁴ He neutral 17.3 MeV	
0.40	0.01	23	⁶¹ Ni ⁷ Li H +4eh [−] → ⁶⁹ Ge EC 1.6 days 25.1 MeV	25.1
			→ ⁵⁷ Fe + ¹² C 18.2 MeV	
			→ ⁵³ Cr + ¹⁶ O 18 MeV	
			→ ⁶¹ Ni + 2 * ⁴ He neutral 17.3 MeV	
0.00	0.01	22	⁶² Ni ⁷ Li H +4eh [−] → ⁷⁰ Ge 26 MeV	26.0
			→ ⁵⁸ Fe + ¹² C 17.6 MeV	
			→ ⁵⁴ Cr + ¹⁶ O 17.1 MeV	
			→ ⁶² Ni + 2 * ⁴ He neutral 17.3 MeV	
0.37	0.00	21	⁶⁴ Ni ⁷ Li H 4eh [−] → ⁷² Ge 27.7 MeV	27.7
			→ ⁵⁴ Cr + ¹⁸ O 12.8 MeV	
			→ ⁶⁴ Ni + 2 * ⁴ He neutral 17.3 MeV	

of self-organizing systems are involved [65]. This is consistent with our proposed attraction reaction model, if target nuclei are bathed in very dense sea of heavy electron quasiparticles.

17. LiAlH₄ Nickel Reaction Examples

Levi reports excess heat and isotopes from a reaction where LiAlH₄ was intended to provide hydrogen [66]. Our attempts to reconcile the observed isotopes with just nickel and hydrogen could only account for reactions with ⁶²Ni and ⁶⁴Ni. Instead, the observations showed that all the nickel isotopes were reacting in related chains, with the nickel 62 isotope being the slowest. Depletions of Ni-58, 60, 61 and 64 isotopes were noted, with copious excess heat.

Table 8 shows a sampling of nickel reactions generating isotopes generated with LiAlH₄. Including the ⁷Li and H together as reactants yielded the reaction of all the nickel isotopes, showed a majority of the observed isotopes, showed the missing neutrons and lowered the effective mass threshold to about 12–25 *m*₀, compared to 30 *m*₀ required in nickel.

The radioactive intermediates are always of the type “Electron Capture” (EC) or “beta emission.” This termination with a radioactive element can appear in many of the reactions, causing tardive thermal power, called “heat after death.”

Table 8 shows both hydrogen and ⁷Li with hydrogen react with aluminum to reveal single fuel reaction resulting in *silicon and chlorine*. Neither was present before, and both are present after the reaction. This implies that a single proton fuel with a single reactant such as nickel, aluminum, chlorine, and a host of common elements, can happen. Thus, one could choose isotopes to favor either electron emission or charged nuclear fragment emission.

Table 9. Potential reactions of Rb driven by electrolysis [68].

Pr{rxn}	Tunnel P	m^*	Rubidium + hydrogen in nickel apparently gives radioactive ^{87}Y	Fracture (MeV)
0.38	0.009	23	$^{85}\text{Rb} + \text{H} + \text{eh}^- \rightarrow ^{86}\text{Sr}$ 9.6 MeV	9.60
0.51	0.01	34	$^{86}\text{Sr} + \text{H} + \text{eh}^- \rightarrow ^{87}\text{Y}$ EC 3.35 days 5.8 MeV	5.80
0.44	0.01	28	$^{85}\text{Rb} + 2\text{H} + 2\text{eh}^- \rightarrow ^{87}\text{Y}$ EC 3.35 days 15.4 MeV	15.4
0.43	0.01	27	$^{85}\text{Rb} + 3\text{H} + 3\text{eh}^- \rightarrow ^{88}\text{Zr}$ EC 83 days	23.3
0.35	0.009	21	$^{87}\text{Rb} + \text{H} + \text{eh}^- \rightarrow ^{88}\text{Sr}$ 17.7 MeV	10.6
0.40	0.01	25	$^{87}\text{Rb} + 2\text{H} + 2\text{eh}^- \rightarrow ^{89}\text{Y}$ 17.7 MeV	17.7
			$\rightarrow ^{85}\text{Rb} + \text{helium neutral}$ 9.7 MeV	
0.40	0.01	25	$^{87}\text{Rb} + 3\text{H} + 3\text{eh}^- \rightarrow ^{90}\text{Zr}$ (observed amu) 26.0 MeV	26.0

18. Electrolytic Production of Radioactive Isotopes

Bush included rubidium carbonate salt electrolytes in a light water electrolytic cell. Table 9 lists some predictions of the proposed theory for reactions of Rb with H. After electrolysis, rubidium was observed to be transmuted into strontium. In addition, a radioactive emission was observed with a half life of about 3.8 days. The mass and half life corresponds to an electron capture isotope ^{87}Y , with a 3.35 days half life, decaying to ^{87}Sr .

19. Deuterium Diffusion in Thin Foils

Iwamura coated thin foils of various metals (Cs, Mo, Rb, and W) onto multiple layer foils of Pd and CaO, then placed them in a vacuum chamber. When he admitted deuterium on one side of the compound foils, the deuterium diffusion through the foils apparently transmuted parts of the top layers into other elements, as shown in Table 10.

A sampling of the isotopes observed (Table 10) shows that the threshold electron quasiparticle mass to cause the reactions appear to be between 9 and 11. In each case reactions of one, two or three pairs of deuterium isotopes with the reactants would result in the isotopes claimed to be observed.

All of the reported Iwamura reactions can be predicted with a relatively low range of (~ 9 to ~ 11) m_0 . H is reactions with multiple deuterium (2, 4 or 6 deuterium) can be an example of the “shrinking of the size of chemistry” proposed and demonstrated by Alvarez.

The threshold electron quasiparticle masses for many isotopes in the periodic table appear to be less than about 40

Table 10. Sampling of Iwamura reactions [69–71]. Not shown is that all the N D₂ reactions should produce catalytic neutral helium.

Pr{rxn}	Tunnel P	m^*	Iwamura N D ₂ transmutations	Fracture (MeV)
0.28	0.00	10	$^{133}\text{Cs} + 2\text{D}_2 + 4\text{eh}^- \rightarrow ^{141}\text{Pr}$ 50.5 MeV	50.5
0.25	0.00	11	$^{84}\text{Sr} + 2\text{D}_2 + 4\text{eh}^- \rightarrow ^{92}\text{Mo}$ 53.4 MeV	53.4
0.24	0.00	11	$^{86}\text{Sr} + 2\text{D}_2 + 4\text{eh}^- \rightarrow ^{94}\text{Mo}$ 56.4 MeV	56.4
0.25	0.00	11	$^{87}\text{Sr} + 2\text{D}_2 + 4\text{eh}^- \rightarrow ^{95}\text{Mo}$ 55.4 MeV	55.4
0.25	0.00	11	$^{88}\text{Sr} + 2\text{D}_2 + 4\text{eh}^- \rightarrow ^{96}\text{Mo}$ 53.4 MeV	53.4
0.30	0.00	11	$^{136}\text{Ba} + 3\text{D}_2 + 6\text{eh}^- \rightarrow ^{148}\text{Sm}$ 69.3 MeV	69.3
			$\rightarrow ^{136}\text{Ba} + ^{12}\text{C}$ 78.8 MeV	
0.31	0.00	11	$^{137}\text{Ba} + 3\text{D}_2 + 6\text{eh}^- \rightarrow ^{149}\text{Sm}$ 68.2 MeV	68.2
0.31	0.00	11	$^{138}\text{Ba} + 3\text{D}_2 + 6\text{eh}^- \rightarrow ^{150}\text{Sm}$ 67.6 MeV	67.6
0.23	0.00	19	$^{44}\text{Ca} + \text{D}_2 + 2\text{eh}^- \rightarrow ^{48}\text{Ti}$ 33.3 MeV	33.3
0.33	0.00	10	$^{184}\text{W} + \text{D}_2 + 2\text{eh}^- \rightarrow ^{188}\text{Os}$ 21.7 MeV	21.7
0.34	0.00	10	$^{182}\text{W} + 2\text{D}_2 + 4\text{eh}^- \rightarrow ^{190}\text{Pt}$ 41.6 MeV	41.6
0.32	0.00		$^{186}\text{W} + 2\text{D}_2 + 4\text{eh}^- \rightarrow ^{194}\text{Pt}$ 44.8 MeV	44.8

m_0 . The theoretical effective masses required for the apparent transmutation reactions reported over the last 25 years using *deuterons* are $m \sim 10 m_0$ to $40 m_0$, all far less than the muon mass of 207.

20. Conclusions

Our model attempts to combine several phenomena:

- single electron bonds between positive ions,
- quantum kinetic energy of electrons squeezed between two positive particles,
- generation of heavy electron quasiparticles,
- nuclear reactions catalyzed by heavy electrons,
- quantum mechanical barrier tunneling,

to explain transmutations observed in many experiments

The potential energy diagram (energy vs. separation distance x) of an electron trapped between a proton and a heavy nucleus has a function similar to the case of an electron trapped between two atoms of a vibrating molecule, such as NO. The vibrational energy of a molecule can be transferred to a single electron, which ejects, leaving the molecule in a lower energy state [72,73].

The validity of our model depends on our ability to create heavy electrons by Eq. (32) that exceed the threshold mass of Eq. (25). If the electron is not heavy enough, the repulsive pressure due to the kinetic energy of confinement (KEC) prevents a nuclear reaction entirely. We can generate the transient heavy electron quasiparticles (lifetime ~ 10 fs) by injection of energy E and phonons with crystal momentum k (lifetime ~ 0.3 – 30 ps) into a lattice, such that some electrons are energized to become close to an inflection point of the band diagram (E vs. k).

The KEC potential barrier is proportional to $1/mx^2$, making it a higher barrier, but much narrower barrier than the usual high-energy ions Coulomb barrier, which is proportional to $1/x$. The electron is never confined at nuclear dimensions, but part of its evanescent wave function tunneling to nuclear dimensions can overcome the repulsion due to KEC that holds R and f apart, facilitating a reaction. The theoretical probability of electron tunneling through the barrier is several percent for favorable cases.

The reaction can apparently transiently place or confine a heavy electron quasiparticle inside the compound nucleus. An electron inside the nucleus allows re-use of the binding energy directly inside the compound nucleus to fracture the nucleus into stable fragments that would be ejected. We have not explored possible electron spin interactions inside the nucleus.

Our model predictions appear to be consistent with transmutation data from many experiments. For example, the secondary product nuclides observed in a Ni+H catalyzed transmutation are consistent with our model (Table 5).

Transmutation reactions might have a variety of applications, including neutralization of radioactive isotopes (such as Cs-137 and Sr-90), industrial heat, electricity generation, and possibly using the ejected isotopes in rockets having a high specific impulse.

These estimates are based on a simplified one-dimensional particle model. We will need to

- check these estimates by solving the Schrödinger equation,
- calculate the distribution of heavy electrons near inflection points,
- include relativistic effects,
- calculate the reaction rates,
- compare the theoretical reaction rates with the experimentally achieved reaction rates, estimated from the number of transmutations measured and from the heat generated,

- design experiments to test the hypothesis described here (e.g., our model predicts that heavy elements could quench some otherwise-abundant reactions).

Acknowledgments

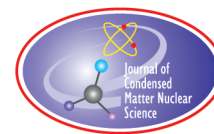
David Nagel and Jerry LaRue provided much helpful guidance.

References

- [1] H. Nienhaus, H.S. Bergh, B. Gergen, A. Majumdar, W.H. Weinberg and E.W. McFarland, Electron–hole pair creation at Ag and Cu surfaces by adsorption of atomic hydrogen and deuterium, *Phys. Rev. Lett.* **82** (2)(1999) 446.
- [2] Ibid.
- [3] Yuhui Huang, Charles T. Rettner, Daniel J. Auerbach, Alec M. Wodtke, Vibrational promotion of electron transfer, *Science* **290** (6) (2000) 211.
- [4] Xiao Z. Ji and Gabor A. Somorjai, Continuous hot electron generation in Pt/TiO₂, Pd/TiO₂ and Pt/GaN catalytic nanodiodes from oxidation of carbon monoxide, *J. Phys. Chem. B* **109** (2005) 22530–22535.
- [5] A. Zuppero and T.J. Dolan, Direct charge ejection for chemical electric generation, ArXiv 0904.4522, 29 April, 2009.
- [6] J.L. LaRue, Tim Schaefer, Daniel Matsiev, Luis Velarde, N. Hendrik Nahler, Daniel J. Auerbach and Alec M. Wodtke, Electron kinetic energies from vibrationally promoted surface exoemission: evidence for a vibrational autodetachment mechanism, *J. Phys. Chem.A* **115** (2011) 14306–14314, dx.doi.org/10.1021/jp205868g.
- [7] Xiao, op. cit.
- [8] L.W. Alvarez, H. Bradner, F.S. Crawford, Jr., J.A. Crawford, T.P. Falk-Vairant, M.L. Good, J.D. Gow, A.H. Rosenfeld, F.Solmitz, M.L. Stevenson, H.K. Tichoy and R.D. Tripp, Catalysis of nuclear reactions by mu mesons, American Physical Society Meeting, Monterey, CA, Dec. 28, 1956, *Phys. Rev.* **105** (1957)1127.
- [9] J.D. Jackson, Catalysis of nuclear reactions between hydrogen isotopes by mu-minus mesons, *Phys. Rev.* **106** (1957) 330.
- [10] Ibid.
- [11] E.J. Bleser, E.W. Anderson, L.M. Lederman, S.L. Meyer, J.L. Rosen, J.E. Rothberg and I.-T. Wang, Muonic molecules in liquid hydrogen, *Phys. Rev.* **132** (6) (1963) 2679–2691.
- [12] Makoto Inagaki, Kazuhiko Ninomiya, Go Yoshida, Wataru Higemoto, Naritoshi Kawamura, Yasuhiro Miyake, Taichi Miura and Atsushi Shinohara, Muon transfer rates from muonic hydrogen atoms to gaseous benzene and cyclohexane, *J. Nucl. Radiochem. Sci.* **18** (2018) 5–8.
- [13] Jean-Philippe Grivet, The hydrogen molecular ion revisited, *J. Chem. Educ.* **79** (1) (2002) 127.
- [14] L. Holmlid, H. Hora, G. Miley and X. Yang, Ultrahigh-density deuterium of Rydberg matter clusters for inertial confinement fusion targets, *Laser and Particle Beams* **27** (2009) 529–532.
- [15] I. Angeli and K.P. Marinova, Table of experimental nuclear ground state charge radii: An update, *Atomic Data and Nuclear Data Tables* **99** (2013) 69–95.
- [16] R.D. Evans, *The Atomic Nucleus*, McGraw-Hill, New York, 1956, p.95.
- [17] Alvarez, op.cit.
- [18] Jackson, op. cit.
- [19] Charles Kittel, *Introduction to Solid State Physics*, 8th Edn., Wiley, Hoboken, NJ, 2005, ISBN-0: 047141526X.
- [20] Saito Nobuo et al., Anomalous enhancement of catalytic activity over a Pd thin film by the effects of resonance oscillation generated on a ferroelectric, *Appl. Surface Sci.* **121/122** (1997) 343–346; Figures 2 and 4.
- [21] S. Kelling et al., Acoustic wave enhancement of the catalytic oxidation of carbon monoxide over Pt(110), *J. Chem. Phys.* **107** (14) (1997) 5609–5613, see Figure 1.
- [22] T. Mitrelias, S. Kelling, R.I. Kvon, V.P. Ostanin, D.A. King, Effect of acoustic excitation on the rate of CO oxidation over Pt{ 110}, *Surf. Sci.* **417**(1) (1998) 97–106.
- [23] N Saito, H. Nishiyama, K. Sato and Y. Inoue, Effects of resonance oscillation with a thickness-extensional mode on activation of thin film metal and metal oxide catalysts deposited on poled ferroelectric substrates, *Appl. Surface Sci.* **144– 145** (1999) 385–389.

- [24] N. Saito and Y. Inoue, Different acoustic wave effects of thickness-extension and thickness-shear mode resonance oscillation on catalytic activity and selectivity of thin Pd and Ag films deposited on ferroelectric LiNbO₃ single crystals, *J. Chem. Phys.* **113** (2) (2000) 469–472.
- [25] Mitrelias, op. cit. J.
- [26] Saito 1997, op. cit.
- [27] Saito 1999, op.cit.
- [28] P.L. Hagelstein, D. Letts and D. Cravens, Terahertz difference frequency response of PdD in two-laser experiments, *J. Condensed Matter Nucl. Sci.* **3** (2010) 59–76.
- [29] A. Houari, S.F. Matar and V. Evert, Electronic structure and crystal phase stability of palladium hydrides, *J. Appl. Phys.* **116** (17) (2014) 173706, 9 p.
- [30] N.I. Kulikov, V.N. Borzunov and A.D. Zvonkov, The electronic band structure and interatomic bond in nickel and titanium hydrides, *Phys. Stat. Sol. (b)* **86** (1978) 83.
- [31] D.P. Rai and R. K. Thapa, A theoretical study of bulk tungsten (W) based on momentum transfer (??-dependent), *Adv. Optics* (2014) 814909, 9 p., <http://dx.doi.org/10.1155/2014/814909>.
- [32] C. Kittel, *Introduction to Solid State Physics*, 2nd Edn., Wiley, 1962, p. 259.
- [33] A. Widom and L. Larsen, Ultra low momentum neutron catalyzed nuclear reactions on metallic hydride surfaces, *Eur. Phys. J. C* **46** (2006) 107.
- [34] Alvarez, op.cit.
- [35] Bleser, op.cit.
- [36] X.Z. Li, Q.M. Wei and B.A. Liu, New simple formula for fusion cross sections of light nuclei, *Nucl. Fusion* **48** (2008) 125003, 3 p.
- [37] Paola Cappellaro, Scattering, tunneling and alpha decay, MIT Lecture Notes on *Introduction to Applied Nuclear Physics*, Ch. 3, accessed at https://ocw.mit.edu/courses/nuclear-engineering/22-02-introduction-to-applied-nuclear-physics-spring-2012/lecture-notes/MIT22_02S12_lec_ch3.pdf.
- [38] Zach Meisel, Ohio U-Lecture 7, AlphaDecay_PHYS7501_F2017_ZM_alpha binding energies, http://inpp.ohiou.edu/~meisel/PHYS7501/file/Lecture7_AlphaDecay_PHYS7501_F2017_ZM.pdf.
- [39] L. Burgi, O. Jeandupeux, H. Brune and K. Kern, *Phys. Rev. Lett.* **B 82** (22) (1999) 4516–4519.
- [40] J. Cao, Y. Gao, H.E. Elsayed-Ali, R.J.D. Miller and D.A. Mantell, Femtosecond photoemission study of ultrafast electron dynamics in single-crystal Au(111) film, *Phys. Rev. B* **58** (16) (1998) 10948–10952.
- [41] Chen Jing, Jacob B. Khurgin and R. Merlin, Stimulated-emission-induced enhancement of the decay rate of longitudinal optical phonons in III-V semiconductors, *Appl. Phys. Lett.* **80** (16) (2002) 2901–2903.
- [42] N. DelFatti, P. Langot, R. Tommasi and F. Vallee, Temperature-dependent electron-lattice thermalization in GaAs, *Phys. Rev. B* **59** (7) (1999) 4576–4579.
- [43] Chin-Yi Tsai, Chih-Hsiung Chen and Tien-Li Sungand, Chin-Yao Tsai and Judy M. Rorison, Theoretical modeling of nonequilibrium optical phonons and electron energy relaxation in GaN, *J. Appl. Phys.* **85** (3) (1999).
- [44] Edmund Storms, *The Explanation of Low Energy Nuclear Reaction*, Infinite Energy Press, Concord, NH, USA, 2014.
- [45] Yasuhiro Iwamura et al., Observation of surface distribution of products by X-ray fluorescence spectrometry during D₂ gas permeation through Pd complexes, *Condensed Matter Nuclear Science*, World Scientific, New Jersey, 2006, pp.178–187.
- [46] Yasuhiro Iwamura, Transmutation reactions induced by deuterium permeation through nano-structured Pd multilayer thin film, *ANS Winter Meeting and Nuclear Technology Expo*, November 11–15, 2012, San Diego, USA.
- [47] A.B. Karabut, Research into low-energy nuclear reactions in cathode sample solid with production of excess heat, stable and radioactive impurity nuclides, *Condensed Matter Nuclear Science*, World Scientific, New Jersey, 2006, pp. 214–230.
- [48] A.B. Karabut and E.A. Karabut, Experimental results on excess power, impurity nuclides and X-ray production in experiments with a high-voltage electric discharge system, *J. Condensed Matter Nucl. Sci.* **8** (2012) 139–158.
- [49] I. Savvatimova, Transmutation of Elements in low-energy glow discharge and the associated processes, *J. Condensed Matter Nucl. Sci.* **6** (2012) 181–198.
- [50] Giuseppe Levi, Evelyn Foschi, Bo Höistad, Roland Pettersson, Lars Tegnér and Hanno Essén, Observation of abundant heat production from a reactor device and of isotopic changes in the fuel. Accessed at URL:

- <http://lenr-canr.org/acrobat/LeviGobservatio.pdf>.
www.sifferkoll.se/sifferkoll/wp-content/uploads/2014/10/LuganoReportSubmit.pdf.
- [51] Michael McKubre, Francis tanzella, paolo tripodi and peter hagelstein, the emergence of a coherent explanation for anomalies observed in D/Pd and H/Pd system: evidence for ^4He and ^3He production in *8th Int. Conf. on Cold Fusion 2000*, Lericci (La Spezia), Italy, Italian Physical Society, Bologna, Italy.
 - [52] Jean-Paul Biberian, Anomalous isotopic composition of silver in a palladium electrode, Abstract, ICCF-21, Fort Collins, Colorado, June 3–8, 2018.
 - [53] Ibid.
 - [54] Ibid.
 - [55] Holmlid, op. cit.
 - [56] Dz. Ganzorig et al., Fission of ^{232}Th and ^{238}U in the interaction with negative muons, *Nucl. Phys. A* **350** (3) (1980) 278–300.
 - [57] Dimitar Alexandrov, Nuclear fusion in solids – experiments and theory, Abstract, ICCF-21, Fort Collins, CO, June 3–8, 2018.
 - [58] Bleser, op. cit.
 - [59] R.F. Christy, The coupling of angular momenta in nuclear reactions, *Phys. Rev.* **89** (4) (1953) 839–842.
 - [60] Yu.N. Bazhutov, Erzion model interpretation of the experiments with hydrogen loading of various metals, *J. Condensed Matter Nucl. Sci.* **13** (2014) 29–37.
 - [61] L.I. Urutskoev, Review of experimental results on low-energy transformation of nucleus RECOM Inst. Kurchatov, Moscow, *Annales de la Fondation Louis de Broglie* **29** (3) (2004) 1149.
 - [62] Ibid.
 - [63] Ibid.
 - [64] S.B. Afanasyev, Cold fusion: superfluidity of deuterons, Abstract, ICCF-21, Fort Collins, CO, June 3–8, 2018.
 - [65] A. Kovacs and D. Wang, Electron mediated nuclear chain reactions , Abstract, ICCF-21, Fort Collins, CO, June 3–8, 2018.
 - [66] Stanislav V. Adamenko, Franco Selleri, Alwyn van der Merwe (Eds.), *Controlled Nucleosynthesis, Breakthroughs in Experiment and Theory*, Springer, Dordrecht, The Netherlands, 2007.
 - [67] Levi, op. cit.
 - [68] Levi, op. cit.
 - [69] R. Bush and R. Eagleton, Evidence for electrolytically induced transmutation and radioactivity correlated with excess heat in electrolytic cells, with light water rubidium salt electrolytes , EPRI. *Proc. Fourth Int. Conf. on Cold Fusion*, 1994.
 - [70] Yasuhiro Iwamura, Mitsuru Sakano and Takehiko Itoh, Elemental analysis of Pd complexes: effects of D_2 gas permeation, *Jpn. J. Appl. Phys.* **41** (2002) 4642–4650, Part 1, No. 7A, July 2002.
 - [71] Y. Iwamura, T. Itoh, S. Sakano, S. Sakai and S. Kuribayashi, Low energy nuclear transmutation in condensed matter induced by D_2 gas permeation through Pd complexes: correlation between deuterium flux and nuclear products, *Proc. Tenth Int. Conf. on Cold Fusion*, 2003, Cambridge, MA, accessed at <http://www.lenr-canr.org/acrobat/IwamuraYlowenergyn.pdf>.
 - [72] Yasuhiro Iwamura, Takehiko Itoh, Y. Terada and T. Ishikawa, Transmutation Reactions Induced by Deuterium Permeation through Nano-structured Pd multilayer thin film, *Transactions of the American Nuclear Society* **107**, San Diego, California, November 11–15, 2012.
 - [73] J.D. White, J. Chen, D. Matsiev, D.J. Auerbach, A.M. Wodtke, Vibrationally promoted electron emission from low work-function metal surfaces, *J. Chem. Phys.* **124** (6) (2006) 064702.
 - [74] J.L. LaRue, op.cit.



Research Article

Remark on Lehnert's Revised Quantum Electrodynamics (RQED) as an Alternative to Francesco Celani's et al. Maxwell–Clifford Equations: With an Outline of Chiral Cosmology Model and its Role to CMNS

Victor Christianto*

Malang Institute of Agriculture (IPM), Malang, Indonesia

Florentin Smarandache[†]

Department of Mathematics and Sciences, University of New Mexico, Gallup, USA

Yunita Umniyati[‡]

Head of Physics Lab, Department of Mechatronics, Swiss-German University, BSD City, Indonesia

Abstract

In a recent paper published in *JCMNS* in 2017, Francesco Celani, Di Tommaso and Vassalo argued that Maxwell equations rewritten in Clifford algebra are sufficient to describe the electron and also ultra-dense deuterium reaction process proposed by Homlid et al. Apparently, Celani et al. believed that their Maxwell–Clifford equations are an excellent candidate to surpass both Classical Electromagnetic and *Zitterbewegung* QM. Meanwhile, in a series of papers, Bo Lehnert proposed a novel and revised version of Quantum Electrodynamics (RQED) based on Proca equations. Therefore, in this paper, we gave an outline of Lehnert's RQED, as an alternative framework to Celani et al Zitterbewegung-Classical EM. Moreover, in a rather old paper, Mario Liu described hydrodynamic Maxwell equations. While he also discussed potential implications of these new approaches to superconductors, such a discussion of electrodynamics of superconductors is made only after Tajmar's paper. (continued in the next page)

© 2020 ISCMNS. All rights reserved. ISSN 2227-3123

Keywords: Chiral medium, Chiral gravitation theory, Electrodynamics of superconductor, Hirsch theory, Hydrodynamics Maxwell equations, LENR, London equations, Maxwell equations, Proca equations, Revised QED

*Corresponding author. http://researchgate.net/profile/Victor_Christianto, E-mail: victorchristianto@gmail.com.

[†]E-mail: florentin.smarandache@laposte.net.

[‡]E-mail: yunita.umniyati@sgu.ac.id.

(continued from the title page)

Therefore, in this paper we present for the first time a derivation of fluidic Maxwell–Proca equations. The name of *fluidic Maxwell–Proca* is proposed because the equations were based on modifying Maxwell–Proca and Hirsch’s theory of electrodynamics of superconductors. It is hoped that this paper may stimulate further investigations and experiments in superconductors. It may be expected to have some impact to cosmology modeling too, for instance we consider a hypothetical argument that the photon mass can be the origin of gravitation. Then, after combining with the so-called chiral modification of Maxwell equations (after Spröessig), we consider chiral Maxwell–Proca equations as a possible alternative of gravitation theory. Such a hypothesis has never considered in the literature to the best of our knowledge. In the last section, we discuss the plausible role of chiral Maxwell–Proca (RQED) in CMNS process. It is hoped that this paper may stimulate further investigations and experiments in particular for elucidating the physics of LENR and UDD reaction from classical electromagnetics.

1. Introduction

In a recent paper published in *JCMNS* in 2017, Francesco Celani, Di Tommaso and Vassalo argued that Maxwell equations rewritten in Clifford algebra are sufficient to describe the electron and also ultra-dense deuterium reaction process proposed by Homlid et al. Apparently, Celani et al. believed that their Maxwell–Clifford equations are quite excellent candidate to surpass both Classical Electromagnetics theory and *Zitterbewegung* QM [1].

In the meantime, it is known that conventional electromagnetic theory based on Maxwell’s equations and quantum mechanics has been successful in its applications in numerous problems in physics, and has sometimes manifested itself in a good agreement with experiments. Nevertheless, as already stated by Feynman, there are unsolved problems leading to difficulties with Maxwell’s equations that are not removed by and not directly associated with quantum mechanics [17–20]. Therefore QED, which is an extension of Maxwell’s equations, also becomes subject to the typical shortcomings of electromagnetic in its conventional form. This reasoning makes a way for Revised Quantum Electrodynamics as proposed by Bo Lehnert [17–19].

Meanwhile, according to J.E. Hirsch, from the outset of superconductivity research it was assumed that no electrostatic fields could exist inside superconductors and this assumption was incorporated into conventional London electrodynamics [23]. Hirsch suggests that there are difficulties with the two London equations. To summarize, London’s equations together with Maxwell’s equations lead to unphysical predictions [22]. Hirsch also proposes a new model for electrodynamics for superconductors [22–23].

In this regard, in a rather old paper, Mario Liu described a hydrodynamic Maxwell equations [25]. While he also discussed potential implications of these new approaches to superconductors, such a discussion of electrodynamics of superconductors is made only after Tajmar’s paper. Therefore, in this paper we present for the first time a derivation of fluidic Maxwell–Proca–Hirsch equations. The name of Maxwell–Proca–Hirsch is proposed because the equations were based on modifying Maxwell–Proca and Hirsch’s theory of electrodynamics of superconductor. Therefore, the aim of the present paper is to propose a version of fluidic Maxwell–Proca model for electrodynamics of superconductor, along with an outline of a chiral cosmology model.

This may be expected to have some impact to cosmology modeling too, which will be discussed in the last section. It is hoped that this paper may stimulate further investigations and experiments in particular for fractal superconductor.

2. Lehnert’s Revised Quantum Electrodynamics

In a series of papers Bo Lehnert proposed a novel and revised version of Quantum Electrodynamics, which he refers to as RQED. His theory is based on the hypothesis of a nonzero electric charge density in the vacuum, and it is based

on Proca-type field equations ([20], p. 23):

$$\left(\frac{1}{c^2} \frac{\partial^2}{\partial t^2} - \nabla^2\right) A_\mu = \mu_0 J_\mu, \quad \mu = 1, 2, 3, 4, \quad (1)$$

where

$$A_\mu = \left(A, \frac{i\phi}{c}\right) \quad (2)$$

with A and ϕ standing for the magnetic vector potential and the electrostatic potential in three-space. In three dimensions, we got ([20], p. 23):

$$\frac{\text{curl } B}{\mu_0} = \varepsilon_0 (\text{div } E) C + \frac{\varepsilon_0 \partial E}{\partial t}, \quad (3)$$

$$\text{curl } E = -\frac{\partial B}{\partial t}, \quad (4)$$

$$B = \text{curl } A, \quad \text{div } B = 0, \quad (5)$$

$$E = -\nabla\phi - \frac{\partial A}{\partial t}, \quad (6)$$

$$\text{div } E = \frac{\bar{\rho}}{\varepsilon_0}. \quad (7)$$

These equations differ from the conventional form with a nonzero electric field divergence equation (7) and by the additional space-charge current density in addition to displacement current at Eq. (3). The extended field equations (3)–(7) are easily found also to become invariant to a gauge transformation ([20], p. 23).

The main characteristic new features of the present theory can be summarized as follows ([20], p. 24):

- (a) The hypothesis of a nonzero electric field divergence in the vacuum introduces an additional degree of freedom, leading to new physical phenomena. The associated nonzero electric charge density thereby acts somewhat like a hidden variable.
- (b) This also abolishes the symmetry between the electric and magnetic fields, and then the field equations obtain the character of intrinsic linear symmetry breaking.
- (c) The theory is both Lorentz and gauge invariant.
- (d) The velocity of light is no longer a scalar quantity, but is represented by a velocity vector of the modulus c .
- (e) Additional results: Lehnert is also able to derive the mass of Z boson and Higgs-like boson [21]. These would pave an alternative way to new physics beyond the Standard Model.

Now it should be clear that Lehnert's RQED is a good alternative theory to QM/QED, and therefore it is also interesting to ask whether this theory can also explain some phenomena related to LENR and UDD reaction proposed by Homlid (as argued by Celani et al.) [1].

It should be noted too that Proca equations can be considered as an extension of Maxwell equations, and they have been derived in various ways. It can be shown that Proca equations can be derived from first principles, and also that Proca equations may have a link with the Klein–Gordon equation [6,7].

One persistent question concerning these Proca equations is how to measure the mass of the photon. This question has been discussed in lengthy by Tu et al. [12]. According to their report, there are various methods to estimate the

Table 1. Upper bound on the dispersion of the speed of light in different ranges of the electromagnetic spectrum, and the corresponding limits on the photon mass ([12], p. 94).

Author (year)	Type of measurement	Limits on m_γ (g)
Ross et al. (1937)	Radio waves transmission overland	5.9×10^{-42}
Mandelstam and Papalexi (1944)	Radio waves transmission over sea	5.0×10^{-43}
Al'pert et al. (1941)	Radio waves transmission over sea	2.5×10^{-43}
Florman (1955)	Radio-wave interferometer	5.7×10^{-42}
Lovell et al. (1964)	Pulsar observations on flour flare stars	1.6×10^{-42}
Frome (1958)	Radio-wave interferometer	4.3×10^{-40}
Warner et al. (1969)	Observations on Crab Nebula pulsar	5.2×10^{-41}
Brown et al. (1973)	Short pulses radiation	1.4×10^{-33}
Bay et al. (1972)	Pulsar emission	3.0×10^{-46}
Schaefer (1999)	Gamma ray bursts	4.2×10^{-44}
	Gamma ray bursts	6.1×10^{-39}

upper bound limits of photon mass. In Table 1, some of upper bound limits of photon mass based on dispersion of speed of light are summarized.

From Table 1 and also from other results as reported in [12], it seems that we can expect that someday photon mass can be observed within experimental bounds.

3. Hirsch's Proposed Revision of London's Equations

According to J.E. Hirsch, from the outset of superconductivity research it was assumed that no electrostatic fields could exist inside superconductors and this assumption was incorporated into conventional London electrodynamics [22] Hirsch suggests that there are difficulties with the two London equations. Therefore he concludes that London's equations together with Maxwell's equations lead to *unphysical* predictions [1] However he still uses four-vectors J and A according to Maxwell's equations:

$$\square^2 A = -\frac{4\pi}{c} J \quad (8)$$

and

$$J - J_0 = -\frac{c}{4\pi\lambda_L^2} (A - A_0). \quad (9)$$

Therefore Hirsch proposes a new fundamental equation for electrodynamics for superconductors as follows [22]

$$\square^2 (A - A_0) = \frac{1}{\lambda_L^2} (A - A_0), \quad (10a)$$

where London penetration depth λ_L is defined as follows [23]:

$$\frac{1}{\lambda_L^2} = \frac{4\pi n_s e^2}{m_e c^2}, \quad (10b)$$

also d'Alembertian operator is defined as [22]:

$$\square^2 = \nabla^2 - \frac{1}{c^2} \frac{\partial^2}{\partial t^2}. \quad (10c)$$

Then he proposes the following equations [22] :

$$\square^2(F - F_0) = \frac{1}{\lambda_L^2}(F - F_0) \quad (11)$$

and

$$\square^2(J - J_0) = \frac{1}{\lambda_L^2}(J - J_0), \quad (12)$$

where F is the usual electromagnetic field tensor and F is the field tensor with entries \vec{E}_0 and 0 from \vec{E} and \vec{B} , respectively, when expressed in the reference frame at rest with respect to the ions.

In the meantime, it is known that Proca equations can also be used to describe electrodynamics of superconductors, see [25–33]. The difference between Proca and Maxwell equations is that Maxwell equations and Lagrangian are based on the hypothesis that the photon has zero mass, but the Proca's Lagrangian is obtained by adding mass term to Maxwell's Lagrangian [33] Therefore, the Proca equation can be written as follows [33]:

$$\partial_\mu F^{\mu\nu} + m_\gamma^2 A_\nu = \frac{4\pi}{c} J^\nu, \quad (13a)$$

where $m_\gamma = \frac{\omega}{c}$ is the inverse of the Compton wavelength associated with photon mass [38]. (Note: 'omega' is the angular frequency $= 2\pi f$, where f is the frequency, the definition of omega involves the "reduced" Compton wavelength, corresponding with the reduced Planck constant \hbar). It is also clear that in the particular case of $m = 0$, then that equation reduces to the Maxwell equation. In terms of the vector potentials, Eq. (13a) can be written as [33]:

$$(\square + m_\gamma)A_\mu = \frac{4\pi}{c} J_\mu. \quad (13b)$$

Similarly, according to Kruglov [31] the Proca equation for a free particle processing the mass m can be written as follows:

$$\partial_\nu \varphi_{\mu\nu}(x) + m^2 \varphi_\mu(x) = 0. \quad (14)$$

Now, the similarity between Eqs. (8) and (13b) are remarkable with the exception that Eq. (8) is in quadratic form. Therefore we propose to consider a modified form of Hirsch's model as follows:

$$(\square^2 - m_\gamma^2)(F - F_0) = \frac{1}{\lambda_L^2}(F - F_0) \quad (15a)$$

and

$$(\square^2 - m_\gamma^2)(J - J_0) = \frac{1}{\lambda_L^2}(J - J_0). \quad (15b)$$

The relevance of the proposed new equations in lieu of Eqs. (11)–(14) should be verified by experiments with superconductors [37]. For convenience, the Eqs. (15a)–(15b) can be given a name: *Maxwell–Proca–Hirsch equations*.

4. Fluidic Maxwell–Proca Equations

In this regard, in a rather old paper, Mario Liu described a hydrodynamic Maxwell equations [24] While he also discussed the potential implications of these new approaches to superconductors, such a discussion of electrodynamics of superconductors is made only after Tajmar’s paper. Therefore, in this section we present for the first time a derivation of *fluidic* Maxwell–Proca–Hirsch equations.

According to Blackledge, Proca equations can be written as follows [7]:

$$\nabla \cdot \vec{E} = \frac{\rho}{\varepsilon_0} - \kappa^2 \phi, \quad (16)$$

$$\nabla \cdot \vec{B} = 0, \quad (17)$$

$$\nabla \times \vec{E} = -\frac{\partial \vec{B}}{\partial t}, \quad (18)$$

$$\nabla \times \vec{B} = \mu_0 j + \varepsilon_0 \mu_0 \frac{\partial \vec{E}}{\partial t} + \kappa^2 \vec{A}, \quad (19)$$

where (without assuming Planck constant, $\hbar = 1$):

$$\nabla \phi = -\frac{\partial \vec{A}}{\partial t} - \vec{E}, \quad (20)$$

$$\vec{B} = \nabla \times \vec{A}, \quad (21)$$

$$\kappa = \frac{mc_0}{\hbar}. \quad (22)$$

Therefore, by using the definitions in Eqs. (16)–(19), and by comparing with hydrodynamic Maxwell equations of Liu ([24], Eq. (2)), now we can arrive at fluidic Maxwell–Proca equations, as follows:

$$\nabla \cdot \vec{E} = \frac{\rho}{\varepsilon_0} - \kappa^2 \phi, \quad (23)$$

$$\nabla \cdot \vec{B} = 0, \quad (24)$$

$$\dot{B} = -\nabla \times E - \nabla \times (\hat{\beta} \nabla \times H_0), \quad (25)$$

$$\varepsilon_0 \mu_0 \dot{E} = \nabla \times B - \mu_0 j - \kappa^2 A - (\hat{\sigma} E_0 + \rho_e v + \hat{\gamma} \nabla T) - \nabla \times (\hat{a} \nabla \times E_0), \quad (26)$$

where:

$$\nabla \phi = -\frac{\partial \vec{A}}{\partial t} - \vec{E}, \quad (27)$$

$$\vec{B} = \nabla \times \vec{A}, \quad (28)$$

$$\kappa = \frac{mc_0}{\hbar}. \quad (29)$$

Since according to Blackledge, the Proca equations can be viewed as a *unified wavefield* model of electromagnetic phenomena [7], therefore we can also regard the fluidic Maxwell–Proca equations as a *unified wavefield* model for electrodynamics of superconductor.

Now, having defined fluidic Maxwell–Proca equations, we are ready to write fluidic Maxwell–Proca equations using the same definition, as follows:

$$(\square_\alpha^2 - \kappa^2)(F - F_0) = \frac{1}{\lambda_L^2}(F - F_0) \quad (30)$$

and

$$(\square_\alpha^2 - \kappa^2)(J - J_0) = \frac{1}{\lambda_L^2}(J - J_0), \quad (31)$$

where

$$\square_\alpha^2 = \nabla^{\alpha 2} - \frac{1}{c^2} \frac{\partial^{\alpha 2}}{\partial t^2}. \quad (32)$$

As far as we know, the above fluidic Maxwell–Proca equations have never been presented elsewhere before. Provided the above equations can be verified with experiments, they can be used to describe electrodynamics of superconductors.

As a last note, it seems interesting to remark here that Kruglov [31] has derived a square-root of Proca equations as a possible model for hadron mass spectrum, therefore perhaps Eqs. (30)–(32) may be *factorized* too to find out a model for hadron masses. However, we leave this problem for future investigations.

5. Towards Chiral Cosmology Model

The Maxwell–Proca electrodynamics corresponding to a finite photon mass causes a substantial change of the Maxwell stress tensor and, under certain circumstances, may cause the electromagnetic stresses to act effectively as “*negative pressure*.” In a recent paper, Ryutov, Budker, Flambaum [34] suggest that such a negative pressure imitates gravitational pull, and may produce an effect similar to gravitation. In the meantime, there are other papers by Longo, Shamir, etc. discussing observations indicating handedness of spiral galaxies, which seem to suggest chiral medium at large scale. However, so far there is no derivation of Maxwell–Proca equations in chiral medium.

In a recent paper, Ryutov, Budker, Flambaum suggest that Maxwell–Proca equations may induce a negative pressure imitates gravitational pull, and may produce effect similar to gravitation [34].

In the meantime, there are other papers by Longo, Shamir et al. discussing observations indicating handedness of spiral galaxies, which seem to suggest chiral medium at large scale. As Shamir reported:

“A morphological feature of spiral galaxies that can be easily identified by the human eye is the handedness—some spiral galaxies spin clockwise, while other spiral galaxies rotate counterclockwise. Previous studies suggest large-scale asymmetry between the number of galaxies that rotate clockwise and the number of galaxies that rotate counterclockwise, and a large-scale correlation between the galaxy handedness and other characteristics can indicate an asymmetry at a cosmological scale” [40].

However, so far there is no derivation of Maxwell–Proca equations in a chiral medium. Therefore, inspired by Ryutov et al paper, in this paper, we present for the first time a possibility to extend Maxwell–Proca-type equations to chiral medium, which may be able to explain origin of handedness of spiral galaxies as reported by Longo et al. [39,40].

The present paper is intended to be a follow-up paper of our preceding paper, reviewing Shpenkov’s interpretation of classical wave equation and its role to explain periodic table of elements and other phenomena [38].

6. Maxwell–Proca Equations in Chiral Medium

Proca equations can be considered as an extension of Maxwell equations, and they have been derived in various ways. It can be shown that Proca equations can be derived from first principles [6], and also that Proca equations may have link with Klein–Gordon equation [7].

It should be noted that the relations between flux densities and the electric and magnetic fields depend on the material. It is well known, for instance, that all organic materials contain carbon and realize in this way some kind of optical activity. Therefore, Lord Kelvin introduced the notion of the chirality measure of a medium. This coefficient expresses the optical activity of the underlying material. The correspondent constitutive laws are the following [35]:

$$D = \varepsilon E + \varepsilon \beta \sqrt{E} \quad (\text{Drude–Born–Feodorov laws}), \quad (33)$$

$$B = \mu H + \mu \beta \sqrt{H}, \quad (34)$$

where $\varepsilon = \varepsilon(t, x)$ is the electric permittivity, $j = j(t, x)$ is the magnetic permeability and the coefficient β describes the *chirality measure* of the material [35].

Now, since we want to obtain Maxwell–Proca equations in chiral medium, then Eq. (28) should be replaced with Eq. (34). But such a hypothetical assertion should be investigated in more detailed.

Since according to Blackledge, the Proca equations can be viewed as a unified wavefield model of electromagnetic phenomena [7], then we can also regard the Maxwell–Proca equations in chiral medium as a further generalization of his *unified wavefield picture*.

7. Plausible Role of Chiral Superconductor Model to LENR/CMNS

According to R.M. Kiehn, chirality already arises in electromagnetic equations, i.e. Maxwell equations [41]:

“From a topological viewpoint, Maxwell’s electrodynamics indicates that the concept of Chirality is to be associated with a third rank tensor density of Topological Spin induced by the interaction of the four vector potentials $\{A, \varphi\}$ and the field excitations (D, H) . The distinct concept of Helicity is to be associated with the third rank tensor field of Topological Torsion induced by the interaction of the 4 vector potentials and field intensities (E, B) ...

In the electromagnetic situation, the constitutive map is often considered to be (within a factor) a linear mapping between two six dimensional vector spaces. As such the constitutive map can have both a right- or a left-handed representation, implying that there are two topologically equivalent states that are not smoothly equivalent about the identity”.

Therefore, here we will review some models of chirality in superconductors and other contexts, in hope that we may elucidate the chirality origin of spiraling wave as considered by Celani et al. for explaining UDD reaction (cf. Homlid).

Here, we summarize some reports on chirality as observed in experiments:

- (a) F. Qin et al. reported “Superconductivity in a chiral nanotube” [42]. Their abstract goes as follows: “Chirality of materials are known to affect optical, magnetic and electric properties, causing a variety of nontrivial phenomena such as circular dichroism for chiral molecules, magnetic Skyrmions in chiral magnets and non-reciprocal carrier transport in chiral conductors. On the other hand, effect of chirality on superconducting transport has not been known. Here we report the nonreciprocity of superconductivity—unambiguous evidence of superconductivity reflecting chiral structure in which the forward and backward supercurrent flows are not equivalent because of inversion symmetry breaking. Such superconductivity is realized via ionic gating

in individual chiral nanotubes of tungsten disulfide. The nonreciprocal signal is significantly enhanced in the superconducting state, being associated with unprecedented quantum Little-Parks oscillations originating from the interference of supercurrent along the circumference of the nanotube. The present results indicate that the nonreciprocity is a viable approach toward the superconductors with chiral or noncentrosymmetric structures". In other words, chirality may play a significant role in electromagnetic character of superconductors.

- (b) In other paper, Kung et al. reported: "Using polarization-resolved resonant Raman spectroscopy, we explore collective spin excitations of the chiral surface states in a three dimensional topological insulator, Bi_2Se_3 . We observe a sharp peak at 150 meV in the pseudovector A2 symmetry channel of the Raman spectra. By comparing the data with calculations, we identify this peak as the transverse *collective spin mode* of surface Dirac fermions. This mode, unlike a Dirac plasmon or a surface plasmon in the charge sector of excitations, is analogous to a spin wave in a partially polarized Fermi liquid, with spin-orbit coupling playing the role of an effective magnetic field" [43]. What we would emphasize here is that the collective spin mode may alter the Dirac fermions, see also [44].
- (c) Karimi et al. studied deviation from Larmor's theorem, their abstract begins as follows: "Larmor's theorem holds for magnetic systems that are invariant under spin rotation. In the presence of spin-orbit coupling this invariance is lost and Larmor's theorem is broken: for systems of interacting electrons, this gives rise to a subtle interplay between the spin-orbit coupling acting on individual single-particle states and *Coulomb many-body effects*" [45]. What we would emphasize here is possible observation of Coulomb many-body effects, and this seems to attract considerable interests recently, see also ([45], part a).

8. Concluding Remarks

In a series of papers, Bo Lehnert proposed a novel and revised version of Quantum Electrodynamics (RQED) based on Proca equations. We submit a viewpoint that Lehnert's RQED is a good alternative theory to QM/QED, and therefore it is also interesting to ask: Can this theory also explain some phenomena related to LENR and UDD reaction of Homlid (as argued by Celani et al)? While we do not pretend to hold all the answers in this regard, we just gave an outline to Proca equations to electrodynamics of superconductors, then to chirality model.

Nonetheless, one of our aims with the present paper is to propose a combined version of London-Proca-Hirsch model for electrodynamics of superconductor. Considering that Proca equations may be used to explain electrodynamics in superconductor, the proposed fluidic London-Proca equations may be able to describe electromagnetic of superconductors. It is hoped that this paper may stimulate further investigations and experiments in particular for superconductor. It may be expected to have some impact to cosmology modeling too.

Another purpose is to submit a new model of gravitation based on a recent paper by Ryutov, Budker, Flambaum, who suggest that Maxwell-Proca equations may induce a negative pressure imitates gravitational pull, and may produce effect similar to gravitation. In the meantime, there are other papers by Longo, Shamir etc. discussing observations indicating handedness of spiral galaxies, which seem to suggest chiral medium at large scale.

However, so far there is no derivation of Maxwell-Proca equations in chiral medium. In this paper, we propose Maxwell-Proca-type equations in chiral medium, which may also explain (albeit hypothetically) origin of handedness of spiral galaxies as reported by M. Longo et al.

It may be expected that one can describe handedness of spiral galaxies by chiral Maxwell-Proca equations. This would need more investigations, both theoretically and empirically

This paper is partly intended to stimulate further investigations and experiments of LENR inspired by classical electrodynamics, as a continuation with our previous report.

9. Postscript

It shall be noted that the present paper is not intended to be a complete description of physics of LENR and UDD reaction (Homlid et al.). Nonetheless, we can remark on three things:

- (1) Although usually Proca equations are considered not gauge invariant, therefore some researchers tried to derive a gauge invariant massive version of Maxwell equations, a recent experiment suggest U(1) gauge invariance of Proca equations, see [46].
- (2) Since Proca equations can be related to electromagnetic Klein–Gordon equation, and from Klein–Gordon equation one can derive hydrino states of hydrogen atom, then one can also expect to derive ultradense hydrogen and hydrino states from Proca equation. This brings us to a consistent picture of hydrogen, see also Mills et al. [47–50].
- (3) Chirality effect of hydrino/UDD may be observed in experiments in the near future.

Acknowledgments

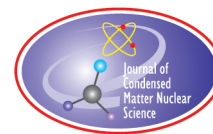
Special thanks to George Shpenkov for sending his papers and books. Discussions with Volodymyr Krasnoholovets and Robert Neil Boyd are gratefully appreciated. Nonetheless, the ideas presented here are our sole responsibility. One of these authors (VC) dedicates this paper to Jesus Christ who always guides him through all valley of darkness (Psalms 23). He is the *Good Shepherd*.

References

- [1] F. Celani, A. Di Tommaso and G. Vassalo, The electron and occam's razor, *J. Condensed Matter Nucl. Sci.* **25** (2017) 1–24, url: www.iscmns.org.
- [2] Niels Gresnigt. Relativistic physics in the Clifford algebra, Ph.D. Thesis, University of Canterbury. January 2009, 139p.
- [3] John Denker. Electromagnetism using geometric algebra versus components. url: <https://www.av8n.com/physics/maxwell-ga.htm>.
- [4] M. Tajmar, Electrodynamics in Superconductor explained by Proca equations, 2008, arXiv:cond-mat/0803.3080.
- [5] Maknickas Algirdas, Spooky action at a distance, in *the Micropolar Electromagnetic Theory*, Dec. 5, 2014, <http://vixra.org/pdf/1411.0549v4.pdf>.
- [6] Gondran Michel, Proca equations derived from first principles, 2009, arXiv:0901.3300 [quant-ph], URL: <http://arxiv.org/pdf/0901.3300.pdf>.
- [7] Blackledge Jonathan M., An approach to unification using a linear systems model for the propagation of broad-band signals, *ISAST Transaction on Electronics and Signal Processing*, Vol. 1, No. 1, 2007, URL: <http://eleceng.dit.ie/papers/100.pdf>.
- [8] Demir Suleyman, Space–time algebra for the generalization of gravitational field equations, *Pramana* (Indian Academy of Sciences) **80** (5) (2013) 811–823, URL: <http://www.ias.ac.in/pramana/v80/p811/fulltext.pdf>.
- [9] Schwinger Julian, DeRaad Jr., Lester L., Milton Kimball A. and Tsai Wu-yang, *Classical Electrodynamics*, Perseus Books. Reading, Massachusetts, 1998, 591 p.
- [10] Penrose Roger, *The Road to Reality: A Complete Guide to the Laws of the Universe*, Jonathan Cape, London, 2004, 1123 p. URL: <http://staff.washington.edu/freizt/penrose.pdf>.
- [11] Christianto Victor, London–Proca–Hirsch equations for electrodynamics of superconductors on Cantor Sets, *Prespacetime Journal*, November 2015, <http://www.prespacetime.com>.
- [12] L.-C. Tu, J. Luo and T. George Gillies, The mass of the photon, *Rep. Prog. Phys.* **68** (2005)77–130, doi:10.1088/0034-4885/68/1/R02.
- [13] Dmitriyev Valery P., *Elasticity and Electromagnetism*, 2004, URL: <http://aether.narod.ru/elastic1.pdf>.
- [14] Zareski David, Is dark matter a particular state of the ether?, *Intr. Res. J. Pure and Appl. Phys.* **3**(3) (2015) 1–7.
- [15] Zareski David, *Unification of Physics by the Ether Elasticity Theory*, LAP Lambert Academic, Saarbrücken, Germany, 2015.

- [16] Zareski David, Unification of physics theories by the ether elasticity theory, *Global J. Sci. Frontier Res., A Physics and Space Science* **14** (6) (2014).
- [17] Bo. Lehnert, A way to revised quantum electrodynamics, *Prog. Phys.* **2** (2012), <http://www.ptep-online.com>.
- [18] Bo. Lehnert, Higgs-Like particle due to revised quantum electrodynamics, *Prog. Phys.* **3** (2013), <http://www.ptep-online.com>.
- [19] Bo. Lehnert, Potentialities of revised quantum electrodynamics. *Prog. Phys.* **4** (2013), <http://www.ptep-online.com>.
- [20] Bo. Lehnert, Mass—radius relations of Z and Higgs-like bosons, *Prog. Phys.* **10** (1) (2014), <http://www.ptep-online.com>.
- [21] Lopez, Adrian E. Rubio and Fernando C. Lombardo, Quantum Electrodynamics of inhomogeneous anisotropic media, EPJ 2015, also in arxiv:1411.7758 [hep-th].
- [22] J.E. Hirsch, Electrodynamics of superconductors, 2003, arXiv:cond-mat/0312619 [cond-mat.str-el.].
- [23] J.E. Hirsch, Correcting 100 years of misunderstanding: electric fields in superconductors, hole superconductivity, and the Meissner effect, 2012, arXiv: 1202.1851 [cond-mat.supr-con].
- [24] Mario Liu, Hydrodynamics theory of electromagnetic fields in continuous media, *Phys. Rev. Lett.* **70** (23) (1993).
- [25] C.J. de Matos and M. Tajmar, Gravitomagnetic London moment and the graviton mass inside a superconductor, 2006, arXiv:gr-qc/0602591.
- [26] Victor Christianto, Florentin Smarandache and Yunita Umniyati, A derivation of Maxwell–Proca equations in chiral medium, and implications to galaxy handedness, *Prespacetime J.*, 2018, Submitted.
- [27] Victor Christianto, A Review of Schrödinger equation and classical wave equation, *Prespacetime J.*, May 2014. URL: www.prespacetime.com. Also available at: <http://vixra.org/abs/1404.0020>.
- [28] Victor Christianto, A derivation of GravitoelectroMagnetic Proca equations in fractional space, *Prespacetime J.*, May 2014, URL: www.prespacetime.com.
- [29] Victor Christianto, An outline of cosmology based on interpretation of the Johannine prologue, *Bull. Soc. Math. Services and Standards (BSMASS)*, Sept. 2014, URL: www.scipress.com.
- [30] Victor Christianto and Biruduganti Rahul, A derivation of Proca equations on cantor sets: a local fractional approach, *Bull. Math. Sci. Appl.* (BMSA), Nov. 2014, URL: www.bmsa.us.
- [31] S.I. Kruglov, “Square root” of the Proca equation: Spin-3/2 field equation, 2004, arXiv:hep-th/0405088.
- [32] M. Dressel, Electrodynamics of Metallic Superconductors, *Adv. Cond. Matt. Phys.*, 2013, Article ID 104379, <http://dx.doi.org/10.1155/2013/104379>.
- [33] Nuray Candemir, Murat Tanish, Kudret Ozdas and Suleyman Demir, Hyperbolic Octonionic Proca–Maxwell equations, *Z. Naturforsch* **63a** (2008) 15–18, URL: <http://www.znaturforsch.com/s63a/s63a0015.pdf>.
- [34] D.D. Ryutov, D. Budker and V.V. Flambaum, A hypothetical effect of the Maxwell–Proca electromagnetic stresses on galaxy rotation curves, arXiv: 1708.09514 (2017).
- [35] W. Sproessig and E. Venturino, An alternative approach for solving Maxwell equations, Part of Algorithms For Approximation IV, *Proc. Int. Symposium*, 2001.
- [36] Carlos V. Gonzalez et al., An enhanced vector diagram of Maxwell’s equations for chiral media, *Rev.Fac. Ing. Univ. Antioquia*, No. 62, Marzo, 2012, pp. 137–144.
- [37] Sergey M. Grudsky et al., On a quaternionic Maxwell equation for the time-dependent electromagnetic field in a chiral medium, arXiv: math-ph/0309062 (2003).
- [38] Leonid G. Kreidik and George P. Shpenkov, Important results of analyzing foundations of quantum mechanics, *Galilean Electrodynamics and QED-EAST* **13** (2) (2002) 23–30, URL: <http://shpenkov.janmax.com/QM-Analysis.pdf>.
- [39] J. Longo Michael, Detection of a dipole in the handedness of spiral galaxies with redshifts $z \sim 0.04$, *Phys. Lett. B* **699** (2011).
- [40] Shamir. Color Lior, Differences between clockwise and counterclockwise spiral galaxies, *Galaxies* **1** (2013) 210–215, doi:10.3390/galaxies1030210; also (a) Lior Shamir, Large-scale photometric asymmetry in galaxy spin patterns, *Publications of the Astronomical Society of Australia* (PASA), doi: 10.1017/pas.2018.xxx. arXiv: 1703.07889.
- [41] R.M. Kiehn, Chirality and helicity in terms of topological spin and topological torsion, Arxiv: physics/0101101v1 (2001).
- [42] F. Qin et al., Superconductivity in chiral nanotube, *Nature communication*, Feb 2017, DOI: 10.1038/ncomms14465.
- [43] H.-H. Kung et al., Chiral spin mode on the surface of a topological insulator, *Phys. Rev. Lett.* **119** (2017) 136802.
- [44] Irene d’Amico et al., Chirality and intrinsic dissipation of spin modes in two-dimensional electron liquids, Arxiv: 1808.15266 (2018).

- [45] Shahrzad Karimi et al., Spin precession and spin waves in a chiral electron gas: beyond Larmor's theorem, Arxiv: 1612.04314 also (a) Karimi, Shahrzad, Ullrich, Carsten A., D'Amico, Irene, orcid.org/0000-0002-4794-1348 et al. (2018), Spin-helix Larmor mode, *Scientific Reports*. 3470, ISSN 2045-232.
- [46] Liang-Cheng Tu, Test of U(1) local gauge invariance of Proca electrodynamics, *Phys. Lett. A* **352** (2006).
- [47] L. Mills Randell, The hydrogen atom revisited, *I.J. Hydrogen Energy* **25** (2000) 1171–1183.
- [48] Norman Dombey, The hydrino and other unlikely states, *Phys. Lett. A* **360** (2006) 62–65.
- [49] Jan Naudts, On the hydrino state of the relativistic hydrogen atom, Arxiv: physics/0507193.
- [50] Antonino Oscar Di Tommaso and Giorgio Vassallo, Electron Structure, Ultra-dense Hydrogen and Low Energy Nuclear Reactions, arXiv: 1809.0575 (2018).



Research Article

On Enhancement of Transmission Probability through a High Potential Barrier Due to an Anti-Zeno Effect

V.A. Namiot

Skobeltsyn Institute of Nuclear Physics, Moscow State University, Moscow 119991, Russia

L.Yu. Shchurova*

Lebedev Physical Institute of Russian Academy of Sciences, Leninsky prosp. 53, Moscow 119991, Russia

Abstract

We consider a situation in which observations themselves can significantly increase a particle transmission probability through a high barrier compared with the particle tunneling probability (a barrier anti-Zeno effect). This may explain the results of cold fusion experiments that have been reported by other authors for various systems. We examine the anti-Zeno effect as a model of a barrier of a special shape, which is similar to the form of barriers to nuclear fusion in a solid, and moreover, has an analytic solution. We have deduced formulas that demonstrate conditions that increase the barrier permeability. Numerical estimates of the particle flows through the barrier are carried out for the conditions of cold fusion experiments.

© 2020 ISCMNS. All rights reserved. ISSN 2227-3123

Keywords: Barrier anti-Zeno effect, Cold nuclear fusion, Particle transmission through a barrier

1. Introduction

How can the observation of a process affect its outcome?

The ancient Greek philosopher Zeno of Elea gave the reasoning in his aporia that “a watched arrow never flies”. According to Zeno, an arrow cannot move if we observe it in mid-air. Indeed, if we observe an arrow in mid-air, it takes place in a space equal to itself, the same for every point in time. Since this fact is absolutely true for any point in time, it means that this fact is true in general. Thus, according to Zeno, any flying arrow is at rest.

However, a rigorous analysis of this reasoning only confirms the obvious conclusion: in the framework of classical mechanics, observation can in no way influence a process.

But in quantum mechanics, in contrast to the classical frame, there may indeed be situations where an observation may affect the process that is being observed [1]. The quantum Zeno effect can manifest itself in emission of photons by a two-level system in an excited state [2–5]. Usually this influence is manifested in the fact that the more we

*Corresponding author. E-mail: ljusia@gmail.com, Tel.: +7 919 7702321.

observe, the fewer photons are emitted. Therefore, in the limit of continuous monitoring, when the measurement time is $\Delta t \rightarrow 0$, emissions can be stopped completely. However, in some cases, the opposite effect can occur, that is, the observation of a process increases the probability of the process occurring. That is the anti-Zeno effect [6–9]. Since its discovery, the quantum anti-Zeno effect has attracted widespread interest both theoretically and experimentally due to its relevance to the foundations of quantum mechanics (see, e.g., [10] and references therein). Many publications are devoted to the problem of increasing the transparency of potential barriers due to the anti-Zeno effect (see, e.g., references in [10,11]). In [12,13], the problem of the probability of particle tunneling through a barrier was considered in a time-dependent framework using the effective Schrödinger equation with a non-Hermitian Hamiltonian. In [12,13], a slight increase in barrier transparency due to the anti-Zeno effect was obtained for systems with quantum dots. The authors of [14,15] have shown that the formation of correlated coherent states of protons is accompanied by a sharp increase in short-term fluctuations of proton energy. As a result, the probabilities of tunneling a slow proton through a high potential barrier increases very significantly, and conditions for cold nuclear fusion may be possible.

Recently, in [16], one of the authors of this paper analyzed a process of particle transmission through a barrier accompanied by a transition from an excited state to the ground state (or a lower excited state) of a two-level system in the barrier. In the state of the two-level system, interacting with the particle is detected. It has been shown that in this case, observation increases the probability of a particle passing through the barrier.

In the quantum Zeno effect, the probability of a measurement-affected process varies inversely with a number of observations n_z per unit of time ($n_z = (\Delta t)^{-1}$), but in here, the probability of passage of a particle through a barrier varies directly with n_z . In some cases, the increase in the probability of passing through the barrier may be many orders of magnitude greater than the probability of the “normal” tunneling, which occurs when there is no observation of the particle. In [16], this effect has been called a barrier anti-Zeno effect.

On the qualitative level, the barrier anti-Zeno effect is as follows. Let us observe a system, and detect (indirectly) a particle inside the barrier. However, particle detection within the barrier leads to the fact that the particle proceeds from sub-barrier states to an above-barrier state. Once in the above-barrier state, the particle has a chance to fly freely over the entire barrier, or at least over a part of it (depending on the form of the barrier), going into the region beyond the barrier.

If a particle reaches the above-barrier state, the probability of penetration in the region behind the barrier is much greater than the tunneling probability, when the particle passes the entire region of the barrier in the sub-barrier state. Accordingly, in many cases, the total probability of passing through the barrier due to the barrier anti-Zeno effect (i.e. the probability of hitting in the above-barrier state, and then passing through the barrier) would be significantly greater than the tunneling probability.

In this paper, we discuss whether the barrier anti-Zeno effect can, at least in principle, increase the penetration probability across a potential barrier in fusion reactions enough to explain the results of cold fusion experiments [17–20]. According to the authors of the papers [17–20], in these experiments, they have observed energy releases which cannot be explained by chemical or any other non-nuclear processes, as well as changes in the elemental and isotopic composition of the samples.

However, in the case of real barriers (as opposed to a simple rectangular barrier model [16]), which could be relevant to cold fusion, it is very difficult to obtain both quantitative and qualitative estimations of the enhanced probability. A particular difficulty lies in the accurate calculation of the matrix elements, which are integrals of rapidly oscillating functions. In this case, small computational errors, associated with the imperfection of the numerical analysis methods or calculating integrands, can completely distort the result. Therefore, in this situation, analytical approaches are of particular importance. Within these approaches, the corresponding integrals can be calculated exactly. Or even if they are calculated approximately, they do not contain errors that completely change the result.

The aim of this paper is to examine the anti-Zeno effect in a model of a potential barrier, which has (at least qualitatively) the form of a potential barrier to nuclear fusion in a solid, and in addition, allows an analytic solution.

We will examine the probability of passing through the barrier due to the anti-Zeno effect, and compare it with the tunneling probability (which can also be calculated analytically). This comparison indicates the conditions under which the contribution of the barrier anti-Zeno effect in the current particle through the barrier exceeds the contribution of the tunneling current by many orders of magnitude.

2. Barrier Anti-Zeno Effect in a One-dimensional Model of Potential Barrier Allowing for an Analytical Solution

Let the potential barrier be described by the expression

$$V(x) = \begin{cases} \frac{1}{2}V_0 \left[1 + \operatorname{th}\left(\frac{x}{2a}\right)\right] + \frac{U_0 x_\alpha}{x_1 - x}, & -x_1 \leq x \leq x_1, \\ 0, & x < -x_1, x > x_1. \end{cases} \quad (1)$$

Here, $x_1 \gg a, x_\alpha$; and $U_0 > V_0$, but $V_0 x_1 \gg U_0 x_\alpha \gg V_0 a$.

A particle A is introduced into the region to the left of the barrier. The mass and energy of this particle are m and E_L , respectively ($V_0 \gg E_L$). The observation of this particle is carried out using a two-level system B , placed in a point x_0 inside the barrier (Fig. 1). The system B , initially located in a first level $E^{(1)}$, interacts with the particle A and goes over to the second level $E^{(2)}$ as a result of this interaction ($E^{(1)} > E^{(2)}$). The transition energy ΔE satisfies the condition

$$V_0 \gg \Delta E. \quad (2)$$

In the case of cold fusion experiments [17–20], multicharged atomic nuclei participate, and the two-level system could be the electron subsystem of the atom. The states of the electron subsystem can change when particle A penetrates the electron shell of an atom. To observe this particle A , we use a device that includes a two-level system in an excited state. The state of a two-level system is observed, that is, after a time step Δt , we check whether it has changed the state from the first to the second one. Such a check can be carried out, e.g., as follows. We split the second level of

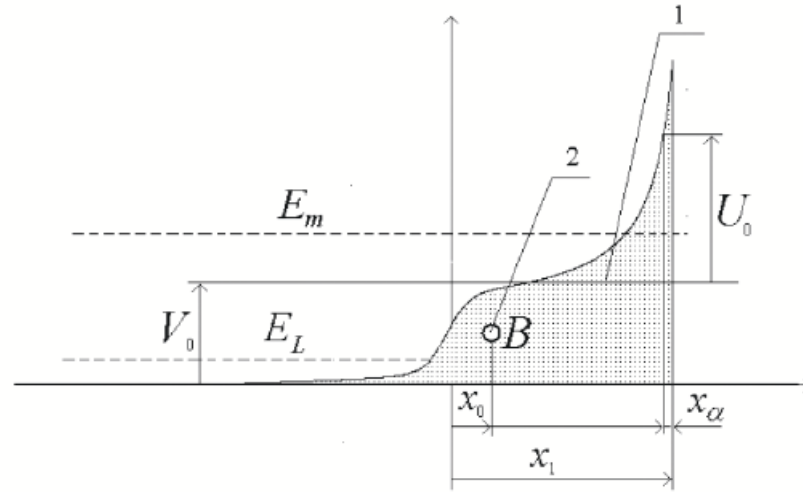


Figure 1. (1) is a potential barrier for a particle A ; (2) is a two-level system B .

the two-level system into two sublevels, the energy difference of which is equal to δE (and $\delta E \ll \Delta E$). (Although after such a splitting, the system is already three-level, but in the case of $\delta E \ll \Delta E$, approximately, it can still be considered as a two-level one.) Sequentially through the time interval Δt , we will send quanta, one by one, with the energy $\hbar\omega = \delta E$, and irradiate the two-level system with these quanta. If the two-level system is at the first level, then these quanta will fly through it, practically without dispersion. But if the system is at the second level, its parameters can be chosen so that the quantum dissipates on it with a probability close to unity. After detecting the scattered quantum (e.g., by a photomultiplier), we can thus determine that the system was at the second level when the scattering occurred. If the quantum was not registered, it means that the system was at the first level. Thus, by checking whether the quantum scattering has occurred, or not, we monitor the state of the two-level system.

If condition (2) is satisfied, the energy ΔE is definitely insufficient to excite the particle A directly to the above-barrier state. However, the presence of the system B (whose state is periodically detected) leads to an increased probability of the particle tunneling through the barrier. In order to calculate this probability we need the total wave function of the entire system ψ_p (which includes both the particle A and the two-level system B).

We use the Dicke model [21] for two-level systems to represent the total wave function in the form

$$\psi_p = \begin{pmatrix} \psi_1(x, t) \\ \psi_2(x, t) \end{pmatrix}, \quad (3)$$

where $|\psi_1(x, t)|^2 \delta x$ yields a probability of finding the particle A in an infinitesimal element δx around x at a time t and the system B in an excited state, and $|\psi_2(x, t)|^2 \delta x$ is probability of finding the particle A in an interval δx around x at a time t and the system B in its lower energy state. The equation for ψ_p has the form

$$(\hat{H}_0 + \hat{H}_{\text{int}}) \cdot \psi_p = i\hbar \frac{\partial \psi_p}{\partial t}, \quad (4)$$

where

$$\hat{H}_0 = \left(-\frac{\hbar^2}{2m} \frac{\partial^2}{\partial x^2} + V(x) \right) \hat{I} + \Delta E \cdot \hat{r}_3,$$

$$\hat{H}_{\text{int}} = 2\hat{g}(x) \cdot \hat{r}_1,$$

and the operators $\hat{r}_1, \hat{r}_2, \hat{r}_3$, and \hat{I} are expressed in terms of the Pauli matrices and the identity matrix,

$$\hat{r}_1 = \frac{1}{2} \begin{pmatrix} 0 & 1 \\ 1 & 0 \end{pmatrix}, \quad \hat{r}_2 = \frac{1}{2} \begin{pmatrix} 0 & -i \\ i & 0 \end{pmatrix}, \quad \hat{r}_3 = \frac{1}{2} \begin{pmatrix} 1 & 0 \\ 0 & -1 \end{pmatrix}, \quad \hat{I} = \begin{pmatrix} 1 & 0 \\ 0 & 1 \end{pmatrix}.$$

\hat{g} describes the short-range interaction of particle A and the two-level system B localized in the barrier near $x = x_0$. A short-range potential is required so that the characteristic region of interaction between the particle A and the two-level system would be concentrated mainly within the potential barrier (in order to register particle A that is in the barrier). We do not select a particular form of the operator $\hat{g}(x)$.

Let us assume that the next check of the system B , it has been found that it is in the first state. Then, neglecting in the zero approximation the interaction of the system B and the particle A , for $t > 0$ (the time is counted from the instant of the inspection), we can write

$$\psi_p^{(0)} = \begin{pmatrix} \phi_L(x) \exp \left[-i \left(E_L + \frac{\Delta E}{2} \right) \frac{t}{\hbar} \right] \\ 0 \end{pmatrix}. \quad (5)$$

Here, $\phi_n(x)$ is the eigen function of the particle A (in the well) which corresponds to the state with the energy E_n (measured from the well bottom) provided the particle does not interact with the system B . In expression (5), we have $n = L$.

In the first order of the perturbation theory, the correction to the zeroth-order approximation has the form

$$\delta\psi_p^{(1)}(x, t) = \left(\sum_i^0 \left\{ \exp \left[-i \left(E_i - \frac{\Delta E}{2} \right) \frac{t}{\hbar} \right] - \exp \left[-i \left(E_L + \frac{\Delta E}{2} \right) \frac{t}{\hbar} \right] \right\} \frac{g_{i,L}(x_0) \phi_i(x)}{E_i - E_L - \Delta E} \right). \quad (6)$$

Here, the matrix element $g_{i,L}(x_0)$ is represented as

$$g_{i,L}(x_0) = \int_{-x_2}^{x_2} \phi_i^*(x) \hat{g}(x - x_0) \phi_L(x) dx. \quad (7)$$

Now, we shall consider only those states whose energy exceeds V_0 . To describe such states, we introduce index m (instead of index i). Using expression (6), we can represent the probability that the particle A will be in a state with energy $E_m > V_0$ after the next test of the system B :

$$P_{m,L}(x_0) = |g_{m,L}|^2 / E_m^2. \quad (8)$$

Let us consider the domain of a few a near the point $x = 0$. In this region, energy E_m is clearly higher than the barrier height. This means that the particle A , having appeared in this region after the next testing of the B , is with a probability of $P_{m,L}$ in the above-barrier state. But in order to overcome the barrier and appear to its right, the particle still need to tunneling through the region of $x \sim x_1$. Thus, the probability, that a particle with the energy of E_m has overcome this region and is to the right of the barrier can be represented as:

$$Z_{m,L} \approx \frac{1}{2} \exp \left\{ -2 \sqrt{\frac{2mU_0x_\alpha}{\hbar^2}} \left[\int_{x_m}^{x_1} \sqrt{\left(\frac{1}{x_1 - x} - \frac{1}{x_1 - x_m} \right)} dx \right] \right\}. \quad (9)$$

Here, x_m is defined by $U_0x_\alpha / (x_1 - x_m) = E_m - V_0$. Using (8) and calculating (9), we can represent the particle flow behind the barrier, due to the anti-Zeno effect, as

$$J_p = \left\{ \sum_m \frac{|g_{m,L}(x_0)|^2}{2(E_m)^2} \exp \left[-2\pi \sqrt{\frac{2m}{\hbar^2(E_m - V_0)}} \cdot U_0x_\alpha \right] \right\} n_z P_B N_A, \quad (10)$$

where P_B is a probability to find the system B in the first (i.e., excited) state, and N_A is a number of particles in the well to the left of the barrier.

Now, let us proceed to calculate the matrix element $g_{m,L}(x_0)$. We assume that the action of the operator $\hat{g}(x)$ on the function $\phi_L(x)$ is reduced to multiplication of $\phi_L(x)$ by a function $g(x)$. We consider the case, where $x_0 \sim a$, and the characteristic scale, on which $g(x)$ is changed, is of the order of a . Then, in a region that gives the main contribution to the matrix element (7), we can represent $g(x)$ in the form:

$$g(x) = g(-x_0) + \left(\frac{dg(x)}{dx} \bigg|_{x=-x_0} \right) x. \quad (11)$$

Since the wave functions that correspond to different energy eigenvalues are orthogonal, the contribution to (7) of any terms, that are independent of x is zero, therefore you can save in (11) only one term containing x .

Using the solutions of the Schrödinger equation with the potential $V(x) = V_0(1 + th(x/(2a)))/2$ (solution to this problem is found, e.g., in [22]) we may represent a solution $\phi_L(x)$, which can be used both in the region to the left of the barrier, and in the region $x \sim 0$, as

$$\phi_L(y) = (2x_2)^{-1/2} y^\nu (1-y)^\mu [F(\mu + \nu, \mu + \nu + 1, 2\mu + 1, 1-y) + (1-y)^{-2\mu} F(-\mu + \nu, -\mu + \nu + 1, -2\mu + 1, 1-y)]. \quad (12)$$

Here, $F(a, b, c, y)$ is the hypergeometric function,

$$y = (1 + \exp(x/a))^{-1}, \quad \mu^2 = -2ma^2 E_L / \hbar^2, \quad \nu^2 = 2ma^2 (V_0 - E_L) / \hbar^2 \approx 2mV_0 a^2 / \hbar^2,$$

$$C_1 = \frac{\Gamma(\nu - \mu) \Gamma(\nu - \mu + 1)}{\Gamma(2\nu + 1) \Gamma(-2\mu)},$$

and $\Gamma(x)$ is the gamma function. Now, the expression for $\phi_m(x)$ can be written in the as

$$\phi_m(x) \approx \sqrt{\frac{2}{x_2}} \sin \left[i \sqrt{\frac{2mE_m}{\hbar^2}} (x - x_2) \right] \equiv \phi_m(y) = \sqrt{\frac{2}{x_2}} \frac{1}{2i} \left[\frac{(1-y)^{i\nu(m)}}{y^{i\nu(m)} \beta_m} - \frac{(1-y)^{-i\nu(m)}}{y^{-i\nu(m)}} \beta_m \right], \quad (13)$$

where $\nu(m) = \sqrt{2mE_m} \cdot a / \hbar$, and $\beta_m = \exp(i\nu(m)x_2/a)$.

Formally, the expression (13) is valid under the condition $E_m \gg V_0$, but in fact it can be used even for $E_m > (3 \div 4) V_0$. Using (11)–(13), we can rewrite the expression for $g_{m,L}(x_0)$ as

$$g_{m,L}(x_0) = \left(\frac{dg(x)}{dx} \Big|_{x=-x_0} \right) \lim_{\gamma \rightarrow 0} \left\{ \frac{\partial}{\partial y} \left[\int_0^1 a^2 \frac{(1-y)^\gamma}{y^\gamma} \phi_m^*(y) \phi_L(y) \frac{dy}{y(1-y)} \right] \right\}. \quad (14)$$

Expression (14) can be calculated analytically, using the formula from [23]:

$$\int_0^1 x^{\rho-1} (1-x)^{\sigma-1} F(\alpha, \beta, \gamma, x) dx = \frac{\Gamma(\rho) \Gamma(\sigma)}{\Gamma(\rho + \sigma)} \cdot {}_3F_2(\alpha, \beta, \rho, \gamma, \rho + \sigma, 1), \quad (15)$$

where ${}_3F_2(\alpha, \beta, \gamma, \delta, \varepsilon, x)$ is the generalized hypergeometric series.

However, the exact analytical expressions for $g_{m,L}(x_0)$ are exceedingly long, so it is very inconvenient to use them. It makes sense to obtain an approximate formula for $g_{m,L}(x_0)$, which has adequate accuracy and is relatively compact and convenient. First of all, we note that a considerable contribution to (14) comes from the region $y \sim 1$, and within this region, we can significantly simplify (12). Next, we take into account the inequality $\nu(m) \gg \nu \gg |\mu|$, as well as the fact that we are interested only in the modulus of $g_{m,L}(x_0)$, i.e. the phase of the matrix element is not important. Taking all of this into account, we can write:

$$|g_{m,L}(x_0)| \approx \left| \frac{Z_0}{x_2} \left[\frac{\pi \sqrt{2\pi\nu}}{\nu(m)} \left(\frac{\nu(m) \cdot e}{\nu} \right)^\nu \exp(-\pi\nu(m)) \right] \right|, \quad (16)$$

where

$$Z_0 = a^2 \left(\frac{dg(x)}{dx} \Big|_{x=-x_0} \right), \quad (17)$$

and e is Euler's number.

Substituting (17) into (10) and carrying out the summation over E_m , we obtain finally the expression for the particle flow J_p behind the barrier:

$$J_p \approx \frac{\pi^2}{\sqrt{2}} \left(\frac{Z_0 a}{U_0 x_\alpha} \right)^2 \left(\frac{\hbar^2}{2m U_0 x_\alpha a^5} \right)^{1/4} \sqrt{e} \left(\frac{U_0 x_\alpha}{V_0 a} e \right)^{2\nu-1/2} \exp \left(-4\pi \sqrt{\frac{2m U_0 x_\alpha a}{\hbar^2}} \right) n_z P_B n_A, \quad (18)$$

where n_A is the particle density in front of the barrier.

As the expression (18) shows, the dependence of J_p on the barrier parameter is determined mainly by the exponent. At the same time, the particle flow J_p depends much weaker on the parameters before the exponent. Therefore, to analyze the dependence of J_p on the barrier parameters, we can confine ourselves to the consideration of the exponential term, and treat all the prefactors as constant. In particular, this analysis shows that J_p is increased when the barrier becomes steeper with decreasing a .

For comparison, we write the expression for the “ordinary” tunneling current J_T through the same barrier:

$$\begin{aligned} J_T &= \frac{n_A}{2} \sqrt{\frac{2E_L}{m}} \exp \left\{ -2 \sqrt{\frac{2m}{\hbar^2}} \left[2 \int_0^{\sqrt{x_1}} \sqrt{(U_0 x_\alpha + V_0 z^2)} dz \right] \right\} \\ &= \frac{n_A}{2} \sqrt{\frac{2E_L}{m}} \exp \left\{ -2 \sqrt{\frac{2m}{\hbar^2}} \left[\sqrt{x_1 (U_0 x_\alpha + V_0 x_1)} + \frac{U_0 x_\alpha}{\sqrt{V_0}} \ln \left(\frac{\sqrt{V_0 x_1} + \sqrt{U_0 x_\alpha + V_0 x_1}}{\sqrt{V_0 x_1}} \right) \right] \right\} \\ &\approx \frac{n_A}{2} \sqrt{\frac{2E_L}{m}} \exp \left\{ -2 \left[\sqrt{\frac{2m V_0}{\hbar^2}} x_1 \left(1 + \left(\frac{1}{2} + \ln(2) \right) \frac{U_0 x_\alpha}{V_0 x_1} \right) \right] \right\}. \end{aligned} \quad (19)$$

Here, as well as in the situation with the particle flow J_p in formula (18), the dependence of the particle flow J_T on the barrier parameters is determined mainly by the exponential function, entering into formula (19).

Comparing the expressions for J_p and J_T , we see that formula (18), in contrast to (19), does not contain x_1 . Consequently, for sufficiently large values of x_1 , which can be estimated as

$$x_1 \gg 2\pi \sqrt{\frac{U_0 x_\alpha a}{V_0}}, \quad (20)$$

an inequality $J_p \gg J_T$ is satisfied. This means that the current through the barrier due to the anti-Zeno effect will probably be dominant in these cases.

Let us give comparative estimates of flows J_p and J_T for the conditions of the cold fusion experiment. Various authors (including the authors of Refs. [17–20]) interpret their observations as cold fusion in which multicharged atomic nuclei participate, and a new heavier multicharged atomic nucleus is formed. Here we estimate the penetration probability of a nucleus (proton) through a potential barrier of a many-electron atomic shell to form a new atomic nucleus.

Let us write the particle flow due to the anti-Zeno effect as $J_p = A_p \exp(\beta_p)$, and the ordinary tunneling current as $J_T = A_T \exp(\beta_T)$, where

$$\beta_p = -4\pi \sqrt{\frac{2m U_0 x_\alpha a}{\hbar^2}}, \quad \beta_T = -2 \left[\sqrt{\frac{2m V_0}{\hbar^2}} \cdot x_1 \cdot \left(1 + 1.2 \cdot \frac{U_0 x_\alpha}{V_0 \cdot x_1} \right) \right].$$

Here, m is the proton mass, U_0 is a height of the potential barrier (fusion barrier), V_0 is the potential of electron shells. The value x_α is the characteristic distance at which nuclear forces act, x_1 is the atomic radius.

In experiments [20], nucleosynthesis was observed at the interaction of slow protons with lithium. We carried out numerical estimates of β_p and β_T for the case of proton penetration to the lithium nucleus. We take $m = 1.67 \times 10^{-24}$ g, $U_0 = 2.1 \times 10^6$ eV, $V_0 = 1.22 \times 10^2$ eV, $x_\alpha = 1.77 \times 10^{-13}$ cm, and $x_1 = 10^{-8}$ cm for estimates and β_p and β_T .

In the expression for β_p , which determines the particle flow due to the barrier anti-Zeno effect, the specified values of U_0 , V_0 , x_α , $x_1 x_\alpha$, only a is a model parameter. The above condition $V_0 x_1 \gg U_0 x_\alpha \gg V_0 a$ (for the potential (1)) is obviously satisfied for $a \leq 10^{-11}$ cm.

Figure 2 shows the value of β_p/β_T depending on the parameter a in the range of parameter values from 10^{-12} to 10^{-11} cm. We have the ratio $\beta_p/\beta_T = 0.05$ at $a = 10^{-11}$ cm, and $\beta_p/\beta_T = 0.016$ at $a = 10^{-12}$ cm. We have obtained the values of $\beta_T = -860$ and $\beta_p = -14$ at $a = 10^{-12}$ cm.

According to our estimates, both J_p and J_T are small, but even in this case, the inequality $J_p \gg J_T$ is satisfied. Thus, the current through the barrier due to the anti-Zeno effect can significantly exceed the tunnel current, and will be dominant in the situation under consideration.

However, there are many factors that may prevent an accurate quantitative estimate of the current, which is caused by the barrier anti-Zeno effect. In particular, the current significantly depends not only on the barrier form, but also on the parameters characterizing this form. The parameter which describes the barrier shape on the left is included in an exponent in the expression for the particle flow. This parameter can change the value of the particle flow by orders of magnitude.

In general, even small variations in barrier parameter can significantly affect the current caused by the barrier anti-

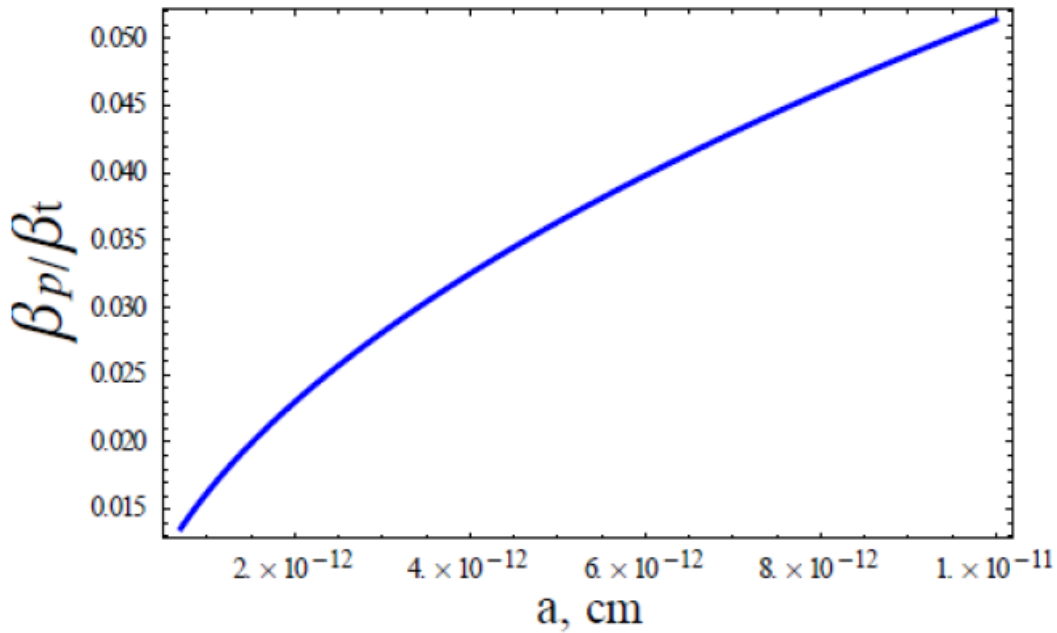


Figure 2. Dependence of β_p/β_T on parameter a . The particle flow $J_p = A_p \exp(\beta_p)$ due to the anti-Zeno effect, and the ordinary tunneling flow $J_T = A_T \exp(\beta_T)$ are determined mainly by the values of β_p and β_T , respectively. (Pre-exponential factors A_p and A_T do not differ by many orders of magnitude.)

Zeno effect. Hence, it may be expected that the current could increase dramatically under special conditions. If we assume that in a cold fusion experiment, the nuclear flow through the potential barrier is indeed due to the anti-Zeno effect, could we increase the maximum current by targeted changes in the experimental set-up? We certainly cannot make any noticeable change in the shape of the potential barrier as it is determined by inner electron shells of atoms. But we cannot exclude that the system can be affected, e.g., by various additives to the test substance. The observation of the particles interacting with the barrier is influenced by these additives. For example, in the problem discussed in this paper, to influence the system, which carries out the process of observation, means to change the function $g(x)$, e.g., to change its characteristic scale, etc.

We cannot be sure that the barrier anti-Zeno effect can explain the experimental results on cold nuclear fusion. However, we believe that it is impossible to exclude such a possibility *a priori*, and we can give a number of arguments in support of it. (a) Using the anti-Zeno effect, it is possible to qualitatively explain the need to pre-heat the test substance to temperatures that are very small compared with the usual temperatures of nuclear fusion reactions. However, these temperatures are comparable with the energy difference between the ground and excited states of a measuring two-level system (this can be the electron atom subsystem). And preheating is necessary so that the probability of the initial finding of a two-level system in an excited state is not too small. (b) The observing system is in a metastable state. (If the observing system were completely stable, it would be impossible to carry out any measurements, and the anti-Zeno effect would be impossible [24].) The metastable system is unstable to relatively large perturbations. Since the duration of the experiments is long, relatively large perturbations can destroy the metastable state. As a result, a partial or complete failure of the regime can occur. Thus, the instability of processes in cold fusion experiments can be explained by the barrier anti-Zeno effect.

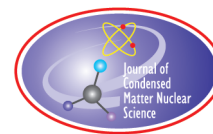
3. Conclusion

In this paper, we have calculated the particle current through the potential barrier of a special form which is similar to that of the barrier preventing fusion of nuclei in a solid. It is shown that under certain conditions, part of the current, which is caused by the barrier anti-Zeno effect, can significantly exceed (in some cases even by many orders of magnitude) the tunneling current. Accordingly, it can be assumed that in the case of cold fusion a barrier anti-Zeno effect could make a considerable contribution to the nuclear current through the barrier.

References

- [1] M.B. Mensky, Quantum Zeno effect in the decay onto an unstable level, *Phys. Lett. A* **257**(5) (1999) 227–231.
- [2] B. Misra and E.C.G. Sudarshan, The Zeno's paradox in quantum theory, *J. Math. Phys.* **18** (1977) 756–791.
- [3] W.M. Itano, D.J. Heinzen, J.J. Bollinger and D.J. Wineland, Quantum Zeno effect, *Phys. Rev. A* **41**(5) (1990) 2295–2300.
- [4] A. Degasperis, L. Fonda and G.C. Chirardi, Does the lifetime of an unstable system depend on the measuring apparatus?, *Nuovo Cimento A* **21**(3) (1974) 471–484.
- [5] D. Home and M.A.B. Whitaker, The many-worlds and relative states interpretations of quantum mechanics, and the quantum Zeno paradox, *J. Phys.: Math. Gen. A* **20**(11) (1987) 3339–3346.
- [6] B. Kaulakys and V. Gontis, Quantum anti-Zeno effect, *Phys. Rev. A* **56**(2) (1997) 1131–1137.
- [7] A. G. Kofman and G. Kurizki, Acceleration of quantum decay processes by frequent observations, *Nature* (London) **405** (2000) 546–550.
- [8] P. Facchi, H. Nakazato and S. Pascazio, From the quantum zeno to the inverse quantum Zeno effect, *Phys. Rev. Lett.* **86**(13) (2001) 2699–2703.
- [9] K. Koshino and A. Shimizu, Quantum Zeno effect by general measurements, *Phys. Rep.* **412** (4) (2005) 191–275.
- [10] M. Majeed and A. Z. Chaudhry, The quantum Zeno and anti-Zeno effects with non-selective projective measurements, *Scientific Reports* **8**(1) (2018) 14887.

- [11] A. Barone, G. Kurizki and A.G. Kofman, Dynamical control of macroscopic quantum tunneling, *Phys. Rev. Lett.* **92**(1–2) (2004) 200403.
- [12] S.A. Gurvitz, Quantum description of classical apparatus: Zeno effect and decoherence, *Quantum Information Processing* **2**(1–2) (2003) 15–35.
- [13] S. Gurvitz, Does the measurement take place when nobody observes it? *Prog. Phys.* **65**(6–8) (2017) 1600065.
- [14] V.I. Vysotskii, M.V. Vysotskyy and S.V. Adamenko, Application of correlated states of interacting particles in non-stationary and periodical modulated LENR systems, *J. Condensed Matter Nucl. Sci.* **13** (2014) 624–636.
- [15] V.I. Vysotskii, M.V. Vysotskyy and S. Bartalucci, Features of the formation of correlated coherent states and nuclear fusion induced by the interaction of slow particles with crystals and free molecules, *J. Exp. Theoret. Phys.* **127**(3) (2018) 479–490.
- [16] V.A. Namiot, On atomic nuclear fusion processes at low temperatures. Enhancement of potential barrier transmission probability due to the so-called barrier anti-Zeno effect, *Biophysics* **61** (2) (2016) 342–349.
- [17] V.I. Vysotskii and A.A. Kornilova, Low-energy nuclear reactions and transmutation of stable and radioactive isotopes in growing biological systems, *J. Condensed Matter Nucl. Sci.* **4** (2011) 146–160.
- [18] G. Levi, E. Foschi, T. Hartman, B. Hoistad, R. Pettersson, L. Tegner and H. Essen, Indication of anomalous heat energy production in a reactor device, Jun. 2013, arXiv:1305.3913 [physics.gen-ph].
- [19] A. Rossi. *Fluid Heater* (United States Patent US 9,115,913 B1) 2015.
- [20] S. Lipinski and H. Lipinski, Hydrogen–Lithium fusion device (Int. Patent WO 2014/189799 A9) 2013.
- [21] R.H. Dicke, Coherence in spontaneous radiation processes, *Phys. Rev.* **93**(1) (1954) 99–110.
- [22] S. Flugge, *Practical Quantum Mechanics*, Vol. 1, Springer, Berlin, 1994, p. 86.
- [23] S. Gradshteyn and I.M. Ryzhik, *Table of Integrals, Series, and Products*, 7th edn., Academic Press/Elsevier, Amsterdam, 2007, p. 814. ”
- [24] J. Zhang, J. Jing, L. Wang and S. Zhu, Criterion for quantum Zeno and anti-Zeno effects, *Phys. Rev. A* **98**(1) (2018) 012135.



Research Article

Atomic Nuclei Binding Energy: Case of ${}_{26}\text{Fe}$ Isotopes

Philippe Hatt*

Route Gouvernementale, 154 / B-1950 Kraainem, Belgium

Abstract

In 1936 Bethe and Bacher and in 1938 Hafstad and Teller predicted that α particle structures could be present in atomic nuclei. In the course of developing a theory of nuclear structure based on the assumption that clusters of nucleons are packed as closely together as possible, Linus Pauling found that the magic numbers have a very simple structural significance. He assumed that in nuclei the nucleons may, as a first approximation, be described as occupying localized 1s orbitals to form small clusters. These small clusters, called spherons, are usually helions (i.e. α particles), tritons and dineutrons. In nuclei containing an odd number of neutrons, a ${}^3\text{He}$ cluster or a deuteron may serve as a spheron. The close-packed-spheron model differs from the conventional liquid-drop model of the nucleus in having spherons rather than nucleons as the units. This is a simplification: ${}^{154}\text{Gd}$, for example, is described in terms of 45 spherons, rather than 154 nucleons. This enables one to determine the systematic of binding energy in a much simpler way than the approach based on individual nucleons. The author developed that idea, i.e. having clusters as basic bricks within the nucleus instead of nucleons. He considered the binding energy of α particle, deuterium, tritium, ${}^3\text{He}$, and the way these spherons are bonded instead of the bonding between individual nucleons. According to that hypothesis the nuclei of the various isotopes of each element are constituted out of α particles and other nucleons grouped in order to form sub-nuclei bound together by four types of bonds called NN, NP, NNP and NPP. So, the author favored an approach trying to breakdown the binding energy value of each element isotope in the sub-values indicated above. That binding energy distribution approach in the nuclei is essential to the comprehension of LENR process.

© 2020 ISCMNS. All rights reserved. ISSN 2227-3123

Keywords: Alpha particle, Deuterium (NP), Dineutron (NN), ${}^3\text{He}$ (NPP), Tritium (NNP)

1. Introduction

Several authors [1] predict that α particle structures could be present in atomic nuclei. Convincing arguments of such structures are provided by systematics of the binding energies of the even–even nuclei with equal number of protons and neutrons. So, a first point to consider concerns the binding energy (E_B) of an α particle and its relationship with the binding energies of deuterium, tritium, and helium-3, which are nuclear clusters smaller than helium-4. A second point is to see if and how these three binding energies play a role in the bonds between the α particles, binding a

*Independent researcher. E-mail: pcf.hatt@gmail.com.

nucleon of one α particle to a nucleon of a second α particle. These issues have already been treated in articles by the same author [2]

The author tried to organize the nucleus in a way similar to Pauling's model of the nuclear structure, with some clusters within the nucleus Pauling called spherons. The sub-nuclei taken into consideration are the α particles and four types of bonds, determined in the following way:

- Deuterium-like bond, called NP with value 2.2246 MeV, linking a neutron of one α particle with a proton of a second α particle, or a neutron or proton outside an α particle to that α particle.
- Tritium-like bond, called NNP with value 8.4818 MeV, linking three nucleons of three different α particles, or one or two nucleons outside an α particle to one or two α particles.
- ^3He -like bond, called NPP with value 7.718 MeV, having a similar function as NNP.
- A dineutron bond, called NN, with value 4.9365 MeV and linking two neutrons not being located within the same α particle. This bond and its value are deduced from the α particle binding energy.

So, the binding energy (E_B) of an isotope is composed of the E_B of the α particles (28.325 MeV each) together with the E_B 's of the various four bonds determined above.

The case of the light element's isotopes like ^{16}O , ^{20}Ne , ^{24}Mg , ^{28}Si , ^{32}S , ^{36}Ar , and ^{40}Ca was already treated [2]. There are by definition only α particles within these nuclei. The problem to solve is how they are bound together. For instance, ^8Be is not stable, as there is no room for bonds between the two α particles, the E_B of that isotope being more or less equal to the E_B of its two α particles. It is not the case of ^{16}O containing four α particles and having a global E_B superior to the E_B of these four α particles together. This difference represents the E_B between the four α particles.

Important remark: The binding energy taken into consideration in this paper is the net binding energy, i.e. the Coulomb energy once deducted from the total strong interaction. The Coulomb energy is a repulsive energy, whereas the nuclear binding energy is an attractive energy. Thus, the actual total energy required to bind nucleons into a nucleus and to overcome the repulsive Coulomb energy is the sum of these two. In other words, the binding energy is the net energy that is left over after the repulsive Coulomb energy is overcome. So, the binding energy taken into consideration in this paper is the energetical counterpart of the mass defect, the first being expressed in MeV, the second in atomic mass units.

1.1. Composition of inter alpha binding energy

The author assumes that the bonds between α particles should link two α in case of NN and NP involving only two nucleons, and three α in case of NNP and NPP bonds involving three nucleons. So, the bonds of type NNN and PPP types are eliminated as not "realistic" and NP, NNP, and NPP are accepted because they are equivalent to deuterium, tritium and ^3He bonds already existing before the α particle is constituted.

As far as NN and PP are concerned, these being part of the α particle binding energy, only NN is accepted as an inter alpha bond for the following reasons.

- With the exception of ^3He there are no stable nuclides containing more protons than neutrons. So, for the stable nuclides, there is only one possible proton outside the α particles. There could, of course, be more neutrons. This fact excludes proton–proton bonds outside an α particle.
- Coming back to ^{16}O and to the binding energy in excess to that of the α , the following is noticed: The four α 's could be linked by a minimum of three bonds, one bond between each α . Or similarly, by one NNP or NPP bond together with one NN or one NP bond. However, the only suitable values are two NP bonds,

together with the neutron–neutron (2 NN) binding energy within α particle. The binding energies of four alpha particles, plus two NP binding energies, plus the “neutronic” (2 NN) part of the α particle binding energy can be summed together, and this sum is equal to the binding energy of ^{16}O . The NN value is deduced from the neutron-neutron binding energy within α particle.

These are the assumptions concerning the four bonds NN, NP, NNP, and NPP. To simplify the author merges NP and NN in one bond called A (for average) = $(\text{NN}/2 + \text{NP}/2)$.

The key idea of the theory is to find a common distribution of binding energy within the various isotopes which could in turn help to understand the LENR process. It is about finding a kinship between these various nuclides. According to the theory there is the following sequence in binding energy:

NP	}	bonds smaller than α particle bond
NNP \Rightarrow NPP		
α particle bond		

So in the case of two or more α particles in a nucleus, it is assumed that the binding energy between these α particles is based on bonds linking their nucleons, and that the value of these bonds is related to the values of NP, NNP, NPP and NN bonds, all of which are part of the α particle binding energy.

1.2. Progression of binding energy

1.2.1. Basic values

$$\text{NP} = 2.2246 \text{ MeV},$$

$$\text{NNP} = 8.4818 \text{ MeV},$$

$$\text{NPP} = 7.7180 \text{ MeV. Difference between NNP and NPP} = 0.7638 \text{ MeV},$$

$$E_B \text{ Alpha particle} = 28.325 \text{ MeV},$$

$$\text{NN} = 4.9365 \text{ MeV}.$$

1.2.2. Determination of binding energy values based on preceding values

$$^5\text{He} = ^4\text{He} + \text{N (neutron)},$$

$$E_B = E_B\alpha - \text{NNP} + \text{NPP} = 28.325 - 0.7638 = 27.5612 \text{ MeV},$$

$$^6\text{Li} = ^4\text{He} + \text{N} + \text{P (proton)},$$

$$E_B = E_B\alpha - \text{NNP} + \text{NPP} + 2\text{NP} = 28.325 - 0.7638 + 4.4492 = 32.01 \text{ MeV},$$

$$^7\text{Li} = ^4\text{He} + 2\text{N} + \text{P},$$

$$E_B = E_B\alpha + 3\text{NP} + \text{NNP}/2 = 28.325 + 6.6738 + 4.2409 = 39.2397 \text{ MeV},$$

$$^9\text{Be} = 2 ^4\text{He} + \text{N},$$

$$E_B = 2 E_B\alpha + 1.5/2 \text{ NN} + 1.5/2 \text{ NP} - \text{NPP}/2 = 56.65 + 3.7024 + 1.6685 - 3.859 = 58.162 \text{ MeV},$$

$$^{10}\text{B} = 2 ^4\text{He} + \text{N} + \text{P},$$

$$E_B = 2 E_B \quad \alpha + \text{NNP}/2 + \text{NPP}/2 = 56.65 + 4.2409 + 3.859 = 64.7499 \text{ MeV},$$

$$^{11}\text{B} = 2 \text{ } ^4\text{He} + 2\text{N} + \text{P},$$

$$E_B = 2 E_B \alpha + 1.5 \text{ NN} + 2 \text{ NP} + \text{NPP} = 76.222 \text{ MeV}.$$

1.2.3. Other examples of nuclei binding energy

$$E_B \quad ^{12}\text{C} = 3 E_B \quad \alpha + \text{NN} + \text{NP} = 92.136 \text{ MeV},$$

$$E_B \quad ^{13}\text{C} = 3 E_B \quad \alpha + \text{NN} + \text{NP} + \text{NP}/2 + \text{NPP}/2 = 97.107 \text{ MeV},$$

$$E_B \quad ^{14}\text{C} = 3 E_B \quad \alpha + 1.5 \text{ NP} + 2\text{NNP} = 105.274 \text{ MeV},$$

$$E_B \quad ^{15}\text{C} = 3 E_B \quad \alpha + \text{NP} + 2.5 \text{ NPP} = 106.495 \text{ MeV},$$

$$E_B \quad ^{16}\text{C} = 3 E_B \quad \alpha + \text{NP} + 2.5 \text{ NPP} + \text{NNP}/2 = 110.735 \text{ MeV},$$

$$E_B \quad ^{14}\text{N} = 3 E_B \quad \alpha + \text{NNP}/2 + 2 \text{ NPP} = 104.652 \text{ MeV},$$

$$E_B \quad ^{15}\text{N} = 3 E_B \quad \alpha + 2\text{NN} + 2\text{NP} + \text{NNP} + \text{NPP} = 115.497 \text{ MeV},$$

$$E_B \quad ^{16}\text{N} = 3 E_B \quad \alpha + 1.5\text{NN} + 2.5\text{NP} + \text{NNP} + 1.5\text{NPP} = 118.000 \text{ MeV},$$

$$E_B \quad ^{16}\text{O} = 4 E_B \quad \alpha + 2\text{NN} + 2\text{NP} = 127.622 \text{ MeV},$$

$$E_B \quad ^{17}\text{O} = 4 E_B \quad \alpha + 1.5\text{NN} + 1.5\text{NP} + \text{NPP} = 131.760 \text{ MeV},$$

$$E_B \quad ^{18}\text{O} = 4 E_B \quad \alpha + 2\text{NN} + 4\text{NP} + \text{NPP} = 139.789 \text{ MeV}.$$

Remark: for all these results the differences between experimental and calculated values are less than 0.026 MeV (source: “The AME 2016 atomic mass evaluation”) [3].

1.2.4. Determining the binding energy of any isotope

These results are obtained by comparing binding energy values of isotopes of the same element and by breaking down these values in NP, NNP, NPP, and α particle binding energy values. The α particle binding energy value is also broken down in 2 NN and PP values. Only NN is active outside the α particle, PP being active within α particle. One single process is used by the author, i.e. looking step by step, isotope of one element after isotope of the same element, for binding energy differences. One should also consider that the mass differences in binding energy values could be positive or negative, the negative values showing a mass reconstitution. Having this in mind one can determine the binding energy value of every nuclide. See the figures displayed in www.philippehatt.com [4]. The geometrical schemas displayed on the author’s website are not designed to build a structure of nuclei, but rather are designed to be a visual support for research, especially to see the kinship between the binding energy distribution among the various nuclides. For instance, in case of ^{16}O the figure is based on four α particles bound by four equal bonds called “A”, actually the average of NN and NP ($\text{NN}/2 + \text{NP}/2$). If a neutron is added it becomes ^{17}O . The author looks for a bond connecting the new neutron to two nucleons located within two of the α particles in the ^{16}O structure. This is the state closest to ^{16}O . The choice is between NNP and NPP. It is NPP which fits, so that bond is taken arbitrarily. Actually, the author uses the three bonds corresponding to the three nuclides pre-existing to the α particle, i.e. NP, NNP, NPP, and a fourth one deduced from α particle bond, i.e. NN.

So, this method is not based on a theory. Instead, it is based on mind experiments, and choosing between a few bonds each time a new neutron or proton enters a nucleus. You choose that one which fits. This unconventional way

is comparable to the work of a chemist looking for several solutions in his experiments and validating that one which fits best. .

Moreover, the author is looking at the compliance of the solution for one nucleus with the solution for another nucleus in order to avoid discrepancies, especially between isotopes of the same element. In doing so, the important thing is symmetry within isotopes of one element and hence between all element's isotopes. Indeed, this work does not address the three-dimensional model of nuclei in the sense that the author is not looking for a structure of these nuclei but rather for the distribution of binding energy among them. Nevertheless, this work could be complementary to those dealing with that topic. The author's work is trying to explain the LENR processes where energy release is a direct consequence of nuclear transmutations, i.e. modification of binding energy values between isotopes present at the beginning and at the end of the LENR reaction.

1.2.5. Calculation of binding energy

As seen, the system for determining the binding energy of the nuclides is based only on calculations and similarities between isotopes of one element or between isotopes of elements close from each other.

Two examples of calculations: E_B of ^8Be and the reason for its instability. E_B of ^9Be and the reason for its stability:

^8Be	$2 \times 28.325 =$	56.6500	$2 \times 28.325 =$	56.6500
	NN/2 =	2.4683	–NNP/2 =	<u>–3.8590</u>
	NP/2 =	<u>1.1123</u>		
		60.2306 MeV		52.7910 MeV

Average: $60.2306/2 + 52.7910/2 = 56.511 \text{ MeV}$ (+0.011 MeV compared with AME 2016 value).

Explanation: the balance between (NN/2 + NP/2) and NNP/2 is negative ($2.4683 + 1.1123 - 3.8590 = -0.2784 \text{ MeV}$). Therefore, there is no bonding possibility between the two α particles and the nucleus is unstable as the reconstitution of mass is more important than the mass defect.

^9Be	$2 \times 28.325 =$	56.6500	$2 \times 28.325 =$	56.6500
	3 NN/2 =	7.4048	–NPP =	<u>–7.7180</u>
	3 NP/2 =	<u>3.3369</u>		
		67.3917 MeV		48.9320 MeV

Average: $67.3917/2 + 48.9320/2 = 58.1640$ (+0.002 MeV compared with AME 2016 value).

Explanation: the introduction of one neutron has occurred in two more A i.e. (NN/2 + NP/2) bonds and also a negative NPP bond double as for ^8Be . Nevertheless, the balance is positive ($7.4048 + 3.3369 - 7.7180 = 3.0237 \text{ MeV}$). The nucleus is stable.

1.2.6. Value of a “line”

The author looks for a relationship between the four values: NN, NP, NNP, and NPP in order to determine a common basic value unit of binding energy. As a result, the binding energy of each nuclide is based on the number of α particles binding energy, multiple of 28.325 MeV, and on a number of “lines” to be broken down in NN, NP, NNP, and NPP.

The following is noticed:

$$\begin{array}{rcl}
 E_B \quad \alpha = & 2 \text{ NN} & 9.873 \\
 & \text{NP} & 2.224 \\
 & \text{NNP} & 7.720 \\
 & \text{NPP} & \underline{8.482} \\
 & & 28.299 \text{ MeV}
 \end{array}$$

$$\begin{array}{rcl}
 E_B \text{ (NN + NP)} = & 4.9365 \\
 & \underline{2.2246} \\
 & 7.1611 \text{ MeV}
 \end{array}$$

$$E_B \text{ NPP} = 7.718 \text{ MeV},$$

$$\text{Difference } E_B \text{ NPP} - E_B \text{ (NN + NP)} = 0.557 \text{ MeV},$$

$$E_B \text{ NP} = 2.2246 \text{ MeV} = 4 \times 0.556 \text{ MeV},$$

$$\text{So, } E_B \text{ NPP} = E_B \text{ (NN + NP)} + 0.25 E_B \text{ NP},$$

$$\text{As well, } E_B \text{ NN} / E_B \text{ NP} = 4.9365 / 2.2246 = 2.219. \quad 2.219 \times 4 = 8.875 \text{ “lines”}. \quad 8.875 \times 0.556 \text{ MeV} = 4.9365 \text{ MeV} = E_B \text{ NN},$$

$$E_B \text{ NNP} = 8.4818 \text{ MeV}. \quad 8.4818 / 0.556 = 15.25 \text{ “lines”},$$

One line is equal to 0.556 MeV; it is the basic E_B value, which allows us to calculate the E_B of any nuclide.

1.2.7. Simplification of calculations

So, to determine the binding energy for each nucleus one needs:

- To use two E_B values: the α particles one (28.325 MeV) and the four others (NN, NP, NNP, and NPP) taken all together.
- To look between NN, NP, NNP, and NPP which one suits. In first place the A bond (NN/2 + NP/2) is used. If there is a rest of lines, it will be distributed between NNP and NPP.

Examples

$$E_B \quad {}^{16}\text{O} = 4 E_B \quad \alpha + 25.75 \text{ lines} = 4 E_B \quad \alpha + 2 \text{ NN} + 2 \text{ NP} = 127.6222 \text{ MeV} (+ 0.003) [3],$$

$$E_B \quad {}^{35}\text{Cl} = 8 E_B \quad \alpha + 128.75 \text{ lines} = 8 E_B \quad \alpha + 10 \text{ NN} + 10 \text{ NP} = 298.211 \text{ MeV} (+ 0.001) [3],$$

$$E_B \text{ } ^{63}\text{Cu} = 14 E_B \text{ } \alpha + 278.375 \text{ lines} = 14 E_B \text{ } \alpha + 13 \text{ NN} + 13 \text{ NP} + 8 \text{ NPP} = 551.3883 \text{ MeV} (+ 0.004) [3].$$

So, according to the author's theory, the nuclei of the various elements are constituted with α particles and other nucleons grouped in order to create sub-nuclei linked by four types of bonds called NN, NP, NNP, and NPP.

For more details, refer to author's former articles [2] where it is shown that the hypothesis of α structures in the α cluster nuclei can, indeed, describe the binding energy systematics. In such an approach, the system in its ground state behaves like a crystal, with stationary configuration and shape and with defined bond values between the various α particles and/or sub-nuclei.

According to author's hypothesis the binding energy of every nuclide is the sum of the binding energy of its different sub-structures and the binding energy among these sub-structures.

This method of determining the binding energy is totally different from those used up to now.

1.3. Values used to calculate binding energy

$$E_B \alpha = 28.325 \text{ MeV}$$

$$E_B \text{ NN} = 4.9365 \text{ MeV} = 8.875 \text{ lines}$$

$$E_B \text{ NP } (^2_1\text{H}) = 2.2246 \text{ MeV} = 4 \text{ lines} \quad \text{One line} = 0.5561589 \text{ MeV} [2]$$

$$E_B \text{ NNP } (^3_1\text{H}) = 8.4818 \text{ MeV} = 15.25 \text{ lines}$$

$$E_B \text{ NPP } (^3_2\text{H}) = 7.7180 \text{ MeV} = 13.875 \text{ lines}$$

The NN and NP are the most used bonds. Generally, they oscillate to form an "A" (A for average) bond equal to $(\text{NN}/2 + \text{NP}/2)$. The NN value (4.9365 MeV) is comparable to the mass of quark down (4.8 MeV) and the NP value (2.2246 MeV) is comparable to the mass of quark up (2.4 MeV).

The NP, NNP and NPP values are those of "The AME 2016 atomic mass evaluation" with four digits after decimal point [3].

1.4. Basic rule for determining the nuclei binding energy

1.4.1. According to author's theory

- The calculation of binding energy of the stable isotopes of each light element satisfies the following rule:
 $E_B n = x E_B \alpha + x E_B (\text{NN}/2 + \text{NP}/2) + y E_B (\text{NN} + \text{NP})$
 $(x = \text{number of } \alpha \text{ particles, } y = \text{number of N and P supplementary within a given nucleus}).$
 This is the case of ^{16}O .
- The basic rule valid for the stable isotopes of elements located at the center of the periodic table, is:
 $E_B n = x E_B \alpha + (x + y) E_B (\text{NN} + \text{NP}).$
 One should note that $(\text{NN} + \text{NP})$ bonds could be replaced by NNP or NPP bonds which have a higher energy value.
 This is the case of $E_B \text{ } ^{63}\text{Cu}$.

Some bonds are not completed, $(NN/2 + NP/2)$ being replaced by NP. This happens in case of non-stable isotopes of an element.

- The rule for the heaviest nuclei is close to the first formulation, valid for the light element's isotopes.

Remark: As the number of nucleons increases the equation valid for the light nuclei becomes close to that one for the isotopes of elements in the center of the Table of elements.

$^{35}\text{Cl} = 8 E_B \alpha + 10 NN + 10 NP$ instead of $8 E_B \alpha + 8 NN + 8 NP (+ 2 NN + 2 NP \text{ for the two N supplementary linked to the } \alpha \text{ particles}) + NPP$.

As seen, the difference is only one NPP. Indeed, this is close to the rule for the isotopes of elements located at the center of the Table of elements. Nevertheless, if E_B ^{35}Cl was based on the same rule as for those ones its E_B should be $8 E_B \alpha + 8 (NN + NP) + 2 (NN + NP) + NPP = 8 E_B \alpha + 10 NN + 10 NP + NPP$.

One NPP is lacking showing that the cross bonds are not completed.

1.4.2. The constraints

For each intermediate-sized nucleus located at near center of the nuclear table, each α particle is linked linearly to another α particle with one A bond. Also, each α particle is linked transversally to another α particle with one A bond. So, Fe which E_B is studied in the following has 13 A linear bonds and 13 A cross bonds because it contains 13 α particles. Nevertheless, A bonds could be replaced by NP, NN, NNP, and NPP bonds.

The N supplementary are linked to two α particles by $(NP + NN)$ bonds or by NNP or NPP bonds.

The P supplementary is linked by NP or NPP bonds, exceptionally by an NNP bond, to one or two α particles.

1.5. Three remarks

- Geometrical structure of atomic nuclei.
In author's theory the binding energy of the nuclei has a unidimensional value, broken down by E_B α , NN, NP, NNP, and NPP. So, this work does not address the three-dimensional model of nuclei in the sense that it is not looking for a structure of these nuclei but rather for the distribution of binding energy among them. Nevertheless, a comparison with 3D nuclei models is attempted in this article showing the various isotopes of Fe behaving like crystals with a stationary configuration and shape, and with defined bond values between the various α particles and other sub-nuclei.
- It is important to know the distribution of the binding energy in each isotope at the beginning and the end of a LENR fusion/transmutation reaction in order to follow accurately that process.
- Studying all the isotopes of Fe could help knowing what happens in the heart of such a reaction. The same exercise was already made with the same results for the isotopes of elements from Ca up to Ag. The work goes on. A similar work could be undertaken with isobars having the same mass number but different atomic numbers.

Table 1. Binding energy (E_B) distribution for ^{52}Fe to ^{61}Fe

Nucleus	Structure	Status	E_B Core				E_B N, P supplementary				Difference with the basic rule, in lines		
			NN	NP	NNP	NPP	NN	NP	NNP	NPP	Total of lines	Average	Difference
^{52}Fe	13 α	Lifetime: 8.2 h	5	17	2	0					142.8750	167.3750	–24.5000
	0 N, 0 P	Mode of decay: β^+ , EC					0	0	0	0	0	= 26 A 0	–
^{53}Fe	13 α	Lifetime: 8.5 min	1	13	3	3					148.2500	167.3750	–19.1250
	1 N, 0 P	Mode of decay: β^+ , EC					0	0	0	1	13.8750 =NPP	= 26 A 12.8750 =2 A	+1.0000
^{54}Fe	13 α	Stable	12	12	0	1					168.3750	167.3750	+1.0000
	2 N, 0 P	Nat. abundance: 5.8%					2	0	0	0	17.7500= 2 NN	= 26 A 25.7500 = 4 A	–8.0000
^{55}Fe	13 α	Lifetime: 2.6 years	14	12	0	0					172.2500	167.3750	+4.8750
	3 N, 0 P	Mode of decay: EC					3	1	0	0	30.6250 = 3 N+1 NP	= 26 A 38.6250 = 6 A	–8.0000
^{55}Fe Fig. 2	13 α	Lifetime: 2.6 years	14	10	0	0					164.2500	167.3750	–3.1250
	3 N, 0 P	Mode of decay: EC					3	3	0	0	38.6250 = 6 A	= 26 A 38.6250 = 6 A	–
^{55}Mn	12 α	Stable	14	10	0	0					164.2500	154.5000	+9.7500
	6 N, 1 P	Nat. abundance: 100%					0	1	3	3	91.3750 =1NP + 3 NNP +3 NPP	= 24 A 91.1250 =12 A+NPP	+0.2500
^{55}Mn Fig. 2	12 α	Stable	12	12	0	0					154.5000	154.5000	–
	6 N, 1 P	Nat. abundance: 100%					0	0.5	6.5	0	101.1250 = 6.5 NNP +0.5 NP	= 24A 91.1250 =12 A +NPP	+1.0000
^{55}Mn Fig. 3	12 α	Stable	12	12	0	0					154.5000	154.5000	–
	6 N, 1 P	Nat. abundance: 100%					0	1	0	7	101.1250 = NP+7NPP	= 24A 91.1250 = 12 A +NPP	+10.0000
^{55}Mn Fig. 4	12 α	Stable	8	8	0	4					158.5000	154.5000	+4.0000
	6 N, 1 P	Nat. abundance: 100%					0	0	0	7	97.1250 =7 NPP	= 24A 91.1250 = 12 A +NPP	+6.0000
^{56}Fe	13 α	Stable	13	13	0	0					167.3750	167.3750	–
	4 N, 0 P	Nat. abundance: 91.8%					3.5	2.5	0.5	0.5	55.6250 = 5 A +NN +NNP/2 + NPP/2	= 26 A 51.500 = 8 A	+4.1250

Nucleus	Structure	Status	E_B Core				E_B N, P supple- mentary				Difference with the basic rule, in lines		
			NN	NP	NNPNPP	NN	NP	NNPNPP	Total of lines	Average	Difference		
^{56}Fe Fig. 2	13 α	Stable	7	9	0	5					167.5000	167.3750	+0.1250
	4 N, 0 P	Nat. abundance: 91.8%					0	0	0	4	55.5000 = 4 NPP	= 26 A 51.5000 =8 A	+4.0000
^{57}Fe	13 α	Stable	13	13	0	0					167.3750	167.3750	–
	5 N, 0 P	Nat. abundance: 2.1%					0	0	0	5	69.3750 =5 NPP	= 26A 64.3750 =10 A	+5.0000
^{58}Fe	13 α	Stable	13	13	0	0					167.3750	167.3750	–
	6 N, 0 P	Nat. abundance: 0.3%					1.5	0.5	2	3	87.4375 = A+NN 2 NNP +3 NPP	= 26 A 77.2500 =12 A	+10.1875
^{59}Fe	13 α	Lifetime: 45.1 days	13	13	0	0					167.3750	167.3750	–
	7 N, 0 P	Mode of decay: β^-					2	2	3	2	99.2500 = 4 A+ 3 NNP +2 NPP	= 9.1250 = 14 A	+9.1250
^{59}Co	13 α	Stable	13	13	0	0					167.3750	167.3750	–
	6N,1 P	Nat. abundance: 100%					3.5	2.5	3	1	100.6875 =5 A + NN +3 NP+NPP	= 26A 91.1250 =12 A +NPP	+9.5625
^{59}Co Fig. 2	13 α	Stable	12	12	1	0					169.7500	167.3750	+ 2.3750
	6N, 1 P	Nat. abundance: 100%					0	1	3	3.5	98.3125 = NP + 3 NNP + 3.5 NPP	= 26A 91.1250 =12 A +NPP	+7.1875
^{60}Fe	13 α	Lifetime: 3×10^5 years	13	13	0	0					167.3750	167.3750	–
	8 N, 0 P	Mode of decay: β^-					0	0	3	5	115.1250 = 3 NNP + 5 NPP	= 26 A 103.0000 =16 A	+12.1250
^{61}Fe	13 α	Lifetime: min	6	13	13	0	0				167.3750	167.3750	–
	9 N, 0 P	Mode of decay: β^-					2.5	2.5	2	4.5	125.1250 = 5 A +2 NNP + 4.5 NPP	= 26A 115.8750 = 18 A	+9.2500

2. Binding Energy Distribution among ^{52}Fe to ^{61}Fe

3. Analysis of Table 1

- (1) The zone of stability stretches from - 7 lines (^{54}Fe) to + 10.1875 (^{58}Fe)
The most abundant isotope is ^{56}Fe with + 4.125 lines.
- (2) Number of N supplementary.
The isotopes which are stable contain 2N, 4N, 5N, and 6N.
 ^{55}Fe with 3 N supplementary is not stable but has a high lifetime.
 ^{60}Fe with 8 N supplementary has a very high lifetime.
- (3) The presence of N supplementary has as consequence the increase of the value of the binding energy of a given nucleus:

– 24. 5000 lines in case of ^{52}Fe which has no N supplementary.

+10.1875 lines for ^{58}Fe .

+12.1250 lines for ^{60}Fe .

But + 9.25 lines for ^{61}Fe .

- (4) As a consequence of the increasing number of N supplementary there is a progressive increase of NN bonds versus NP ones in order to achieve a maximum of parity between both bonds to create as many A bonds as locations (26 in case of ^{26}Fe).
- (5) ^{52}Fe (see Table 1 and Fig. 1 in the appendices)

There are 26 linear and cross-bonds, but only 10A bonds (instead of 26) linking the α particles on the top and the bottom of the structure. Also, 2 NNP are replacing 4A bonds. The cross-bonds are of NP type. Actually, there are some bonds missing in order to achieve the shape of the structure. The table indicates a deficit of 24.5 lines. The structure cannot be stable until the linear and cross-bonds are of A type, hence the EC and β^+ decay.

- (6) ^{53}Fe (see Table 1 and Fig. 2)

This structure is similar to that one for ^{52}Fe .

Nevertheless, more linear bonds are of NNP and NPP type. There is a deficit of 19.125 lines in the core which shows that the presence of one N supplementary has occurred an increase of the number of lines: + 5.375 in the core of the structure if compared with ^{52}Fe . This structure is not stable for the same reasons as ^{52}Fe .

- (7) ^{54}Fe (see Table 1 and Fig. 3)

The core of this structure is almost perfectly shaped, hence its stability. The 2 supplementary N are bound to the core with each 1 NN bond. Even if there is a global deficit of 7 lines, it allows the structure to be stable. The NPP bond on the top and the 2 NN bonds of the 2 N supplementary are interchangeable to assume the stability.

- (8) ^{55}Fe (see Table 1 and Figs. 4 and 5)

This structure is comparable to ^{54}Fe . Nevertheless, to achieve the bonding of the 3 N supplementary it is

necessary to use at minimum 6A bonds ($3 \times 2A$). The 2 NN bonds on the top of the structure and the 2 NN bonds of the 2 N supplementary are interchangeable. Nevertheless, if one wants to interchange the 3 N supplementary bonds with the structure of the top, the result is 6A bonds for the 3 N supplementary and 4 NN bonds for the top of the structure. As result there is no more bonds between the α particle on the top and the other 4 α particles (see Fig. 5). This leads to an α particle without bonding and so, to EC or to β^+ decay. The α particle splits into 3 N and 1 P (see Fig. 6).

(9) ^{55}Mn (see Table 1 and Fig. 6)

Compared to ^{55}Fe (see Fig. 5), the 3 N supplementary are bonded with 3 NPP instead of $3 \times 2A$ bonds. The 3 N and 1 P issued from the splitting of α particle on the top of the structure are bonded with 3 NNP and 1 NP to the 4 α particles sub-structure.

(10) ^{55}Mn Fig. 2 (see Table 1 and Fig. 7)

The structure in Fig. 6 is not stable and a rearrangement is necessary. Instead of 4 NN bonds linking the 3 N and the P to the top structure in Fig. 6, there are 4 A on the Fig. 7. Moreover, the P is bonded with the 3 N and no longer with the α particles. It is now bonded alternately to 2 N (NNP/2) and to 1 N (NP/2). Therefore, the 3 NPP bonds of the 3 N supplementary on the bottom of the structure become NNP bonds.

(11) ^{55}Mn Fig. 3 (see Table 1 and Fig. 8)

There are other rearrangements within ^{55}Mn . Now, the 6 N supplementary are linked to the α particles with 6 NPP bonds. The P supplementary is also linked to α particles with 1 NPP bond and linked to two N supplementary with 2 NP/2 bonds. Nevertheless, this last link is creating one NP bond supplementary to the 14 (7 NNP) necessary.

(12) ^{55}Mn Fig. 4 (see Table and Fig. 9)

So, this NP bond supplementary, of value 4 lines is distributed between the 8A cross bonds, which become 4 NPP bonds. The number of bonds in the core is 24 and that one of the N and P supplementary is 14.

(13) ^{56}Fe (see Table 1 and Fig. 10)

The linear and cross bonds are equal to 26A. This configuration is the best possible. The 4 N are linked to the α particles with 5A, NN, NNP/2 and NPP/2 bonds.

(14) ^{56}Fe Fig. 2 (see Table 1 and Fig. 11)

To avoid the unevenness on the preceding structure, one can distribute the bonds in the way presented on Fig. 11. The interchangeability between the structures in Figs. 10 and 11 create more stability.

(15) ^{57}Fe (see Table 1 and Fig. 12)

The ^{57}Fe core structure is perfect. The 5 N supplementary are linked to the α particles with 5 NPP bonds which is an odd number. Nevertheless, the structure is stable.

(16) ^{58}Fe (see Table 1 and Fig. 13)

The core structure is perfect, the 6 N supplementary are linked to the α particles with A, NN, 2 NNP, 3 NPP bonds. In order to have 6 NPP bonds for the 6 N supplementary the number of lines in the core should be increased with 4.1875 lines. This would mean 19A, 3 NPP and NNP/2 bonds in the core instead of 26A bonds.

(17) ^{59}Fe (see Table 1 and Fig. 14)

The core structure of ^{59}Fe is perfectly shaped, as it is for ^{58}Fe . Nevertheless, there are 7 N supplementary and an excess of 9.125 lines. This configuration leads to β^- decay.

(18) ^{59}Co (see table and figures 15 and 16)

^{59}Co is the decay result of ^{59}Fe , 1 N supplementary decaying into P, the bond remaining the same (NPP). One bond of another N supplementary is consequently modified from NPP to (NN + A) bonds (see figure 15). After rearrangement, the structure looks like it does in Fig. 16.

(19) ^{60}Fe (see Table 1 and Fig. 17)

^{60}Fe structure is not stable but has a long lifetime. Nevertheless, the core structure is stable (26A) and there are 8 N supplementary linked to the α particles with 5 NPP and 3 NNP. Note the similarity with ^{57}Fe . Both ^{57}Fe and ^{60}Fe have a core structure with 26A. ^{57}Fe has 5 N supplementary linked to α particles with 5 NPP as well as ^{60}Fe , but ^{60}Fe has 3 N supplementary more linked to α particles with 3 NNP bonds.

Let us take the EB of both isotopes (AME 2016):

^{57}Fe	^{60}Fe	Difference
499.9059 MeV	525.3511 MeV	25.4452 MeV
This difference is equal to 3×8.4817 MeV or 3 NNP		

(20) ^{61}Fe (see Table 1 and Fig. 18)

^{61}Fe is comparable to the structure ^{60}Fe . Nevertheless, the N supplementary are too numerous. So, 1 N decays rapidly into P.

4. The Author's Method of Calculation

4.1. Mind experiments

As already said (see Section 1.2.4), the author's method of calculation is not based on a theory, but rather on mind experiments. This is comparable to the work of a chemist looking for several solutions in his experiments and validating that one which fits best. Each time a new neutron or proton enters a nucleus, its binding energy value is modified by reshaping its structure among NN, NP, NNP, NPP and in case EB α values.

4.2. Examples of calculation for ^{55}Mn , ^{59}Co , and ^{63}Cu

According to the general rule (see Section 1.4) the binding energy of these three nuclei should be the following:

Experimental values of the binding energy of the three nuclei minus totals are determined in Table 2:

^{55}Mn : 482.0762 MeV (AME 2016 value) - 476.5178 MeV = 5.5584 MeV or 10 lines (for value of lines see Section 1.2.6).

^{59}Co : 517.3141 MeV (AME 2016 value) - 512.0039 MeV = 5.3102 MeV or 9.5625 lines.

^{63}Cu : 551.3847 MeV (AME 2016 value) - 547.4900 MeV = 3.8947 MeV or 7 lines.

Table 2. Theoretical binding energy values among ^{55}Mn , ^{59}Co , and ^{63}Cu .

	^{55}Mn : 12 α , 6 N, 1 P		^{59}Co : 13 α , 6 N, 1 P		^{63}Cu : 14 α , 6 N, 1 P	
αE_B	EB 12 α	339.9000	E_B 13 α	368.2250	E_B 14 α	396.5500
Core E_B	12	85.9332	13	93.0943	14	100.2554
	(NN+NP)		(NN+NP)		(NN+NP)	
N suppl.	6	42.9666	6	42.9666	6	42.9666
E_B	(NN+NP)		(NN+NP)		(NN+NP)	
P suppl.	NPP	7.7180	NPP	7.7180	NPP	7.7180
E_B						
Total		476.5178		512.0039		547.4900
(MeV)						

So, these lines must be added to the former calculations (see Table 2).

Results

- ^{55}Mn : 24A (12 NN + 12 NP) + 4 lines = 16A + 4 NPP (see Fig. 9).
 12A (6 NN + 6 NP) + 6 lines = 6 NPP.
 NPP = NPP.
- ^{59}Co : 26A (13 NN + 13 NP) = 26A (see Fig. 15).
 12A (6 NN + 6 NP) + 9.5625 lines = 5A + NN + 3 NNP.
 NPP = NPP.
- ^{59}Co : Alternative solution:
 26A (13 NN + 13 NP) + 2.375 lines = 24A + NNP (see Fig. 16).
 12A (6 NN + 6 NP) + 10.1250 lines = 3 NNP + 3 NPP.
 NPP - 2.9375 lines = NP + NPP/2.
 (2.375 + 10.125 - 2.9375 = 9.5625 lines).
- ^{63}Cu : 28A (14 NN + 14 NP) + 7 lines = 14A + 7 NPP (no figure).
 12A (6 NN + 6 NP) = 12A.
 NPP = NPP.

4.3. Decay of ^{63}Ni into ^{63}Cu

^{63}Ni decays β^- into ^{63}Cu . See Table 3, their respective binding energy structure according to the author's theory.

Comparing the two calculation results one notes the following:

(3.5 NN + 3.5 NP + 3.5 NNP) of ^{63}Ni have decayed into 7 NPP of ^{63}Cu .

In other terms (7 NN + 7 NP + 7 NNP) / 2 decayed into 7 NPP.

So, the (NN + NP) bonds and NNP bonds which alternate within ^{63}Ni decay into NPP bonds within ^{63}Cu . Consequently, one N supplementary of ^{63}Ni decays into one P to create ^{63}Cu .

5. Conclusion

The distribution of binding energy in each isotope as shown above is fundamental for understanding the LENR process, and especially the transmutation process. It allows us to determine how the binding energy evolves, nucleus

Table 3. Comparison of binding energy distribution among ^{63}Ni and ^{63}Cu .

^{63}Ni	14 α , 7N supplementary EB in MeV = 552.1001 Lifetime: 92 years Mode of decay: β^-		^{63}Cu	14 α , 6N, 1P supplementary EB in MeV = 551.3847 Stable Nat. abundance: 69.2 %	
	$\left\{ \begin{array}{l} 14 \text{ x } 28.325 \\ 10.5 \text{ x } 4.9365 \\ 10.5 \text{ x } 2.2246 \\ 3.5 \text{ x } 8.4818 \\ 0 \text{ x } 7.7180 \end{array} \right\}$	$\left\{ \begin{array}{l} 396.5500 \\ 51.8333 \\ 23.3583 \\ 29.6863 \\ 0 \end{array} \right\}$ MeV		$\left\{ \begin{array}{l} 14 \text{ x } 28.325 \\ 7 \text{ x } 4.9365 \\ 7 \text{ x } 2.2246 \\ 0 \text{ x } 8.4818 \\ 7 \text{ x } 7.7180 \end{array} \right\}$	$\left\{ \begin{array}{l} 396.5500 \\ 34.5555 \\ 15.5722 \\ 0 \\ 54.0260 \end{array} \right\}$ MeV
	$\left\{ \begin{array}{l} 6 \text{ x } 4.9365 \\ 6 \text{ x } 2.2246 \\ 0 \text{ x } 8.4818 \end{array} \right\}$	$\left\{ \begin{array}{l} 29.6190 \\ 13.3476 \\ 0 \end{array} \right\}$		$\left\{ \begin{array}{l} 6 \text{ x } 4.9365 \\ 6 \text{ x } 2.2246 \\ 0 \text{ x } 8.4818 \end{array} \right\}$	$\left\{ \begin{array}{l} 29.6190 \\ 13.3476 \\ 0 \end{array} \right\}$
	$\left\{ \begin{array}{l} 1 \text{ x } 7.7180 \end{array} \right\}$	$\left\{ \begin{array}{l} 7.7180 \end{array} \right\}$		$\left\{ \begin{array}{l} 1 \text{ x } 7.7180 \end{array} \right\}$	$\left\{ \begin{array}{l} 7.7180 \end{array} \right\}$
		552.1125 MeV			551.3883 MeV
		+ 0.012			+ 0.004

after nucleus, isotope after isotope. This is essential for LENR process comprehension, because the difference in the distribution of binding energy between the elements present at the beginning of the reaction and at the final stage is directly related to the energy released. Many more examples are displayed in author's book on Atomic Nuclei Binding Energy [4].

Basically, only five bond types are necessary to describe the systematics of the binding energy within the nuclei.

- (1) The binding energy of the NP bond, which is the deuterium binding energy.
- (2) The binding energy of the NNP bond, which the tritium binding energy.
- (3) The binding energy of the NPP bond, which is the ^3He binding energy.
- (4) The binding energy of the NN bond, which is part of the α particle binding energy.
- (5) The binding energy of the α particle, which includes all the binding energies above. (Note that the PP binding energy within the α particle is equal to the binding energies of NP + NNP + NPP).

Each α particle is linked to two other α particles in a linear way and in a cross way. As well, each N supplementary is linked to two α particles by (NN + NP) bonds. These bonds could be replaced by NNP or NPP bonds. So, the stability of an element isotope is reached if the number of lines is optimal. If the number of lines is not big enough the isotope of that element decays EC or β^+ if the number of lines is too big the isotope decays β^- .

So, the examples of Fe isotopes containing 52 up to 61 nucleons presented in this paper show that:

- Fe is stable with 54, 56, 57, and 58 nucleons, i.e. $13\alpha + 2\text{N}$, 4N , 5N , and 6N supplementary.
- Mn is stable with 55 nucleons, i.e. $12\alpha + 6\text{N} + 1\text{P}$ supplementary.
- Co is stable with 59 nucleons, i.e. $13\alpha + 6\text{N} + 1\text{P}$ supplementary.

On one side the increase of the number of neutrons is linked to the strong interaction, and on the other side the transformation of one proton into one neutron (β^+ decay) or one neutron into one proton (β^- decay) is the consequence of the weak interaction.

Both decay processes are the consequence of the number of supplementary neutrons. With 2, 4, 5, and 6 neutrons Fe is stable. With fewer neutron's Fe decays β^+ into Mn. With more neutron's Fe decays β^- into Co. Nevertheless,

with three supplementary neutrons Fe decays into Mn (^{55}Mn). This is due to the equilibrium between NP and NN bonds.

^{52}Fe and ^{53}Fe have a deficit of NN bonds compared to NP bonds. ^{55}Fe suffers an excess of NN bonds (see Figs. 1, 2, 4–9). To assure the equilibrium between the bonds the number of neutrons versus protons must change, hence the β^+ decay or disintegration of an α particle into three neutrons and one proton, instead of two neutrons and two protons. Mn has 12α and Fe has 13α .

If the number of neutrons increases the number of bonds also increases. Therefore, a new equilibrium between neutrons and protons must occur. One neutron decays β^- into a proton and ^{59}Fe becomes ^{59}Co .

So, strong interaction leads to three modes of decay (β^+ and EC) if there are not enough neutrons and β^- if there are too many neutrons in order to maintain the equilibrium between NN and NP bonds, hence the importance of the A bonds as average $(\text{NN}/2 + \text{NP}/2)$.

The valley of stability for each element is very narrow, i.e. for Fe it is limited to ^{54}Fe to ^{58}Fe and to 13α particles without any proton outside the α particles. For ^{55}Mn as well as for ^{59}Co (difference one α) there is one proton outside the α particles, and the valley of stability is limited to these two isotopes for these elements. ^{60}Co decays into ^{60}Ni , one neutron decaying β^- . This operation creates one proton more and hence one α particle more: Ni has 14α particles.

The example of Iron given in this paper is one of the numerous nuclei the author has studied. Presently, the binding energy of all isotopes of the elements up to atomic number 47 (Silver) have been determined and this work continues. Some other nuclei binding energies were also determined, especially those of atomic number from 82 to 94.

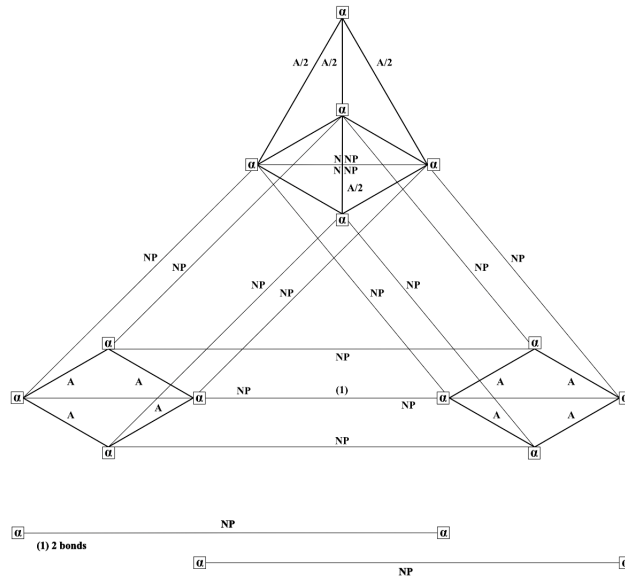
References

- [1] L. Pauling, *Science* **150** (1965) d 297. K. Ikeda, N. Takigawa and H. Horiuchi, *Prog. Theoret. Phys. Suppl.* (1968) E 464.
- [2] Philippe Hatt, *J. Condensed Matter Nucl. Sci.* **26** (2018) 45–53, *J. Condensed Matter Nucl. Sci.* **29** (2019) 260–274.
- [3] The AME 2016 atomic mass evaluation.
- [4] www.philippehatt.com.

Appendix A. $^{52}_{26}\text{Fe}$ Structure: 13 α , 0 N, 0 P

Linear and cross bonds: 10A, 12 NP, 2 NNP

N supplementary bonds: 0



h

$^{52}_{26}\text{Fe}$	13 α , 0N, 0P supplementary	E_B (MeV)=447.6978
Lifetime=8.2 h Mode of decay: β^-	$\left\{ \begin{array}{l} 13 \times 28.3250 \\ 6.5 - 1.5 \times 4.9365 \\ 6.5 + 10.5 \times 2.2246 \\ 2 \times 8.4818 \\ 0 \times 7.7180 \end{array} \right\}$	368.2250 MeV
		24.685
		37.8182
		16.9636
		0
	$\left\{ \begin{array}{l} 0 \times 4.9365 \\ 0 \times 2.2246 \\ 0 \times 8.4818 \\ 0 \times 7.7180 \end{array} \right\}$	0
		0
		0
		0
		447.6893 MeV
		-0.009

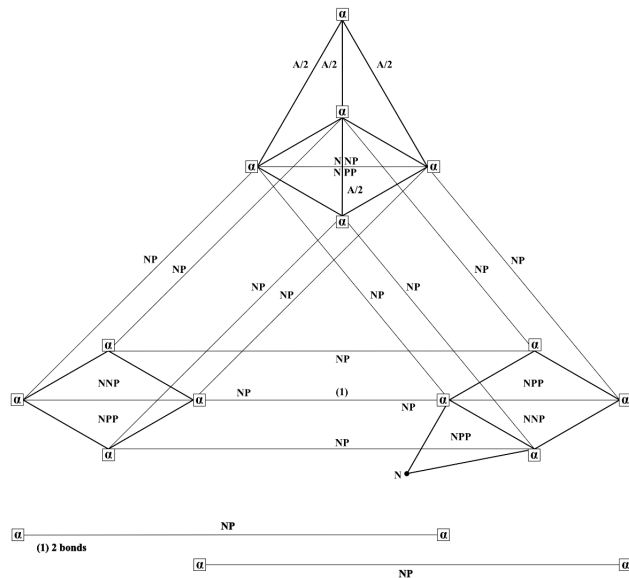
Figure 1. Binding energy distribution among ^{52}Fe

Appendix B. $^{53}_{26}\text{Fe}$

Structure: 13 α , 1 N, 0 P

Linear and cross bonds: 2 A, 12 NP, 3 NNP, 3 NPP

N supplementary bonds: NPP



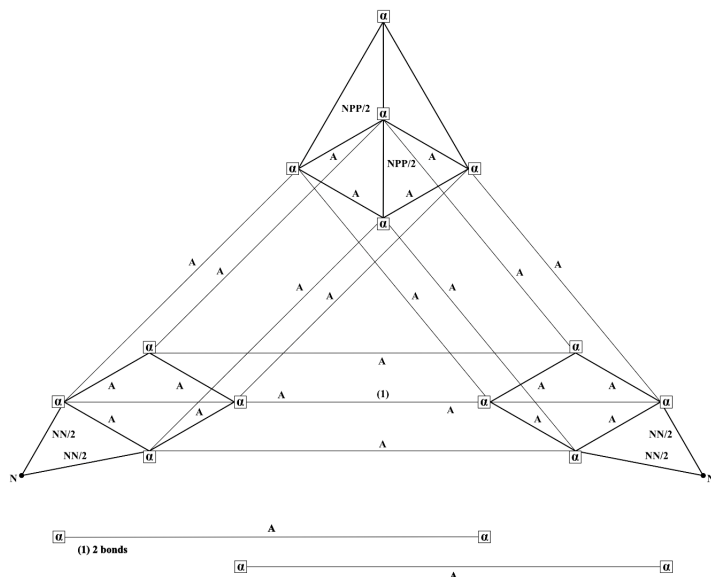
$^{53}_{26}\text{Fe}$	13 α , 1N, 0P supplementary	E_B (MeV)=458.3863
Lifetime=8.5 min	$\left\{ \begin{array}{l} 13 \times 28.3250 \\ 6.5 - 5.5 \times 4.9365 \\ 6.5 + 10.5 \times 2.2246 \end{array} \right\}$	$\left\{ \begin{array}{l} 368.2250 \text{ MeV} \\ 4.9365 \\ 28.9198 \end{array} \right\}$
Mode of decay: β^+ ,	$\left\{ \begin{array}{l} 3 \times 8.4818 \\ 3 \times 7.7180 \end{array} \right\}$	$\left\{ \begin{array}{l} 25,4454 \\ 23.1540 \end{array} \right\}$
EC	$\left\{ \begin{array}{l} 0 \times 4.9365 \\ 0 \times 2.2246 \\ 0 \times 8.4818 \\ 0 \times 7.7180 \end{array} \right\}$	$\left\{ \begin{array}{l} 0 \\ 0 \\ 0 \\ 7.7180 \end{array} \right\}$
		458.3987 MeV +0.012

Figure 2. Binding energy distribution among ^{53}Fe .

Appendix C. $^{54}_{26}\text{Fe}$ Structure: 13 α , 2 N, 0 P

Linear and cross bonds: 24 A, NPP

N supplementary bonds: 2 NN



$^{54}_{26}\text{Fe}$	13 α , 2 N, 0P supplementary	E_B (MeV)=471.7646
Stable Nat, abundance: 5.8 %	$\left\{ \begin{array}{l} 13 \times 28.3250 \\ 6.5 - 5.5 \times 4.9365 \\ 6.5 + 5.5 \times 2.2246 \\ 0 \times 8.4818 \\ 1 \times 7.7180 \end{array} \right\}$	368.2250 MeV
		4.9365
		59.2380
		26.69524454
		0
	$\left\{ \begin{array}{l} 2 \times 4.9365 \\ 0 \times 2.2246 \\ 0 \times 8.4818 \\ 0 \times 7.7180 \end{array} \right\}$	9.8730
		0
		0
		0
		471.7492 MeV
		-0.015

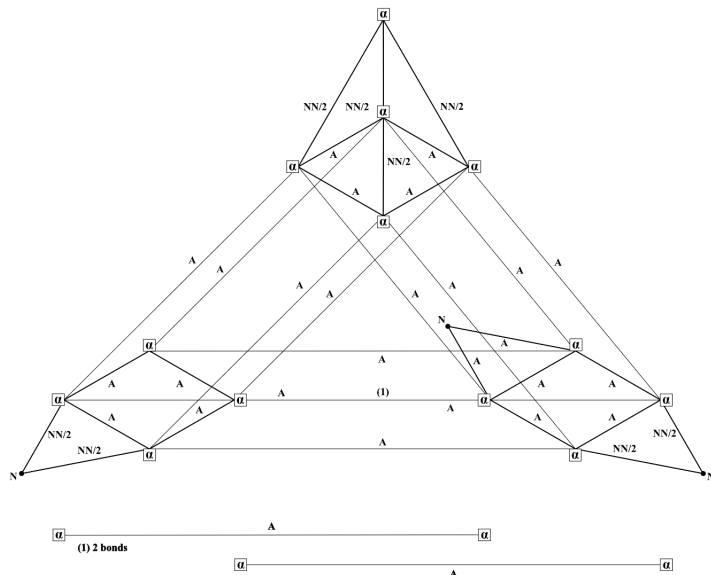
Figure 3. Binding energy distribution among ^{54}Fe .

Appendix D. $^{55}_{26}\text{Fe}$

Structure: 13 α , 3 N, 0 P

Linear and cross bonds: 24 A, 2 NN

N supplementary bonds: 2 A, 2 NN



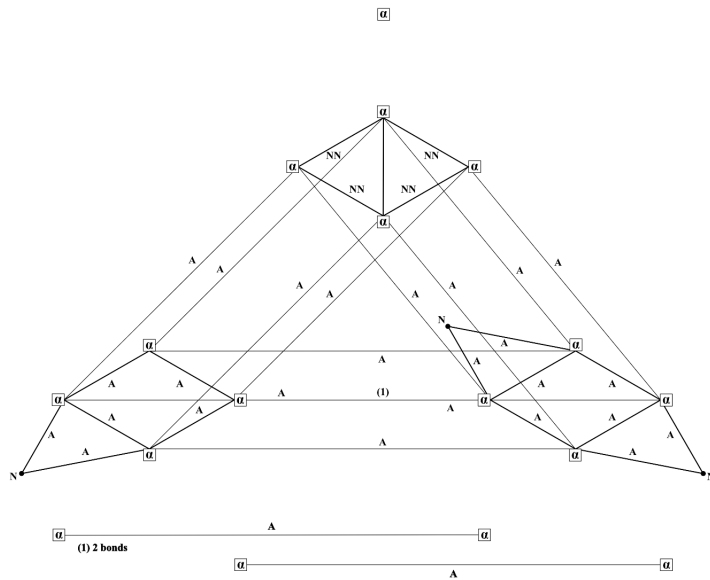
$^{55}_{26}\text{Fe}$	13 α , 3 N, 0P supplementary	E_B (MeV)=481.0627
Lifetime = 2.6 years Mode of decay: EC	$\left\{ \begin{array}{l} 13 \times 28.3250 \\ 6.5 - 7.5 \times 4.9365 \\ 6.5 + 5.5 \times 2.2246 \\ 0 \times 8.4818 \\ 0 \times 7.7180 \end{array} \right\}$	$\left\{ \begin{array}{l} 368.2250 \text{ MeV} \\ 69.1110 \\ 26.6952 \\ 0 \\ 0 \end{array} \right\}$
	$\left\{ \begin{array}{l} 3 \times 4.9365 \\ 1 \times 2.2246 \\ 0 \times 8.4818 \\ 0 \times 7.7180 \end{array} \right\}$	$\left\{ \begin{array}{l} 14.8095 \\ 2.2246 \\ 0 \\ 0 \end{array} \right\}$
		$\overline{481.0653 \text{ MeV}}$
		$+0.003$

Figure 4. Binding energy distribution among ^{55}Fe .

Appendix E. $^{55}_{26}\text{Fe}$ Fig. 2Structure: 13 α , 3 N, 0 P

Linear and cross bonds: 20 A, 4 NN

N supplementary bonds: 6 A



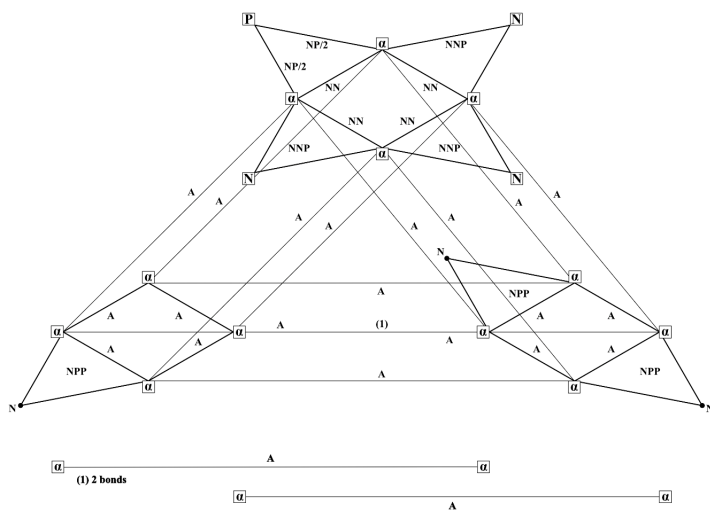
$^{55}_{26}\text{Fe}$ Fig.2	13 α , 3 N, 0P supplementary	E_B (MeV)=481.0627
Lifetime = 2.6 years Mode of decay: EC	$\left\{ \begin{array}{l} 13 \times 28.3250 \\ 6.5 - 7.5 \times 4.9365 \\ 6.5 + 3.5 \times 2.2246 \\ 0 \times 8.4818 \\ 0 \times 7.7180 \end{array} \right\}$	$\left\{ \begin{array}{l} 368.2250 \text{ MeV} \\ 69.1110 \\ 22.2460 \\ 0 \\ 0 \end{array} \right\}$
	$\left\{ \begin{array}{l} 3 \times 4.9365 \\ 3 \times 2.2246 \\ 0 \times 8.4818 \\ 0 \times 7.7180 \end{array} \right\}$	$\left\{ \begin{array}{l} 14.8095 \\ 6.6738 \\ 0 \\ 0 \end{array} \right\}$
		$\overline{481.0653 \text{ MeV}}$
		$+0.003$

Figure 5. Binding energy distribution among ^{55}Fe .

Appendix F. $^{55}_{25}\text{Mn}$

Structure: 12 α , 6 N, 1 P

Linear and cross bonds: NP, 3 NNP, 3 NPP



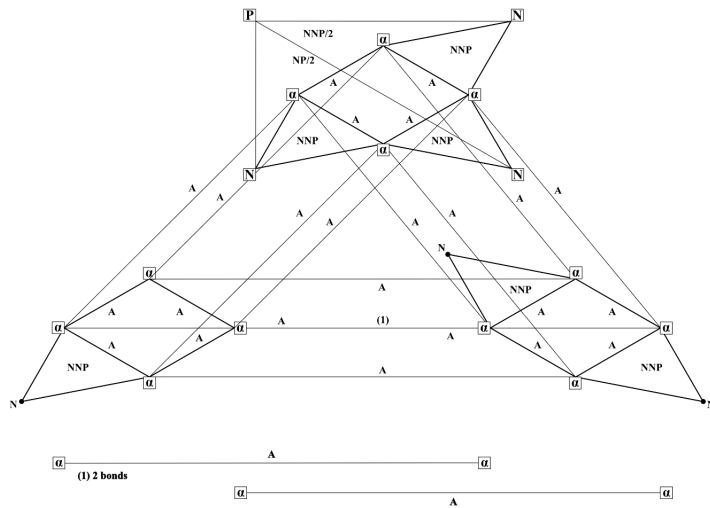
$^{55}_{25}\text{Mn}$	12 α , 6 N, 1P supplementary	E_B (MeV)=482.0762
Stable Nat. abundance 100%	$\left\{ \begin{array}{l} 12 \times 28.3250 \\ 6.5 - 7.5 \times 4.9365 \\ 6.5 + 3.5 \times 2.2246 \\ 0 \times 8.4818 \\ 0 \times 7.7180 \end{array} \right\}$	339.9000 MeV
		69.1110
		22.2460
		0
		0
	$\left\{ \begin{array}{l} 0 \times 4.9365 \\ 1 \times 2.2246 \\ 3 \times 8.4818 \\ 3 \times 7.7180 \end{array} \right\}$	0
		2.2246
		25.4454
		23.1540
		$\overline{482.0810 \text{ MeV}}$
		+0.005

Figure 6. Binding energy distribution among ^{55}Mn .

Appendix G. $^{55}_{25}\text{Mn}$ Fig. 2Structure: 12 α , 6 N, 1 P

Linear and cross bonds: 24 A

N, P supplementary bonds: NP/2, 6.5 NNP



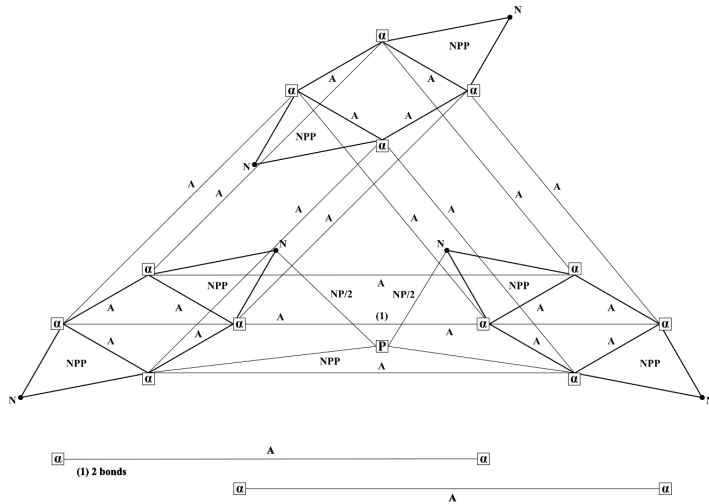
$^{55}_{25}\text{Mn}$ Fig. 2	12 α , 6 N, 1P supplementary	E_B (MeV)=482.0762
Stable Nat. abundance 100%	$\left\{ \begin{array}{l} 12 \times 28.3250 \\ 6 + 6 \times 4.9365 \\ 6 + 6 \times 2.2246 \\ 0 \times 8.4818 \\ 0 \times 7.7180 \end{array} \right\}$	339.9000 MeV 59.2380 26.6952 0 0
	$\left\{ \begin{array}{l} 0 \times 4.9365 \\ 1 \times 2.2246 \\ 3 \times 8.4818 \\ 3 \times 7.7180 \end{array} \right\}$	0 1.1123 55.1317 0
		$\overline{482.0772 \text{ MeV}}$
		+0.001

Figure 7. Binding energy distribution among ^{55}Mn .

Appendix H. $^{55}_{25}\text{Mn}$ Fig. 3Structure: 12 α , 6 N, 1 P

Linear and cross bonds: 24 A

N, P supplementary bonds: NP, 7 NNP



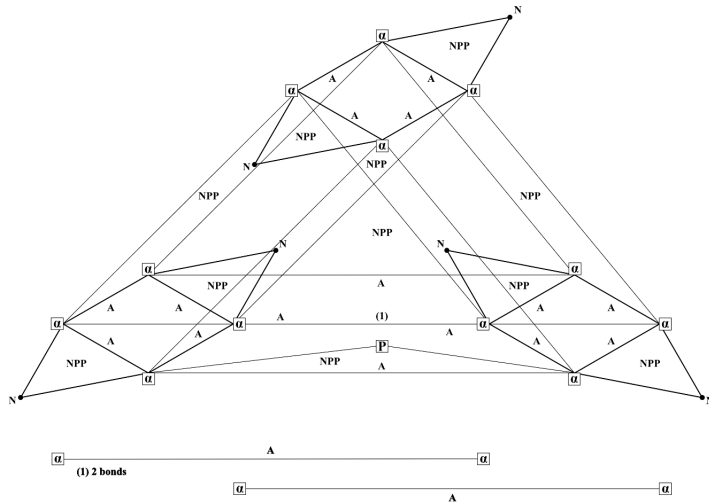
$^{55}_{25}\text{Mn}$ Fig. 3	12 α , 6 N, 1P supplementary	E_B (MeV)=482.0762
Stable Nat. abundance 100%	$\left\{ \begin{array}{l} 12 \times 28.3250 \\ 6 + 6 \times 4.9365 \\ 6 + 6 \times 2.2246 \\ 0 \times 8.4818 \\ 0 \times 7.7180 \end{array} \right\}$	339.9000 MeV
		59.2380
		26.6952
		0
		0
	$\left\{ \begin{array}{l} 0 \times 4.9365 \\ 1 \times 2.2246 \\ 0 \times 8.4818 \\ 7 \times 7.7180 \end{array} \right\}$	0
		2.2246
		0
		54.0260
		$\overline{482.0260 \text{ MeV}}$
		+0.008

Figure 8. Binding energy distribution among ^{55}Mn .

Appendix I. $^{55}_{25}\text{Mn}$ Fig. 4Structure: 12 α , 6 N, 1 P

Linear and cross bonds: 16 A, 4 NPP

N, P supplementary bonds: 7 NPP



$^{55}_{25}\text{Mn}$ Fig. 4	12 α , 6 N, 1P supplementary	E_B (MeV)=482.0762
Stable Nat. abundance 100%	$\left\{ \begin{array}{l} 12 \times 28.3250 \\ 6 + 2 \times 4.9365 \\ 6 + 2 \times 2.2246 \\ 0 \times 8.4818 \\ 4 \times 7.7180 \end{array} \right\}$	339.9000 MeV
		39.4920
		17.7968
		0
		30.8720
	$\left\{ \begin{array}{l} 0 \times 4.9365 \\ 0 \times 0 \\ 0 \times 8.4818 \\ 7 \times 7.7180 \end{array} \right\}$	0
		2.2246
		0
		54.0260
		$\overline{482.0868 \text{ MeV}}$
		+0.011

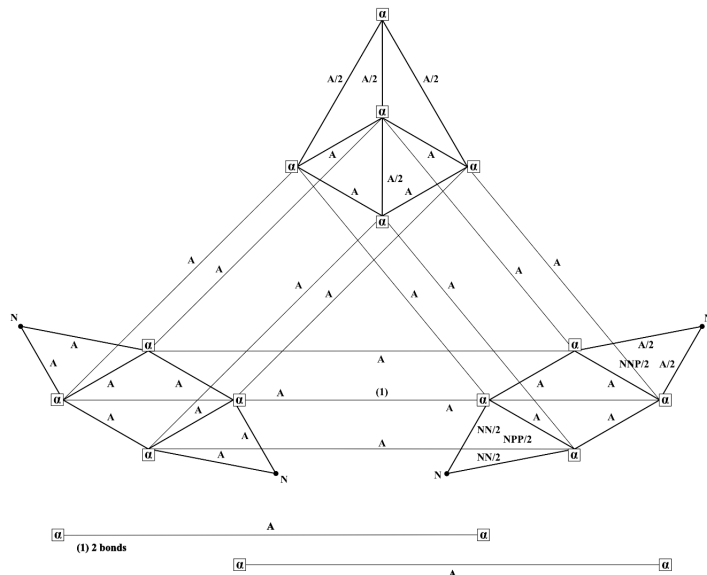
Figure 9. Binding energy distribution among ^{55}Mn .

Appendix J. $^{56}_{26}\text{Fe}$

Structure: 13 α , 4 N, 0 P

Linear and cross bonds: 26 A

N, P supplementary bonds: 5 A, NN, NNP/2, NPP/2



$^{56}_{26}\text{Fe}$	13 α , 4 N, 0 P supplementary	E_B (MeV)=492.2598
Stable Nat. abundance 91.8%	$\left\{ \begin{array}{l} 13 \times 28.3250 \\ 6.5 + 6.5 \times 4.9365 \\ 6.5 + 6.5 \times 2.2246 \\ 0 \times 8.4818 \\ 0 \times 7.7180 \end{array} \right\}$	368.2250 MeV 64.1745 28.9198 0 0
	$\left\{ \begin{array}{l} 3.5 \times 4.9365 \\ 2.5 \times 0 \\ 0.5 \times 8.4818 \\ 0.5 \times 7.7180 \end{array} \right\}$	17.2778 5.5615 4.2409 3.8590
		$\overline{492.2585 \text{ MeV}}$
		-0.001

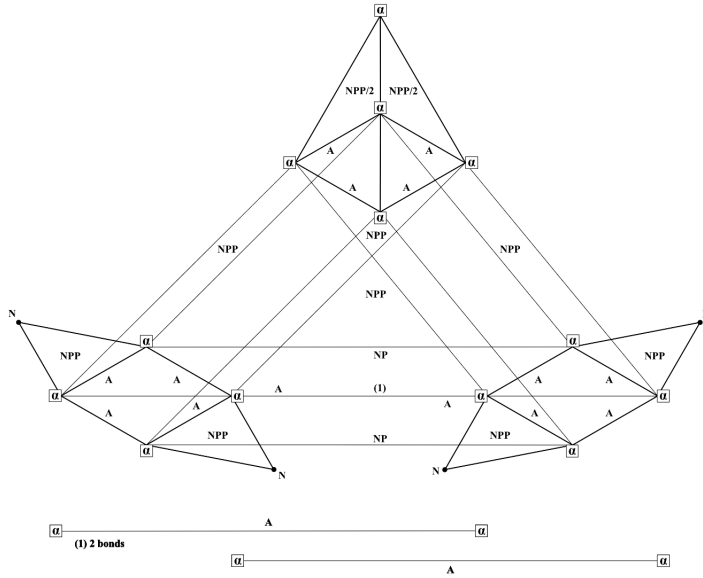
Figure 10. Binding energy distribution among ^{56}Fe .

Appendix K. $^{56}_{26}\text{Fe}$ Fig.2

Structure: 13 α , 4 N, 0 P

Linear and cross bonds: 14 A, 2 NP, 5 NPP

N, P supplementary bonds: 4 NPP



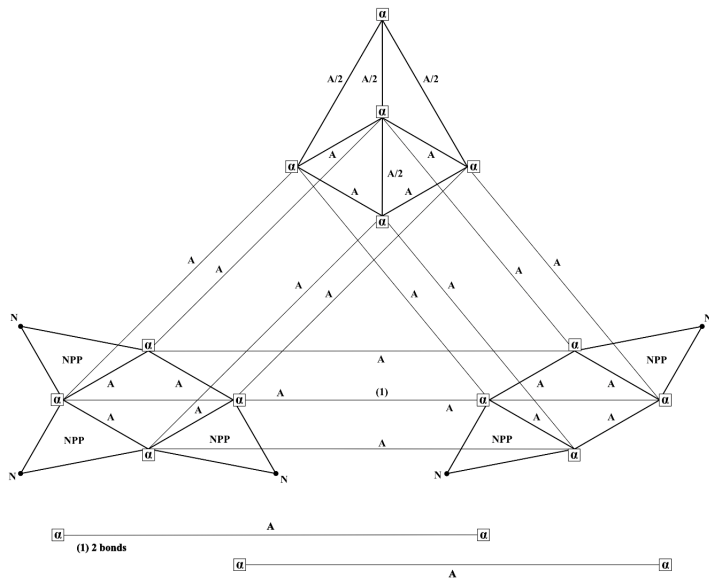
$^{56}_{26}\text{Fe}$ Fig.2	13 α , 4 N, 0 P supplementary	E_B (MeV)=492.2598
Stable Nat. abundance 91.8%	$\left\{ \begin{array}{l} 13 \times 28.3250 \\ 6.5 + 0.5 \times 4.9365 \\ 6.5 + 2.5 \times 2.2246 \\ 0 \times 8.4818 \\ 5 \times 7.7180 \end{array} \right\}$	368.2250 MeV
		34.5555
		20.0214
		0
		38.5900
	$\left\{ \begin{array}{l} 0 \times 4.9365 \\ 0 \times 2.2246 \\ 0 \times 8.4818 \\ 5 \times 7.7180 \end{array} \right\}$	0
		0
		0
		30.8720
		$\overline{492.2639 \text{ MeV}}$
		+0.004

Figure 11. Binding energy distribution among ^{56}Fe .

Appendix L. $^{57}_{26}\text{Fe}$ Structure: 13 α , 5 N, 0 P

Linear and cross bonds: 26 A

N, P supplementary bonds: 5 NPP



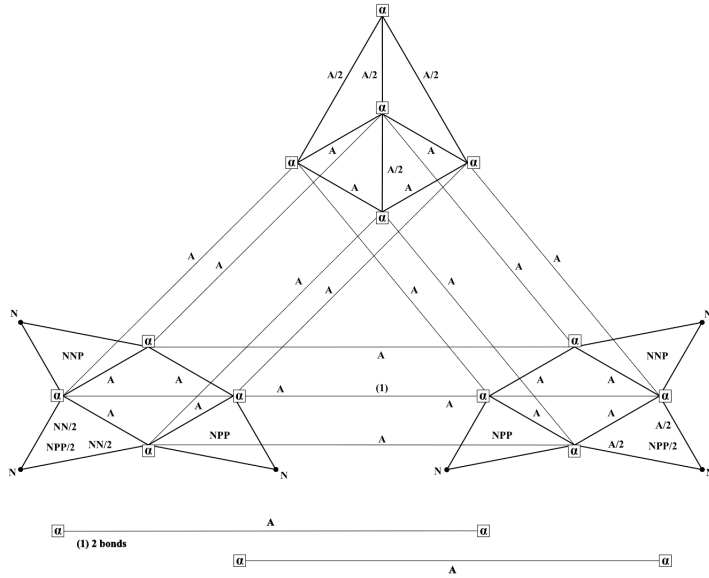
$^{57}_{26}\text{Fe}$	13 α , 5 N, 0 P supplementary	E_B (MeV)=499.9059
Stable Nat. abundance 2.1%	$\left\{ \begin{array}{l} 13 \times 28.3250 \\ 6.5 + 6.5 \times 4.9365 \\ 6.5 + 6.5 \times 2.2246 \\ 0 \times 8.4818 \\ 0 \times 7.7180 \end{array} \right\}$	368.2250 MeV 64.1745 28.9198 0 0
	$\left\{ \begin{array}{l} 0 \times 4.9365 \\ 0 \times 2.2246 \\ 0 \times 8.4818 \\ 5 \times 7.7180 \end{array} \right\}$	0 0 0 38.5900
		<u>499.9093 MeV</u>
		+0.004

Figure 12. Binding energy distribution among ^{57}Fe .

Appendix M. $^{58}_{26}\text{Fe}$ Structure: 13 α , 6 N, 0 P

Linear and cross bonds: 26 A

N, P supplementary bonds: A, NN, 2 NP, 3 NPP



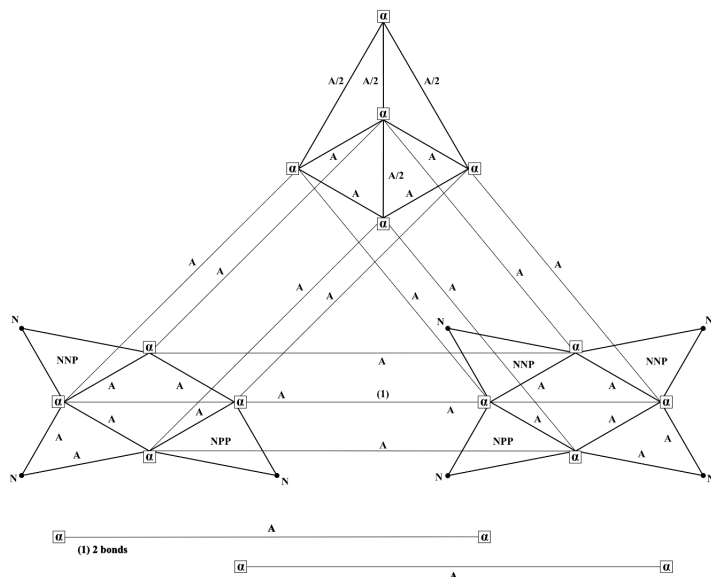
$^{58}_{26}\text{Fe}$	13 α , 6 N, 0 P supplementary	E_B (MeV)=509.9505
Stable Nat. abundance 0.3%	$\left\{ \begin{array}{l} 13 \times 28.3250 \\ 6.5 + 6.5 \times 4.9365 \\ 6.5 + 6.5 \times 2.2246 \\ 0 \times 8.4818 \\ 0 \times 7.7180 \end{array} \right\}$	368.2250 MeV 64.1745 28.9198 0 0
	$\left\{ \begin{array}{l} 1.5 \times 4.9365 \\ 0.5 \times 2.2246 \\ 2 \times 8.4818 \\ 3 \times 7.7180 \end{array} \right\}$	7.4048 1.1123 16.9636 23.1540
		$\overline{509.9540 \text{ MeV}}$
		+0.003

Figure 13. Binding energy distribution among ^{58}Fe .

Appendix N. $^{59}_{26}\text{Fe}$ Structure: 13 α , 7 N, 0 P

Linear and cross bonds: 26 A

N, P supplementary bonds: 4 A, 3 NNP, 2 NPP



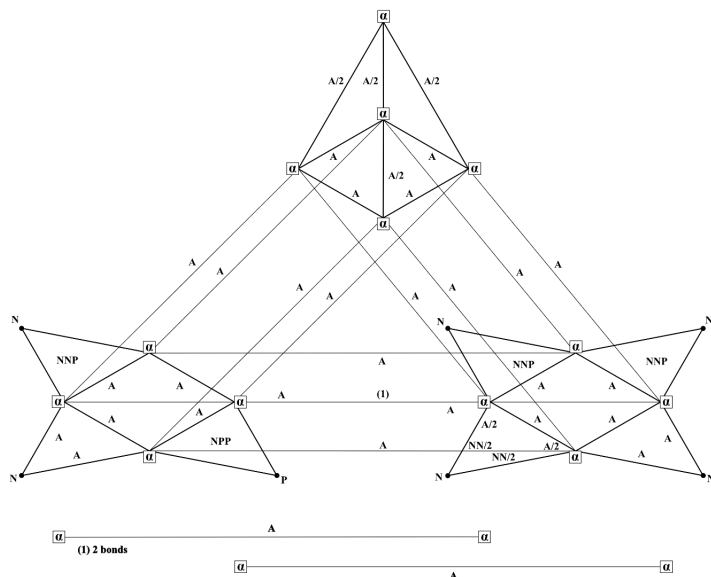
$^{59}_{26}\text{Fe}$	13 α , 7 N, 0 P supplementary	E_B (MeV)=516.5315
Lifetime: 45.1 days Mode of decay: β^-	$\left\{ \begin{array}{l} 13 \times 28.3250 \\ 6.5 + 6.5 \times 4.9365 \\ 6.5 + 6.5 \times 2.2246 \\ 0 \times 8.4818 \\ 0 \times 7.7180 \end{array} \right\}$	368.2250 MeV
		64.1745
		28.9198
		0
		0
	$\left\{ \begin{array}{l} 2 \times 4.9365 \\ 2 \times 2.2246 \\ 3 \times 8.4818 \\ 2 \times 7.7180 \end{array} \right\}$	9.8730
		4.4492
		25.4454
		15.4360
		$\overline{516.5229 \text{ MeV}}$
		-0.008

Figure 14. Binding energy distribution among ^{59}Fe .

Appendix O. $^{59}_{27}\text{Co}$ Structure: 13 α , 6 N, 1 P

Linear and cross bonds: 26 A

N, P supplementary bonds: 5 A, NN, 3 NNP, 1 NPP



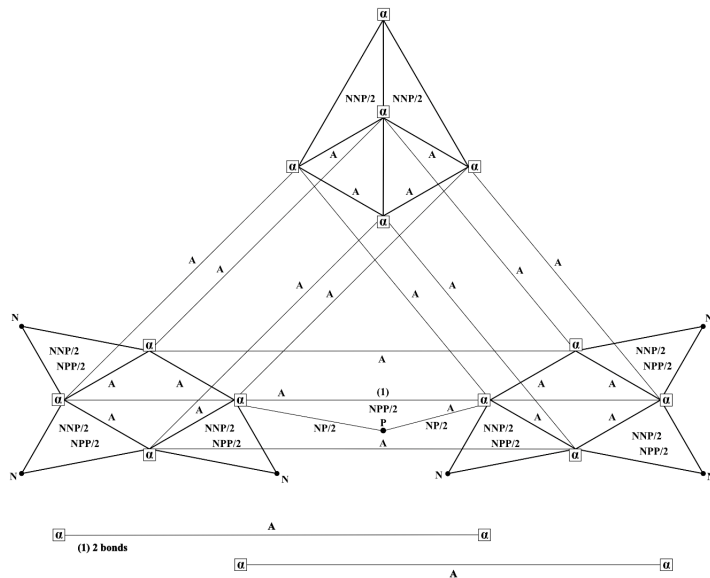
$^{59}_{27}\text{Co}$	13 α , 6 N, 1 P supplementary	E_B (MeV)=517.3141
Stable Nat. abundance 100%	$\left\{ \begin{array}{l} 13 \times 28.3250 \\ 6.5 + 6.5 \times 4.9365 \\ 6.5 + 6.5 \times 2.2246 \\ 0 \times 8.4818 \\ 0 \times 7.7180 \end{array} \right\}$	$\begin{array}{r} 368.2250 \text{ MeV} \\ 64.1745 \\ 28.9198 \\ 0 \\ 0 \end{array}$
	$\left\{ \begin{array}{l} 3.5 \times 4.9365 \\ 2.5 \times 2.2246 \\ 3 \times 8.4818 \\ 1 \times 7.7180 \end{array} \right\}$	$\begin{array}{r} 17.2778 \\ 5.5615 \\ 25.4454 \\ 7.7180 \end{array}$
		$\overline{517.3220 \text{ MeV}}$
		+0.008

Figure 15. Binding energy distribution among ^{59}Co .

Appendix P. $^{60}_{26}\text{Co}$ Fig. 2Structure: 13 α , 6 N, 1 P

Linear and cross bonds: 26 A, NNP

N, P supplementary bonds: NP, 3 NNP, 3 NNP, 3.5 NPP



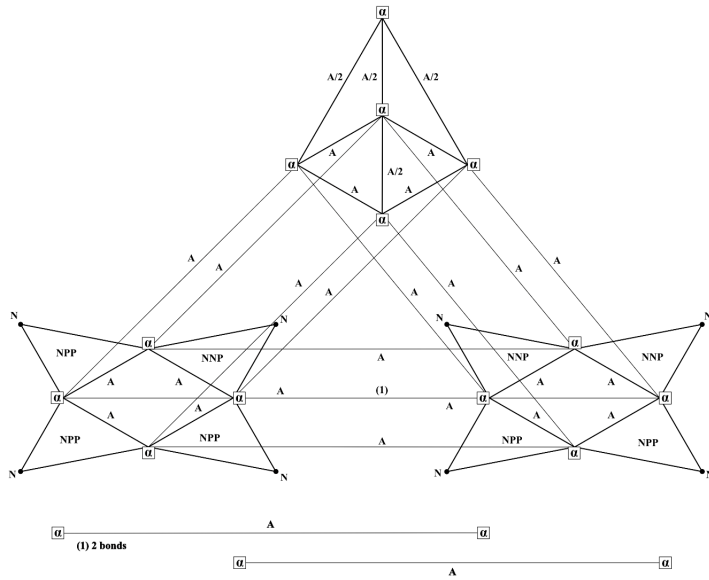
$^{59}_{27}\text{Co}$ Fig. 2	13 α , 6 N, 1 P supplementary	E_B (MeV)=517.3141
Stable Nat. abundance 100%	$\left\{ \begin{array}{l} 13 \times 28.3250 \\ 6.5 + 5.5 \times 4.9365 \\ 6.5 + 5.5 \times 2.2246 \\ 1 \times 8.4818 \\ 0 \times 7.7180 \end{array} \right\}$	$\begin{array}{l} 368.2250 \text{ MeV} \\ 59.2380 \\ 26.6952 \\ 8.4818 \\ 0 \end{array}$
	$\left\{ \begin{array}{l} 0 \times 4.9365 \\ 1 \times 2.2246 \\ 3 \times 8.4818 \\ 3.5 \times 7.7180 \end{array} \right\}$	$\begin{array}{l} 0 \\ 2.2846 \\ 25.4454 \\ 27.0130 \end{array}$
		$\overline{517.3230 \text{ MeV}}$
		-0.009

Figure 16. Binding energy distribution among ^{59}Co .

Appendix Q. ${}^{60}_{26}\text{Fe}$ Structure: 13 α , 8 N, 0 P

Linear and cross bonds: 26 A

N, P supplementary bonds: NP, 3 NNP, 5 NPP



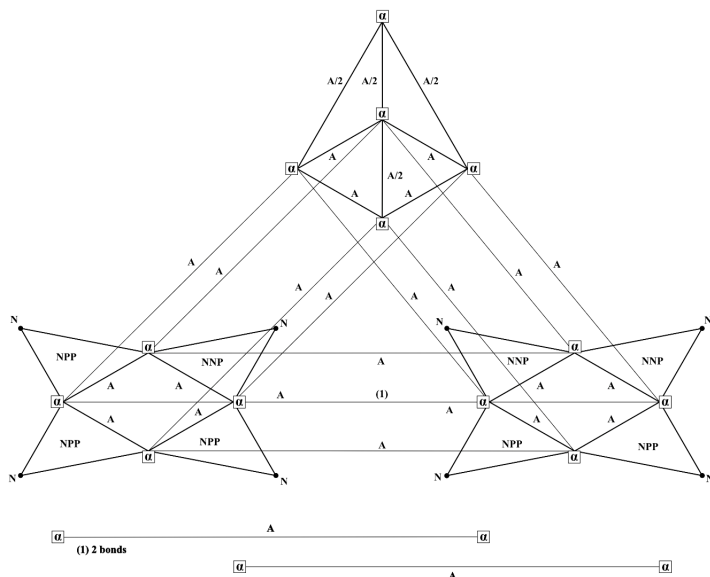
${}^{60}_{26}\text{Fe}$	13 α , 8 N, 0 P supplementary	E_B (MeV)=525.3511
Lifetime: 3×10^5 years Mode of decay: β^-	$\left\{ \begin{array}{l} 13 \times 28.3250 \\ 6.5 + 6.5 \times 4.9365 \\ 6.5 + 6.5 \times 2.2246 \\ 0 \times 8.4818 \\ 0 \times 7.7180 \end{array} \right\}$	368.2250 MeV 64.1745 28.9198 0 0
	$\left\{ \begin{array}{l} 0 \times 4.9365 \\ 0 \times 2.2246 \\ 3 \times 8.4818 \\ 5 \times 7.7180 \end{array} \right\}$	0 0 25.4454 38.5900
		$\overline{525.3547 \text{ MeV}}$
		+0.004

Figure 17. Binding energy distribution among ${}^{60}\text{Fe}$.

Appendix R. ${}^{61}_{26}\text{Fe}$ Structure: 13 α , 9 N, 0 P

Linear and cross bonds: 26 A

N, P supplementary bonds: 5 A, 2 NNP, 4.5 NPP



${}^{61}_{26}\text{Fe}$	13 α , 9 N, 0 P supplementary	E_B (MeV)=530.9298
Lifetime: 6 min Mode of decay: β^-	$\left\{ \begin{array}{l} 13 \times 28.3250 \\ 6.5 + 6.5 \times 4.9365 \\ 6.5 + 6.5 \times 2.2246 \\ 0 \times 8.4818 \\ 0 \times 7.7180 \end{array} \right\}$	$\begin{array}{l} 368.2250 \text{ MeV} \\ 64.1745 \\ 28.9198 \\ 0 \\ 0 \end{array}$
	$\left\{ \begin{array}{l} 2.5 \times 4.9365 \\ 2.5 \times 2.2246 \\ 2 \times 8.4818 \\ 4.5 \times 7.7180 \end{array} \right\}$	$\begin{array}{l} 12.3413 \\ 5.5615 \\ 16.9636 \\ 34.7310 \end{array}$
		$\overline{530.9167 \text{ MeV}}$
		-0.013

Figure 18. Binding energy distribution among ${}^{61}\text{Fe}$.